EUROPEAN COMMISSION

Community research

PAMINA
Performance Assessment Methodologies in Application to Guide the Development of the Safety Case

(Contract Number: FP6-036404)

Report on the benchmarks on rock salt
DELIVERABLE (D-N°:D4.1.1)

Author(s): **D. Buhmann, J. Grupa, J. Hart, R.-P. Hirsekorn**
A. Ionescu, C. Lerch, A. Rübel, A. Schneider, T.J. Schröder

Date of issue of this report: **31/08/2009**

Start date of project : **01/10/2006** Duration : 36 Months

Project co-funded by the European Commission under the Euratom Research and Training Programme on Nuclear Energy within the Sixth Framework Programme (2002-2006)		
Dissemination Level		
PU	Public	X
RE	Restricted to a group specified by the partners of the [PAMINA] project	
CO	Confidential, only for partners of the [PAMINA] project	


PAMINA

This report was compiled from contributions by the following authors:
(in alphabetical order)

Dieter Buhmann (GRS)

Jacques Grupa (NRG)

Jaap Hart (NRG)

Rolf-Peter Hirsekorn (GRS)

Alice Ionescu (GRS)

Christian Lerch (DBE-TEC)

André Rübel (GRS)

Anke Schneider (GRS)

Thomas J. Schröder (NRG)

DBE-TEC:	**Deutsche Gesellschaft zum Bau und Betrieb von Endlagern für Abfallstoffe (DBE) - Technology GmbH, Peine, Germany**
GRS:	**Gesellschaft für Anlagen- und Reaktorsicherheit (GRS) mbH, Braunschweig, Germany**
NRG:	**Nuclear Research consultancy Group (NRG), Petten, The Netherlands**


PAMINA

Foreword

The work presented in this report was developed within the Integrated Project PAMINA: **P**erformance **A**ssessment **M**ethodologies **IN A**pplication to Guide the Development of the Safety Case. This project is part of the Sixth Framework Programme of the European Commission. It brings together 25 organisations from ten European countries and one EC Joint Research Centre in order to improve and harmonise methodologies and tools for demonstrating the safety of deep geological disposal of long-lived radioactive waste for different waste types, repository designs and geological environments. The results will be of interest to national waste management organisations, regulators and lay stakeholders.

The work is organised in four Research and Technology Development Components (RTDCs) and one additional component dealing with knowledge management and dissemination of knowledge:

- In RTDC 1 the aim is to evaluate the state of the art of methodologies and approaches needed for assessing the safety of deep geological disposal, on the basis of comprehensive review of international practice. This work includes the identification of any deficiencies in methods and tools.

- In RTDC 2 the aim is to establish a framework and methodology for the treatment of uncertainty during PA and safety case development. Guidance on, and examples of, good practice will be provided on the communication and treatment of different types of uncertainty, spatial variability, the development of probabilistic safety assessment tools, and techniques for sensitivity and uncertainty analysis.

- In RTDC 3 the aim is to develop methodologies and tools for integrated PA for various geological disposal concepts. This work includes the development of PA scenarios, of the PA approach to gas migration processes, of the PA approach to radionuclide source term modelling, and of safety and performance indicators.

- In RTDC 4 the aim is to conduct several benchmark exercises on specific processes, in which quantitative comparisons are made between approaches that rely on simplifying assumptions and models, and those that rely on complex models that take into account a more complete process conceptualization in space and time.

The work presented in this report was performed in the scope of RTDC 4.

All PAMINA reports can be downloaded from http://www.ip-pamina.eu.


PAMINA

Contents


PAMINA

1. Introduction

The objectives of component four of the PAMINA project is to evaluate whether using more detailed and more realistic modelling approaches with the help of actual high-performance tools

- provide an added value in comparison with more simplified approaches used by PA codes, and
- are required to include processes not yet fully accounted for in performance assessment.

The evaluations consist in comparisons of the results from fully integrated models and supporting numerical codes with a high level of geometrical accuracy and results from usual compartmental, semi-analytical or simplified models and codes. By performing three benchmark exercises, each focussing on specific processes relevant for repository designs in salt rock, the relevance, advantages and limitations inherent to each approach and their associated tools will be assessed. The three processes investigated are the

- convergence of salt, the
- intrusion of brine into a backfilled drift and the
- radionuclide transport by density driven exchange.

In a repository design in a rock salt formation, after placement of the waste canisters, the drifts, boreholes, and chambers will be backfilled. One of the key elements of the long term performance of a disposal facility in rock salt is the creep behaviour of the rock salt. The remaining void volume will decrease over time due to the convergence process. In a normal evolution, in general, all open volumes and volumes filled with compactable material, such as salt grit, are compressed and become very low permeable. This provides for the long-term isolation of the waste from our environment, since no medium is present that could mobilise and transport radionuclides from the waste forms to the geosphere.

Complex codes have been used to develop and test creep models for rock salt, and have been validated in various in situ experiments (such as the subsequent BAMBUS projects in the Asse facility). These complex codes can now also be used to predict the creep behaviour in promising rock salt formations that have not yet been investigated. Since the complex codes are based on FEM or similar numerical methods, their application is limited to the prediction of the convergence behaviour of one or two galleries of the whole repository. For PA, it is required to be able to model the convergence behaviour of each ‘compartment’ of the facility. The number of calculational nodes needed to model the complete facility with the complex codes is however far beyond the present hardware capabilities. Since the convergence behaviour is a key ingredient to the long-term performance, alternative methods for application in PA codes have been developed. The results from PA codes and rock me-

chanic codes are compared in chapter 2 to validate the applicability of the models implemented in the PA codes.

In general, there is no transport medium present from the very beginning in a repository in a salt formation. However, in other evolution scenarios one may consider the presence of brine inside the repository, e.g. by brine intrusion from either outside of the salt formation or from undetected brine inclusions in the neighbourhood of the repository. The intruding brine may successively fill up the residual voids within the backfilled drifts and chambers or boreholes of the repository, eventually gets into contact with the disposed wastes, where the brine becomes contaminated with radionuclides as soon as the container fails. Convergence of the salt rock or other processes like gas production may enhance the release of contaminated brine out of the repository into the overburden and finally into the biosphere. Thus, the process of brine intrusion, where brine percolates through barrier systems like crushed salt backfill and the process of convergence of the salt rock as one of the relevant driving processes for a potential release of contaminated brine are important processes, which have to be understood very well.

In the present codes used for the performance assessment of brine intrusion into backfilled drifts, the flow resistance of these drifts is assumed to be independent of the gas or brine saturation of the backfill. Although it is known that under unsaturated conditions, the flow differs from the fully saturated case, PA codes are usually using a constant permeability. Related processes like the settling of crushed salt when becoming wet or the dissolution of backfill by contact with unsaturated brine is often represented by a simplified model using a fit parameter. Therefore, a benchmark exercise is defined addressing the inflow of brine into a backfilled gallery. In Chapter 3, the results of this benchmark exercise is summarized and the results of two PA codes and the more complex code HYDRUS code, that takes unsaturated flow into account, are compared.

Because the creep of the rock salt under some conditions occurs relatively slow, other transport processes for the contamination in the brine can be relevant. One of these processes is the density gradient driven exchange. For example, the density of brine in heated sections of the facility (due to heat generating waste) is decreased. This density difference leads to convective exchange flows that have the potential of being more effective than advective transport of contamination. Another process is the dispersive component of advective transport in porous media, which is characterised by the dispersion length. The results from PA codes and the more complex code PORFLOW is compared in chapter 4 to validate the applicability of the models implemented in the PA codes.

2. Benchmark on convergence

2.1 Introduction

The disposal of radioactive waste in a salt formation will take place in disposal chambers or disposal boreholes. These chambers and boreholes are connected with the shaft area via drifts and galleries. Since rock salt is a plastic material, it will flow (or creep) towards the area with decreased stress, i.e. towards the excavations. This means that with time the volume of the excavation decreases as long as the stress against the wall of the excavation is less than the lithostatic pressure. This process is referred to as convergence of the rock salt.

In general, the convergence depends on the load capacity of the overlaying salt rock and overburden as well as on the pressure within the cavities and on the resistance of backfill material against compaction. As the pressure inside the cavity may originate from intruded brine or from gas, the expression *fluid pressure* will be used, except if the pressure of liquid or gas is meant in particular.

The transport of contaminants, e.g. radionuclides, is influenced by the convergence in different ways: If intrusion of liquid takes place at late times, the convergence has reduced the pore volume and only a small amount of brine would reach the disposed waste. In addition the flow resistance of backfilled cavities has been increased, so that the intrusion of liquid may be strongly impeded. On the other hand, after the drift and the disposal location are flooded with liquid, the convergence dominates the release of contaminated brine from the repository for the long-term.

During liquid intrusion into a cavity the fluid pressure rises. At the beginning, this pressure corresponds to that of the liquid column in the cavity. If the liquid column extends up to the aquifer, the fluid pressure increases to the hydrostatic pressure corresponding to the depth of the respective cavity in the flooded disposal facility. The fluid pressure reduces the convergence and thus sustains the cavity. If gas is produced and/or stored in the cavity, beside the pressure of liquid also that of gas reduces convergence. Due to flow resistances in the repository the fluid pressure may rise above the hydrostatic value. This so-called hydraulic pressure intensifies the sustaining action of the fluid pressure and thus further reduces convergence.

In a backfilled cavity the progressive compaction of backfill reduces the convergence rate. From experimental investigations it turns out that dry backfill shows quite different compaction behaviour than wet or brine saturated backfill.

A benchmark exercise studying the effect of convergence of rock salt cavities for five different test cases has been performed. It was investigated by this exercise, how reliable the simplifying assumptions and models in PA codes are in predicting convergence processes, if these predictions are compared to more complex process models implemented in rock mechanics codes. Furthermore, it was evaluated whether the more complex and more realistic

modelling approaches provide added value and whether they are required to include processes not yet fully accounted for in PA.

The rock mechanics calculations have been performed by DBE-TEC with the FLAC code to get the results for a detailed modelling of the convergence process. The PA code calculations have been done by GRS using the LOPOS module of the EMOS code and by NRG using the REPOS[1] code. Suitable parameter values for LOPOS and REPOS were derived by comparison to some of the results of the rock mechanics calculations.

In the following, the test cases are described (chapter 2.2), followed by a detailed description of the conceptual models of convergence in the PA codes and the 3D rock mechanics code (chapter 2.3). In chapter 2.4 the results of the benchmark calculations with both PA codes are presented, and in chapter 2.5 the results of these calculations are compared.

2.2 Benchmark tests

2.2.1 Definition of test cases

To compare the results from calculations with different models of convergence, as implemented in the EMOS code (near-field modules REPOS used by NRG and LOPOS used by GRS), with each other and with those obtained from rock mechanics calculations with FLAC performed by DBE-TEC, several test cases have been established. The benchmark calculations are based on a simplified model of a repository in a salt formation consisting of a cavity as indicated in Fig. 2.2.1. The cavity might be a chamber or a gallery, the shaft gives the brine access to the cavity and provides the boundary conditions for the fluid pressure. The shaft has been considered only in the EMOS calculations, where it is modelled as a vertical circular tube backfilled with non-compactable material. Its permeability is selected to achieve a constant fluid pressure, with different values for the test cases. The realization of this fluid pressure is discussed below. To simplify the rock mechanics calculations a homogeneous isotropic rock formation around the cavity is assumed.

[1] This code is sometimes referred to as REPOS-ECN, because it's a modified version of the original REPOS module as implemented in the EMOS package of GRS. For simplicity, in the following it is called REPOS only.

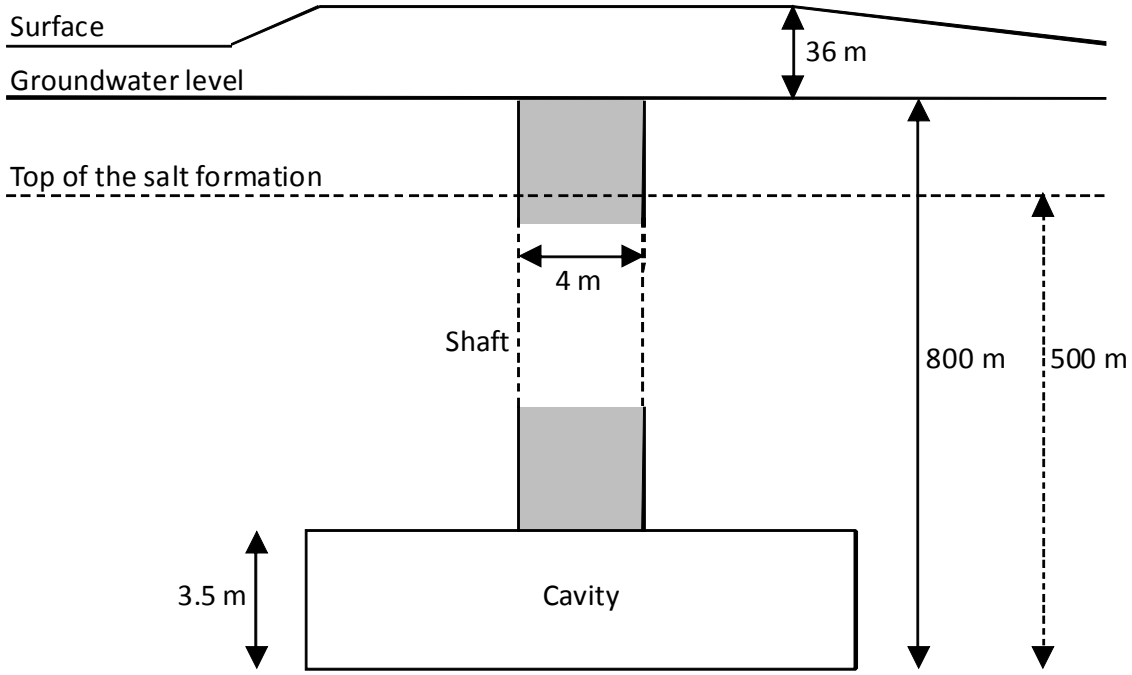

Fig. 2.2.1: Schematic representation of the repository

The following test cases have been defined; see also the sketches in chapter 2.2.2. The results of the calculations in chapter 2.4 will refer to these cases by the numbers given in the bullets below.

Case 1:

- Open cavity with no backfill
  - 1a: no brine, atmospheric pressure
  - 1b: with constant fluid pressure, brine up to the top of the salt formation
  - 1c: with constant fluid pressure, brine up to the surface
  - 1d: with time dependent fluid pressure, brine up to the surface

Case 2:

- Backfilled cavity completely filled with crushed salt, atmospheric pressure
  - 2a: dry crushed salt
  - 2b: wet crushed salt

Case 3:

- Backfilled cavity completely filled with crushed salt
  - 3a: with constant fluid pressure, brine up to the top of the salt formation
  - 3b: with constant fluid pressure, brine up to the surface
  - 3c: with time dependent fluid pressure, brine up to the surface

Case 4:

- Cavity with a layer of uncompactable material at the bottom
  - 4a: no backfill in the residual volume, no brine, atmospheric pressure
  - 4b: residual volume backfilled with crushed salt, no brine, atmospheric pressure

Case 5:

- Cavity filled with crushed salt around a steel container lying on the floor
  - 5a: no brine, atmospheric pressure
  - 5b: with constant fluid pressure, brine up to the top of the salt formation
  - 5c: with constant fluid pressure, brine up to the surface
  - 5d: with time dependent fluid pressure, brine up to the surface

The results of the rock mechanics calculations of test cases 1a, 2a and 2b are used for the calibration of the convergence models implemented in EMOS. In the EMOS module LOPOS these are case 1a, to find the parameter values of the explicit time dependence of the convergence rate (cf. chapter 2.3.1.2.2) and the asymptotic value of the convergence rate, i.e. the stationary value at late times. Cases 2a and 2b are expected to give the specific backfill parameters of the convergence model of EMOS.

The FLAC code has been applied to a cross section of a cavity having the size and dimension as used in the BAMBUS project [1]. For the EMOS calculations a definite size of the cross section is not considered, however, its area is approximated by a rectangle as given in table 2.2.1.

The fluid pressure dependence of the convergence is investigated under different boundary conditions. As a first variant, atmospheric pressure is applied. In the second variant, a hydrostatic pressure of brine is applied, where the repository is filled with brine up to the top of the salt formation. The third variant assumes a hydrostatic pressure from brine filled up to the surface. The corresponding hydrostatic pressure values are given in table 2.2.1.

To simplify the benchmark calculations and to find a systematic behaviour of the pressure dependence, the test case models are adjusted in such a way that the fluid pressure remains

constant during the convergence process except in test cases 1d, 3c, and 5d. The time dependent fluid pressures applied in test cases 1d, 3c, and 5d are calculated with the EMOS codes and then act as boundary conditions in the rock mechanics calculations.

The convergence and backfill compaction are modelled differently in the codes. FLAC uses the constitutive law BGRa for the convergence of the salt rock and the CWIPP and/or Hein for backfill compaction (cf. section 2.3.4). LOPOS uses the parameters given in the LOPOS code description 1, where the values of the parameters are obtained by approximation of the FLAC results of test cases 1a, 2a and 2b. EMOS-ECN uses the formulas given in the REPOS code description with parameter values also obtained by approximation of the FLAC results (cf. 2.3.3).

In test cases 4a and 4b a layer of concrete is assumed, whose elastic behaviour is considered in the FLAC code using parameters as given in table 2.2.1. In test cases 5a to 5d a steel container is assumed whose elastic behaviour is also considered using the corresponding parameters of table 2.2.1.

To model a constant fluid pressure in EMOS the following procedure was proposed:

- A constant fluid pressure can be achieved in LOPOS by giving the shaft a very small flow resistance and connecting shaft and cavity perpendicular to each other, such that the convergence cannot increase the fluid pressure.

  In REPOS a constant very small resistance can be given to the cavity explicitly, neglecting the relation between porosity and permeability of backfill.

To model a time dependent fluid pressure in EMOS the following procedure was proposed:

- A time dependent fluid pressure is automatically achieved in EMOS by giving the shaft a considerable flow resistance. Its value will be fixed after the convergence parameters are determined from the results of the rock mechanics calculation (case1a).

To model the fluid pressure in FLAC the following procedure was proposed:

- In FLAC the fluid pressure in the cavity is achieved by stress boundary condition, where the stress value can be constant as well as varying over time.

For simplicity, the rock pressure and the hydrostatic fluid pressure are obtained assuming a depth-independent average rock density and an average brine density, respectively.

In the following, the results for the convergence rate, the volume decrease, and – for backfilled cavities – the porosity evolution are given as functions of time. In addition, the convergence rates as functions of porosity are plotted for the backfilled cavities.

2.2.2 General data for the test case modelling

Schematic representations of the repository model used in the various test cases are given in figures 2.2.2 to 2.2.5. Parameter values describing the geometry of the cavity, the depth of the repository, initial values of pressure, porosity etc. used in the various test cases and codes are given in table 2.2.1. The initial value of the convergence rate and its stationary value at very late times follow from the results of the rock mechanics calculation in test case 1a. A number of parameters are specific for the different codes. These parameters are given in chapters 2.3 and 2.4.2 for the LOPOS code, and in chapter 2.4.3 for the REPOS code.

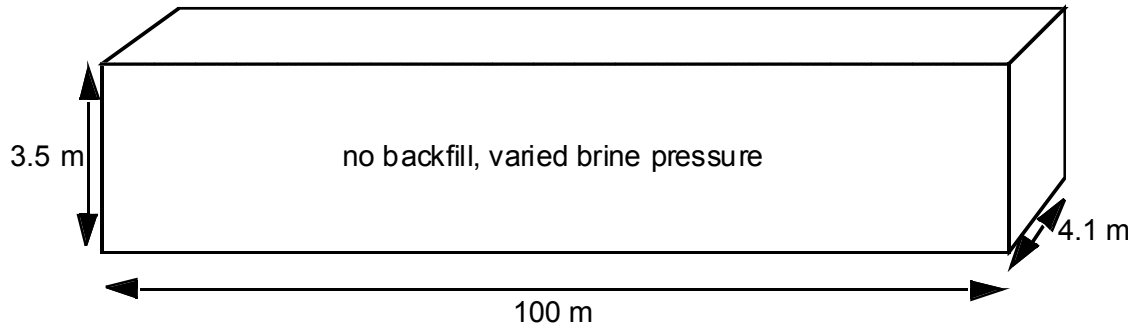

Fig. 2.2.2: Model cavity for cases 1a – d

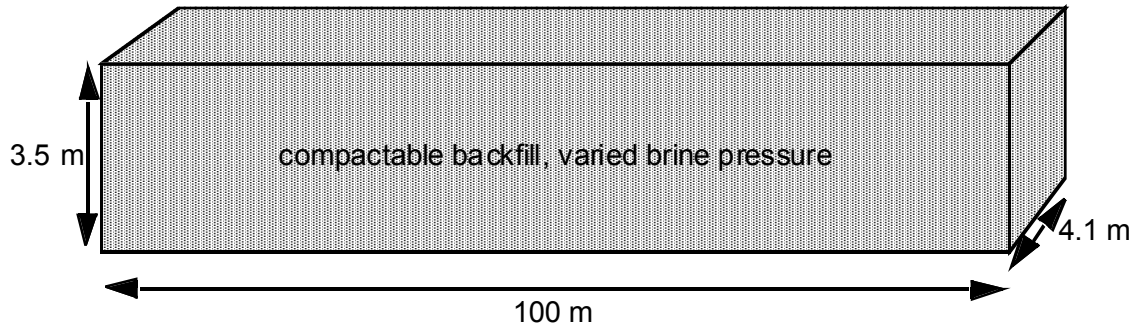

Fig. 2.2.3: Model cavity for cases 2a,b, 3a – c

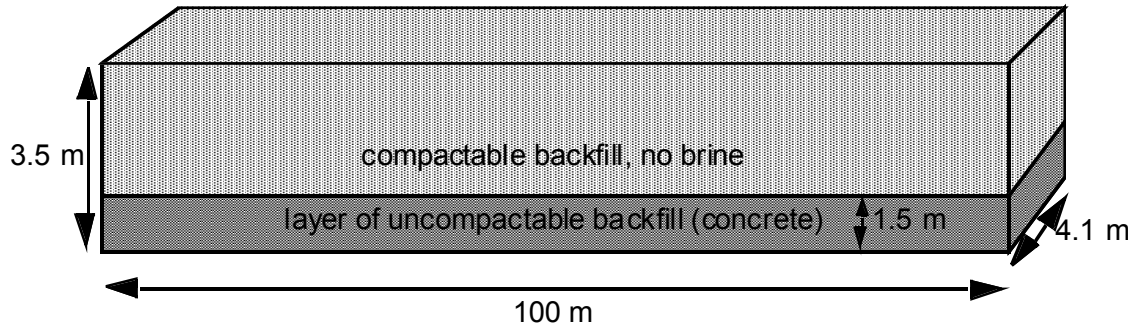

Fig. 2.2.4: Model cavity for cases 4a, b

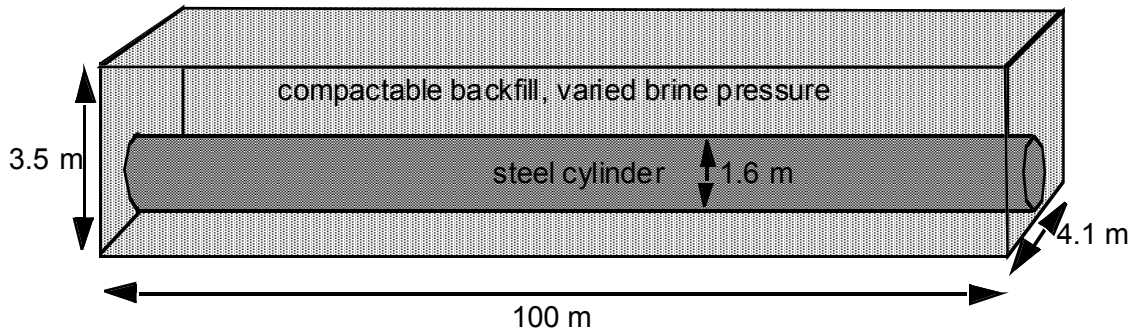

Fig. 2.2.5: Model cavity for cases 5a - d

Tab. 2.2.1: General data for test cases

Parameter	Case 1	Case 2	Case 3	Case 4	Case 5
depth of the repository referred to sea level: (reference level) [m]	-800	-800	-800	-800	-800
top of the salt formation [m]	-300	-300	-300	-300	-300
surface [m]	36	36	36	36	36
groundwater level [m]	0	0	0	0	0
atmospheric pressure [MPa]	0.1	0.1	0.1	0.1	0.1
mean rock density [kg/m^3]	2187	2187	2187	2187	2187
rock pressure at reference level [MPa]	17.94	17.94	17.94	17.94	17.94
brine density [kg/m^3]	1200	1200	1200	1200	1200
hydrostatic pressure at the bottom of the cavity [MPa]	a: 0.00 b: 5.89 c: 9.42 d: var.	a: 0.00 b: 0.00	a: 5.89 b: 9.42 c: var.	a: 0.00 b: 0.00	a: 0.00 b: 5.89 c: 9.42 d: var.
rock temperature at reference level [K]	310	310	310	310	310
initial value of backfill porosity (crushed salt) [-]	-	0.35	0.35	0.35	0.35
stress exponent [-]	5	5	5	5	5
height of the cavity [m]	3.5	3.5	3.5	3.5	3.5
width of the cavity [m]	4.1	4.1	4.1	4.1	4.1

Parameter		Case 1	Case 2	Case 3	Case 4	Case 5
length of the cavity	[m]	100	100	100	100	100
thickness of the layer of concrete at the bottom of the cavity	[m]	-	-	-	1.5	-
E module of concrete	[MPa]	-	-	-	15 000	-
sheer module í of concrete	[-]	-	-	-	0.25	-
diameter of the steel cylinder (hypothetic row of containers)	[m]	-	-	-	-	1.6
length of the steel cylinder	[m]	-	-	-	-	100
E module of steel	[MPa]	-	-	-	210 000	-
sheer module *í* of steel	[-]	-	-	-	0.30	-

2.3 Description of the models

2.3.1 GRS (LOPOS) convergence model

The convergence model used in the LOPOS code of GRS takes into account the effects of fluid pressure and backfill compaction. The values of the parameters of the convergence formula in general have to be derived from rock mechanics calculations corresponding to the properties of the geological formation at the repository site. In this project, the values have been derived from the rock mechanics calculations performed by DBE-TEC.

2.3.1.1 Modelling

The volume of a cavity decreases in time by convergence. The rate of decrease is calculated by

$$\frac{d}{dt}V(t) = -K(t)\cdot V(t), \qquad 2.3.1$$

i.e. the volume change is proportional to the volume $V(t)$ at time t and the proportionality factor is the convergence rate $K(t)$. The convergence rate is, thus, defined as the volume change related to the current volume, and sometimes is called the logarithmic convergence rate. In LOPOS, the convergence rate is modelled as a product of factors and functions

$$K = K_{ref} \cdot f_{loc} \cdot f_t \cdot f_p \cdot f_\phi \cdot f_T \,, \qquad 2.3.2$$

describing the dependence of the convergence rate on different quantities, discussed in the following.

The quantity K_{ref} is called reference convergence rate. It gives the stationary convergence rate of a cavity containing neither backfill nor fluid, with reference conditions of the salt rock concerning temperature, rock pressure and composition of the salt, located on the reference level z_{ref} of the repository. The stationary value will be reached at the limit $t \to \infty$. The remaining factors stand for the following dependencies:

- f_{loc}: local properties of the surrounding salt rock,
- f_t: "explicit time dependence" of the convergence process,
- f_p: resistance against convergence due to fluid pressure *p* of liquid or gas,
- f_ϕ: resistance against convergence by the porous medium. This resistance depends on the porosity ϕ, which decreases by compaction of dry or wet backfill,
- f_T: acceleration of convergence by increase of temperature T due to heat producing waste.

Local properties are the salt composition around the considered cavity, the depth z where the cavity is located, the distance to the margins of the salt dome, possible anhydrite layers or the presence of other cavities in the neighbourhood. "Explicit time dependence" refers to the time evolution of the convergence rate, which is not due to time dependence of fluid pressure, porosity or temperature. The functions f_p and f_ϕ provide the dependences of the convergence rate on the fluid pressure and on the backfill porosity, respectively. The function f_T describes the temperature dependence of the convergence rate with respect to an increased temperature which lies above the local rock temperature and comes from heat producing waste.

Some of the factors reduce the convergence rate, e.g. the support by fluid pressure or backfill compaction. These factors are, thus, smaller than one. Other factors increase the convergence rate. These are the temperature increase and the explicit time dependence. These factors are greater than one. The dependence on local properties may either increase or decrease the convergence rate.

In the following subsections the individual factors of eq. 2.3.2 are described in more detail.

2.3.1.2 Dependence on local properties

In general, the convergence rate depends on local properties of the surrounding rock and on the depth where the cavity is located. The depth determines the convergence rate via the rock pressure as well as the rock temperature. All local properties are summarised in the factor f_{loc}, which, thus, describes a deviation from a reference situation and might vary from cavity to cavity. However, it is assumed to be constant in time.

The specific value of f_{loc} is determined by comparing the convergence rate of a reference cavity with convergence rates obtained either from rock mechanics calculations for a cavity with neither backfill nor liquid but air under atmospheric pressure or from experimental investigations.

2.3.1.2.1. Fluid pressure dependence

The fluid pressure supports the rock formation and reduces convergence. The dependence of the convergence rate on fluid pressure is described by the function f_p:

$$f_p(p) = \left(1 - \frac{p(z,t) - p_{atm}}{p_R(z)}\right)^m . \qquad 2.3.3$$

Here m is the stress exponent, $p(z,t)$ the fluid pressure at time t in the depth z of the cavity and $p_R(z)$ the local rock pressure. For simplicity, the fluid pressure is reduced by the atmospheric pressure p_{atm} so that the function f_p becomes 1 for an air filled cavity ($p = p_{atm}$).

In equation 2.3.3 the ratio between fluid pressure $p(z,t)$ - p_{atm} and the local rock pressure $p_R(z)$ at depth z significantly influences the convergence rate. In an idealised infinite salt formation the local rock pressure is determined by the density and thickness of the overlying strata. For a real repository in a limited, highly pierced salt rock it is more convenient to replace the local rock pressure in eq. 2.3.3 by an advanced approach

$$p_R(z) = p_R(z_{ref}) - f_{p_R} \cdot (z - z_{ref}) \rho_S g , \qquad 2.3.4$$

where $p_R(z_{ref})$ is the rock pressure on the reference level z_{ref}, g refers to the acceleration of gravity, ρ_S defines the average rock density and (z - z_{ref}) is the distance of the considered floor from the reference level. The parameter f_{p_R} can be acquired from e.g. comparison of convergence rates with those resulting from rock mechanics calculations.

At the beginning, the fluid pressure corresponds to the atmospheric pressure p_{atm} of about 0.1 MPa. The stress exponent m is determined by the constitutive law of rock salt. A value of $m = 5$ is used here. During liquid intrusion the fluid pressure in the considered cavity is given

by the current fluid level and, in case of gas storage – mainly after production of gas in the cavity –, from increasing gas pressure. After filling of the cavity the fluid pressure is given by the hydraulic conditions in the repository and may rise significantly above the hydrostatic pressure.

In general, the fluid pressure p changes with time and, thus, the convergence rate is "implicitly" time dependent via fluid pressure. The behaviour of the convergence rate, where different constant and time dependent fluid pressures are applied, is investigated in the test cases given below.

2.3.1.2.2. "Explicit time dependence"

Investigations of cavities of a repository and rock mechanics calculations show that the convergence rate of a recently excavated not backfilled chamber changes significantly with time and may be reduced over several orders of magnitude ([9], [4]). The time span during which the convergence rate approaches the stationary value depends on the fluid pressure inside the cavity. However, this time dependence also shows up for a constant or even vanishing fluid pressure.

To describe this behaviour the function f_t is introduced. For large times the convergence rate of a not backfilled cavity with constant fluid pressure and not increased temperature, located in the depth z, approaches a constant local value, i.e. with vanishing fluid pressure ($f_p \equiv 1$) one has

$$\lim_{t\to\infty} K(z,t) = K_{ref} \cdot f_{loc}\,, \qquad 2.3.5$$

where K_{ref} is the stationary value at the reference level and $K_{ref} \cdot f_{loc}$ gives the local stationary value for a cavity in the depth z.

With ongoing convergence the current value of the convergence rate K approaches the local stationary value $K_{ref} \cdot f_{loc}$. For a simple implementation of this effect we assume a monotonously decreasing function for f_t which approaches 1 and depends on the history of the convergence process, i.e.

$$f_t = 1 + \frac{A}{\int_{t_0}^{0} K(t')dt' + \int_0^t K(t')dt'} = 1 + \frac{A}{\lambda_S + \int_0^t K(t')dt'}\,, \qquad 2.3.6$$

where the parameter λ_S refers to the previous history of the cavity from the excavation to the time-zero point of the model calculation. The integral of the convergence rate (right-hand side of the equation) yields the convergence of the cavity between t_0 and the current time t. The further the convergence runs, the greater the integral will be and, thus, the denominator

of the above expression. The function f_t approaches 1, where the parameter A will be used to fit this approach.

From the definition of the convergence rate in eq. 2.3.1 follows

$$\int_0^t K(t')dt' = \ln\left(\frac{V_0}{V(t)}\right), \qquad 2.3.7$$

where V_0 is the initial volume of the cavity at time t = 0. Applying this expression yields the following formula for f_t,

$$f_t = 1 + \frac{A}{\lambda_S + \ln(V_0/V)}. \qquad 2.3.8$$

The two parameters λ_S and A are used to fit the convergence rate to results from rock mechanics calculation. If $\lambda_S \neq 0$, it might be of advantage to substitute the parameter A by the following:

For t = 0 one has $K = K_0, f_p$ = 1, f_T = 1, f_t = 1+ A/λ_S and $f_\phi = f_\phi(\phi_0)$, so that

$$K_0 = K_0(z_{ref}) \cdot f_{loc} = K_{ref} \cdot f_{loc} \cdot f_\phi(\phi_0) \cdot \left(1 + \frac{A}{\lambda_S}\right) \qquad 2.3.9$$

holds. Therefore, the parameter A can be replaced by

$$A = \lambda_S \cdot \left(\frac{K_0(z_{ref})}{K_{ref} \cdot f_\phi(\phi_0)} - 1\right). \qquad 2.3.10$$

This procedure is advantageous, if the initial value K_0 of the convergence rate at t = 0 can be taken from in-situ experiments or follows from rock mechanics calculations. The stationary value K_{ref} cannot be directly found by in-situ experiments but may be determined by extrapolation of measured time evolutions of the convergence rate or can be taken from results of rock mechanics calculations. The value of the backfill function $f_\phi(\phi_0)$ follows from the formula given in the next chapter.

The “explicit time dependence” of the convergence rate is investigated in the test cases. Convergence rates obtained with the above formula are then compared with those from rock mechanics calculations and those from the alternative approach given by NRG.

2.3.1.2.3. Backfill dependence

In a backfilled cavity the convergence is strongly reduced by the continuous compaction of the backfill material. For backfill material consisting of crushed salt, the resistance against convergence can be described by a function of the backfill porosity. In general, there is a so-called reference porosity which describes a limit of the porosity of the backfill, below which a resistance against convergence occurs. For higher porosity there is no resistance and with lower porosity the resistance may completely suppress the convergence. This dependence of the convergence rate on the backfill porosity is described by the function $f_\phi(\phi,\phi_r)$, for which in ref. [3] the following relation was derived,

$$f_\phi(\phi,\phi_r)=\left[1+\frac{h(\phi,\phi_r)}{[\phi\cdot g(\phi,\phi_r)]^{1/m}}\right]^{-m} \quad \text{for } \phi<\phi_r\,, \tag{2.3.11}$$

where the quantity ϕ_r is the reference porosity. The reference porosity will take the same value for similar backfill materials but may differ, if other materials than crushed salt are used. In the derivation of eq. 2.3.11 also the constitutive law of secondary creep of rock salt has been used. Thus, the exponent m is the same as in eq. 2.3.3. Since the porosity, in general, is time dependent an additional time dependence of the convergence rate results.

There are some boundary conditions which the porosity function should fulfil. Since there is no reduction of the convergence rate for porosities greater than ϕ_r one has

$$f_\phi(\phi,\phi_r)=1 \quad \text{for } \phi\geq\phi_r\,. \tag{2.3.12}$$

Furthermore, the resistance against convergence sets up continuously at $\phi = \phi_r$, i.e.

$$\left.\frac{df}{d\phi}\right|_{\phi=\phi_r}=0\,. \tag{2.3.13}$$

For very small porosity the convergence rate may behave like that of a single pore, i.e. a very small cavity with no backfill. Thus, one has $f_\phi(\phi)\approx\phi$ or

$$\left.\frac{df}{d\phi}\right|_{\phi=0_r}=1\,. \tag{2.3.14}$$

For a vanishing porosity the function $f_\phi(\phi)$ approaches zero, i.e.

$$f(\phi=0)=0\,. \tag{2.3.15}$$

Applying these boundary conditions to the functions $h(\phi,\phi_r)$ and $g(\phi,\phi_r)$ in eq. 2.3.11 one has

$$h(\phi=0)=1\,, \tag{2.3.16}$$

$$h(\phi=\phi_r)=0\,, \tag{2.3.17}$$

$$\left.\frac{dh}{d\phi}\right|_{\phi=\phi_{rr}}=0 \tag{2.3.18}$$

and for $g(\phi,\phi_r)$

$$g(\phi=0)=1 \tag{2.3.19}$$

Instead of a second order approximation for $h(\phi,\phi_r)$, which is used in [3], a third order approximation is used here,

$$h(\phi,\phi_r)=h_0+h_1\frac{\phi}{\phi_r}+h_2\left(\frac{\phi}{\phi_r}\right)^2+h_3\left(\frac{\phi}{\phi_r}\right)^3 \tag{2.3.20}$$

and for $g(\phi,\phi_r)$ instead of a linear approximation, a second order approximation is used,

$$g(\phi,\phi_r)=g_0+g_1\frac{\phi}{\phi_r}+g_2\left(\frac{\phi}{\phi_r}\right)^2. \tag{2.3.21}$$

With the above boundary conditions some of the parameters in 2.3.20 and 2.3.21 are fixed as

$$h_0=1\,, \tag{2.3.22}$$

$$h_2=-(3+2h_1)\,, \tag{2.3.23}$$

$$h_3=h_1+2 \tag{2.3.24}$$

and

$$g_0=1\,. \tag{2.3.25}$$

This finally yields

$$h(\phi,\phi_r)=\left(1-\frac{\phi}{\phi_r}\right)^2\cdot\left\{1+(2+h_1)\frac{\phi}{\phi_r}\right\} \qquad 2.3.26$$

and

$$g(\phi,\phi_r)=1+g_1\frac{\phi}{\phi_r}+g_2\left(\frac{\phi}{\phi_r}\right)^2. \qquad 2.3.27$$

Thus, 3 parameters h_1, g_1 and g_2 remain as fitting parameters. Their values can be determined by comparing convergence rates with results from rock mechanics calculations. The additional parameter ϕ_r which is assumed to be specific for different backfill materials, is not used as fitting parameter.

Determination of the parameters of the porosity function f_ϕ is the task of test case 2. The earlier PSE-formula [3] for the support property of backfill can be derived from 2.3.11 by using h_1 = -2, g_1 = -1 and g_2 = 0.

2.3.1.2.4. Temperature dependence

An increase of temperature in and around the cavity yields a higher convergence rate. This effect is described by the function $f_T(\mathrm{T})$. The temperature increase is caused by heat producing waste and can result in several ten degrees above the local rock temperature. The temperature function is taken from ref. [3] and was modified in ref. [12]. With this modification one has

$$f_T(T)=\frac{1}{1+a}\exp\left(\frac{Q_1}{R}\left(\frac{1}{T_G(z_{ref})}-\frac{1}{T(z)}\right)\right)\left\{1+a\exp\left(\frac{\Delta Q}{R}\left(\frac{1}{T_G(z)}-\frac{1}{T(z)}\right)\right)\right\}, \qquad 2.3.28$$

where

Q_1, Q_2	activation energies of the creep process,
$\Delta Q=Q_2-Q_1$	difference between these parameters,
z_{ref}	reference level,
$T_G(z_{ref})$	rock temperature at the reference level,
$\Delta z=z-z_{ref}$	difference between the cavity's floor and the reference level,
$T_G(z)=T_G-\Delta z\cdot\nabla T$	local rock temperature in depth z,

∇T	geothermal gradient,
$T(z) = \Delta T + T_G(z)$	local temperature in depth z and
ΔT	temperature increase above the local rock temperature.

The parameter $a \neq 0$ allows for taking into account different creep behaviour of rock salt in different temperature regions, where the different activation energies Q_1 or Q_2 apply.

2.3.2 Parameter dependences of GRS model

In the following the dependences of the convergence rate on the model parameters are investigated, calculated with the LOPOS module of the EMOS code. The model parameters to be varied are the initial convergence rate K_0, the reference convergence rate K_{ref} and the backfill parameters h_1, g_1 and g_2. The simplified model of a repository is used here as discussed in chapter 2.2.1. Variations of K_0 and K_{ref}, respectively, are based on test case 1a, where all the other convergence and design parameters remain fixed. Variations of h_1, g_1 and g_2, respectively, are based on test case 2a, where a backfilled cavity is used. Again, all the other convergence and design parameters remain fixed. The parameter variations are performed under the pressure boundary condition of a constant atmospheric pressure of 0.1 MPa everywhere in the repository.

As in the rock mechanics calculation the simulation time starts immediately after excavation at time $t = 0$, in eq. 2.3.8 for the explicit time dependence, used in the GRS model, the parameter λ_S should be zero. In the present implementation of the model within the LOPOS code, corresponding to eq. 2.3.10, a λ_S value of zero cannot be used. Since, however, due to the increasing value of K_0 in eq. 2.3.10, when λ_S approximates zero, the function f_t in eq. 2.3.8 then only depends on the product $K_0 \cdot \lambda_S$ and it is, therefore, justified to use a very small value of λ_S instead of zero. Consequently, in all test cases below, the fixed value $\lambda_S = 10^{-6}$ is used. The initial convergence rate K_0 is varied between $K_0 = 50$ a^{-1} and $K_0 = 150$ a^{-1}, in the following.

The reference convergence rate K_{ref} in many cases can be directly obtained from rock mechanics calculations by extrapolating the respective results to very large times. The time evolution of the convergence rate for a variation of K_{ref} between $K_{ref} = 1.5 \cdot 10^{-3}$ a^{-1} and $K_{ref} = 3.5 \cdot 10^{-3}$ a^{-1} is investigated.

2.3.2.1 Dependence of the convergence rate on K_0 and K_{ref}

With the parameter λ_S being fixed, for test cases 1a to c there are only two fitting parameters left: K_0 which stands for the “initial value” of the convergence rate and K_{ref} which provides the limit at late times. The general behaviour of the convergence rate resulting from the GRS model, when K_0 is varied, is shown in figure 2.3.6. Here, a fixed value $K_{ref} = 2.5 \cdot 10^{-3}$ [1/a] is

used. With increasing K_0 the curves of the convergence rate are shifted, on the logarithmic scale almost parallel, to larger values. The change of the convergence rate by varying the parameter K_{ref} is given in figure 2.3.7, where a fixed value K_0 = 100 [1/a] is used. Figure 2.3.7 demonstrates that with smaller K_{ref} the approach to the stationary values occurs at later times.

Of course, with the parameter K_0 the convergence rate at early times can be fitted to results of rock mechanics calculations, while with the parameter K_{ref} the convergence rate value at late times can be modified. Both parameter variations show, however, that the steep decrease of the convergence rate curves at early times cannot be changed by variation of these parameters.

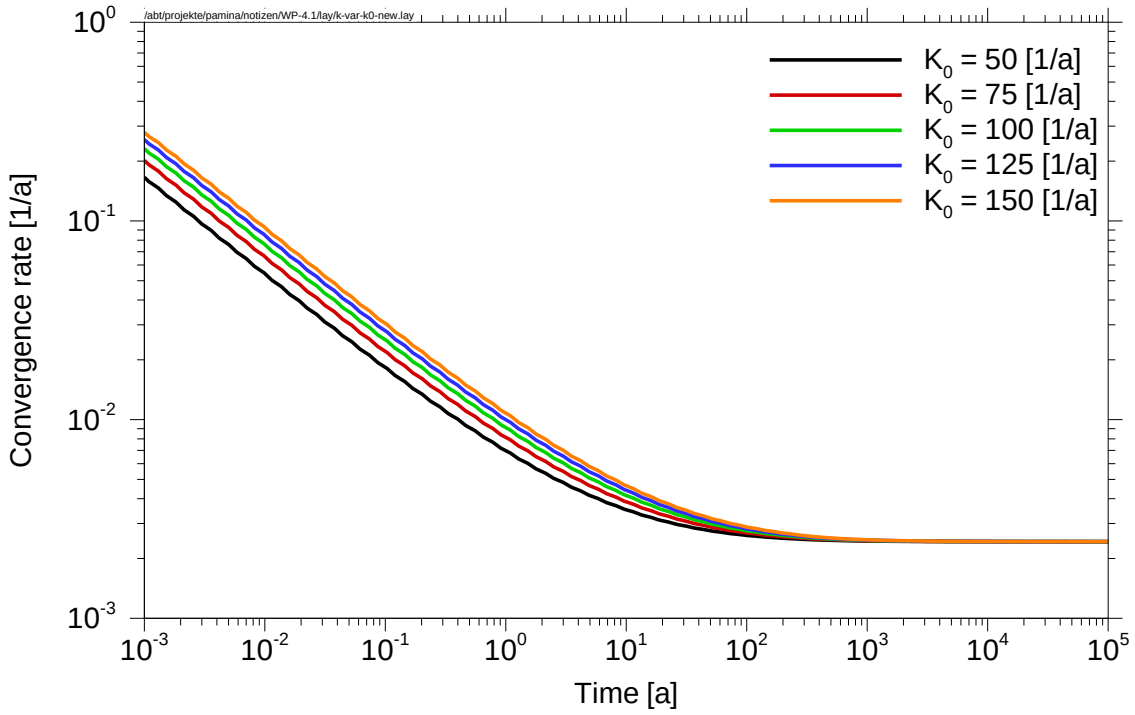

Fig. 2.3.6: Variation of the parameter K_0

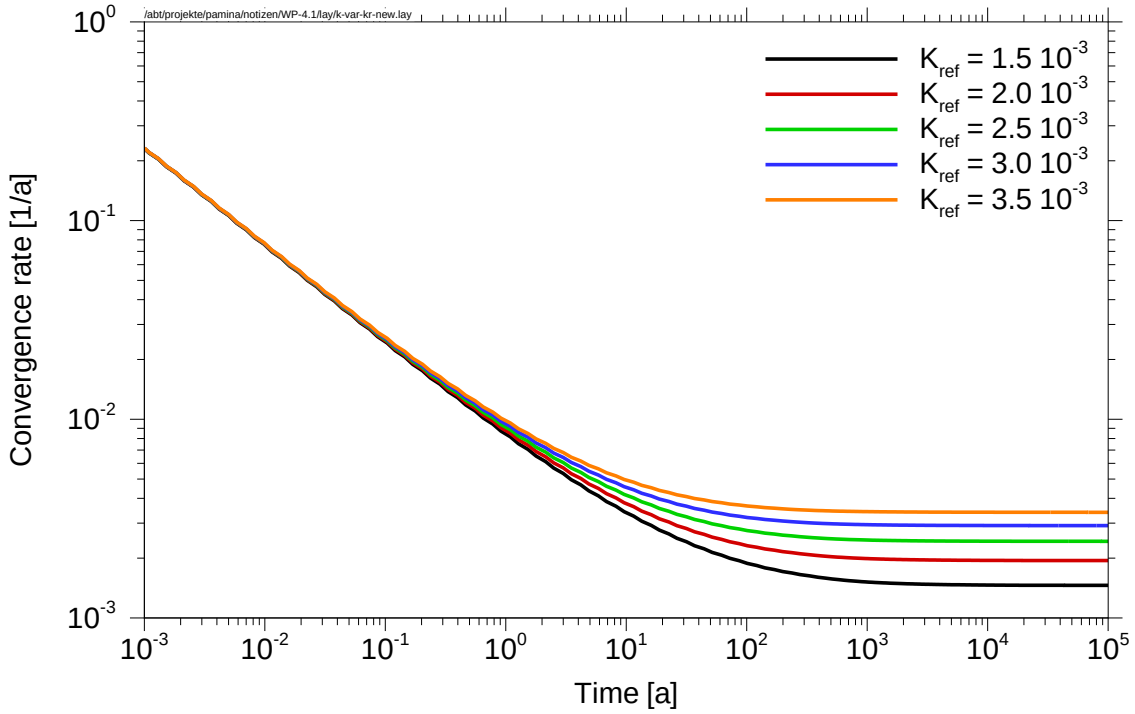

Fig. 2.3.7: Variation of the parameter K_{ref}

2.3.2.2 Dependence of the backfill resistance on the backfill parameters

The convergence rate behaviour on variation of the backfill parameters h_1, g_1, and g_2 is investigated using the simplified model of a repository, defined for test case 2a in chapter 2.2.2. The parameters K_0, K_{ref} and λ_S take the following values:

K_0 = 100 [1/a], K_{ref} = 2.5·10^{-3} [1/a], λ_S = 10^{-6}.

In figure 2.3.8 the time evolution of the convergence rate for a variation of h_1, only, is given, while the parameter values of g_1 and g_2 are fixed to g_1 = -1 and g_2 = 100. Figure 2.3.9 shows the corresponding results for the time evolution of the backfill porosity.

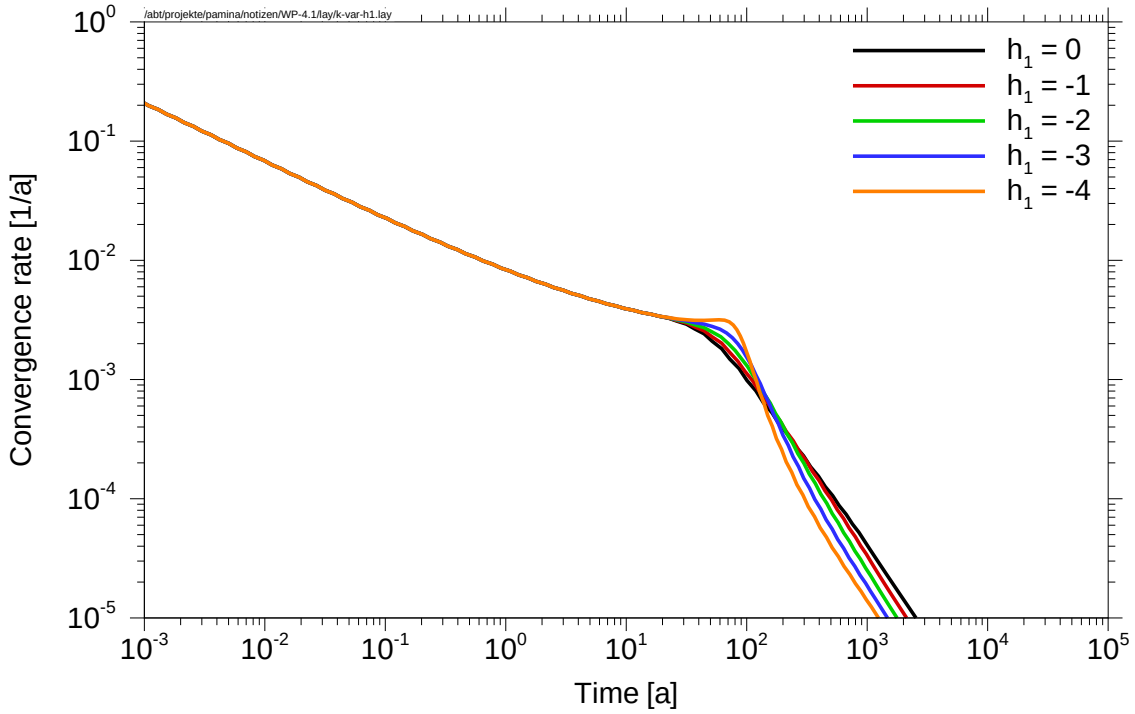

Fig. 2.3.8: Variation of the backfill parameter h_1: convergence rate

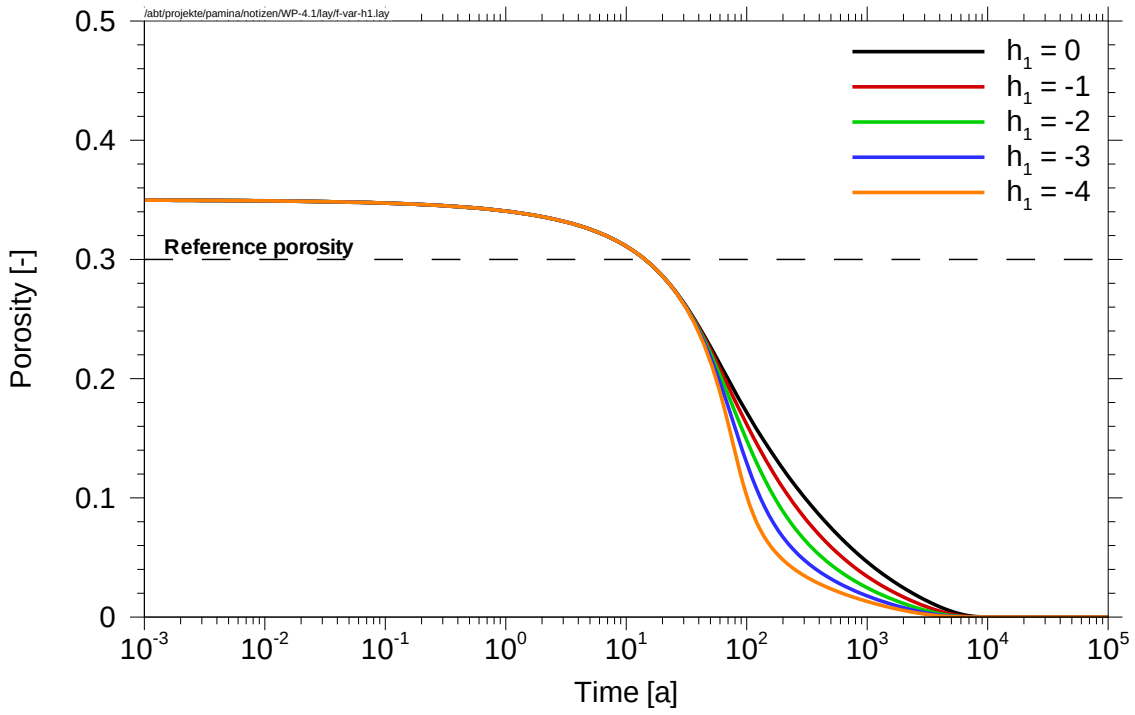

Fig. 2.3.9: Variation of the backfill parameter h_1: backfill porosity

An effect on the convergence rate, of course, cannot be expected before the backfill porosity goes below the reference porosity (cf. eq. 2.3.12), which occurs at about 14.3 a. With de-

creasing values of h_1 the convergence rate increases when the backfill porosities are close to the reference porosity. As a consequence the porosity than decreases faster and the convergence rate becomes significantly smaller. At late times the convergence rate curves are almost parallel on the logarithmic scale. This parallelism is not observed for backfill compaction. Therefore, the parameter h_1 will not be varied for fitting the convergence rates in the test cases below.

In figure 2.3.10 the time evolution of the convergence rate for a variation of g_1 is given, where the parameter values of h_1 and g_2 are fixed to h_1 = -2 and g_2 = 100. Figure 2.3.11 shows the corresponding results for the backfill porosity.

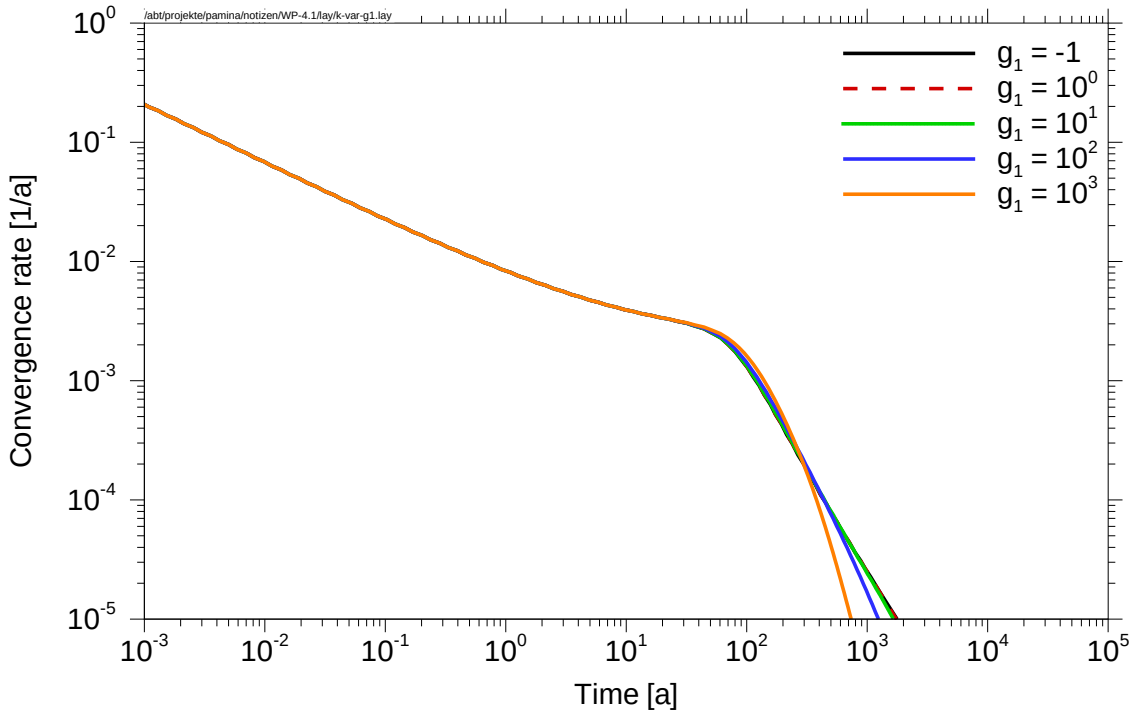

Fig. 2.3.10: Variation of the backfill parameter g_1: convergence rate

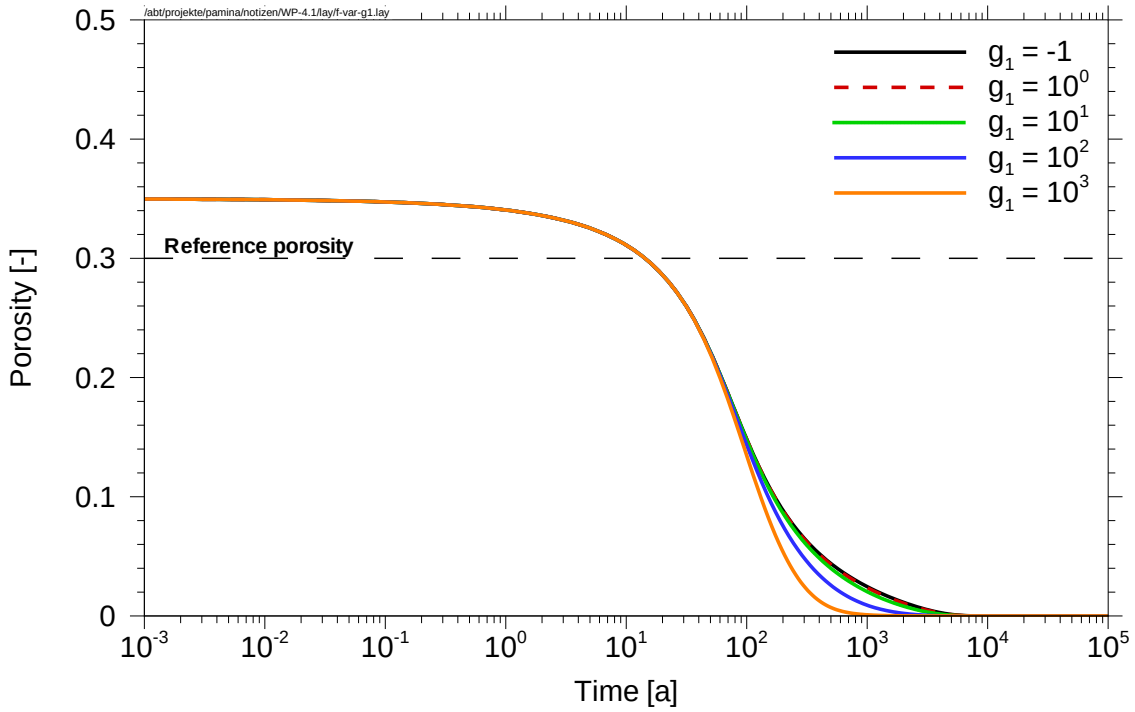

Fig. 2.3.11: Variation of the backfill parameter g_1: backfill porosity

Again, an effect on the convergence rate cannot be expected before the backfill porosity goes below the reference porosity. The influence of the g_1 parameter variation on the porosity evolution is less pronounced than that of parameter h_1. To see any effect of the variation of g_1, its value must be varied over several orders of magnitude. The results then are similar to that obtained with a variation of the parameter g_2, at least at late times (cf. figures 2.3.12 and 2.3.13, below). It turns out, that a variation of g_1 for fitting the convergence rates is not necessary. The PSE value of g_1 = -1 is therefore applied for all test cases below.

In figure 2.3.12 the results for a variation of g_2 are given, where the parameter values of h_1 and g_1 are fixed to h_1 = -2 and g_1 = -1, respectively. Figure 2.3.13 shows the corresponding results for the backfill porosity.

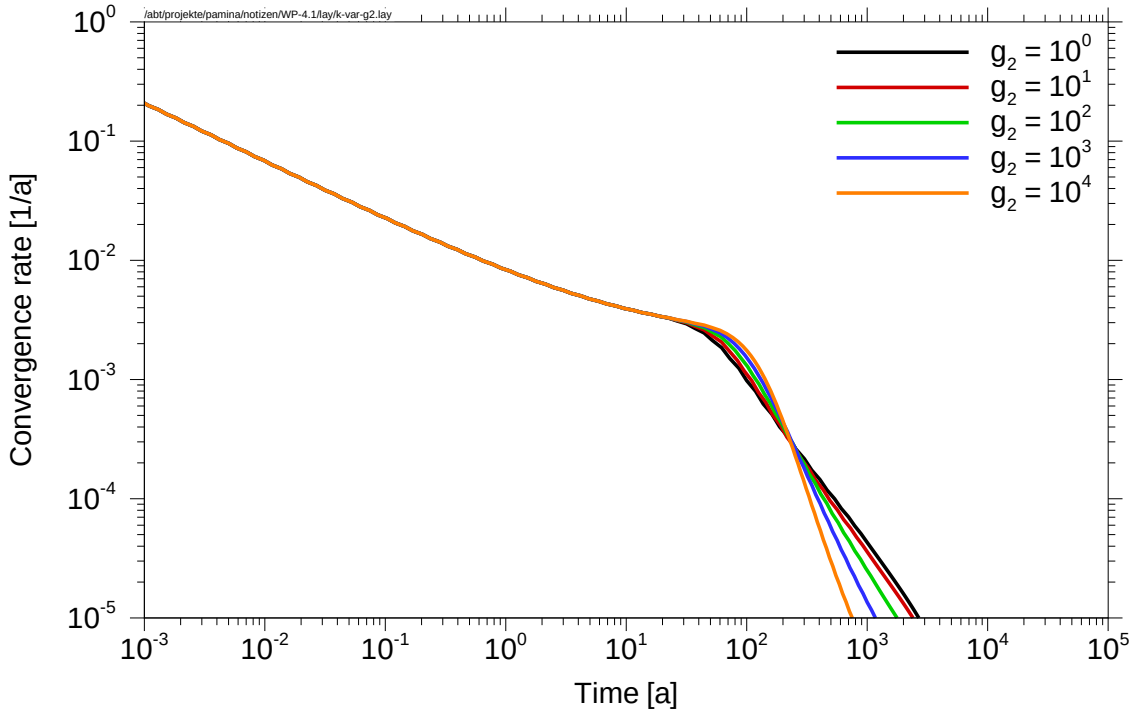

Fig. 2.3.12: Variation of the backfill parameter g_2: convergence rate

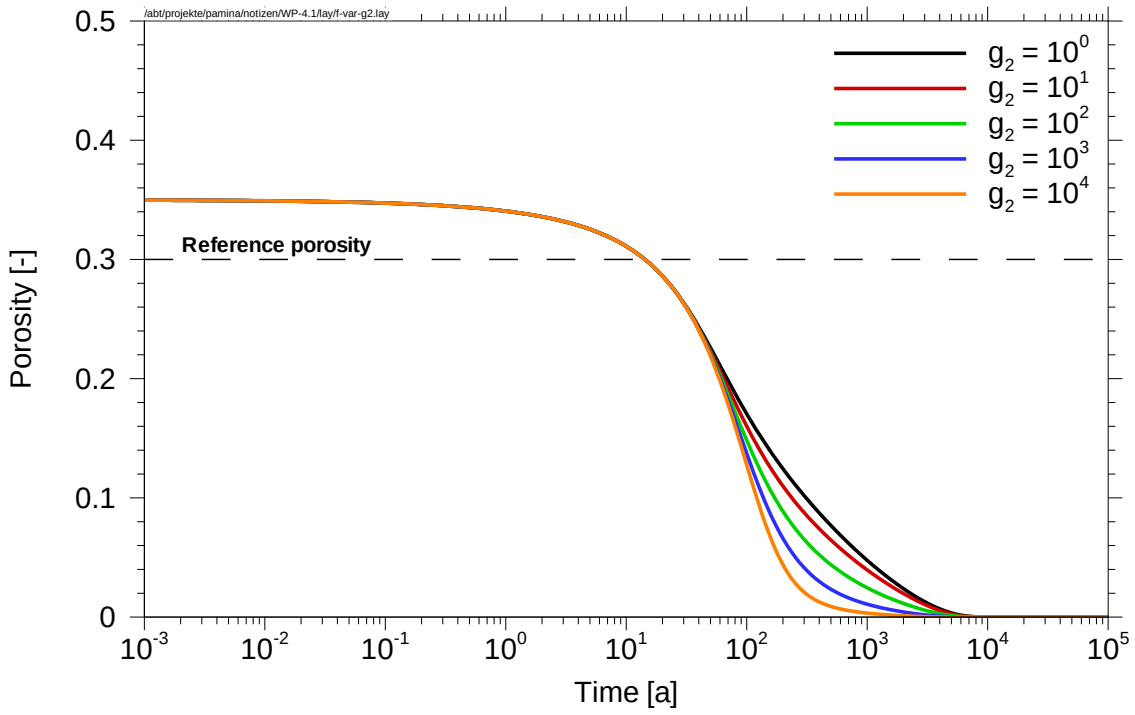

Fig. 2.3.13: Variation of the backfill parameter g_2: backfill porosity

Variation of g_2 shows the characteristic behaviour of more or less wet backfill on the convergence rate, i.e. an increase of the convergence rate at the beginning of its support and con-

sequently a greater resistance against compaction at later times. The parameter g_2 will, therefore, be used as fit parameter for dry and wet backfill.

2.3.3 NRG (REPOS) convergence model

In situ measurements and laboratory measurements on rock salt samples show that the closure rate of excavations in rock salt formations can largely be described by secondary creep[2]. The in situ measurements show that the secondary creep condition develops in days to weeks. Moreover, the in situ deviatoric stresses are small and constant, allowing the secondary creep condition to remain until the volume of the excavation has reduced to zero. Secondary creep is usually expressed in a Norton law:

$$\dot{\varepsilon}_{ij} = A\left(\frac{\sigma_{eq}}{\sigma_u}\right)^n S_{ij} \qquad 2.3.29$$

$\dot{\varepsilon}_{ij}$ strain rate tensor (year^{-1})
A coefficient in Norton's creep law (year^{-1})
σ_{eq} equivalent stress (MPa)
σ_u unit stress (1 MPa)
n stress exponent
S_{ij} deviatoric stress tensor

In a Universal Testing Machine (UTM) this equation simplifies to:

$$\dot{\varepsilon} = -\frac{1}{\ell}\frac{d\ell}{dt} = A^{UTM}\left(\frac{\sigma}{\sigma_u}\right)^n \qquad 2.3.30$$

where:

$\dot{\varepsilon}$ strain rate of the sample (year^{-1})
ℓ length of the rock salt sample in the UTM (m)
t time (year)
A^{UTM} coefficient similar to the coefficient in Norton's creep law [year^{-1}]
σ stress applied by the UTM on the sample (MPa)
σ_u unit stress (1 MPa)
n stress exponent

In a UTM, secondary creep will lead to a constant strain rate, which is also called stationary creep or steady state creep. The coefficient A in Norton's creep law, see eq. 2.3.29, can be derived from A^{UTM}, as measured in a UTM.

---

[2] For the in situ geometry secondary creep does not result in stationary creep or steady state creep.

However, it must be recognised that the measurements result in broad ranges for the values of A and n. Factors that influence the in situ determined values of A and n are:

1. the amount and the nature of in homogeneities in the internal structure of the rock salt and its (chemical) composition;

2. the amount of moist in the rock salt;

3. the deformation history of the rock salt;

4. uncertainty in the actual value of the lithostatic stress at some distance from the excavation;

5. the value of the activation energy Q, where the temperature dependency is commonly accounted for through the Arrhenius law: $A = A_0 \exp(Q/RT)$.

These factors also imply that values of A derived from measurements in a laboratory (UTM) can deviate significantly from the in situ values, since in homogeneities, deformation history and uncertainty in the stress conditions are not represented in the Universal Testing Machine, mainly due to the preparation and (small) size of the sample.

At a temperature of about 320 K, most reported in situ values for A are in the range of 10^{-8} to 10^{-7} $year^{-1}$, and n is in the range of 5 - 6. This broad range causes large uncertainties in the predictions of the convergence rate: in practical situations the uncertainty bandwidth (the ratio between the maximum and the minimum predicted convergence rate) is about 30.

2.3.3.1 Convergence of Rock Salt – Transient Convergence (REPOS)

The transient convergence model was developed ([10], [9]) as a quasi-analytical solution to eq. 2.3.29 for a spherical and a cylindrical shape of the excavation. In the original version of REPOS it was assumed that the convergence rate of excavations was constant (i.e. steady state), see e.g. EVEREST Fig 7.4.6.1 [4]. However, true steady state creep will only occur in a geometry and stress field that is obtained in a Universal Testing Machine. The rock salt geometry surrounding an excavation differs from the geometry of a rock salt sample in a Universal Testing Machine, and it can be shown that secondary creep will result in a gradually decreasing convergence rate for the in situ geometry. Moreover, the stress field in the surrounding rock salt depends on the elastic behaviour. It was already recognised in the EVEREST project that this transient behaviour of the rock salt creep should not be ignored. Using these ingredients an equation is found that is very similar to steady state creep as in eq. 2.3.30:

$$K = -\frac{1}{V}\frac{dV}{dt} = A^{tc}(t)\left(\frac{\sigma}{\sigma_u}\right)^n \qquad 2.3.31$$

where:

K convergence rate of the excavation (year^{-1}), which is constant in the secondary creep condition

V volume of the excavation (m^3)

t time (year)

A^{tc} time dependent coefficient (year^{-1})

σ difference between the stress against the wall of the excavation (practically zero for an open excavation) and the lithostatic stress at some distance from the excavation (equal to the lithostatic stress at the location of the excavation if the rock was undisturbed) (MPa)

σ_u unit stress (1 MPa)

n stress exponent

A^{tc} decreases gradually with time, and its effect on κ is described by an analytical equation in combination with an integral that can be calculated by a numerical procedure. The procedure that is used to obtain the convergence rate at some time t is as follows. First a dimensionless time τ is calculated using eq. 2.3.32.

$$d\tau = \frac{dt}{t^*} = \frac{dt}{\frac{\sigma_u}{EA}\left(\frac{\sigma\sqrt{3}}{\sigma_u}\right)^{-(n-1)}} \qquad 2.3.32$$

Then the dimensionless convergence rate κ can be found by a pre-calculated 'key curve' of κ versus τ, which is shown in Figure 2.3.14. This 'key curve' contains amongst others the integral mentioned above.

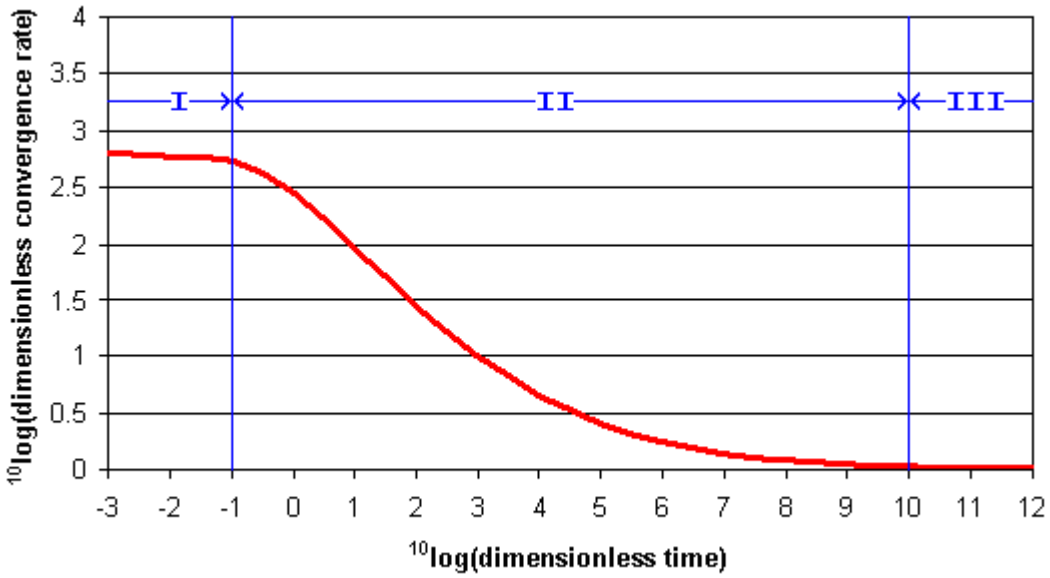

Fig. 2.3.14: Normalised time vs. normalised convergence rate for n = 5 and E = 25 GPa

The actual convergence rate can be calculated from the dimensionless κ using equation 2.3.33:

$$K = \kappa\kappa^* = \kappa A\sqrt{3}\left(\frac{\sigma\sqrt{3}}{\sigma_u n}\right)^n \qquad 2.3.33$$

It should be noted that the coefficient A in equations 2.3.32 and 2.3.33 is the coefficient for secondary creep. In principle the value of A can be measured in a Universal Testing Machine, but, as mentioned before, the laboratory conditions deviate significantly from in situ conditions, so laboratory measurements on (small) rock salt samples often lead to values of A that are not applicable to the in situ condition.

2.3.3.2 Performance of the Transient Convergence Model

In the BAMBUS project report [1] the results of convergence measurements in a “Non-backfilled Borehole” are reported. To test the performance of the transient convergence model as implemented in REPOS (NRG), is compared with one of these measurements.

Tab. 2.3.1 Data for the performance test of the transient convergence model

Experimental data	
Depth	1250 m
Initial diameter	600 mm
Temperature	320 K
Lithostatic pressure	26 MPa
Duration of the test	150 days (4 years)
Fit data	
Best fit for A(320 K)*	3.88E-7 $year^{-1}$
Best fit for n	5
Youngs modulus E	25 GPa (fixed in REPOS)

*Note: this value is 3.7 times higher than what is used by default in REPOS

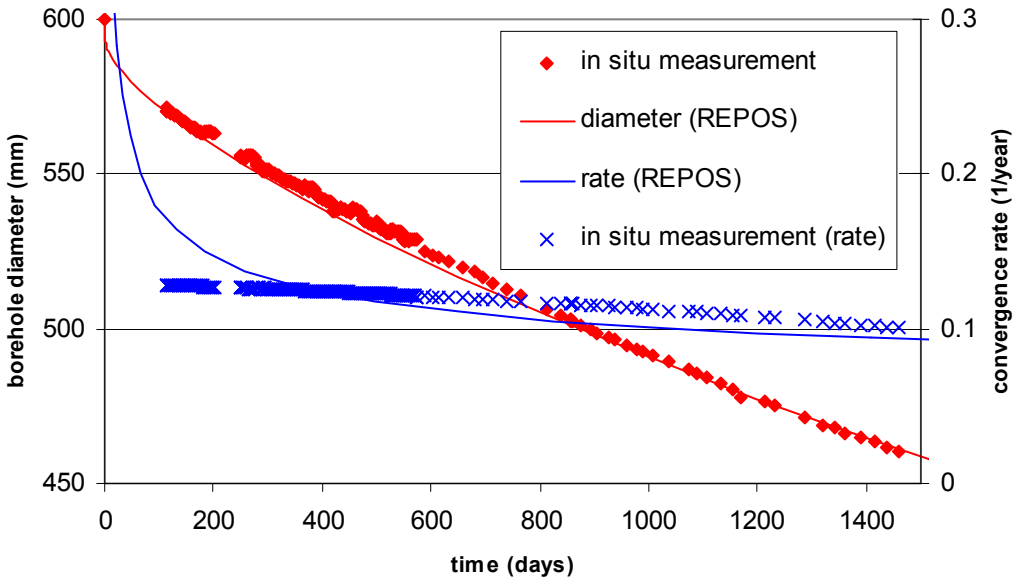

Fig. 2.3.15: Comparison of the REPOS convergence model with the measurements in a deep open borehole (free convergence at 1230 m depth)

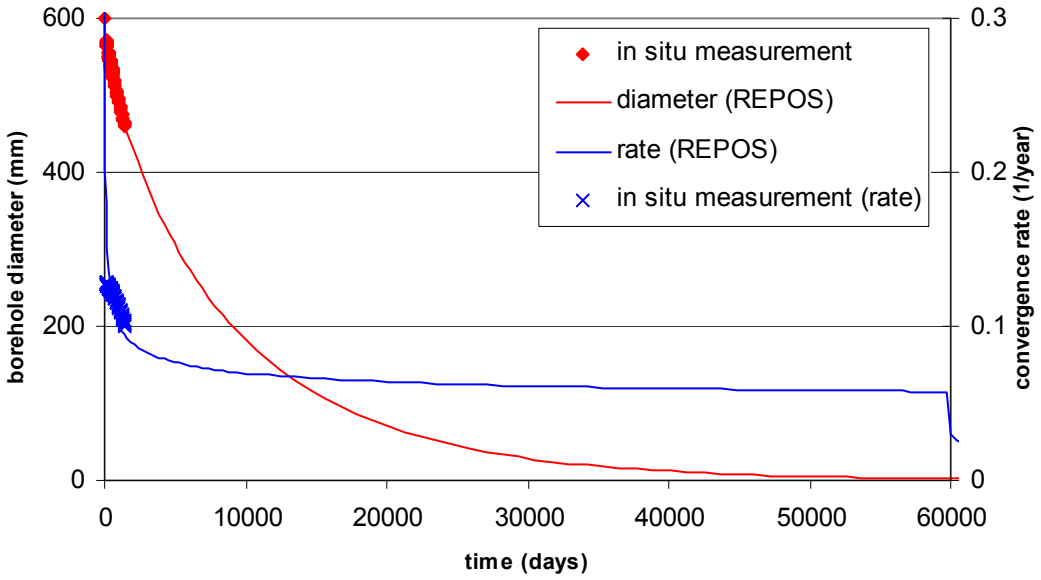

Fig. 2.3.16: Comparison of the REPOS convergence model with the measurements in a deep open borehole (free convergence at 1230 m depth), and the extrapolation to closure of the borehole

Figure 2.3.15 shows that in the first days to months a relatively fast convergence occurred, and after that a slowly decreasing convergence rate is found. The overall shape of the model curve does not fit well enough with the measured data to allow extrapolation to much longer times. It must however be noticed that in [9] various measurements are reported that support the transient convergence model.

Figure 2.3.17 shows the points in (dimensionless) times of the measurements shown in Figures 2.3.15 and 2.3.16.

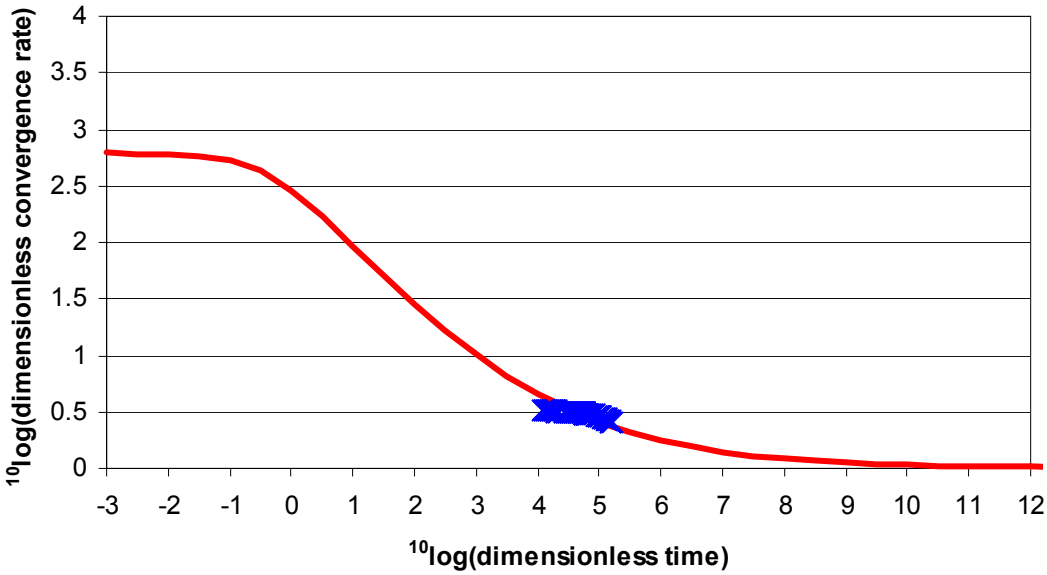

Fig. 2.3.17: Normalised time vs. normalised convergence rate for n = 5 and E = 25 GPa, including the measurement represented in dimensionless time and dimensionless strain rate

2.3.3.3 Compaction of Crushed Salt

2.3.3.3.1. The coupled creep model (CCM)

In REPOS (NRG), two processes that contribute to compaction of crushed salt are implemented [14], [4]. The modelled processes are:

1. Recrystallization-facilitated Dislocation Creep
2. Pressure Solution Creep

These processes govern the compaction at low porosities (< 20%) and relatively low stresses (< 40 MPa). At high porosities the process of *grain rearrangement* often governs the compaction behaviour of the crushed salt, which is not accounted for in the model.

The compaction rate β is calculated as:

$$\beta = -\frac{1}{V}\frac{dV}{dt} = \beta_{PS} + \beta_{recr} \qquad 2.3.34$$

where:

β compaction rate (1/year)

V volume of the section of the excavation that is backfilled with crushed salt (m^3)
β_{PS} compaction rate (1/year) due to pressure solution
β_{recr} compation rate (1/year) due to recrystallization-facilitated dislocation creep

β_{PS} and β_{recr} are given by:

$$\beta_{recr} = \frac{B_{recr}}{d_g^2} e^{-dH/RT} h(\phi) \left(\frac{\sigma}{\sigma_u} \right)^5 \quad 2.3.35$$

$$\beta_{PS} = Q \frac{A_{PS}}{T d_g^2} f(\phi) \sigma \quad 2.3.36$$

$$Q = \min\left(1, \frac{S}{S_{full}}\right) = \min\left(1, \frac{V_{brine}/V_{pore}}{S_{full}}\right) \quad 2.3.37$$

where:

B_{recr} constant (μm^2/year), typically in the range from 5.33E+9 to 7.99e+11 μm^2/year
d_g grain size (μm)
dH activation energy for the recrystallization-facilitated dislocation creep process (typically 65000 J)
R gas constant: 8.314 J/mol.K
T temperature (K)
$h(\phi)$ porosity dependence of the recrystallization-facilitated dislocation creep process [10] – Figure 2.3.18
σ stress applied on the crushed salt (MPa)
σ_u unit stress (1 MPa)
Q moisture factor
A_{ps} constant (μm^2/year/MPa), typically in the range from 2.78e+6 to 1.57e+8 μm^2/year/MPa
$f(\phi)$ porosity dependence of the pressure solution creep process [10] – Figure 2.3.18
S fraction of the pore space filled with brine [10]
S_{full} value of S where PS is fully active, in the range from 0.2 to 0.8
V_{brine} volume of the brine in the pores
V_{pore} volume of the pores

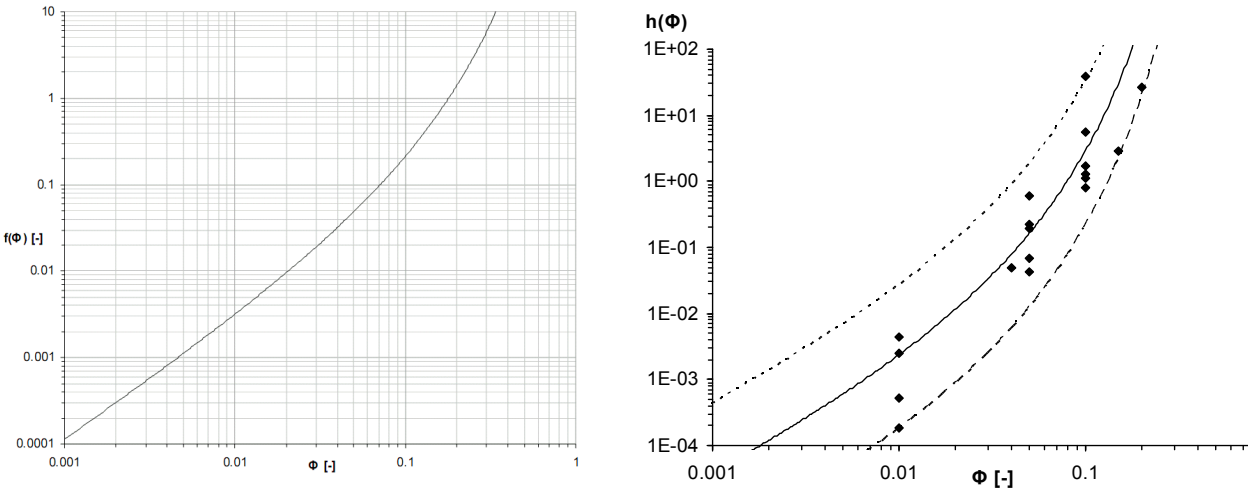

Fig. 2.3.18: The functions $f(\phi)$ - pressure solution creep (left) and $h(\phi)$ - recrystallization-facilitated dislocation creep (right)

2.3.3.3.2. Compaction behaviour of the Bambus Backfill Mix (BBM)

The compaction model has been calibrated for relatively small grain sizes (70 - 600 μm). For the benchmark larger grain sizes are assumed than used for the calibration of the model. Moreover, the assumed backfill mix has a very broad grain size distribution.

Tab. 2.3.2: Grain size distribution of the BAMBUS-backfill mix (BAMBUS-I 'Asse Salt' – initial porosity: 31%)

Sieve size (mm)	Sieve passage (mass-%)
31.5	100.00%
16	97.10%
8	86.89%
4	66.79%
2	39.29%
1	20.53%
0.5	11.26%
0.25	6.49%
0.125	2.97%
0.063	0.49%
0.001	0.07%

The effect of the grain size distribution on the rheological behaviour of crystalline materials is still an issue of ongoing research. In [13] two extreme approaches are used to quantify the effect:

1. Stress is uniform throughout the material

2. Strain rate (or convergence rate) is uniform throughout the material

It is shown that assuming uniform stress will always give larger overall strain rate than assuming uniform strain rate. The actual strain rate is expected to be found between these two extremes. Another result mentioned in [13] is that the difference between the two approaches has a maximum when the standard deviation of a log-normal grain size distribution (applied to the number of grains) is about 0.8. For small (< 0.1) and large values (> 1.4) of the standard deviation, the two 'extreme' methods give the same result. The BAMBUS Backfill Mix does not fit the lognormal grain size distribution as defined in [13], but the root of the variance of a logarithmic representation of the grain size distribution has a value of > 1000. Even though there are large differences between the reference material used in the paper [13] and the backfill mix assumed here, it is reasonable to conclude that for the backfill mix both approaches should give similar results and should be adequate to cover the effect of the grain size distribution.

Since the assumption of uniform stress is mathematically much easier to apply, this approach is chosen. For each grain size class specified in table 2.3.2 the convergence rate at a given stress level can be determined, and also their contributions to the total strain rate of the backfill mix.

In the present version of REPOS (NRG) the calculation of the mechanical balance between converging rock salt, the backfill material and brine uses a single grain size value. To reflect the grain size distribution of the backfill, a porosity dependent grain size is introduced, the effective grain size d_{eff}. Figure 2.3.19 shows the effective grain size as a function of the porosity of the Bambus Backfill Mix.

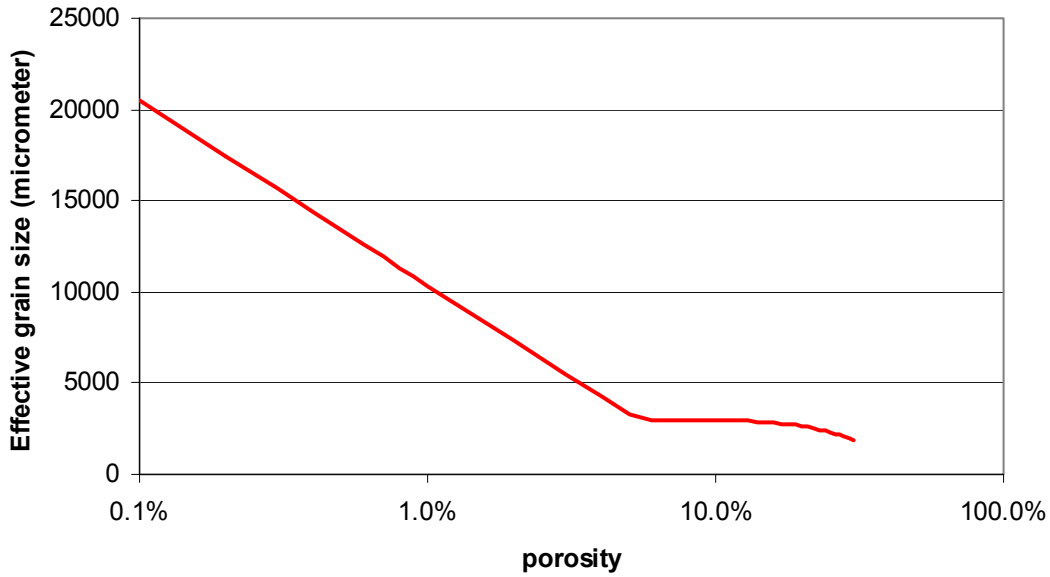

Fig. 2.3.19: Effective grains size that represents the 'Bambus Backfill Mix'

2.3.3.3.3. Test of the CCM2-BBM salt grit compaction model

The performance of the Coupled Creep Model for the Bambus Backfill Mix (in short: the CCM2-BBM model) has been tested by a comparison with measurements on the Bambus Backfill Mix as reported in the BAMBUS-I final report [4]. The experimental results reported in Bambus-I, figures 3.2 (BGR experiment) and 4.8 (FZK experiment) have been plotted in stress-strain diagrams (see Figures 2.3.20 and 2.3.21). Also the expected in situ ranges have been plotted.

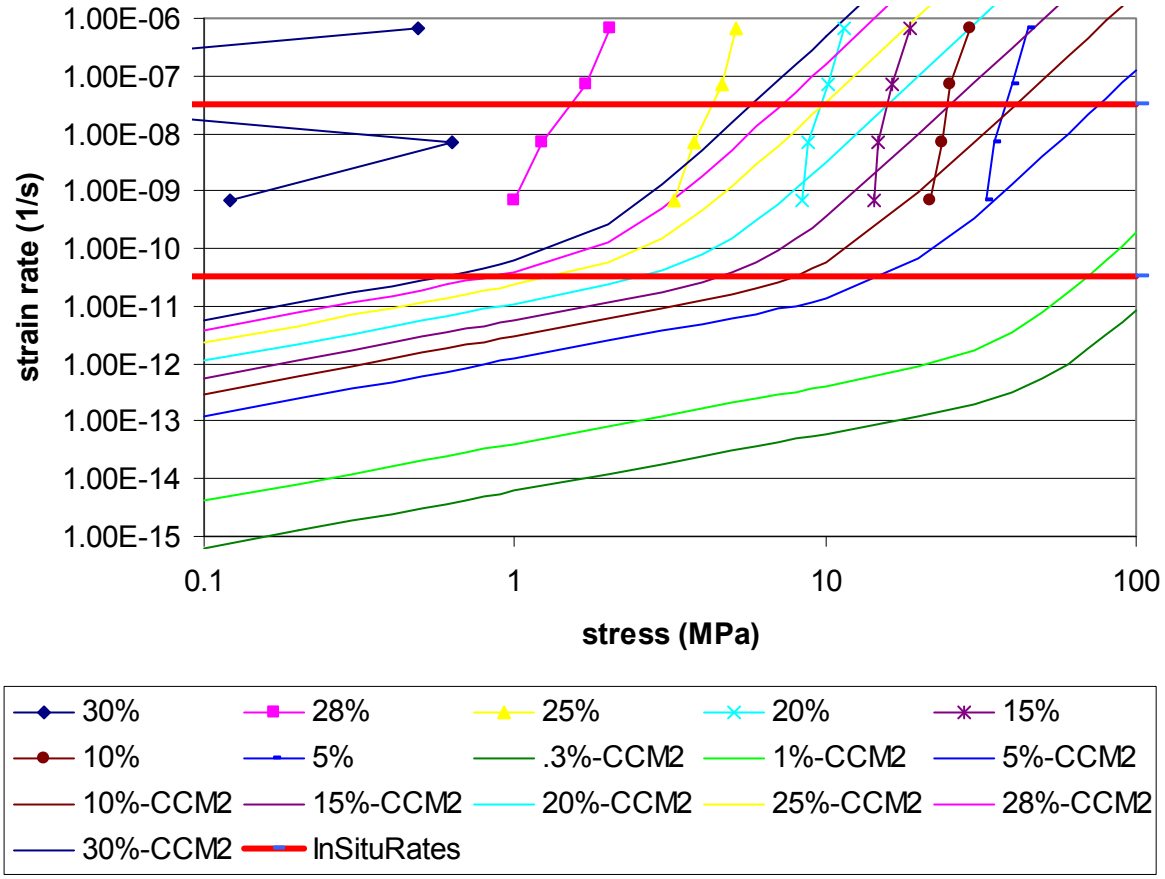

Fig. 2.3.20: Comparison of the CCM2-BBM model with measurements reported in Bambus-I (BGR experiment reported in Figure 3.2 in the Bambus-I report)

From Figures 2.3.20 and 2.3.21, the following observations are made:

1. The CCM2-BBM model under predicts the strain rate at low stress (1 MPa) and high strain rate (1 year^{-1}), i.e. at early times after disposal.

2. The CCM2-BBM model tends to over predict strain rates at high stress (20 MPa) and low strain rates (1e-3 year^{-1} = ca. 1e-11 s^{-1})

3. The in situ compaction seems to occur in the Recrystallization-facilitated Dislocation Creep range rather than in the PS range.

4. The measured slopes in the Recrystallization-facilitated Dislocation Creep range are steeper than in the CCM2-BBM model (σ^n against σ^5, where the measured value of n > 12).

In [8] the result of a more extensive study of the FZK measurements reported in table 3.4 in [1] is reported. Here it is concluded that the best estimate for the exponent n is 3.812. It is also mentioned in both reports that especially the BGR measurements (Figure 2.3.20) are

affected by friction in the Universal Testing Machine during the compaction of the sample. At relative low stress the force is below the limiting friction, and the piston will not move. At stress levels where the limiting friction is just exceeded, the exponent n seems to be very high.

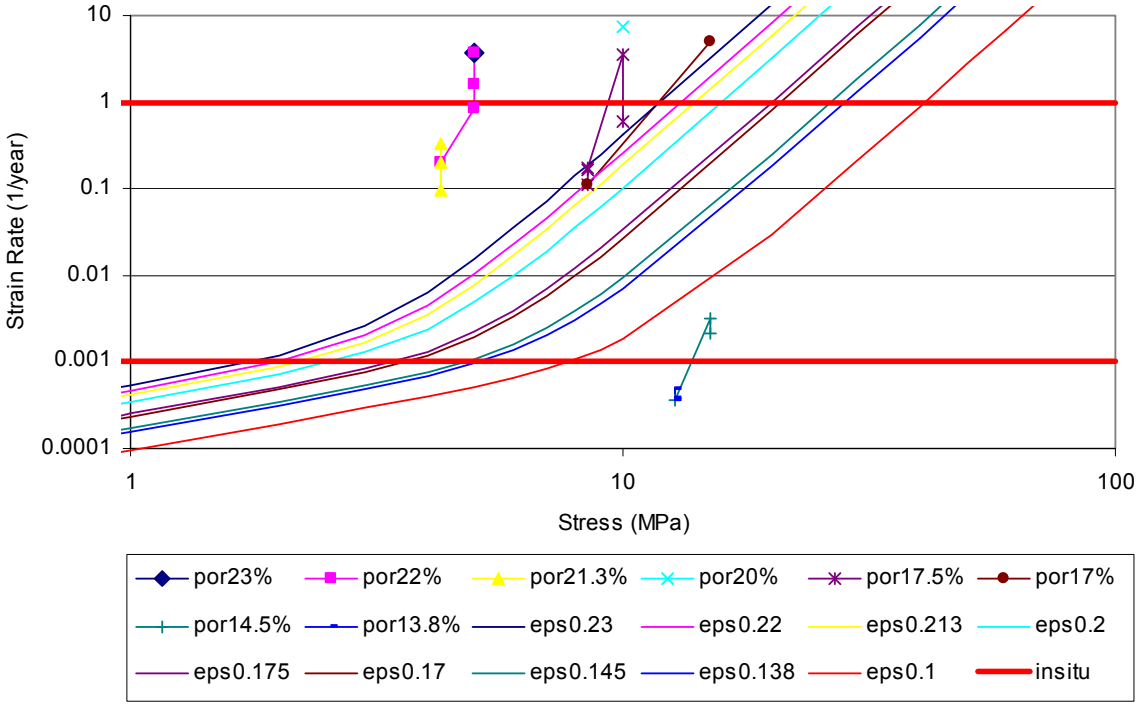

Fig. 2.3.21: Comparison of the CCM2-BBM model with measurements reported in Bambus-I (FZK experiment reported in Figure 4.8 in the Bambus-I report)

2.3.3.3.4. Conclusion

The CCM2-BBM model has a firm experimental basis, but only for relative small grain sizes. Moreover, the experimental data are obtained from a sequence of related experiments [14]. These experiments clearly show Pressure Solution driven compaction. This process also has a firm theoretical basis, i.e. it is based on basic thermo dynamical principles. The experiments also confirm the empirical model for Recrystallization-facilitated Dislocation Creep, in particular that the creep rate is proportional to σ^5. However, it was also observed that for large stresses (larger than 20 MPa) the measured values of the power increase to 8 and higher.

Scaling up the CCM2-BBM model to large grain sizes and to a broad grain size distribution can be done mathematically as described in the previous section.

The experimental results described in Bambus-I [1] show that:

- The CCM2-BBM model does insufficiently account for compaction due to grain rearrangement. This process is much more effective for broad grain size distributions than

for narrow grain size distributions. For the Bambus Backfill Mix grain rearrangement seems to be the dominant process for porosities larger than 20%.

- The measured slopes in the Recrystallization-facilitated Dislocation Creep range for the Bambus Backfill Mix investigated here (Figures 2.3.20 and 2.3.21) are steeper than in the CCM2-BBM model (σ^n against σ^5, where the measured value of n > 12). However, this may be due to friction in the Universal Testing Machine. Other measurements (see [8]) suggest that n = 3.812.
- The experiments do not show the Pressure Solution Creep (PS) behaviour, but also do not contradict the PS behaviour, except for one specific data point, since stresses and strain rates are almost always out of the PS range.

2.3.3.4 Key data used in the NRG benchmark calculations

Transient Convergence Model

Two parameters, the coefficient in Norton's creep law [$year^{-1}$] A and the stress exponent n as defined in equation 2.3.30 depend on local site conditions. For the benchmark it was decided to choose n =5. The value of A was not specified, but the default value in REPOS i.e. A(T = 310 K) = 2.08E-06 1/s and σ_u = 1 MPa, gives a good match with the results of the other partners.

Crushed Salt Compaction Model

The CCM2-BBM model as implemented in REPOS does not account sufficiently for compaction due to *grain rearrangements*. Therefore, the threshold for compaction resistance in REPOS has been set to 20%, i.e. in the calculation it is assumed that crushed salt with a porosity larger than 20% does not resist to compaction at all. The stress exponent for Recrystallization-facilitated Dislocation Creep has been left to 5.

2.3.4 Models of 3D convergence calculations with FLAC

2.3.4.1 Convergence and Rate of Convergence

The behaviour of an excavated cavity over time is described by the convergence and the convergence rate. The convergence C describes the total volume change compared to the volume at the beginning.

$$C(t) = \frac{V_0 - V(t)}{V_0} \qquad 2.3.38$$

with:

V_0 Volume at the time of excavation
$V(t)$ Volume at the current time

Starting at a value of 0 at the beginning, a value of 1 is reached with entire convergence of the volume, i.e. the excavation is closed completely.

The convergence rate $\dot{\kappa}$ describes the velocity of the current volume change related to the current volume.

$$\dot{\kappa}(t) = -\frac{\dot{V}(t)}{V(t)} \qquad 2.3.39$$

with:

$\dot{V}(t)$ Velocity of the volume change at the current time

It has to be noted that there are two frames of reference within these two equations. These are the initial state in case of the convergence C, eq. 2.3.38, represented by V_0, and the current state in case of the convergence rate $\dot{\kappa}$, eq. 2.3.39, represented by V. These different frames lead to the fact that the rate $\dot{\kappa}$ cannot be derived directly from the convergence C over time, thus, the ratio between the current volume and the initial volume has to be taken into account as an additional multiplicative factor.

$$\dot{\kappa}(t) = -\frac{\dot{V}(t)}{V_0} \cdot \frac{V_0}{V(t)} = \frac{\dot{C}(t)}{1 - C(t)} \qquad 2.3.40$$

where

$\dot{C}(t)$ Derivation of the convergence over time

$$\dot{C}(t) = \frac{dC(t)}{dt} = -\frac{\dot{V}(t)}{V_0}$$

On the other hand, κ as integration of $\dot{\kappa}$ over time leads to

$$\kappa(t) = -\ln\frac{V(t)}{V_0} = -\ln(1 - C(t)) \qquad 2.3.41$$

Typical phases of the convergence behaviour of an empty cavity are shown in figure 2.3.22. The convergence behaviour over time is divided into four periods depending on the convergence rate: A transient phase I at the beginning with a decreasing convergence rate caused by stress redistribution, a nearly stationary phase II, a contact period III with very variable rate due to the development of contacts between the walls, the floor, and the roof as well as the final closure period IV, where the remaining cavity in the knuckles of the roof will be eliminated. The first nearly vertical fall of the convergence rate marks the limit between these two last phases.

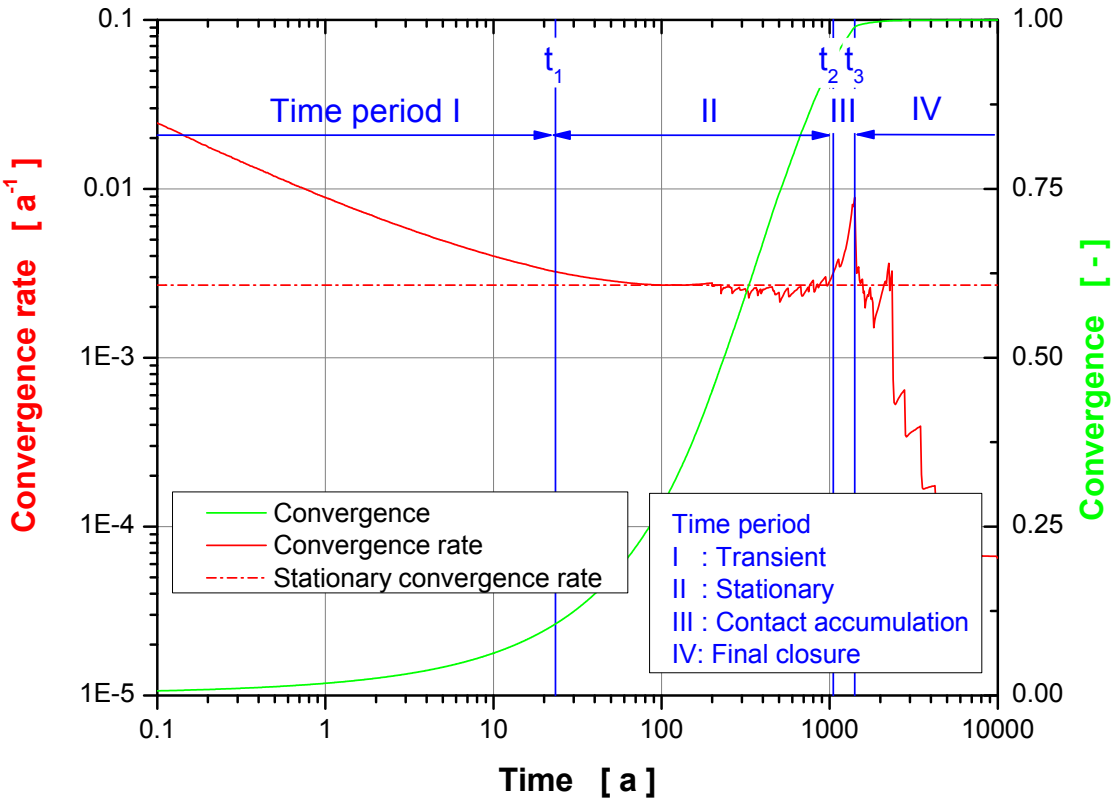

Fig. 2.3.22: Convergence and convergence rate of an empty cavity

The convergence rate during phase II, $\dot{\kappa}_{II}$, offers only small changes in the reference case of an empty excavation. So, the convergence rate in this period is also called stationary convergence rate $\dot{\kappa}_{stat}$. The value itself is given by the minimum during this phase before con-

tacts start to appear, the duration of the stationary phase II is determined by an admissible deviation of 20 % compared to this value of stationary convergence rate. Thus, the stationary convergence rate is marked at a single point in time. The average value $\dot{\kappa}_{avg,II}$ is the mean value over time during this period. Hence, the characterising parameters, which particularly mark the second period, are the following:

t_1	Start of phase II with nearly stationary convergence rate
t_2	End of nearly stationary phase II
C_1	Convergence at the beginning of the nearly stationary convergence phase t_1
C_2	Convergence at the end of the phase with nearly stationary convergence t_2
$\dot{\kappa}_{stat}$	Stationary convergence rate
$\dot{\kappa}_{avg,II}$	Average convergence rate in phase II

If the convergence rate is shown as a function of the convergence, it appears that phase II is the decisive phase of the closing process of a cavity without backfill, figure 2.3.23. More than 80% of the convergence occurs in phase II and less than 10 % during the contact period and the final closure period.

The end of period III, t_3, marks the time where floor and roof meet. It depends on the initial geometry whether the floor and the roof meet at this point in time or both walls. The system behaviour changes significantly in both cases which leads to a steep decrease in the convergence rate.

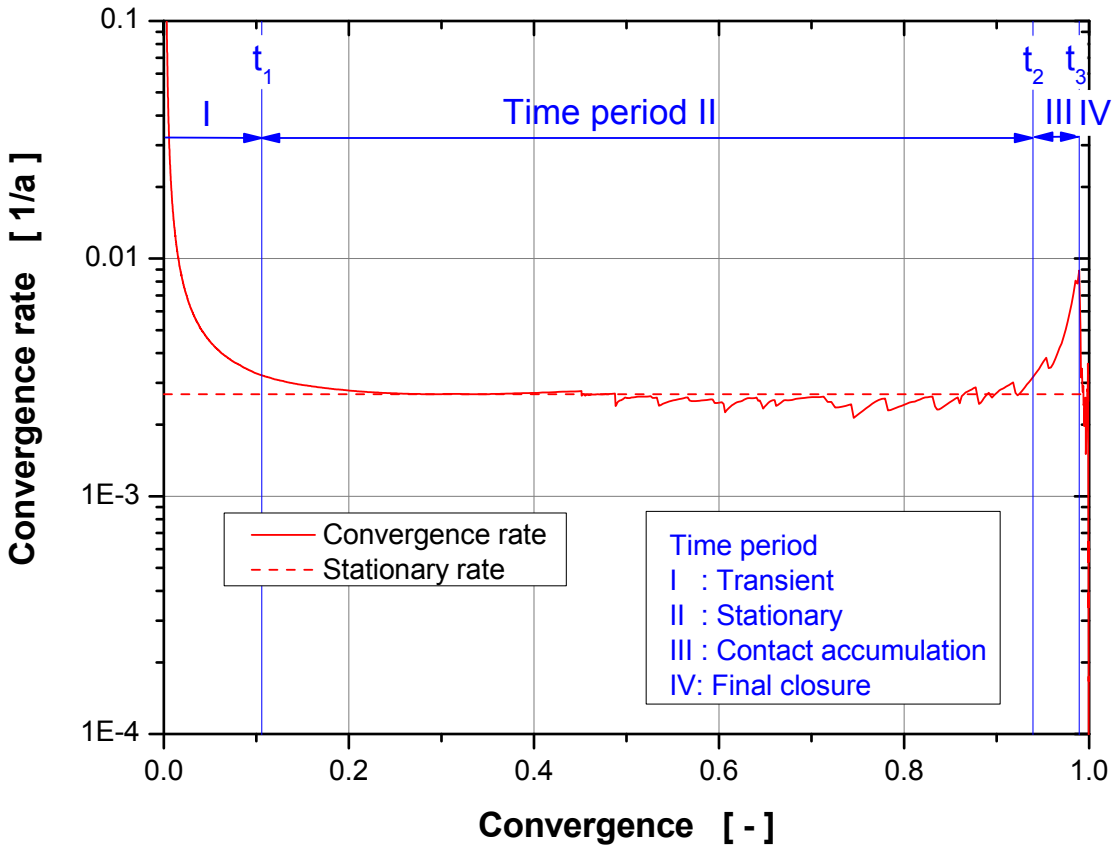

Fig. 2.3.23: Convergence rate as a function of convergence in an empty cavity

The mathematical representation of the in-situ closing process is influenced by the discretization and the numerical method used. This influence becomes apparent in the number and the intensity of the contacts. It can be seen in the discontinued evolution of the convergence rate starting approximately in the second half of period II. The increase in the convergence rate until the end of period III is motivated physically. It has to be noted that spalling probably occurs in-situ if no essential supporting pressure affects the contour of the excavation. Besides, it is insignificant whether the supporting pressure is caused due to fluid or backfill. The possibility of spalling is not considered in the continuum models used here.

The behaviour of a cavity which is backfilled with a porous compactible material is described in a similar way, however, convergence and convergence rate have to be replaced by compaction and compaction rate. Thus, the equations given above, eq. 2.3.38 to 2.3.41, are also valid if convergence is replaced by compaction. Nevertheless, according to the initial porosity of this porous compactible backfill material, the compaction (convergence) reaches only the value of the initial porosity at the final state of complete compaction instead of a value of 1.

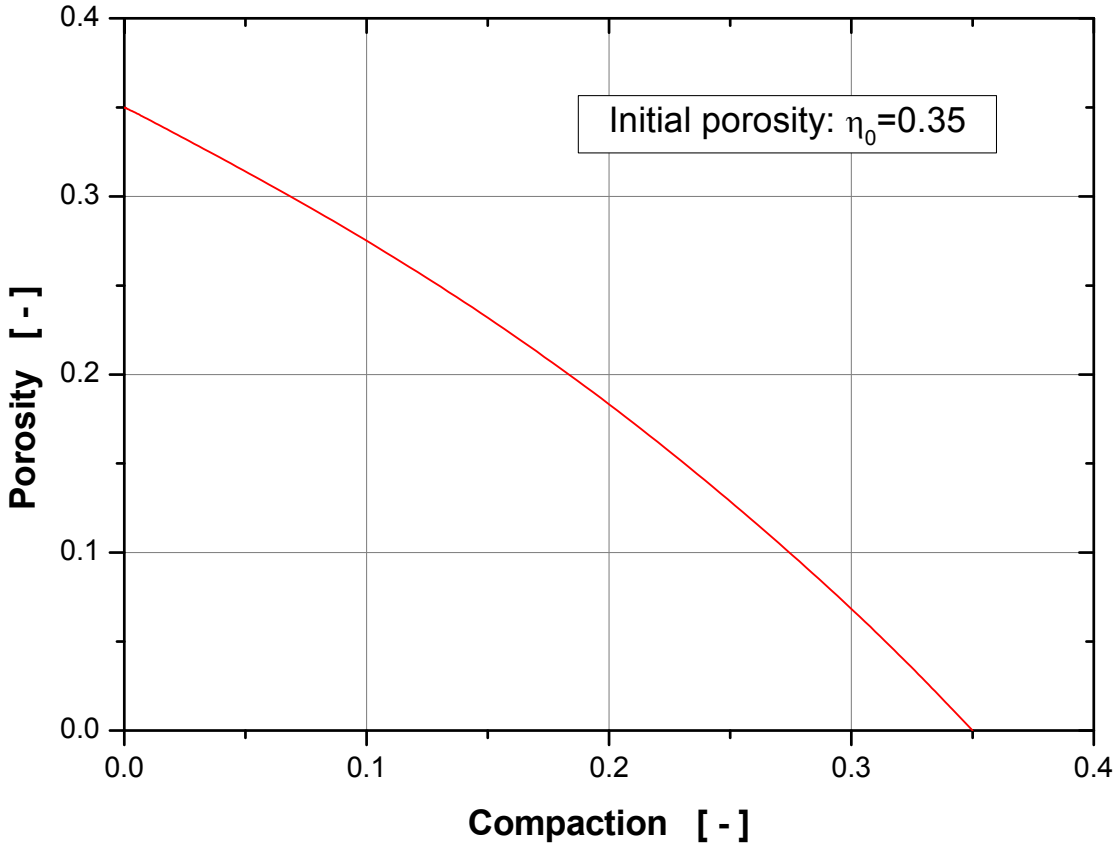

Fig. 2.3.24: Porosity as a function of compaction with an initial porosity of 0.35

The porosity η is related to compaction by eq. 2.3.42. This function is shown in figure 2.3.24 for a given initial porosity η_0 =0.35.

$$\eta(t) = \frac{\eta_0 - C(t)}{1 - C(t)} \qquad 2.3.42$$

The behaviour of the cavity's backfill compaction process over time is shown in figure 2.3.25. The convergence rate of the empty cavity is added for comparison. The compaction process is also divided into four periods: A transient phase I at the beginning with decreasing compaction rate caused by stress redistributions similar to the behaviour of the empty cavity, a phase II with small changes in compaction rate, a compaction phase III with increasing backfill pressure and thus decreasing compaction rate, and a final phase IV, where the remaining very small amount of porosity in the backfill material is eliminated. Essentially, phase IV is characterised by the elastic behaviour of the mostly compacted backfill which goes on until the initial rock pressure is attained.

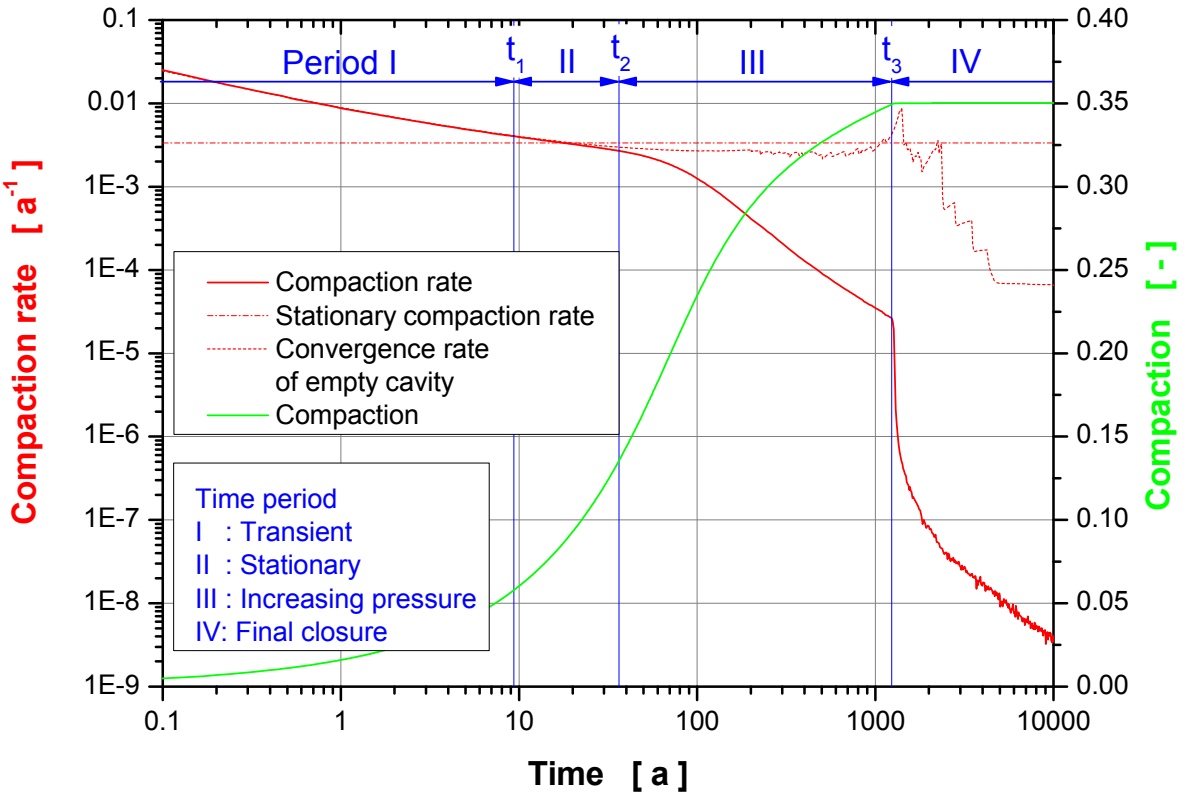

Fig. 2.3.25: Compaction and compaction rate of a cavity backfilled with crushed salt

It has to be noted that there is no difference between the behaviour of an empty cavity and a backfilled cavity during period I, figure 2.3.25. The reason for this is the negligible amount of compaction including only a small backfill pressure which does not affect the convergence. During period II, the compaction gains some geo-mechanic importance but its influence is still small. Nevertheless, due to the increasing backfill pressure during period II and especially later during period III, figure 2.3.26, the compaction rate decreases monotonically. This leads to a behaviour with less distinctive stationary behaviour during phase II, and the duration of phase II is much shorter than the duration of period II in an empty cavity. Thus, in the case of a backfilled cavity, phase II is defined by the maximum of the derivation of the convergence rate over time, i.e. the change of velocity of the closure. Also, unlike in the convergence process of the empty cavity, no distinguished contacts occur due to total backfill of the cavity.

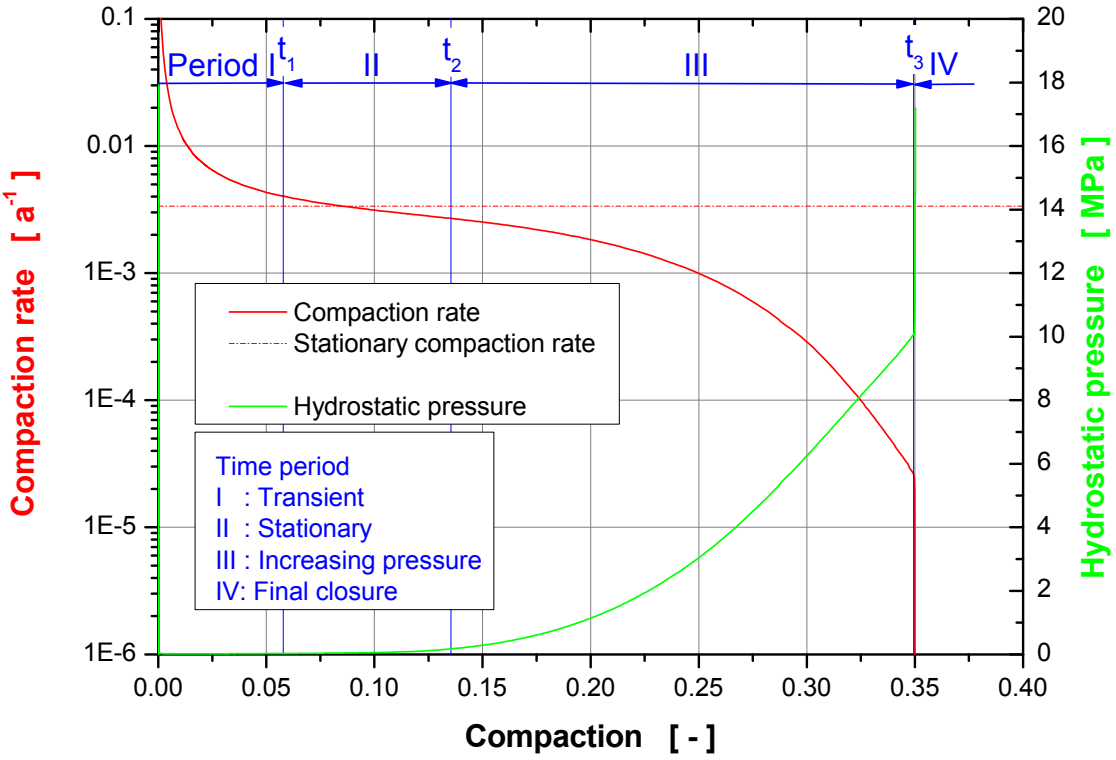

Fig. 2.3.26: Backfill pressure over porosity in a cavity filled with dry crushed salt

While the consideration of only phase I and II leads to suitably good results for a cavity without backfill material, such a simplified approach is not suitable to describe the convergence behaviour of a backfilled cavity. So, the knowledge of backfill resistance during compaction is essential for backfilled cavities.

Generally, the characterizing convergence rate during phase II, i.e. the stationary convergence rate, shows one of the following behaviours:

- The convergence rate has a stationary behaviour: $\dot{\kappa}_{stat} = \dot{\kappa}_{II}$
- The convergence rate passes a minimum during phase II: $\dot{\kappa}_{stat} = \dot{\kappa}_{II,\min}$
- The convergence rate decreases during the whole time but the deviation of the convergence rate over time $\ddot{\kappa}_{II}$ passes a maximum: $\dot{\kappa}_{stat} = \dot{\kappa}_{II}\left(\ddot{\kappa}_{II,\max}\right)$.

2.3.4.2 Numerical Model

2.3.4.2.1. Material behaviour

In the following the constitutive laws are quoted for the materials used. These materials are rock salt as host rock, crushed salt as backfill material, salt concrete in the case of a ground-covering layer for cavities that are partly backfilled, and steel for the cask. Only mechanical

effects are considered. Thermal effects are taken into account as long as they are caused by the naturally existing thermal gradient in the host rock, but no influence due to heat production from the emplaced waste or the hydration of the concrete. In general, all material behaviour is assumed as homogeneous and isotropic. Basically, the respective constitutive laws are described by an additive decomposition of the different parts of the strain rate tensor. Often, Hooke's law is applied for the elastic behaviour, hence, it is a linear relation between stresses and elastic strains.

The host rock is described by an elastic-viscoplastic constitutive law with a Young's modulus of E = 25 GPa and a Poisson ratio of ν = 0.27 as material parameters of the elastic part. The viscoplastic behaviour, also called creeping, is a multiplicative decomposition of a power law according to the J_2 flow theory for the stress part and an Arrhenius term for thermal behaviour, [[2]]. The given constitutive law, eq. 2.3.43, describes only stationary creeping and no transient behaviour.

$$\dot{\varepsilon}_{eff}^{cr}(t) = A \cdot e^{-\frac{Q}{R \cdot T(z)}} \left(\frac{\sigma_{eff}(t)}{\hat{\sigma}} \right)^n \qquad 2.3.43$$

where

T(z)	Absolute temperature
$\dot{\varepsilon}_{eff}^{cr}(t)$	Effective stationary creep rate
$\sigma_{eff}(t)$	von Mises effective stress
$\sigma_{eff}(t) = \sqrt{3J_2(t)} = \sqrt{3/2 \cdot S_{ij}(t) : S_{ji}(t)}$, $S_{ij}(t) = \sigma_{ij}(t) - \sigma_0(t) I_{ij}$, $\sigma_0(t) = 1/3 \cdot \sigma_{ii}(t)$	
$\sigma_{ij}(t)$	Stress state
$S_{ij}(t)$	Stress deviator
$\sigma_0(t)$	Hydrostatic stress

The material parameters are a structural factor A = 0.18 1/d, an activation energy Q = 54 kJ/mol, the universal gas constant R = 8.314 J/(mol·K), and a standardisation stress $\hat{\sigma}$ = 1 MPa. The stress exponent n = 5 is already given by the benchmark definition in section 2.2.1.

Crushed salt is described by a porous elastic-viscoplastic constitutive law. Instead of the original version in FLAC3D [7], an extended version of the constitutive law is used to describe the compaction behaviour. The modifications are to address a more detailed stress dependence and to include a temperature dependence. The essential points of this material law are:

- Fractional density F_D

$$F_D(t) = \frac{\rho(t)}{\rho_f} = 1 - \eta(t) \qquad 2.3.44$$

$\rho(t)$ Current density
$\eta(t)$ Current porosity

- Porosity-dependent Young's Modulus *E*

$$E(t) = E_f \, e^{-c_E \frac{\eta(t)}{1-\eta_0}} \qquad 2.3.45$$

- Porosity-dependent viscoplastic compaction

$$\dot{\varepsilon}_{co}^{vol}(t) = B_0 \, e^{-\frac{Q}{RT(z)}} \frac{e^{B_2 \rho(t)}}{\rho(t)} \left(1 - e^{B_1 \left(\frac{-\sigma_0(t)}{\hat{\sigma}} \right)^{B_3}} \right) \qquad 2.3.46$$

- Porosity-dependent shear deformation

$$\dot{\varepsilon}_{eff}^{sh}(t) = A \, e^{-\frac{Q}{RT(z)}} \left(\frac{1}{F_D(t)} \frac{\sigma_{eff}(t)}{\hat{\sigma}} \right)^n \qquad 2.3.47$$

The material parameters for the compaction behaviour result from an adjustment to the data in [1]. The following parameters are used: Density at total compaction, i. e. density of rock salt, ρ_f = 2187 kg/m^3, Young's Modulus at total compaction, i. e. Young's Modulus of host rock, E_f = 25 GPa, the Poisson ratio ν = 0.27 is also the same as for rock salt, material parameter c_E = 8.3, and the material parameters for viscoplastic compaction B_0 = 1.04·10^{20} s^{-1}, B_1 = 6.6, B_2 = -0.027 m^3/kg, B_3 = 0.33. B_0 = 5,85·10^{21} s^{-1} is used for wet backfill. The initial porosity η_0 = 0.35 is already given in the benchmark definition, chapter 2.2.2. The material parameters for shear deformation, eq. 2.3.47, correspond to those of rock salt. Remark: Compaction is admissible if the stress state is within the range of pressure, the final compaction is not yet reached, and only in the direction of porosity reduction. The behaviour under shear conditions reaches the behaviour of intact rock salt at total compaction due to the fractional density.

The material behaviour of salt concrete is purely elastic. The material parameters are already given in chapter 2.2.2 with a Young's Modulus of *E* = 15 GPa and a Poisson ratio of ν = 0.25. Also, the material behaviour of the cask is assumed to be elastic. The given parameters are Young's Modulus *E* = 210 GPa and Poisson ratio ν = 0.3.

2.3.4.2.2. Geologic and geometric situation

The length of the excavation is assumed to be very large. Thus, the calculations are carried out with the assumption of plain strain conditions. The excavation geometry used is comparable to the geometry in the BAMBUS project, [1]. Figure 2.3.27 shows the drift's cross-

section. The dimensions of the whole drift are: 4 m width on the floor level, 0.25 m wall curvature push vault, 2.5 m width of the horizontal part of the roof, and 3.5 m drift height. A further cross-section is shown in 2.3.27 in addition to the used cross-section. The stationary convergence rate for this improved profile is approx. 35 % higher than the convergence rate of the BAMBUS drift if empty cavities are compared. It should be noted that both cross-sections are realistic. The higher rate is the result of the larger width and the stress-optimised design of the drift profile.

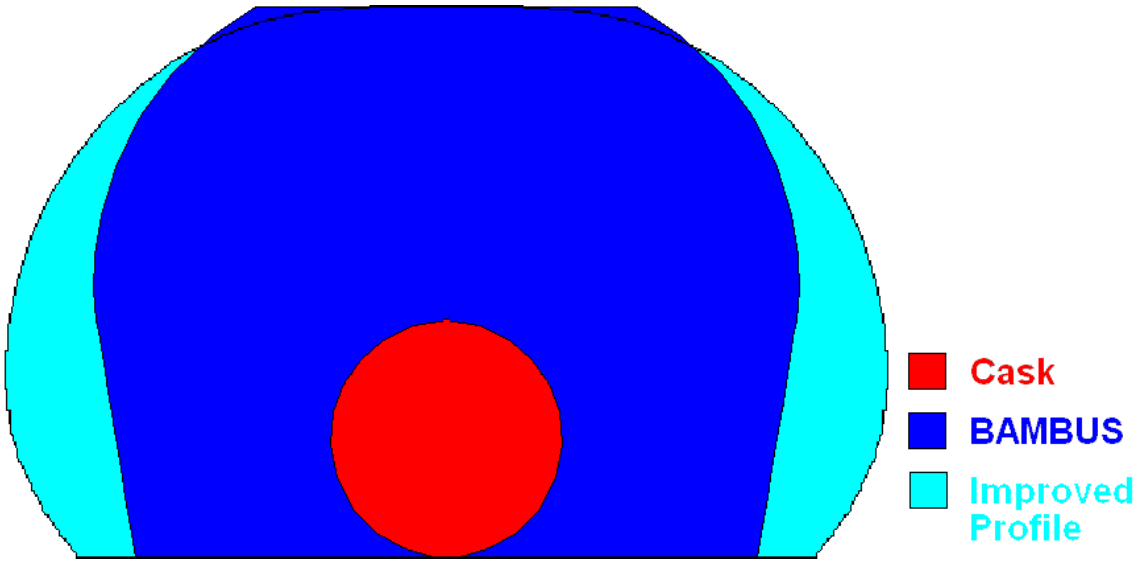

Fig. 2.3.27: Drift profile in two different cross-sections

The symmetry of the drift is used in the model, 2.3.28. The outer edges of the calculation area are at a distance of approx. 80 m to the symmetry line in horizontal direction, to the roof in upper vertical direction as well as to the floor in lower vertical direction. The zone size on the contour amounts to 0.15 m to 0.2 m. The discretization of the system results in a total of 2288 zones and 2359 nodes in a plane. Contact elements are on the outline of the excavation to detect imminent contact between floor, wall, and roof. The 3D-code FLAC^{3D} is used, [7]. In order to simulate plain strain conditions, only one column of elements exists in axial direction. FLAC^{3D} is a numerical code based on the finite difference method.

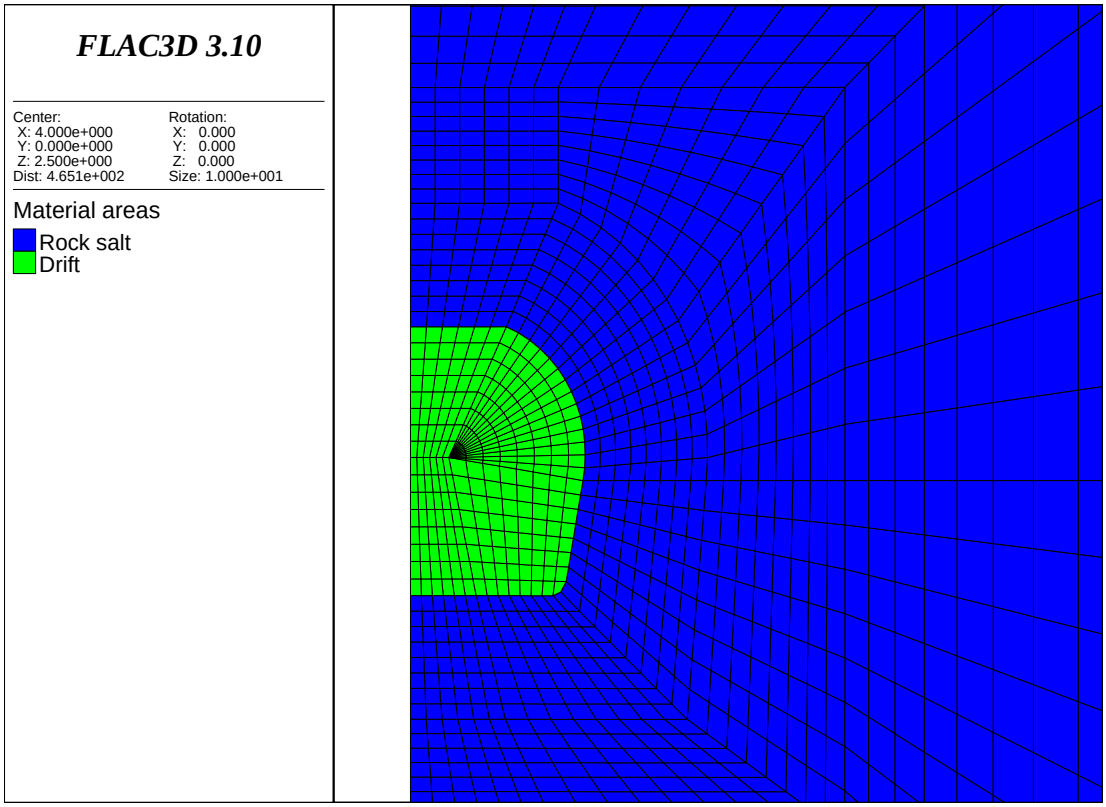

Fig. 2.3.28: Discretization of the drift

The boundary and initial conditions are as follows: No displacements in normal direction and no friction in tangential direction on all boundaries except the upper one which is loaded with stress conditions. These stress conditions are a normal stress according to the initial stress state on that level. The initial stress state is supposed to be lithostatic isotropic with a stress level of 17.94 MPa at floor level and a gradient with respect to the given host rock density. The temperature is set to a constant 36.85 °C over space and time in the whole model. The calculation period covers a time period of 100,000 a.

Two fixed water levels are considered in the case of fluid pressure: A fluid pressure of 5.89 MPa represents a brine level up to the top of the salt dome and a fluid pressure of 9.42 MPa a brine level up to the surface. As a third case of a flooded state, a time-dependent fluid pressure is regarded. There is no time between excavation and backfilling and/or flooding in all cases of backfilling and flooding and, thus, no time of free convergence in these cases.

The cross-section of the drift is 14.52 m^2 at the initial state. The lower 5.95 m^2, i.e. 41 % of the whole cross-section of the drift, are concreted if salt concrete is used, 2.3.29. If a cask is taken into account, 2.3.30, it is modelled with a diameter of 1.6 m and a contact area on the floor of 0.4 m width. With 1.99 m^2, the cask shares about 14 % of the drift cross-section at the beginning of the convergence process.

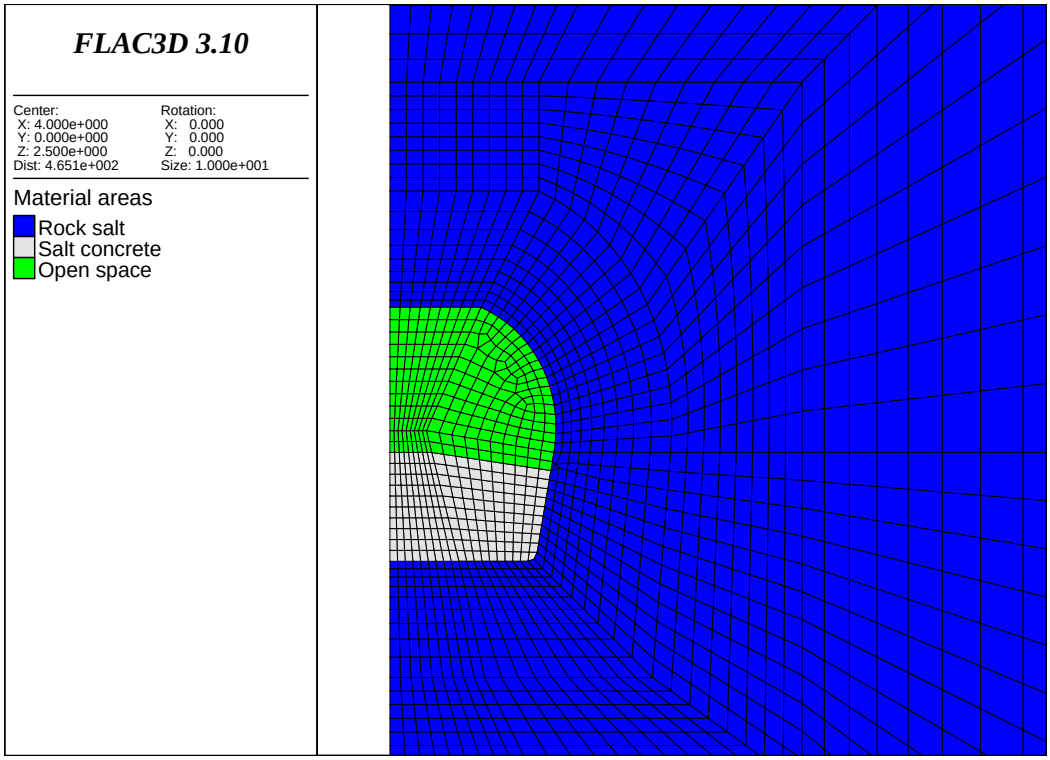

Fig. 2.3.29: Discretization with salt concrete

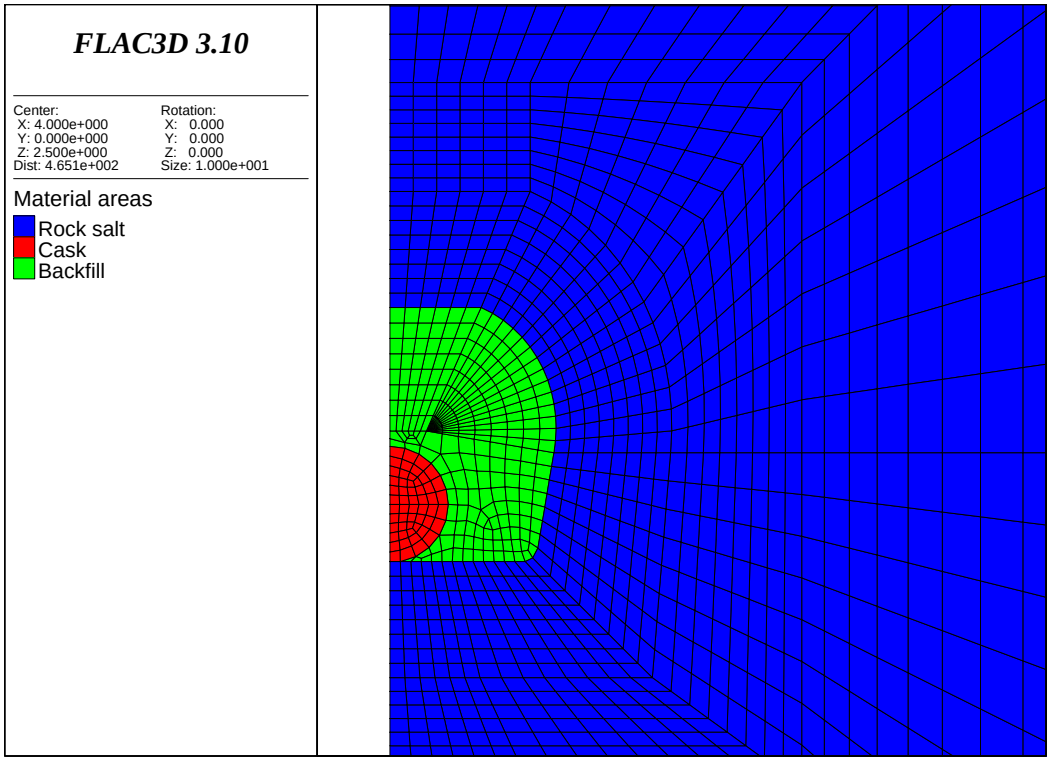

Fig. 2.3.30: Discretization with cask in the drift

2.4 Results of the benchmark calculations

2.4.1 Application of the 3D model FLAC

The five cases and their variations from chapter 2.2.1 are re-grouped depending on their backfill situation because the concrete on the floor and the emplaced cask do not have much influence on the convergence. Besides, the variations of case 2 are represented twice to show the influence of the backfill material under different conditions:

- without backfill: Case 1 (a to d) and Case 4a
- pure backfill: Case 2 (a and b)
- dry backfill: Case 2a, Case 4b, and Case 5a
- wet backfill: Case 2b, Case 3 (a to c), and Case 5 (b to d)

The results are shown in three figures each for every group: First, the development of the convergence over time is given, second, the convergence rate over time is shown, and third, the convergence rate over convergence is given. Convergence has to be replaced by compaction resp. convergence rate by compaction rate if backfill is considered. 2.3.31 to 2.3.33 show the results for the cases without backfill material, 2.3.34 to 2.3.36 give the results for the pure backfill cases, 2.3.37 to 2.3.39 show the results for dry backfill, and 2.3.40 to 2.3.42 show the results for wet backfill. At this point, the general description of convergence behaviour in chapter 2.3.4.1 should be referred to. The characteristic data regarding time points, specific values of convergence rate and convergence are summarised in table 2.4.1.

Tab. 2.4.1: Characteristic parameters of the convergence process

		Stationary convergence rate [a^{-1}]	Average convergence rate in phase II [a^{-1}]	Begin of period II t_1 [a]	Compaction at t_1 [%]	Porosity at t_1 [%]	End of period II t_2 [a]	Compaction at t_2 [%]	Porosity at t_2 [%]	End of period III t_3 [a]	Compaction at t_3 [%]	Porosity at t_3 [%]
1a	Empty	$2.7 \cdot 10^{-3}$	$2.7 \cdot 10^{-3}$	25	11	-	1050	94	-	1400	99	-
1b	fluid pressure 5.9 MPa	$3.6 \cdot 10^{-4}$	$3.8 \cdot 10^{-4}$	125	7	-	9000	97	-	11000	99	-
1c	fluid pressure 9.4 MPa	$6.6 \cdot 10^{-5}$	$6.6 \cdot 10^{-5}$	350	4	-	55000	98	-	65000	99	-
1d	var. fluid pressure	$6.0 \cdot 10^{-5}$	$6.1 \cdot 10^{-5}$	475	5	-	70000	99	-	80000	99	-
2a	dry backfill	$3.4 \cdot 10^{-3}$	$3.2 \cdot 10^{-3}$	10	6	31	40	14	25	1200	35	0
2b	wet backfill	$2.8 \cdot 10^{-3}$	$2.7 \cdot 10^{-3}$	15	8	29	70	21	18	300	35	0
3a	wet backfill, fluid pressure 5.9 MPa	$3.6 \cdot 10^{-4}$	$3.4 \cdot 10^{-4}$	100	6	31	650	22	16	1900	35	1
3b	wet backfill, fluid pressure 9.4 MPa	$6.5 \cdot 10^{-5}$	$6.2 \cdot 10^{-5}$	350	4	32	3750	22	17	12000	35	0
3c	wet backfill, var. fluid pressure	$5.5 \cdot 10^{-5}$	$5.5 \cdot 10^{-5}$	650	6	31	4750	25	13	12000	35	0
4a	partly con-crete	$2.5 \cdot 10^{-3}$	$2.3 \cdot 10^{-3}$	30	12	-	1200	94	-	1500	98	-
4b	partly con-crete and dry backfill	$3.5 \cdot 10^{-3}$	$3.4 \cdot 10^{-3}$	7	5	32	25	10	28	1420	35	0
5a	cask, dry backfill	$4.1 \cdot 10^{-3}$	$3.9 \cdot 10^{-3}$	7	5	31	25	12	26	1000	35	0
5b	cask, wet backfill, fluid pressure 5.9 MPa	$3.7 \cdot 10^{-4}$	$3.6 \cdot 10^{-4}$	150	9	28	700	25	13	1600	34	2
5c	cask, wet backfill, fluid pressure 9.4 MPa	$7.4 \cdot 10^{-5}$	$7.1 \cdot 10^{-5}$	300	4	32	3500	24	15	7500	33	3
5d	cask, wet backfill, var. fluid pressure	$7.0 \cdot 10^{-5}$	$6.7 \cdot 10^{-5}$	375	5	32	4000	25	13	7500	33	3

Figures 2.3.31 to 2.3.33 give the results for the group without backfill. The main effect is the fluid pressure. This effect is discussed separately later with the normalised results. Two further aspects with small influence on the convergence rate are the salt concrete in the lower part of the excavation and the time-depending fluid pressure. The small effect from the salt concrete in the lower part of the excavation can be observed when the results without fluid pressure are compared. The stationary convergence rate in the case of the concrete layer is approx. 7 % less than in the case of an empty cavity, the values of the average rate during phase II differ by 13 %, figure 2.3.32. This difference between the average values is the result from contact behaviour, thus, it is also caused numerically. Basically, it depends on the filling degree and the material properties of the concrete to what extent the introduced concrete layer influences the convergence behaviour. It is a non-linear dependence between the influence on convergence rate and filling degree, so the low influence of the concrete layer shown here cannot be generalised for any filling degree. This non-linear behaviour is the interference between geometry and additional stability. The geometric aspect is the height-width relation of the remaining open space if a salt concrete layer is at the bottom. Here, the geometry of the open space is flattened compared to the initial geometry, which leads to an increase in the convergence rate. A stability aspect comes from the concrete layer, which restrict the uplift of the floor. A blocked movement from this side reduces the convergence rate. It has to be noticed that no strength limit is considered for the concrete layer, hence, breakage of the layer is not taken into account. Over all, with increasing filling degree of the cavity with salt concrete the influence on the convergence rate may become stronger.

The other aspect within this group is the influence of the time-depending fluid pressure compared to the calculation with a fixed fluid pressure of 9.4 MPa. The difference in the convergence behaviour between both variations appears less during phase I, which is the phase of stress redistributions as well as the period of the biggest pressure difference between fixed and time-depending fluid pressure, but during the stationary phase II between approx. 800 a and 4000 a. Though a stationary convergence rate lower by approx. 9% is observed with variable fluid pressure, table 2.4.1, the average value of the convergence rate during period II varies only by about 7%. This behaviour is not the result of the current pressure difference between the two cases because the difference during these years is in the range of 0.4 % to 0.3 % but caused by the viscoplastic material behaviour. At about 2000 a, the convergence behaviour with variable fluid pressure starts to approximate the level of fixed fluid pressure.

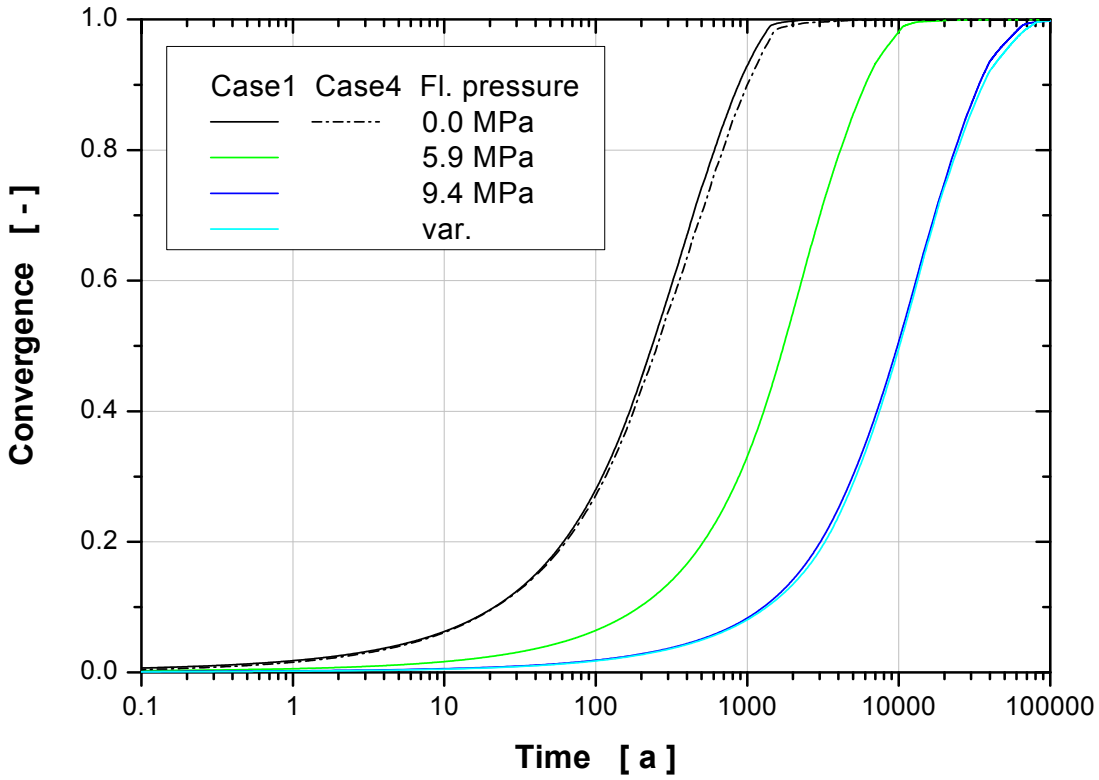

Fig. 2.3.31: Convergence over time for variants without backfill

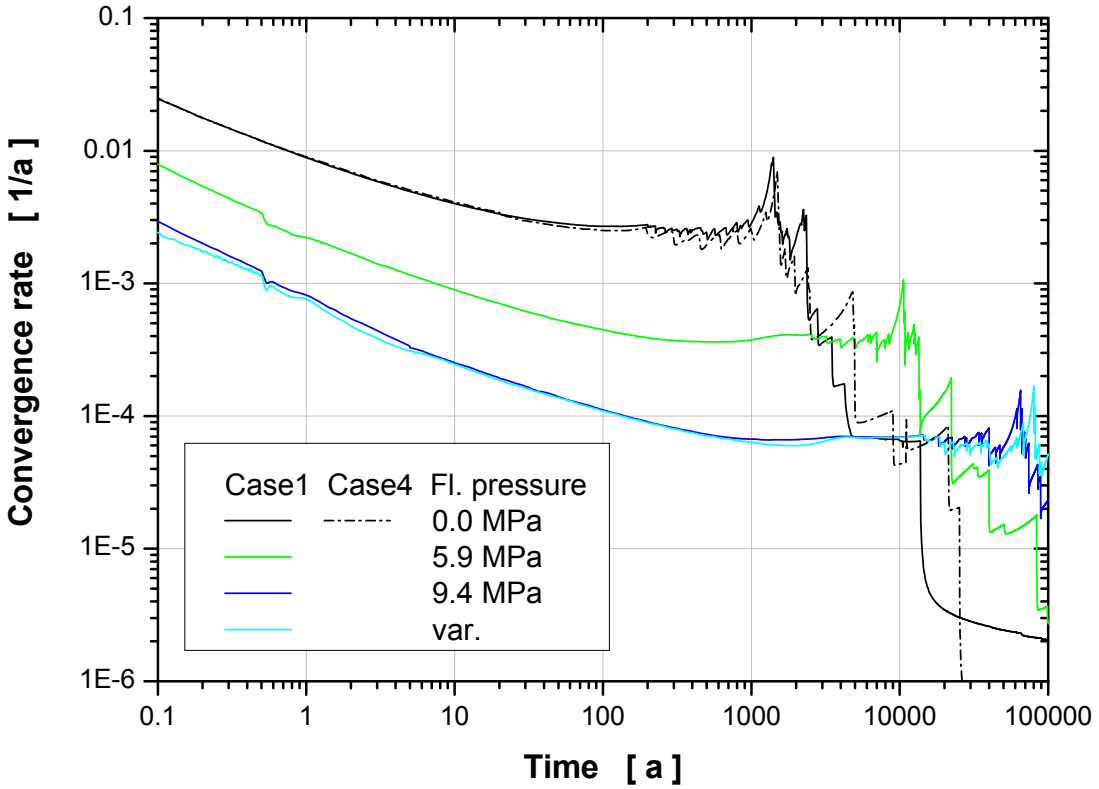

Fig. 2.3.32: Convergence rate over time for variants without backfill

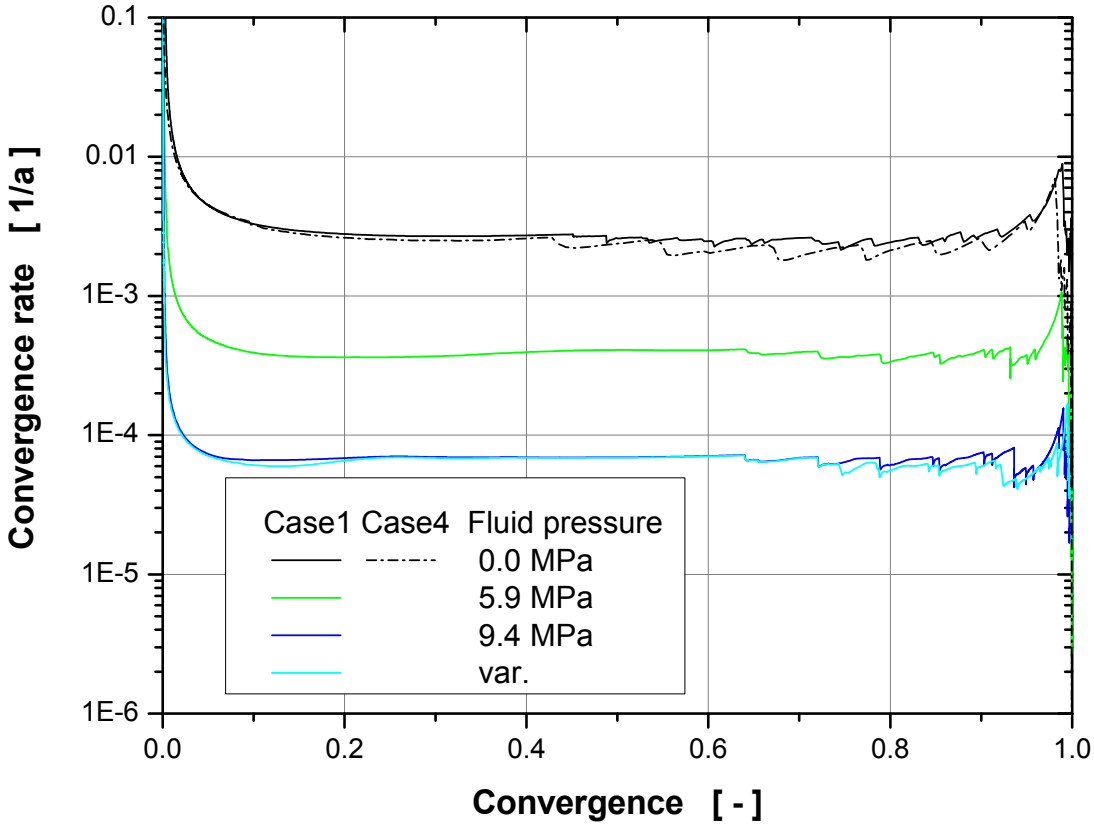

Fig. 2.3.33: Convergence rate over convergence for variants without backfill

The influence of the different material behaviours of the dry and wet backfill on the increase of the supporting backfill pressure is shown in the second group. The behaviours of these two materials do not differ from their mathematical descriptions, a difference exists merely in the values of the factor which describes the creep intensity, eq. 2.3.46. As already shown in the comparison of the convergence behaviour of the open cavity and the cavity filled with dry backfill, figure 2.3.25, the influence of the backfill starts to become apparent in period II. The use of another mathematical description, e.g. as given in [1], may influence this point in time slightly. As the wet backfill reacts with a lower backfill pressure compared with the dry material under the same compression state, i. e. the same compaction and the same compaction rate, the convergence behaviour of the variation filled with wet material follows the behaviour of the open excavation a little bit longer. Due to the higher compaction rate, the state of total compaction is reached earlier than in a cavity filled with dry backfill. This increase in backfill pressure, especially in the range of higher stresses and thus in the range of lower porosity, is the point of main interest if backfill is taken into account. Unfortunately, the material behaviour of crushed salt shows significant uncertainties, in particular in the range of low porosities but also with respect to the amount of humidity. The aspect of low porosities is currently being investigated in several projects. Accordingly, changes can arise in the predicted behaviour with improved data in the range of low porosities.

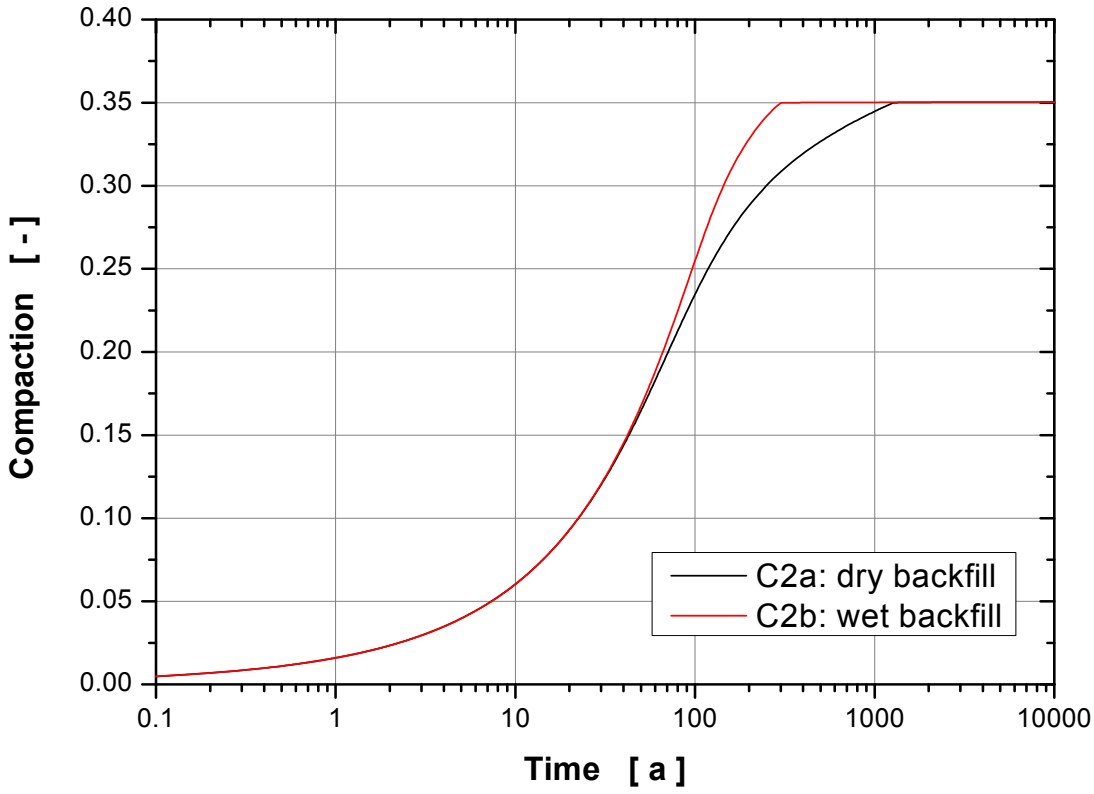

Fig. 2.3.34: Compaction over for variants with pure backfill

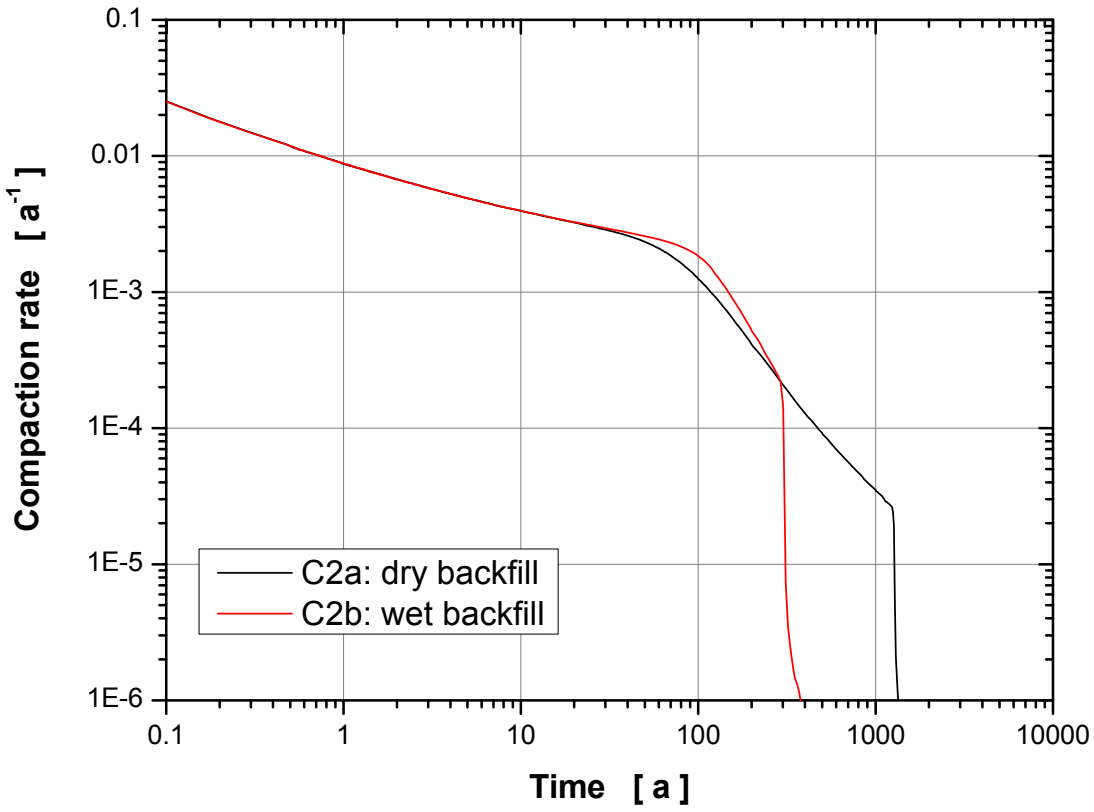

Fig. 2.3.35: Compaction rate over time for variants with pure backfill

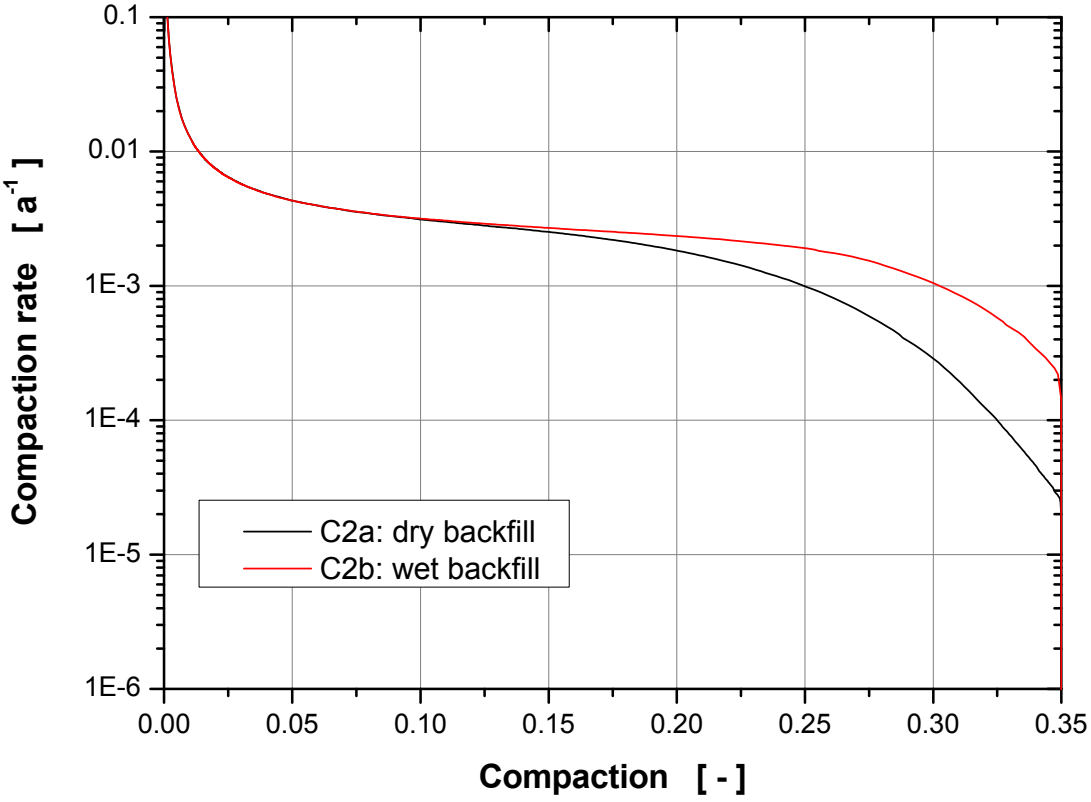

Fig. 2.3.36: Convergence rate over convergence for variants with pure backfill

Figures 2.3.37 to 2.3.39 show the results for dry backfill. The aspect of an emplaced concrete layer is taken up again in this group, however, with respect to backfill instead of an open remaining space. The difference between the stationary rates of the variants with concrete layer, C4b, and with pure backfill, C2a, is about 3 %, which is less than in the variations without backfill, C4a and C1a. However, if the convergence rate over time is compared, the difference in the convergence rate considering a concrete layer is in the same range. Depending on time, the convergence rate from the variants with concrete layer is between approx. 15 % above and below the corresponding rate without the layer. Beside the concrete layer, a further variation is included in the group investigated here with the cask variation, C5a. This cask leads to an increase in the convergence rate during the first two phases compared to the case of pure backfill while the convergence rate of the variant considering the concrete layer is below this rate. This behaviour changes later while the backfill pressure increases. The variant with the cask and the one with the concrete layer are the upper and the lower limits of convergence behaviour within this group. Within these variants, the time of nearly total compaction, t_3, is reached in the range between 1,000 a and 1,500 a. The difference in the convergence rate between these two variants and their average value for a given fixed time amounts to up to 8 %. This amount is the same as already observed within the group without backfill.

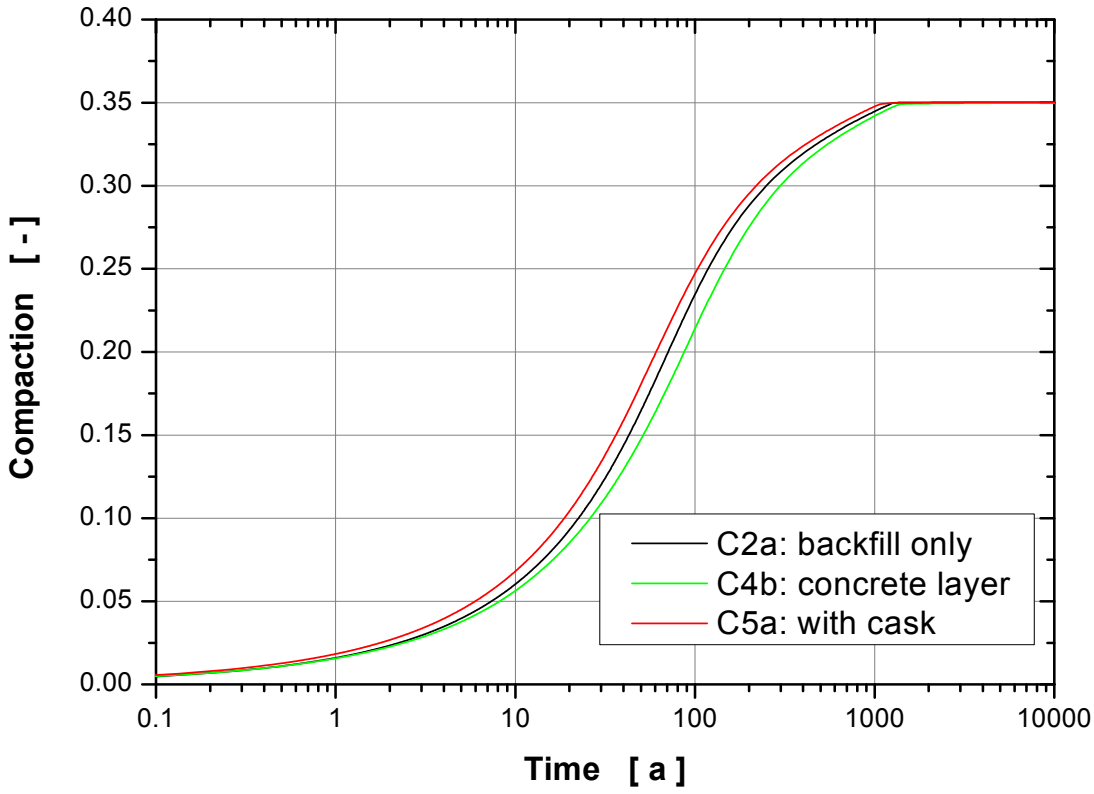

Fig. 2.3.37: Compaction over time for variants with dry backfill

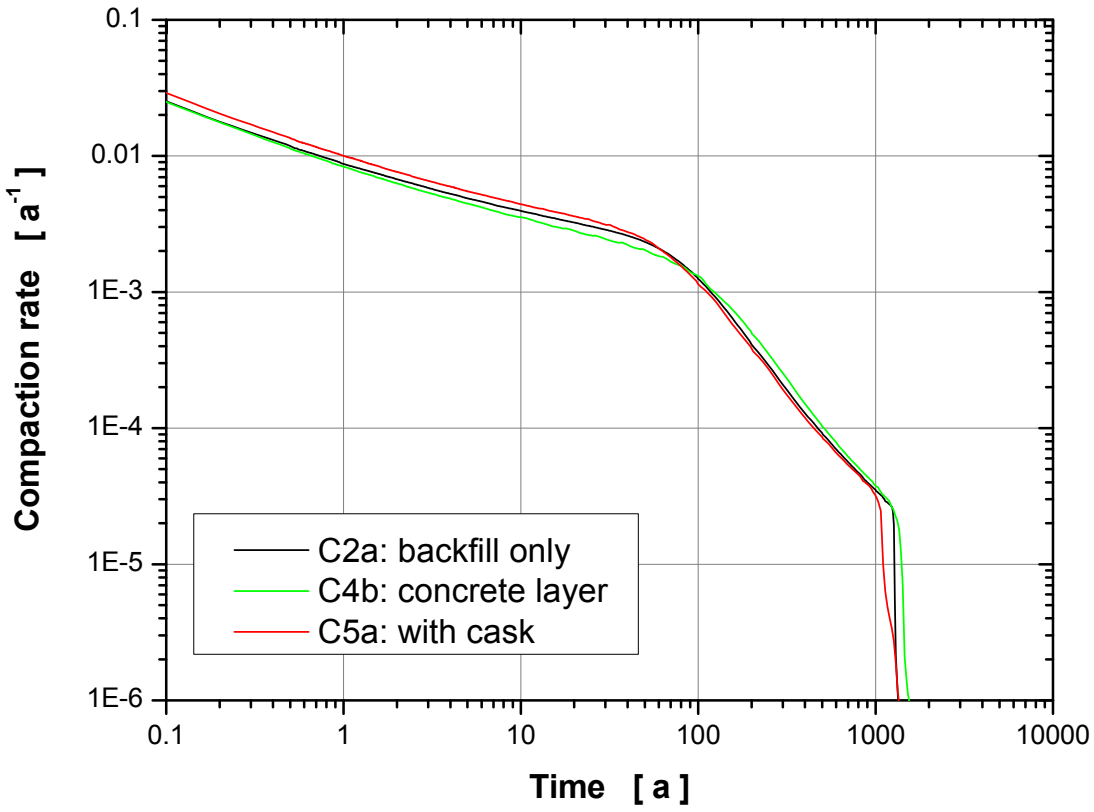

Fig. 2.3.38: Compaction rate over time for variants with dry backfill

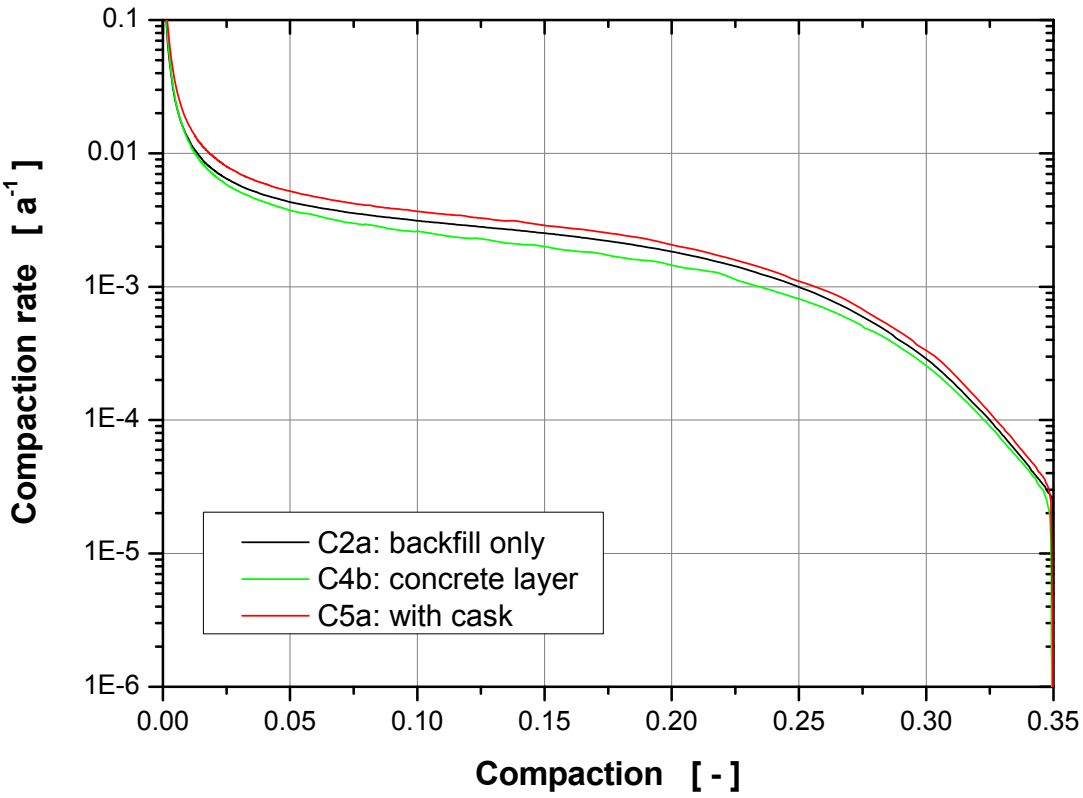

Fig. 2.3.39: Compaction rate over compaction for variants with dry backfill

Figures 2.3.40 to 2.3.42 show the results of the variations with wet backfill material. Beside the main effect from fluid pressure, two aspects with minor effect are considered. These are the cask and the time-depending fluid pressure. Both effects were already taken into account before. If a cask is considered, the convergence rate for a fixed given time is approx. 10 % to 15 % higher than without cask. This behaviour was already found at a comparable rate with dry backfill. As with the variations without backfill material, the fluid pressure is the decisive quantity in the calculations with backfill with wet crushed salt. The convergence behaviour is determined by the long-lasting pressure; hence, no significant difference exists in the behaviour under pressure varying over time and constant fluid pressure of 9.4 MPa. All in all, the effects of the supporting pressure of the fluid are comparable to those in an unfilled excavation.

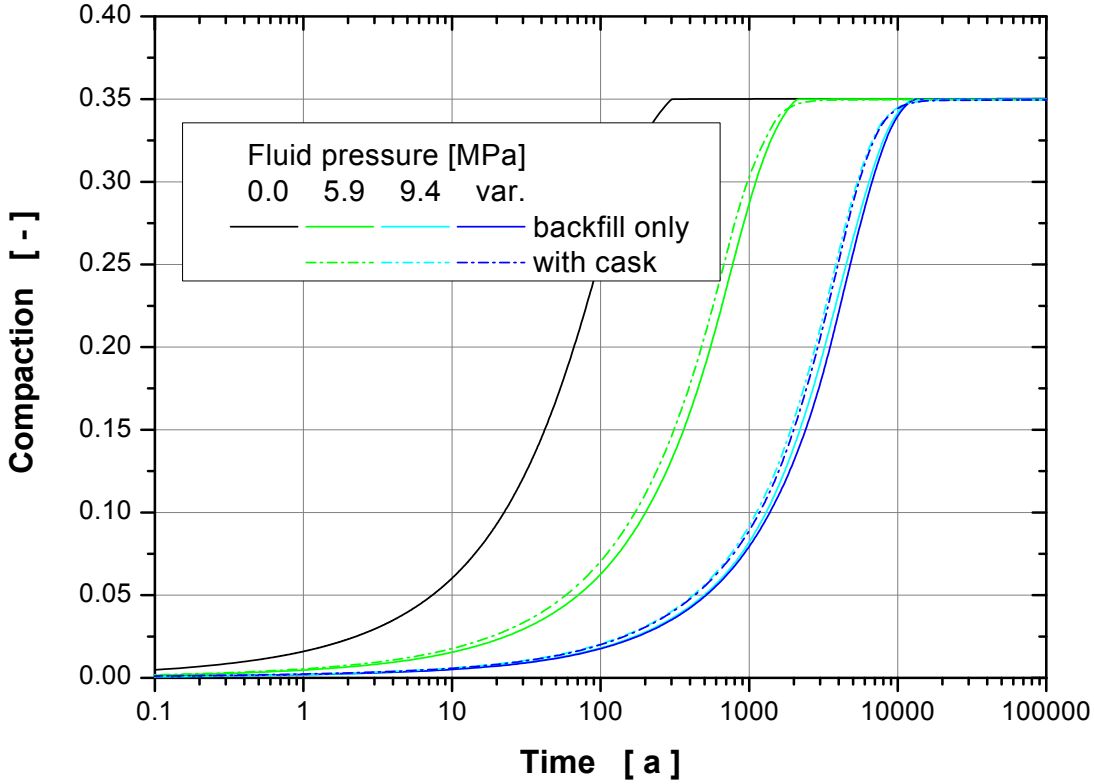

Fig. 2.3.40: Compaction over time for variants with wet backfill

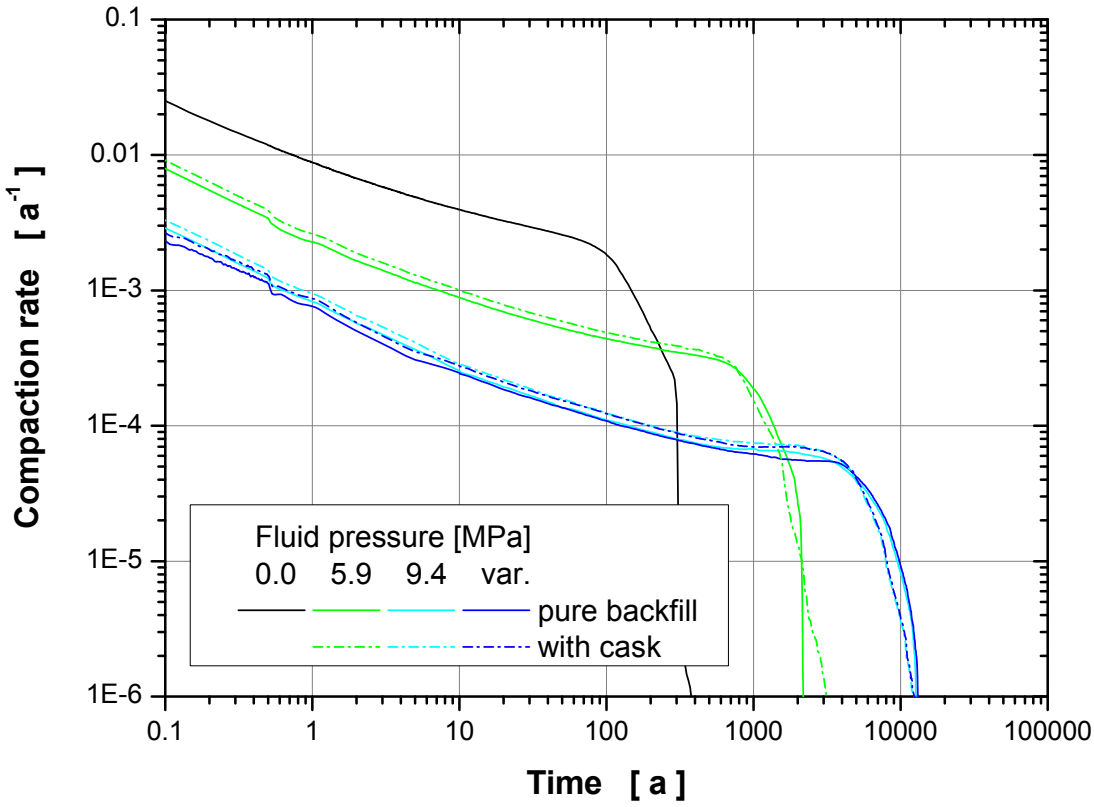

Fig. 2.3.41: Compaction rate over time for variants with wet backfill

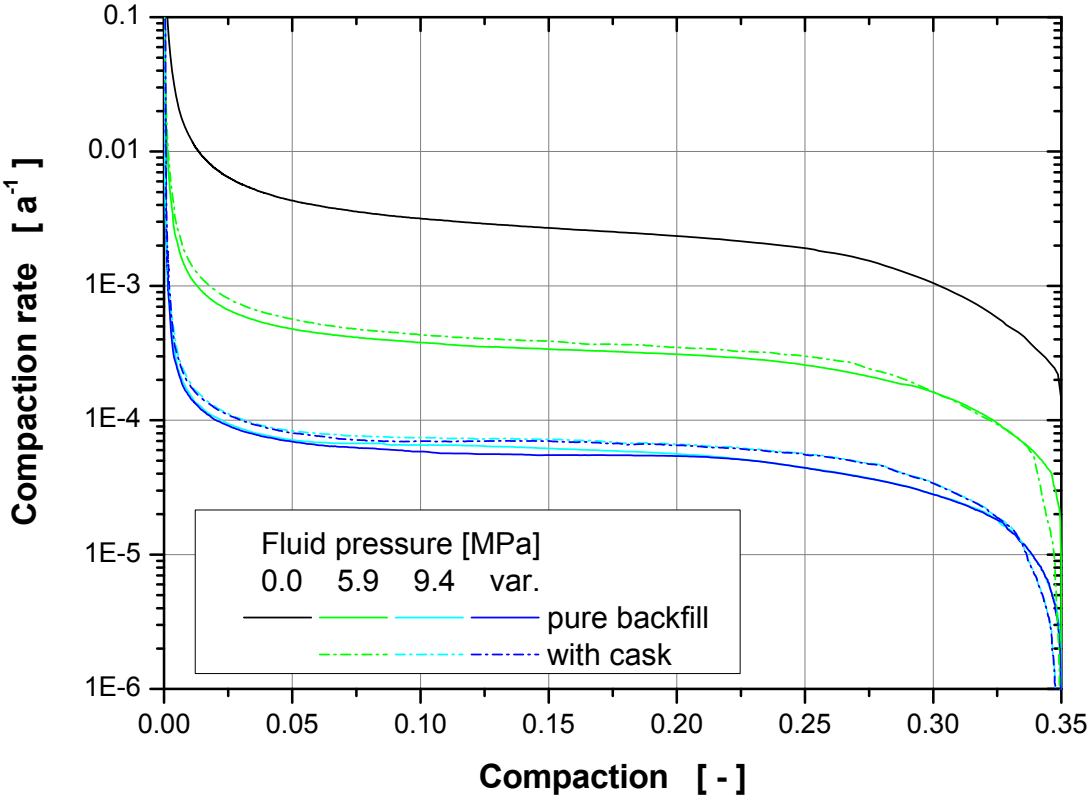

Fig. 2.3.42: Compaction rate over compaction for variants with wet backfill

Normalized results

EMOS codes without an own geo-mechanical part use a multiplicative decomposition of separate functional parts f_i to a reference $\dot{\kappa}_{\mathrm{Re}f}$ to include additional or differing aspects, e.g. depth, temperature, backfill behaviour, or fluid pressure on convergence behaviour.

$$\dot{\kappa} = \dot{\kappa}_{\mathrm{Re}f} \cdot \prod_i f_i \qquad 2.3.48$$

Here, the reference is the behaviour of the open and dry excavation in the given reference scenario. Thus, no fluid pressure is considered in the reference scenario. The focus in these final representations, figures 2.3.43 to 2.3.45, lies on the additional functional part of the fluid pressure resp. on the normalization with fluid pressure. The results of the calculation without backfill and with wet backfill are compared to each other within a common frame. Furthermore, the convergence rate and the time are standardised in the calculations with respect to the fluid pressure. The transformation occurs on the basis of the effective pressure difference and the material law of the surrounding rock salt.

$$\frac{\dot{\kappa}_{norm}\left(t_{norm}, p(t)\right)}{\dot{\kappa}\left(t, p = 0MPa\right)} = \left(\frac{\sigma_i + p(t)}{\sigma_i}\right)^n = \left(1 + \frac{p(t)}{\sigma_i}\right)^n \qquad 2.3.49$$

$$\frac{t_{norm}(p(t))}{t(p=0MPa)} = \frac{1}{\left(1+\frac{p(t)}{\sigma_i}\right)^n} \qquad 2.3.50$$

where

$p(t)$	Fluid pressure
σ_i	Initial lithostatic stress

The value of the stress exponent n is the same as in eq. 2.3.43, i.e. n = 5. Note that stress components are signed positive for tension and negative for pressure. So, the value of the initial lithostatic stress is negative.

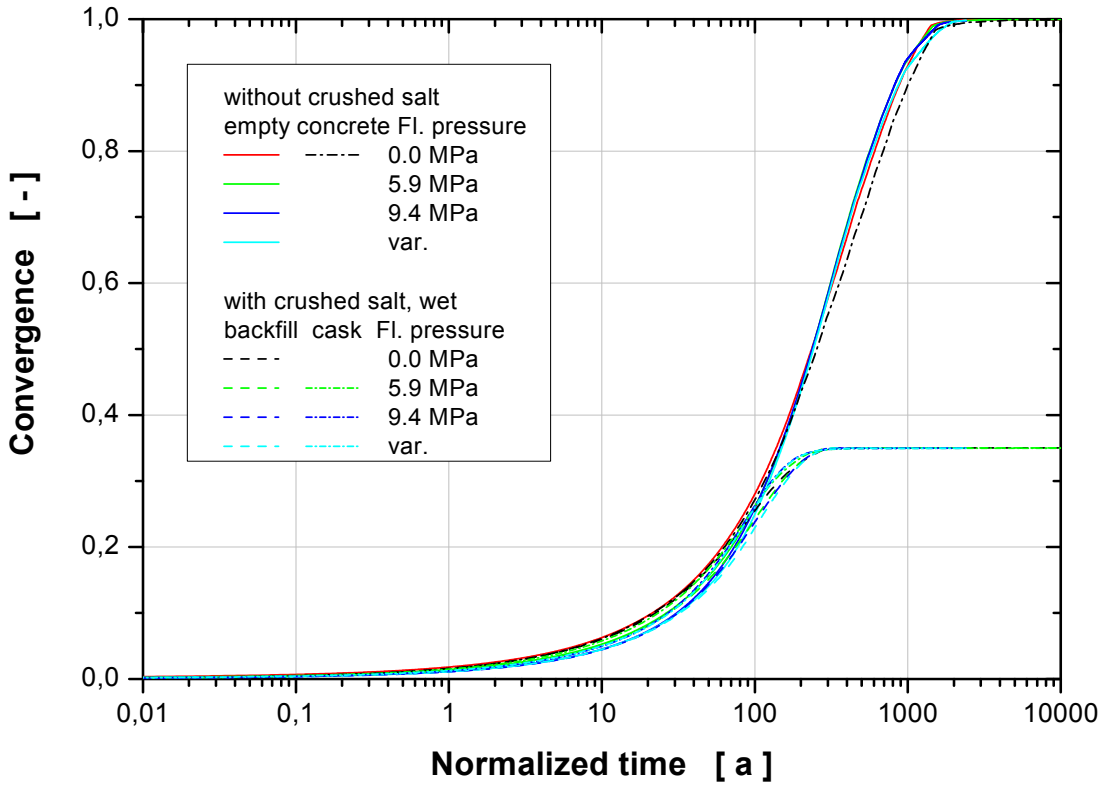

Fig. 2.3.43: Convergence (compaction) over time for variants without and with wet backfill

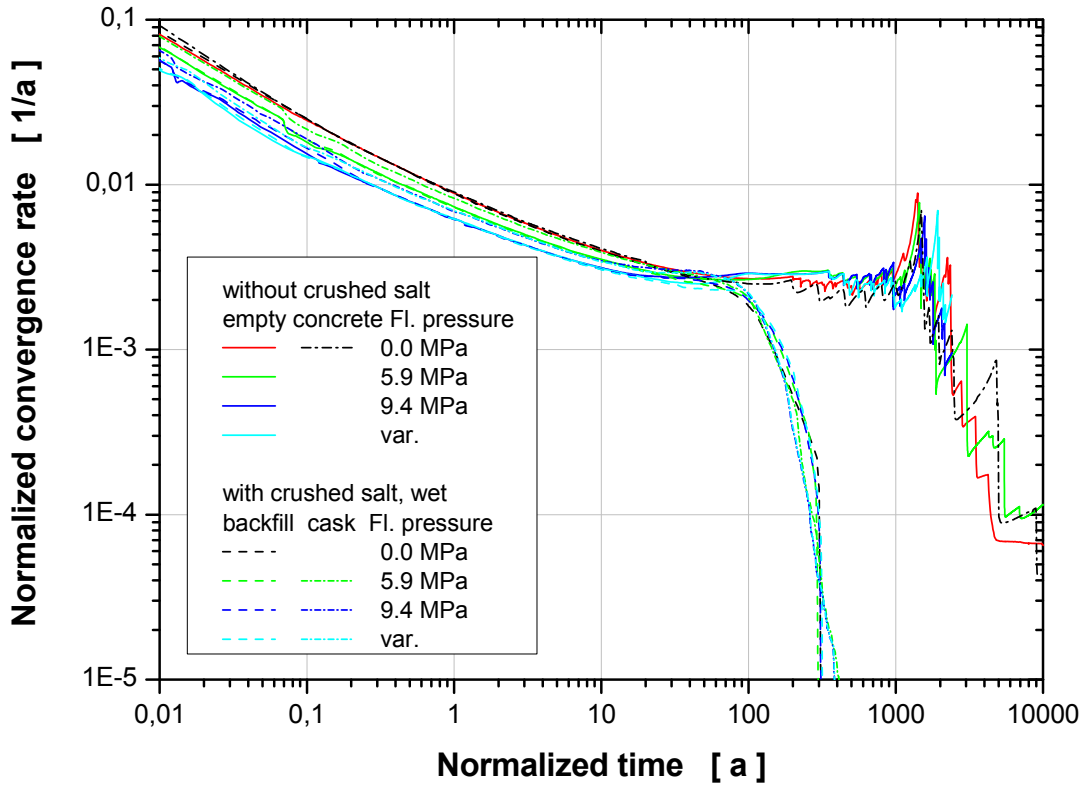

Fig. 2.3.44: Convergence rate over time for variants without and with wet backfill

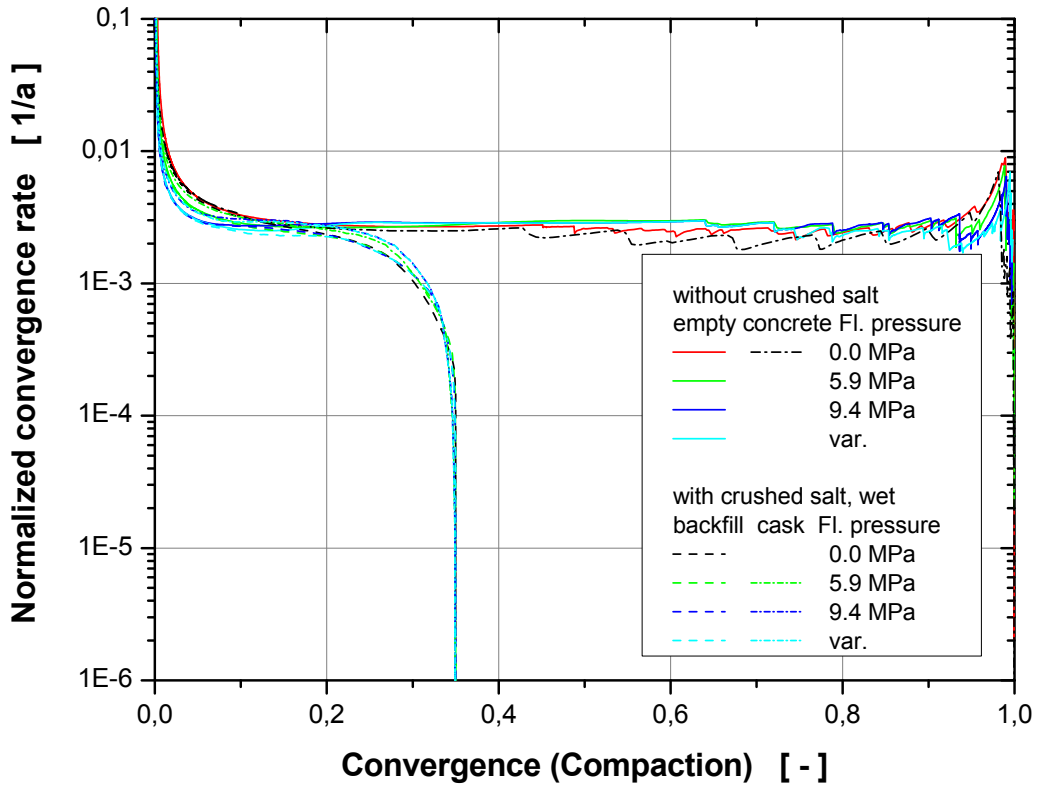

Fig. 2.3.45: Convergence rate over convergence for variants without and with wet backfill

Figures 2.3.43 to 2.3.45 show the results normalized by fluid pressure. A red line marks the reference of an open non-flooded cavity in these figures. The range between the results of different calculations during the transient phase I of the convergence process is a little bit larger than during the stationary period II. In the first period, the results of the reference scenario are nearly almost close to the top of all variations. The variants with lower convergence rate are in a range up to 40 % less during this transient phase compared with the reference case. The duration of this phase is a relatively short period which is not so significant for the long-term safety. The difference is caused by the fact that the normalization using equation 2.3.49 and eq. 2.3.50 does not completely describe the aspect of the stress redistribution around the excavation at the beginning. Within the stationary phase, there are more variants with slightly higher convergence rates than the reference case. Due to the increasing backfill pressure, all variants can be placed either in the group of backfilled cavity or in the group of cavities without backfill. Within each group the convergence behaviour is close to each other over the whole time.

2.4.2 Application of the LOPOS model to the test cases

The GRS model of convergence is applied to test cases, for which results of rock mechanics calculations are given by DBE-TEC. The reference convergence rate K_{ref} in many cases can be directly obtained from the rock mechanics calculations by extrapolating the respective results to very large times. Since in the rock mechanics calculation the simulation time starts immediately after excavation at time t = 0, in eq. 2.3.8 for the explicit time dependence, used in the GRS model, the parameter λ_S should be zero. However, for very small times the function f_t only depends on the product $K_0 \cdot \lambda_S$ (cf. Appendix B) and it is, therefore, justified to use a very small value of λ_S instead of zero and a corresponding large value of K_0. Consequently, in all test cases below, the fixed value $\lambda_S = 10^{-6}$ is used.

2.4.2.1 Results of test cases 1a, 1b, and 1c

The comparison of the convergence rates, calculated with different but constant values of the fluid pressure (cf. test case description in chapter 2.2.2), with those of the rock mechanics calculations is presented in figure 2.4.1, while figure 2.4.2 shows the time evolution of the volume of the cavity. The best match of the results is achieved with $K_0 = 80$ [a^{-1}] and $K_{ref} = 2.5 \cdot 10^{-3}$ [a^{-1}]. With these parameter values it is found that for all the three constant-pressure boundaries the convergence rates as well as the volumes match really well.

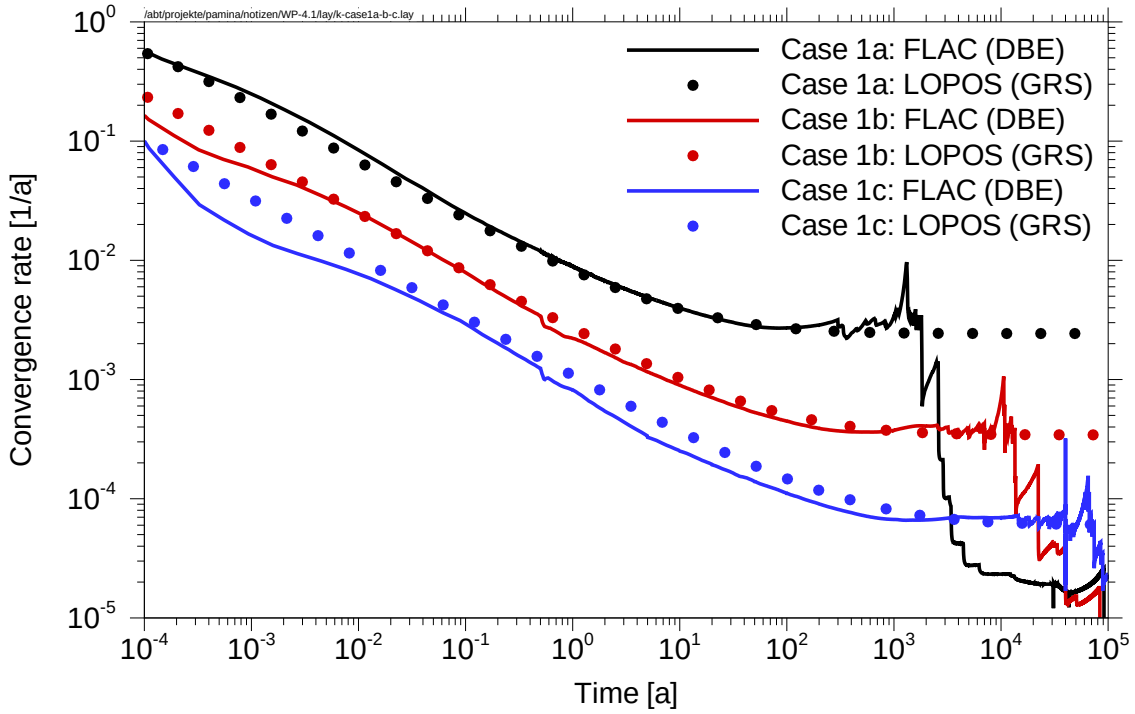

Fig. 2.4.1: Comparison of convergence rates: Cases 1a, 1b, 1c

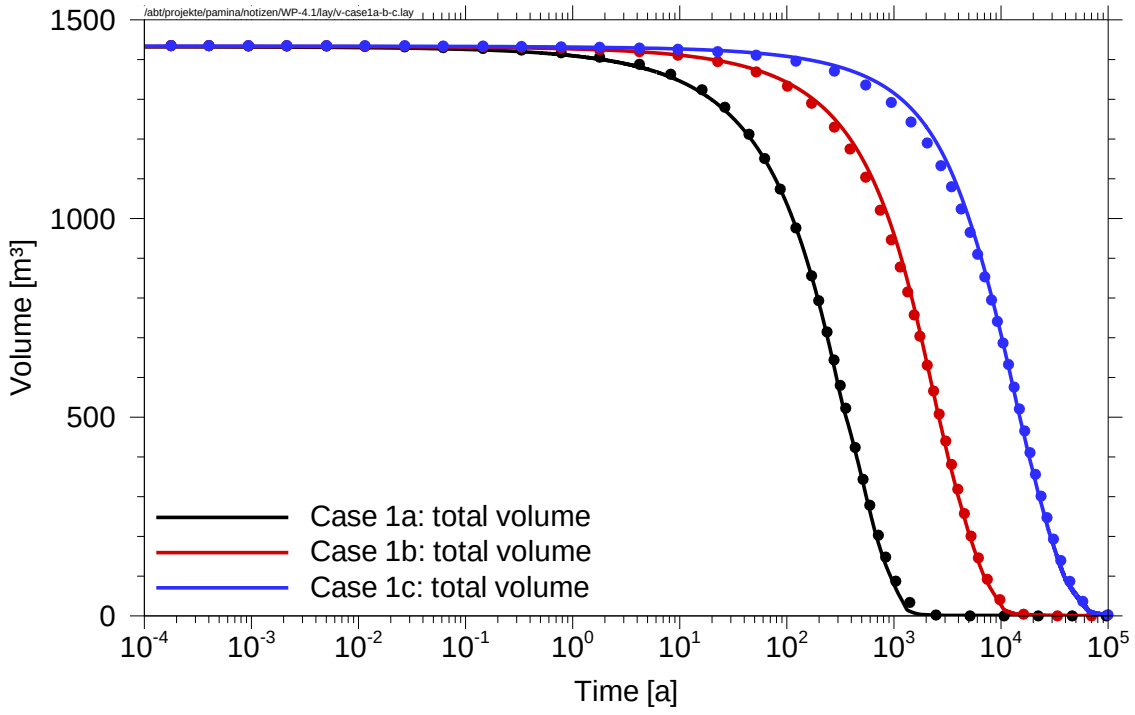

Fig. 2.4.2: Comparison of time evolution of volumes: Cases 1a, 1b, 1c

2.4.2.2 *Results of test case 1d*

In figure 2.4.3, the convergence rates obtained with the LOPOS model are compared for some test cases. For case 1a atmospheric and for case 1c a constant hydrostatic pressure is applied, which corresponds to a completely brine-filled repository and a negligible flow resistance of the cavity, the shaft segment and its sealing. In case 1d the cavity and the shaft are continuously flooded over a time span of 50 a. During this period the fluid pressure in the cavity increases, until it reaches the hydrostatic pressure of the completely filled repository. Additionally, the shaft sealing permeability is reduced to 10^{-16} m^2, which after 50 a yields a hydraulic pressure increase in the cavity above the hydrostatic value, which is driven by the convergence, when brine is squeezed out of the cavity through the high flow resistance of the shaft sealing.

At the beginning, the convergence rate equals that of case 1a (air filled cavity). With increasing fluid pressure the convergence rate is reduced. After increase of the fluid pressure above the hydrostatic value, the convergence rate is reduced below that of case 1c (completely filled repository). While the fluid pressure decreases to the hydrostatic value, the convergence rate curve approaches that of case 1c. The case 1d time evolution of the cavity's volume is shown in Fig. 2.4.4. At the beginning it follows that of case 1a and later it approaches that of case 1c, as to be expected.

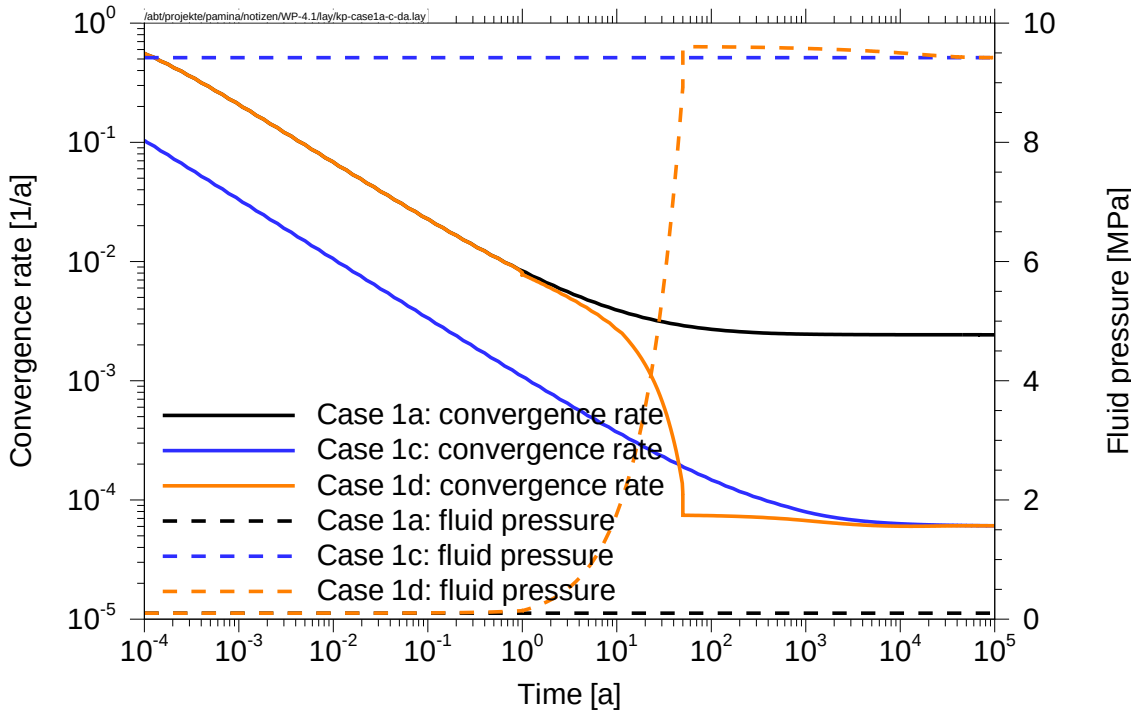

Fig. 2.4.3: Convergence rate and fluid pressure of cavity in test cases 1a, 1c and 1d

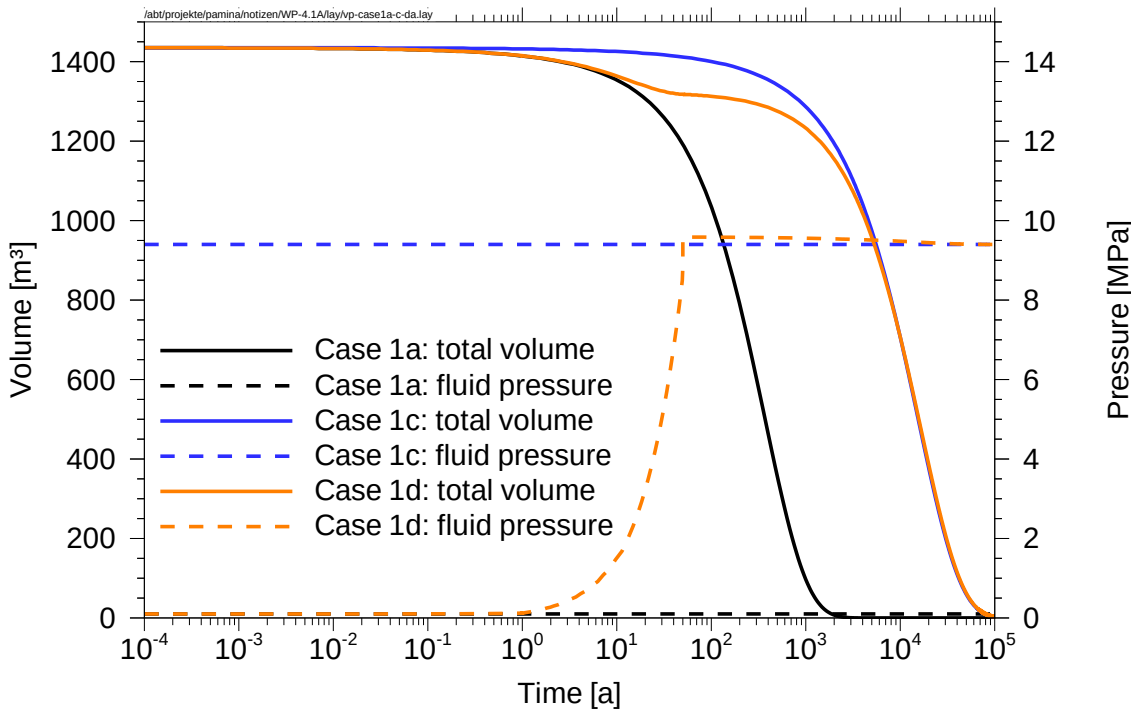

Fig. 2.4.4: Volumes and fluid pressure of cavity in test cases 1a, 1c and 1d

Figure 2.4.5 shows the result of the rock mechanics calculation and that of the LOPOS calculation for case 1d. Here, a clear difference between the results can be observed at very early times. However, in the rock mechanics calculation the convergence rate is calculated from the cross section reduction of the cavity by numerical differentiation. In LOPOS the convergence rate is calculated directly with the formulas given in chapter 2.3. The consequences of the different convergence rates at early times are negligible as can be seen in Fig. 2.4.6, where the time evolutions of the volumes are compared.

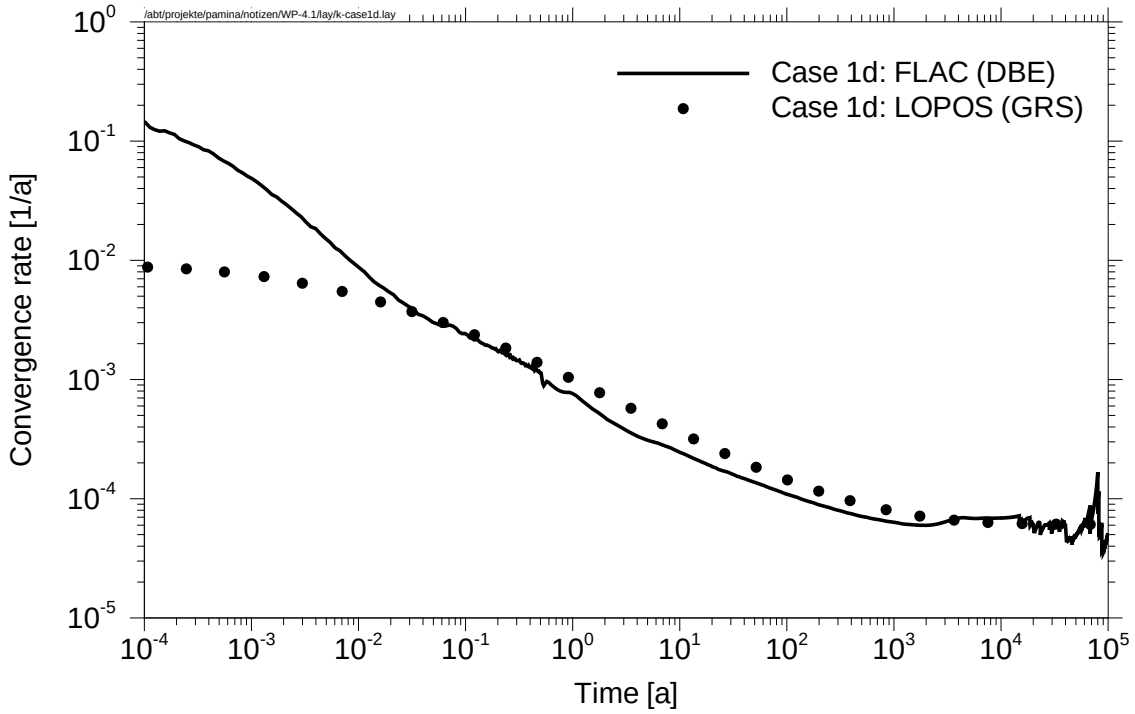

Fig. 2.4.5: Comparison of convergence rates: Case 1d

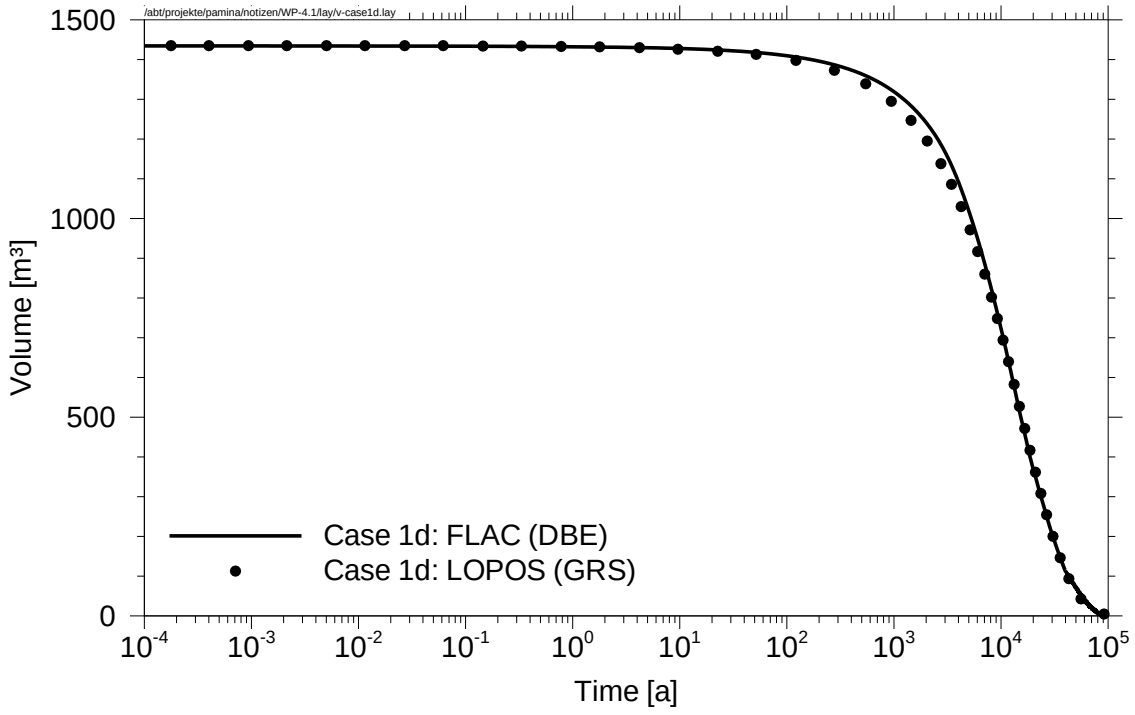

Fig. 2.4.6: Comparison of time evolution of volumes: Case 1d

2.4.2.3 *Results of test cases 2a and 2b*

Figure 2.4.7 shows the results of the convergence rate calculations of cases 2a and 2b. The LOPOS results are obtained by fitting only the parameter g_2, which is assumed to be responsible for the difference in the convergence rate results for dry and wet backfill. A parameter value of $g_2 = 10^2$ gives a good match with results from the rock mechanics calculations for dry backfill. For wet backfill g_2 is increased to $g_2 = 10^4$, giving also a good match.

Fig 2.4.8 shows the time evolution of the cavity's volume. The coincidence with results from the rock mechanics calculation is really well.

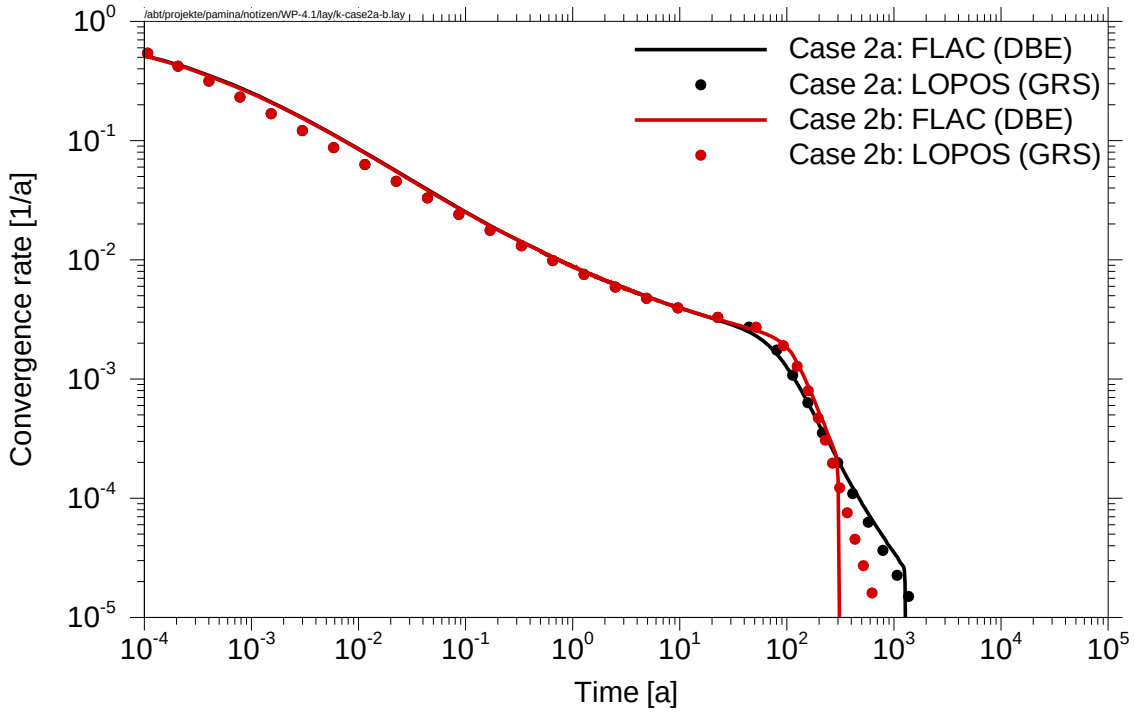

Fig. 2.4.7: Comparison of convergence rates: Cases 2a and 2b

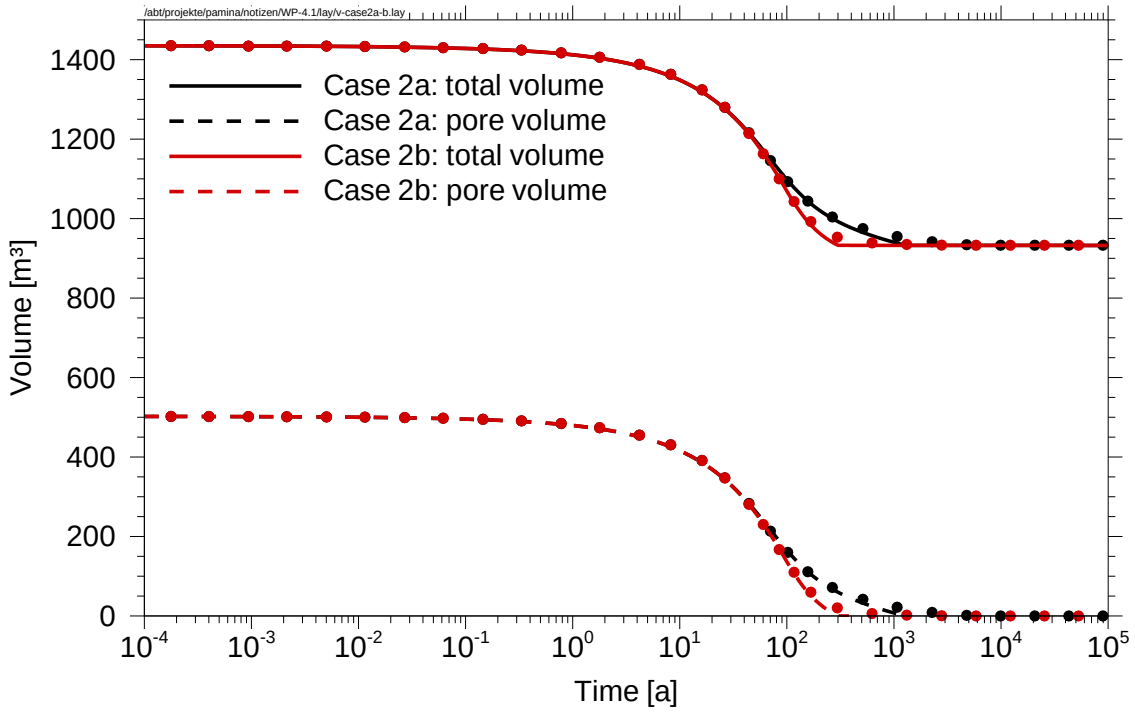

Fig. 2.4.8: Comparison of time evolution of volumes: Cases 2a and 2b

2.4.2.4 Results of test cases 3a to 3c

Figure 2.4.9 shows the results of the convergence rate calculations of cases 3a and 3b. Here, the same constant fluid pressures as in cases 1b and 1c are taken as boundary conditions. The parameter value g_2 for wet backfill is used. No additional parameter fits are necessary to get the results given in the curves. Fig. 2.4.10 shows the time evolution of the cavity's volume. The coincidence with results obtained from the corresponding rock mechanics calculations is really well.

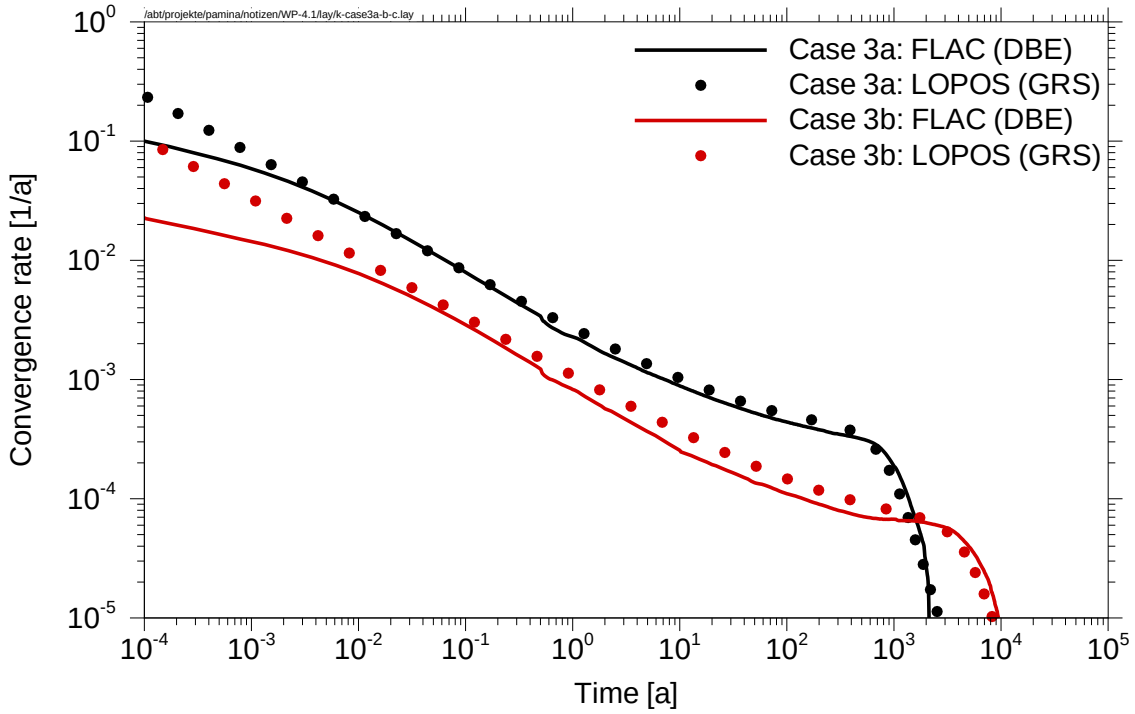

Fig. 2.4.9: Comparison of convergence rates: Cases 3a and 3b

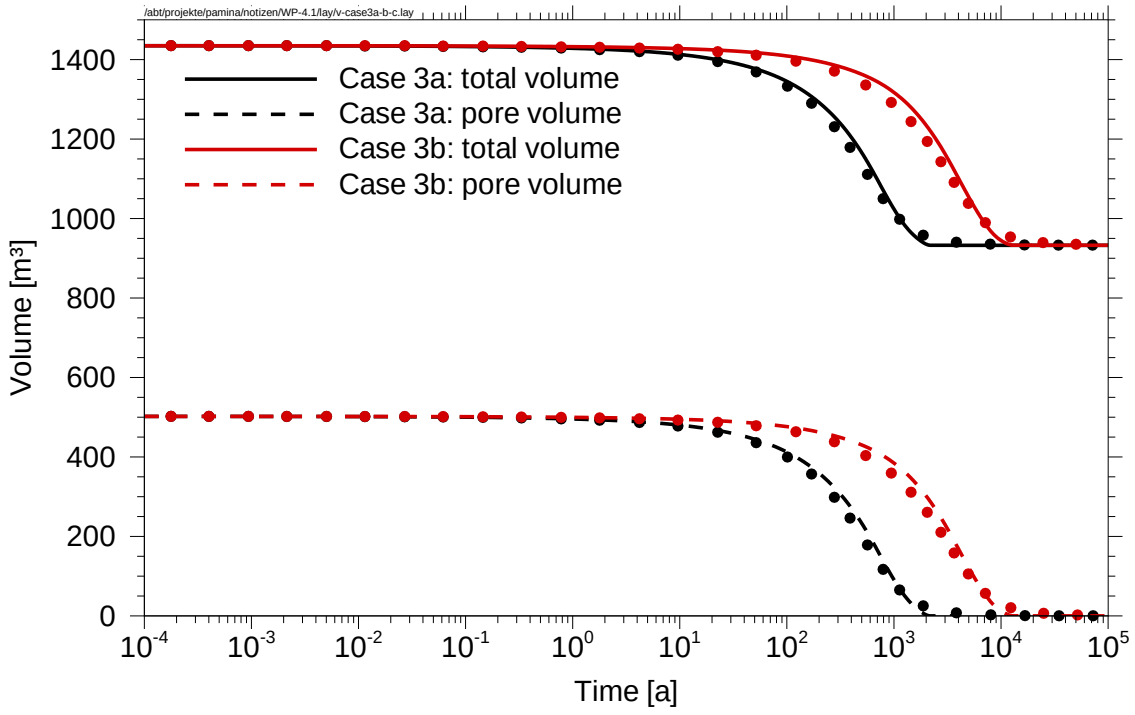

Fig. 2.4.10: Comparison of time evolution of volumes: Cases 3a and 3b

2.4.2.5 *Results of test case 3c*

In case 3c the fluid pressure is raised as in case 1d. Here, the LOPOS model yields the same hydraulic pressure in the cavity, since the backfill of that cavity has almost no influence on the flow resistance of the repository as a whole. This effect can be explained by the segment structure, where the rather flat cavity is located perpendicular to the shaft segment. The results given in the following figures are obtained with no additional parameter fitting.

Figures 2.4.11 and 2.4.12 show the results of the LOPOS calculations. Convergence rates and volumes resulting for case 2b (air filled cavity and wet backfill), case 3b (completely filled repository) and case 3c (progressive fill-up of the repository) are compared. The convergence rate of case 3c shows the influence of the increased pressure. At the beginning it follows that curve of 2b, after 50 a the over pressure in the repository reduces the convergence rate below that of case 3b, but at late times it approaches that of case 3b. Figure 2.4.12 shows the corresponding time evolution of the cavity's volumes.

Figures 2.4.13 and 2.4.14 show the results of the rock mechanics calculation compared with those of the LOPOS calculation. Again, there are some differences between the results for the convergence rates. The same explanation as for case 1d holds. Figure 2.4.14 shows the time evolution of the total and the pore volume of the cavity. Although the convergence rates differ, the volumes match rather well.

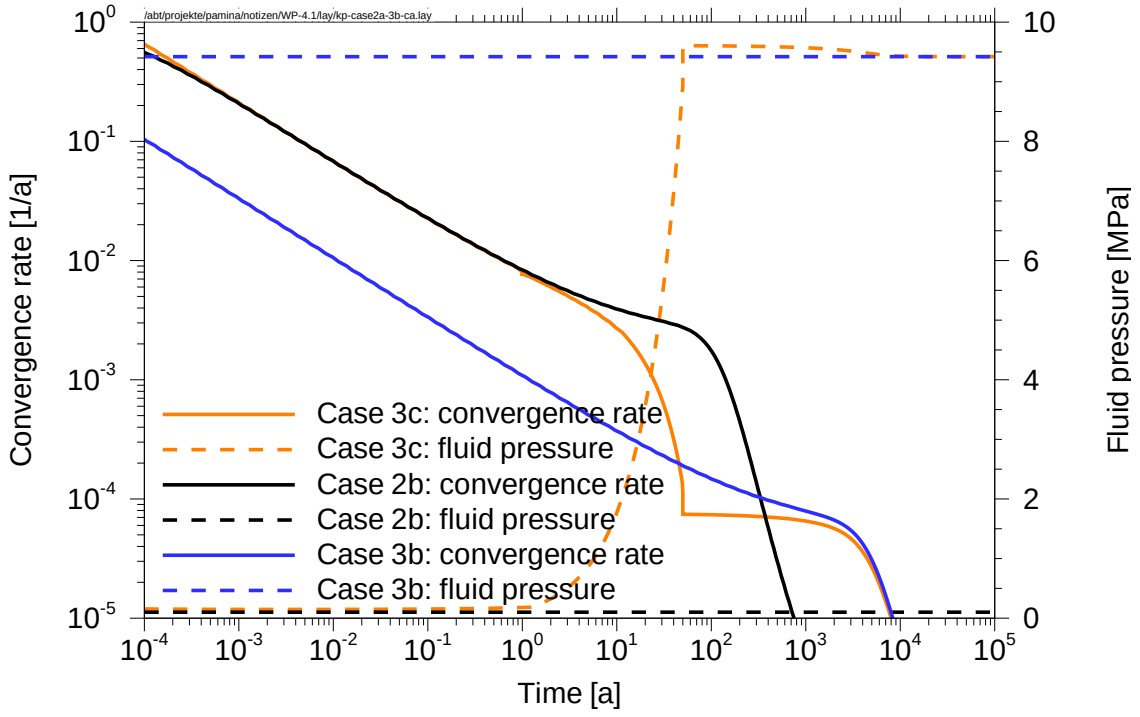

Fig. 2.4.11: Convergence rate and fluid pressure of cavity in test cases 2a, 3b and 3c

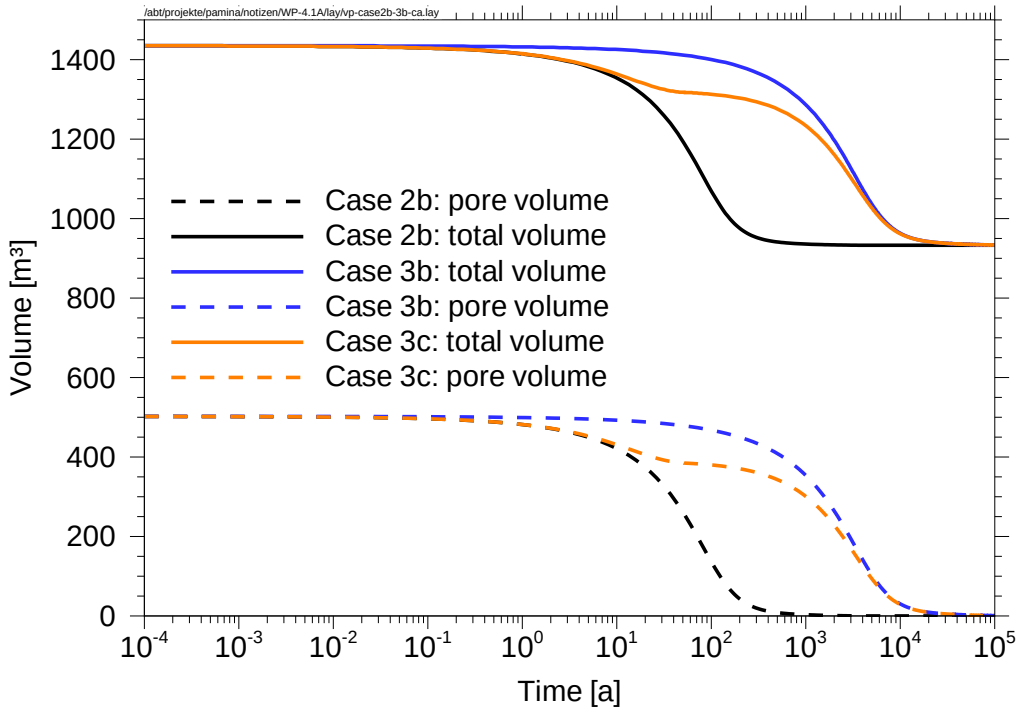

Fig. 2.4.12: Volumes of cavity in test cases 2b, 3b and 3c

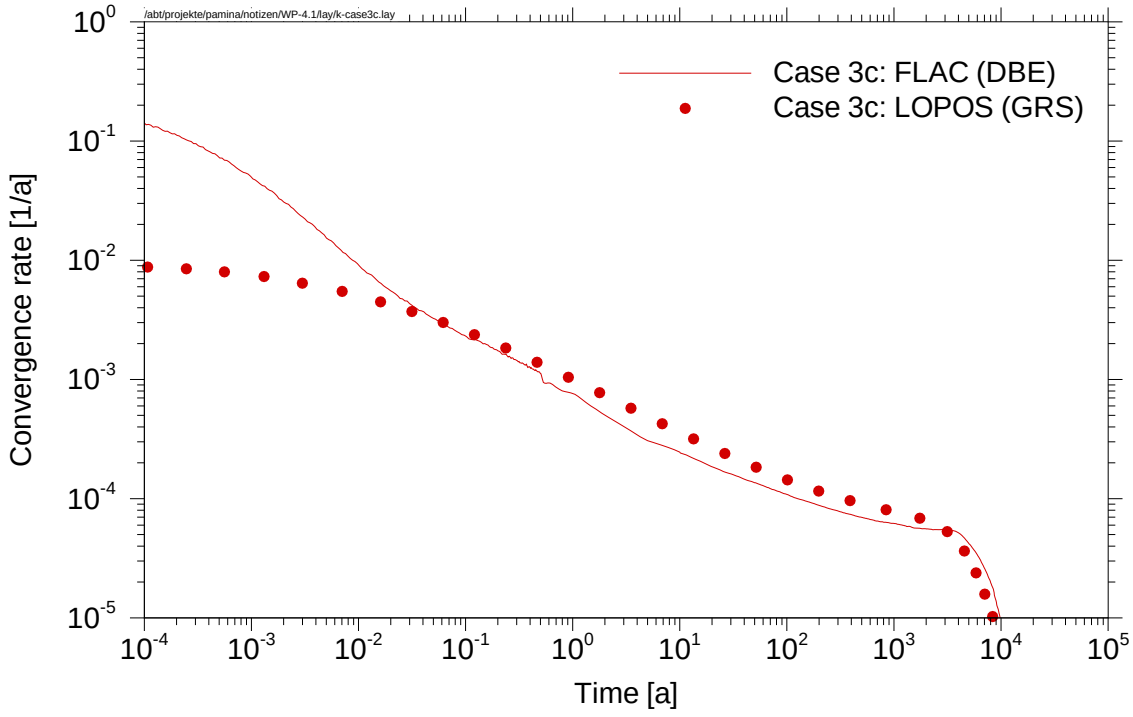

Fig. 2.4.13: Comparison of convergence rates: Case 3c

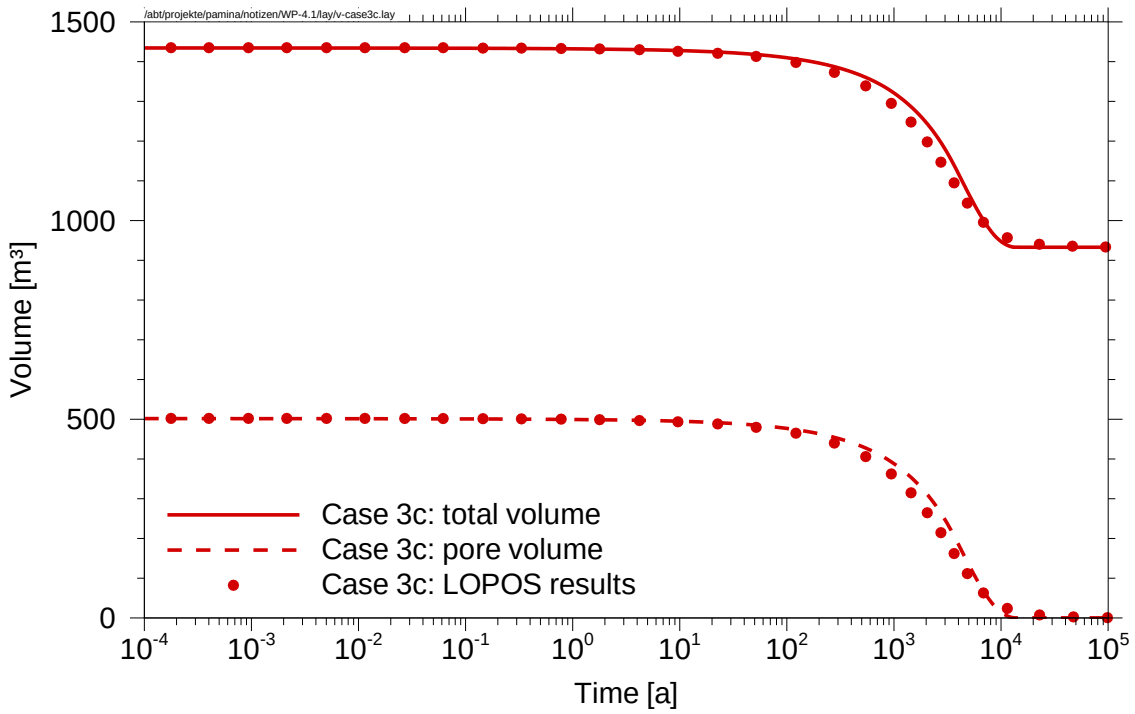

Fig. 2.4.14: Comparison of time evolution of volumes: Case 3c

2.4.2.6 Results of test cases 4a and 4b

In cases 4a and 4b a layer of incompactable material is assumed to be placed at the bottom of the cavity. In case 4a the remaining volume is not backfilled, in case 4b the remaining volume is filled with dry backfill. In these cases the volume which is influenced by convergence is reduced to that of the empty or the backfilled part of the cavity, respectively. The volume filled with incompactable material does not change during convergence of the cavity.

Figure 2.4.15 shows the results for the convergence rate, which is the same as in the corresponding case 1a (cavity without backfill) and almost the same as in case 2a (cavity with dry backfill), respectively. Only for late times the smaller volume of compactable backfill reduces the convergence rate. Figure 2.4.16 shows the results for the time evolution of the cavity's volume. The results are obtained with no additional parameter fits. The coincidence with results from the rock mechanics calculations is really well.

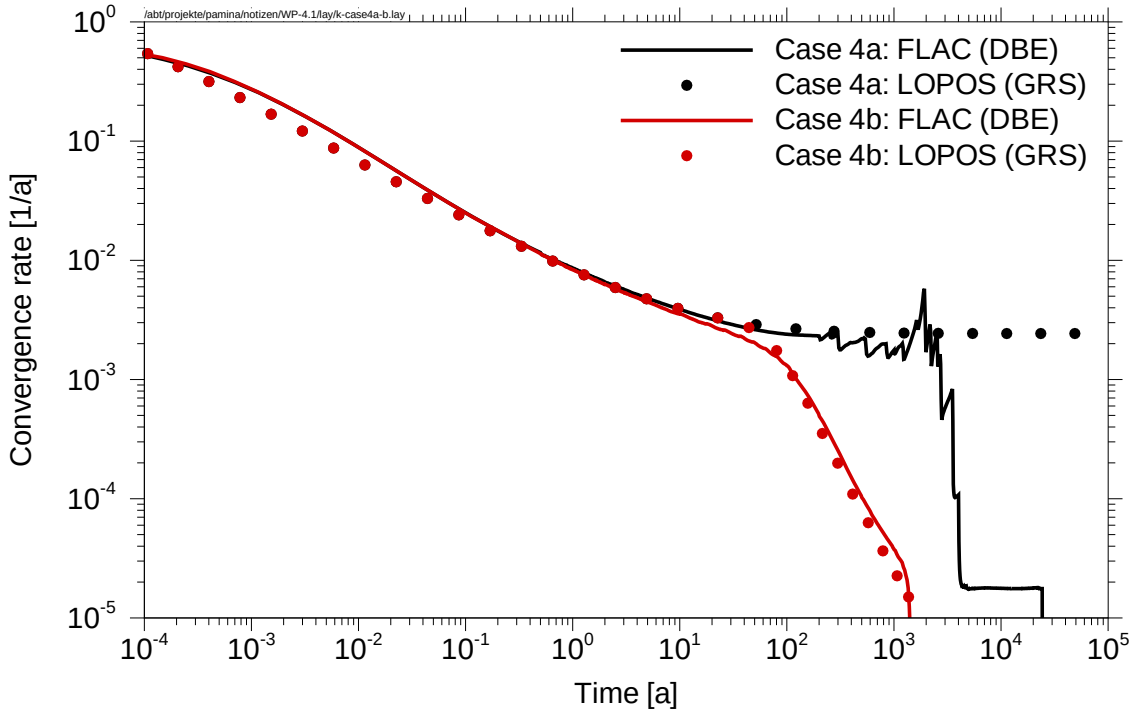

Fig. 2.4.15: Comparison of convergence rates: Cases 4a and 4b

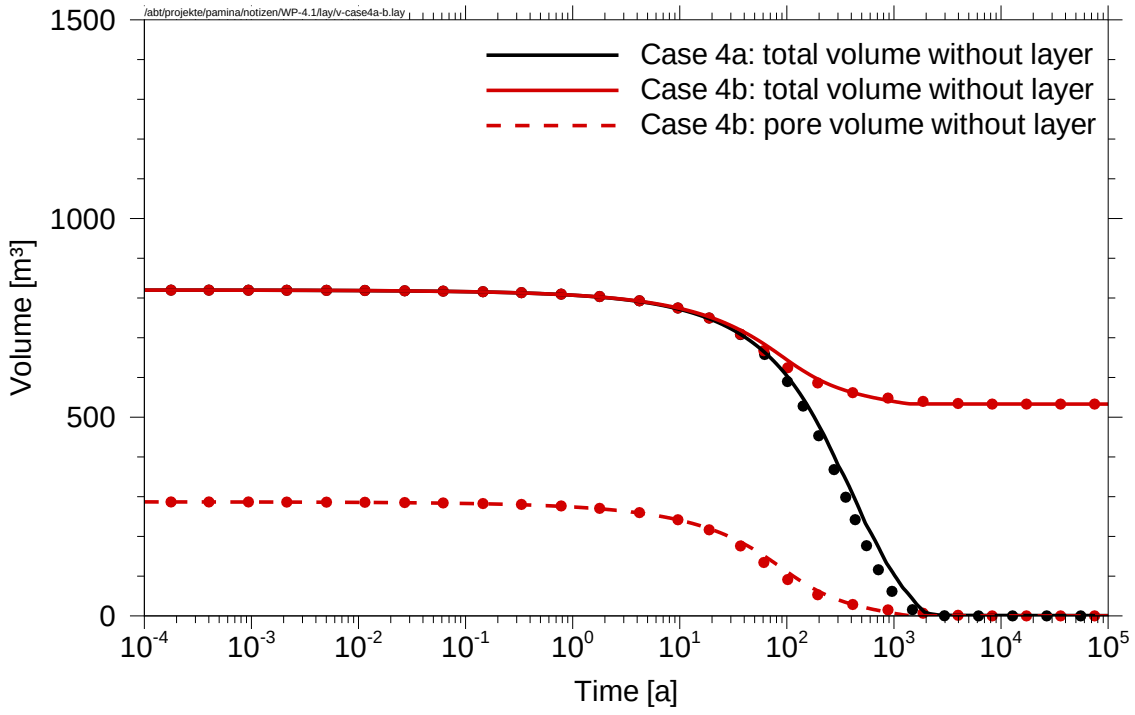

Fig. 2.4.16: Comparison of time evolution of volumes: Cases 4a and 4b

2.4.2.7 *Results of test cases 5a to 5c*

In cases 5a, 5b, and 5c it is assumed that a steel container is place on the floor of the cavity. Different hydrostatic fluid pressures are present in the cavity as given in cases 1a, 1b, and 1c. Figure 2.4.17 shows the convergence rates. The results are almost the same as obtained for cases 2a, 3a and 3b, respectively, except for late times where the smaller volume of compactable backfill reduces the convergence rate. Figure 2.4.18 shows results for the time evolution of the cavity's volume. Comparison with the corresponding results from rock mechanics calculation shows a really good match.

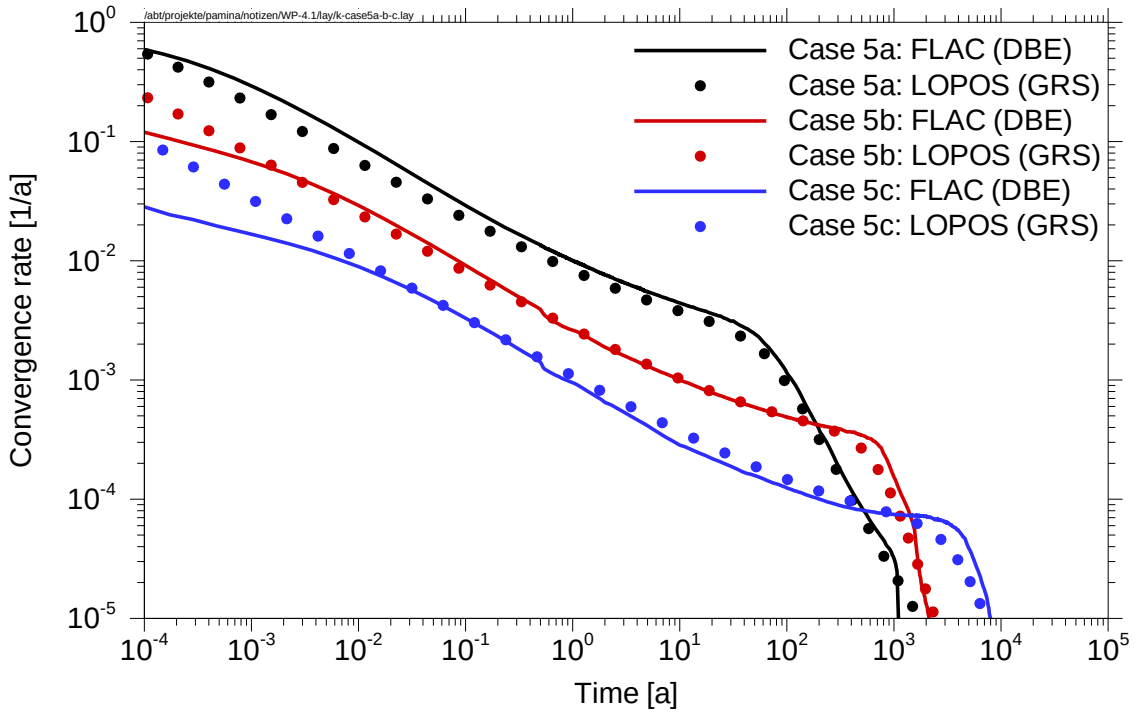

Fig. 2.4.17: Comparison of convergence rates: Cases 5a, 5b, 5c

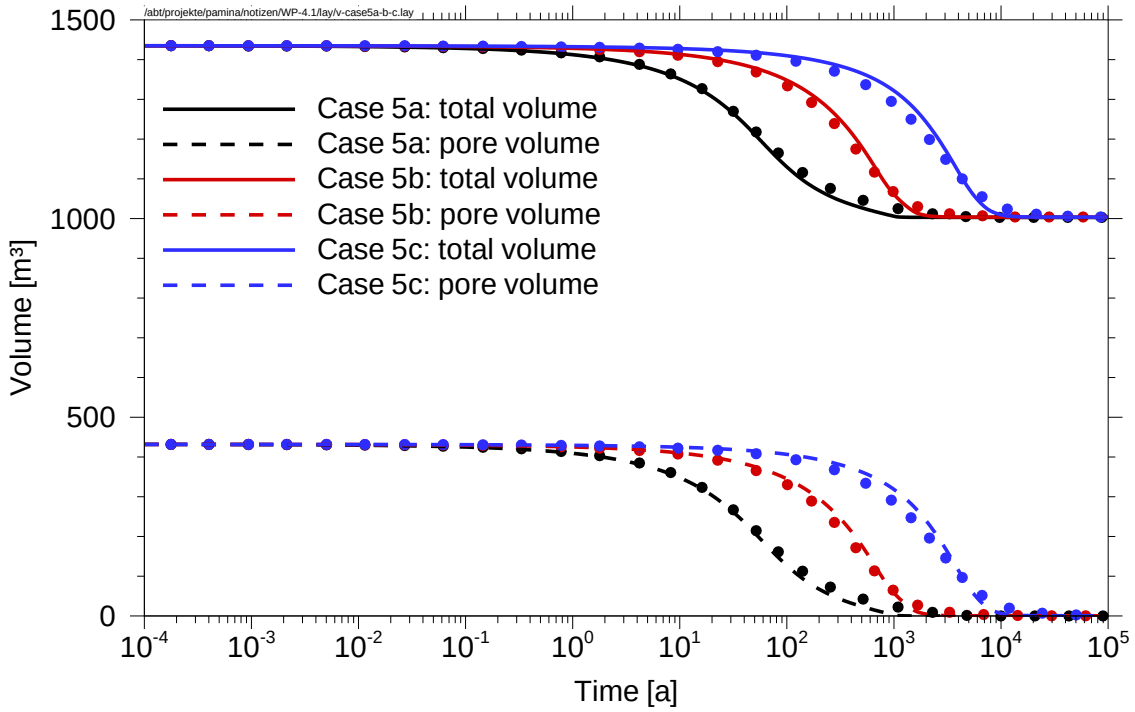

Fig. 2.4.18: Comparison of time evolution of volumes: Cases 5a, 5b, 5c

2.4.2.8 Result of test case 5d

In case 5d the fluid pressure is raised as in case 1d. Additionally, compared to case 3c, the steel container is place at the bottom of the cavity, reducing the backfill volume which can be compacted. Again the LOPOS model yields the same hydraulic pressure in the cavity, since the backfill of that cavity has almost no influence on the flow resistance of the repository as a whole. The results given in the figures are obtained with no additional parameter fitting.

In Figures 2.4.19 and 2.4.20 the results of the LOPOS calculations for cases 5a, 5c and 5d are compared. The convergence rate of case 5d shows the influence of the increased pressure. At the beginning it follows that of case 5a. Again, after 50 a, the convergence rate decreases below that of case 5c, due to the hydraulic over pressure. At late times it approaches the case-5c curve. Figure 2.4.20 shows the corresponding results for the time evolution of the cavity's volumes.

Figures 2.4.21 and 2.4.22 show the results of the rock mechanics calculation compared with those of the LOPOS calculation. Again, there are some differences between the results for the convergence rate. The same explanation as for case 1d holds. Figure 2.4.22 shows the time evolution of the total and the pore volume of the cavity. Although the convergence rates differ, the volumes match really well.

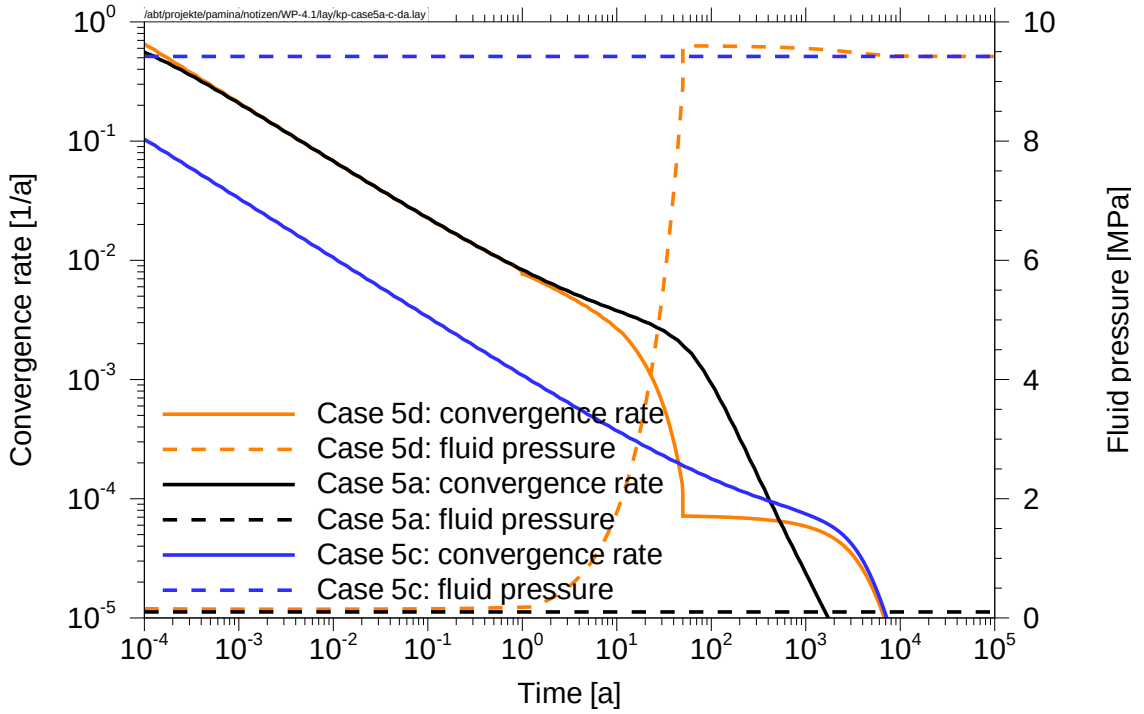

Fig. 2.4.19: Convergence rate and fluid pressure of cavity in cases 5a, 5c and 5d

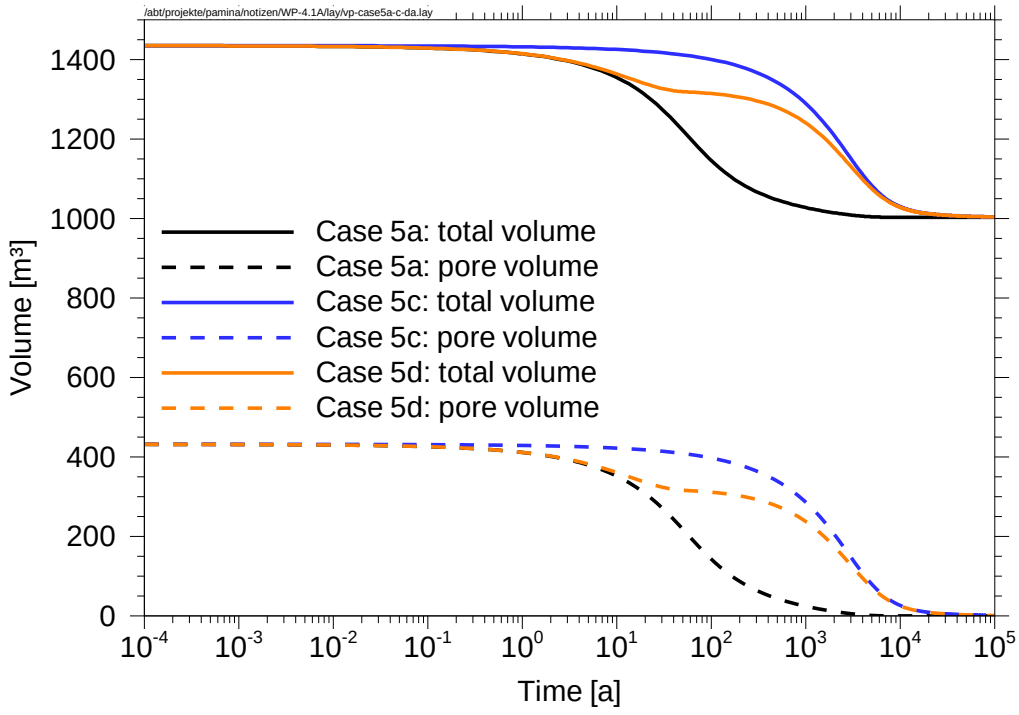

Fig. 2.4.20: Volumes of cavity in test cases 5a, 5c and 5d

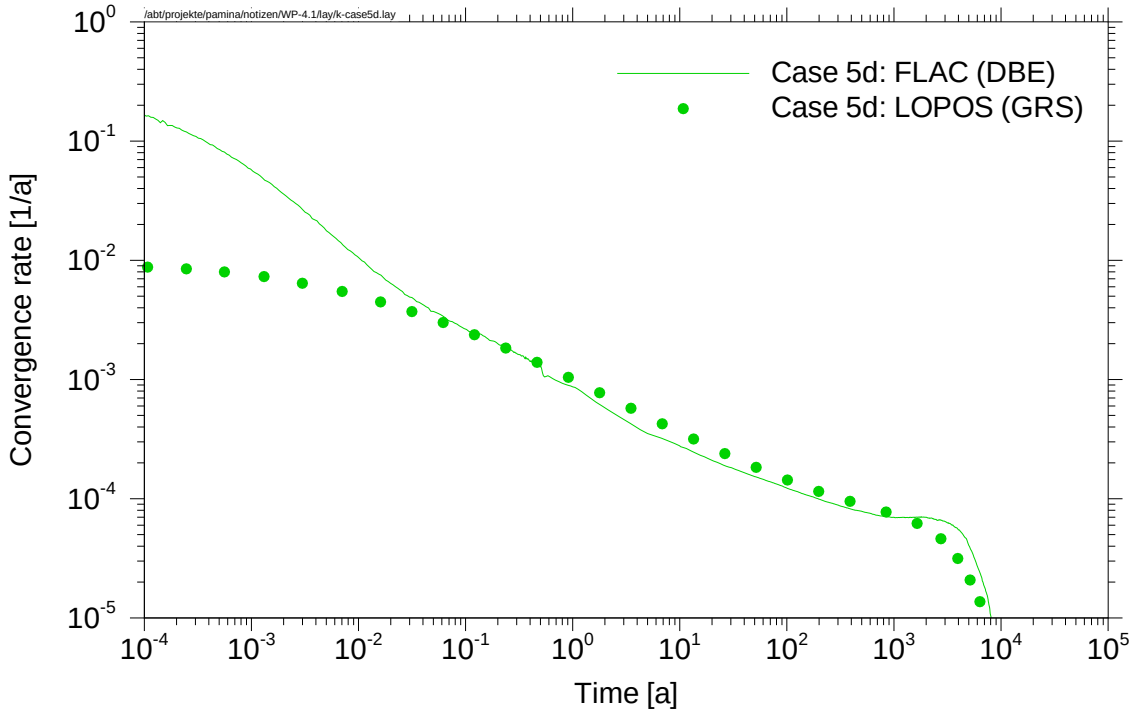

Fig. 2.4.21: Comparison of convergence rates: Case 5d

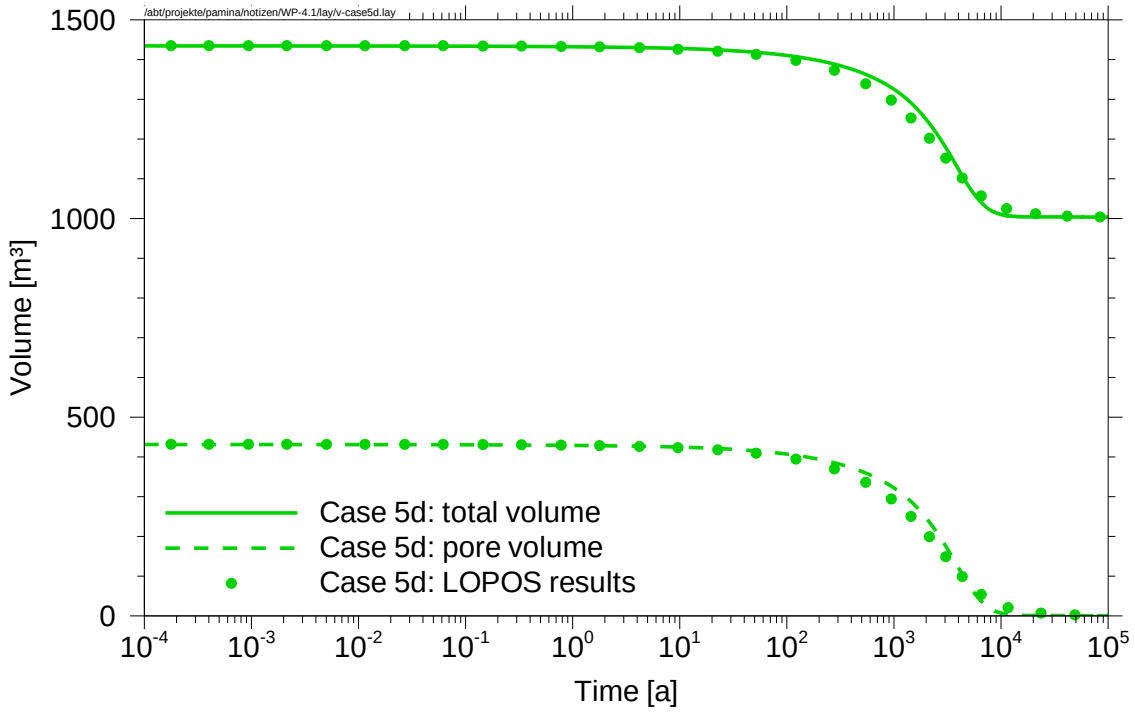

Fig. 2.4.22: Comparison of time evolution of volumes: Case 5d

2.4.3 Application of the NRG model (REPOS) to the test cases

2.4.3.1 Case 1 – Open cavity with no backfill

The brine intrusion is modelled to occur at 10^{-2} years; consequently cases 1b, 1c and 1d show a significant drop at about 10^{-2} years. At this point in time the convergence rate decreases proportionally to the decrease of σ^5, where σ is the difference between the pressure against the wall of the excavation and the lithostatic stress at some distance from the excavation, as defined for eq. 2.3.30.

Moreover, in the calculation scheme the increment of the dimensionless time $\Delta\tau$ depends on the actual timestep $\Delta t \cdot \sigma^4$, i.e. the increment of the dimensionless time step decreases by a factor 5, resp 20 and 26 for the cases 1b, 1c and 1d. As a consequence, the decrease with time of the dimensionless convergence rate κ is much smaller for the cases 1b, 1c and 1d compared to 1a. In Figure 2.4.24 this results in the almost horizontal 'platforms' directly after the brine intrusion. An alternative calculation scheme to deal with the sudden change in σ is discussed in [5].

Figure 2.4.23 shows that the effects that occur in the first year do not have significant effects on the volumes and porosities in the system, and do not have a significant impact on the long term convergence rates.

Tab. 2.4.1: Description and data for Case 1

	Description	Key data
Case 1a	no brine, atmospheric pressure	p_{air} = 0.1 MPa
Case 1b	with constant fluid pressure, brine up to the top of the salt formation	p_{brine} = 5.89 MPa
Case 1c	with constant fluid pressure, brine up to the surface	p_{brine} = 9.42 MPa
Case 1d	with time dependent fluid pressure, brine up to the surface	p_{brine} = 9.42 + p_{dyn} MPa

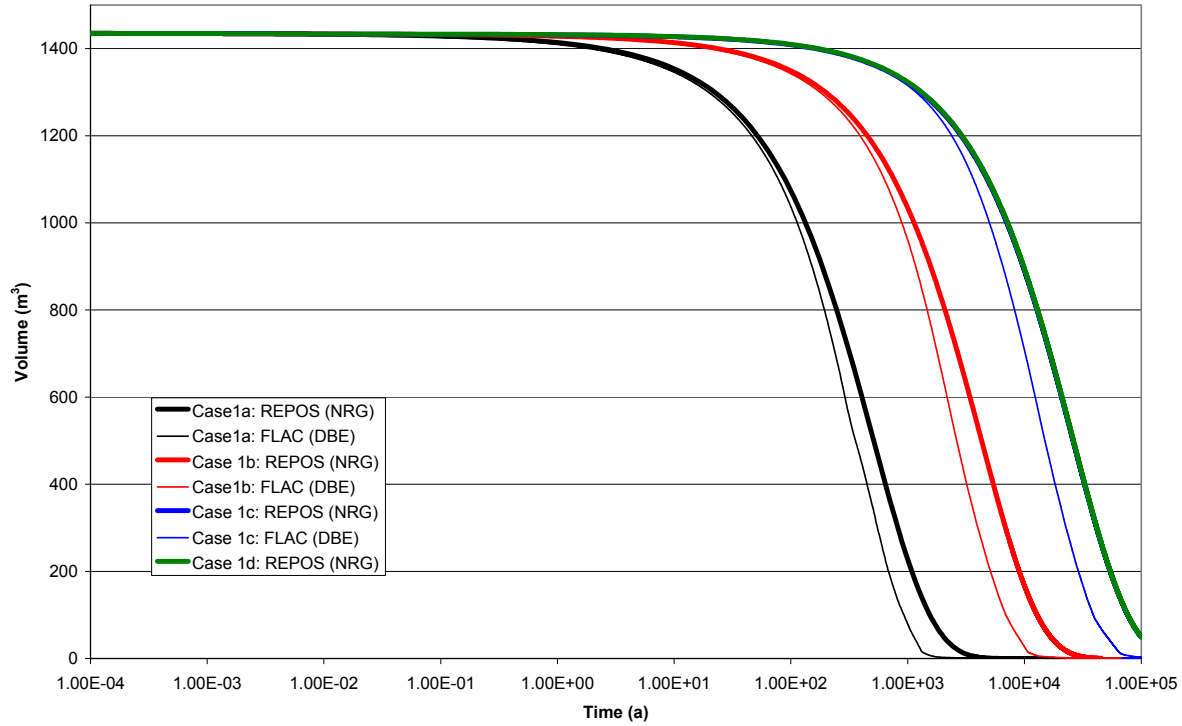

Fig. 2.4.23: Comparison of time evolution of volumes: Cases 1a, 1b, 1c and 1d (REPOS result 1c is not visible, because the line is concealed by REPOS result 1d)

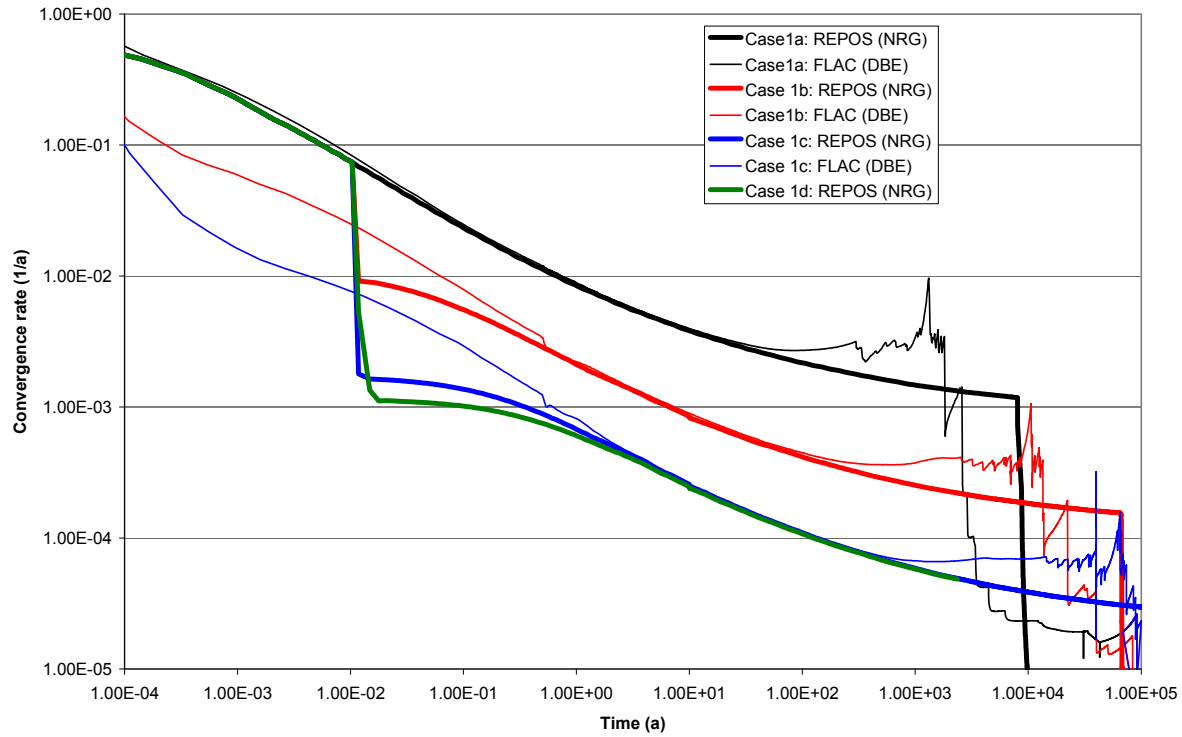

Fig. 2.4.24: Comparison of convergence rates: Cases 1a, 1b, 1c and 1d

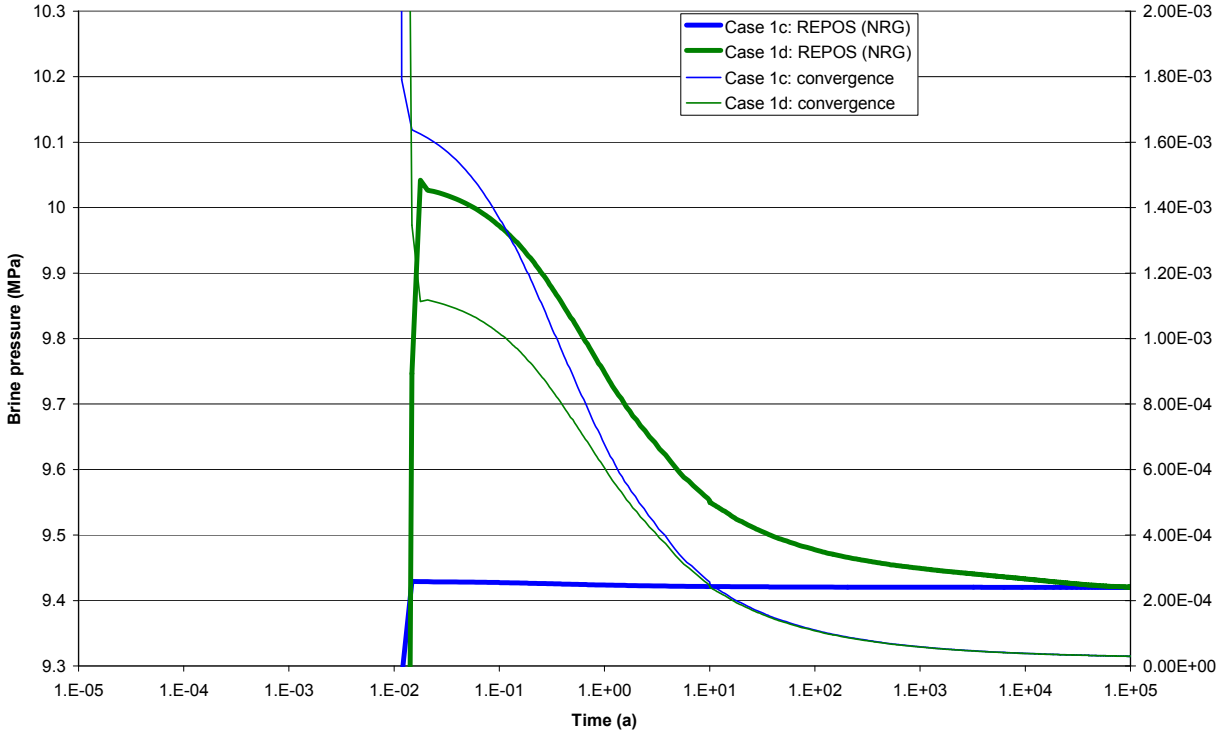

Fig. 2.4.25: Convergence rate and fluid pressure of test cases 1c and 1d

2.4.3.2 *Case 2 – Cavity backfilled with Crushed Salt*

Figure 2.4.26 shows the evolution of the volume of the cavity (starting at 1435 m^3 and decreasing to 932 m^3), and the evolution of the pore volume (starting at 502.25 m^3, since the initial porosity of the backfill is 35%, and decreasing to zero).

The following observations are made:

- After 63 years the porosity has reached 20%. In the REPOS calculation it has been assumed that backfill with a porosity larger than 20% the backfill does not resist compaction.
- After 320 years, in case 2b (brine saturated backfill), the porosity found in the FLAC calculation has become almost zero. The porosity found with REPOS is larger, about 1.5% at 320 years. This explains the larger convergence rate found with REPOS for times larger than 320 years when the backfill is lower than 1%. At this porosity, the permeability of the compacted backfill is so small, that even at the very small convergence rate of $< 10^{-5}$ per year the brine gets more or less trapped in the pores and a brine pressure build-up occurs.

Tab. 2.4.2: Description and data for Case 2

	Description	Key data
Case 2a	cavity backfilled, no brine, atmospheric pressure	p_{air} = 0.1 MPa
Case 2b	cavity backfilled, saturated, atmospheric pressure	p_{brine} = 0.1 MPa

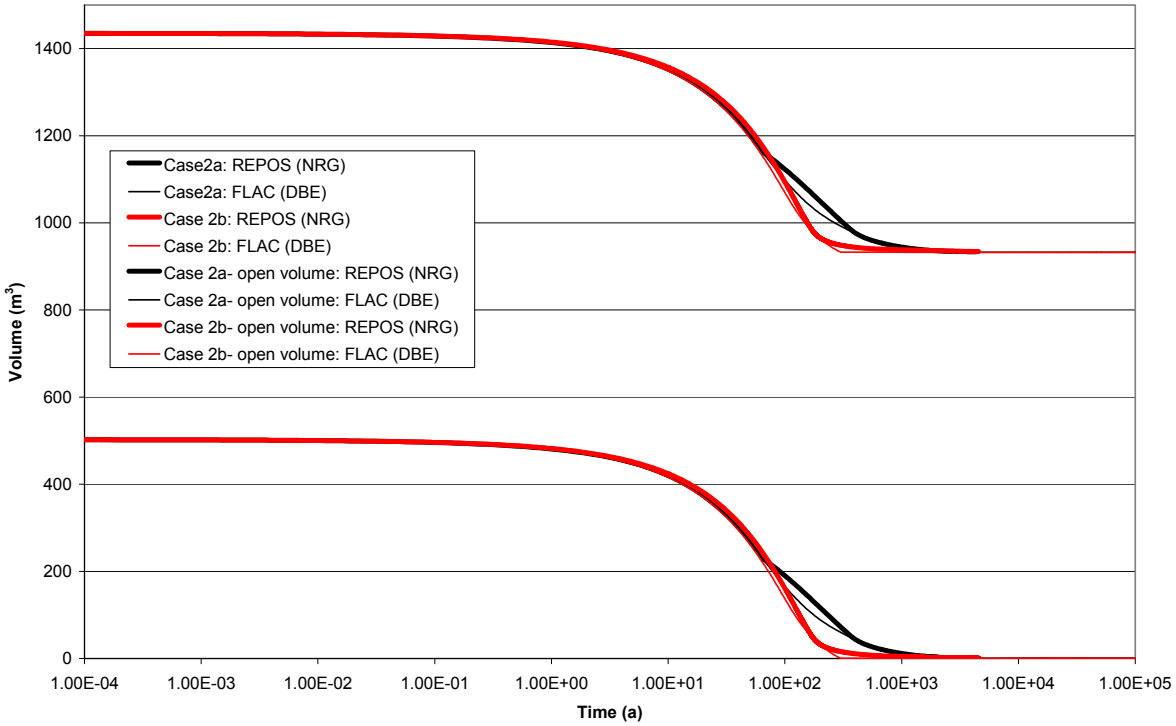

Fig. 2.4.26: Comparison of time evolution of volumes: Cases 2a and 2b. The volume of the cavity and the pore volume are shown (starting at about 500 m^3).

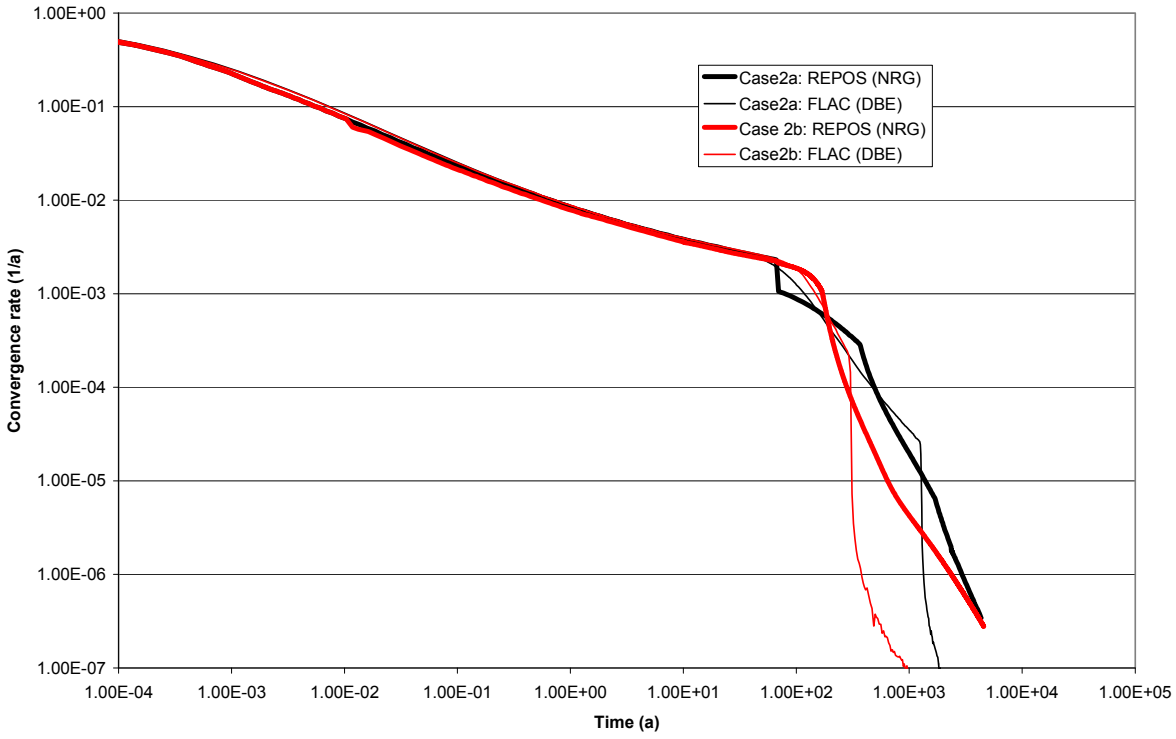

Fig. 2.4.27: Comparison of convergence rates: Cases 2a and 2b

2.4.3.3 *Case 3 – Cavity backfilled with crushed salt, saturated and hydrostatic pressure*

Figure 2.4.28 shows the evolution of the volume of the cavity (starting at 1435 m^3 and decreasing to 932 m^3), and the evolution of the pore volume (starting at 502.25 m^3, since the initial porosity of the backfill is 35%, and decreasing to zero).

The brine intrusion is modelled to occur at 1E-2 years; consequently cases 3a, 3b and 3c show a significant drop at about 1E-2 years. At this point in time, the convergence rate decreases. This sequence of events is already discussed in Section 2.4.3.1.

Tab. 2.4.3: Description and data for Case 3

	Description	Key data
Case 3a	with constant fluid pressure, brine up to the top of the salt formation	p_{brine} = 5.89 MPa
Case 3b	with constant fluid pressure, brine up to the surface	p_{brine} = 9.42 MPa
Case 3c	with time dependent fluid pressure, brine up to the surface	p_{brine} = 9.42 + p_{dyn} MPa

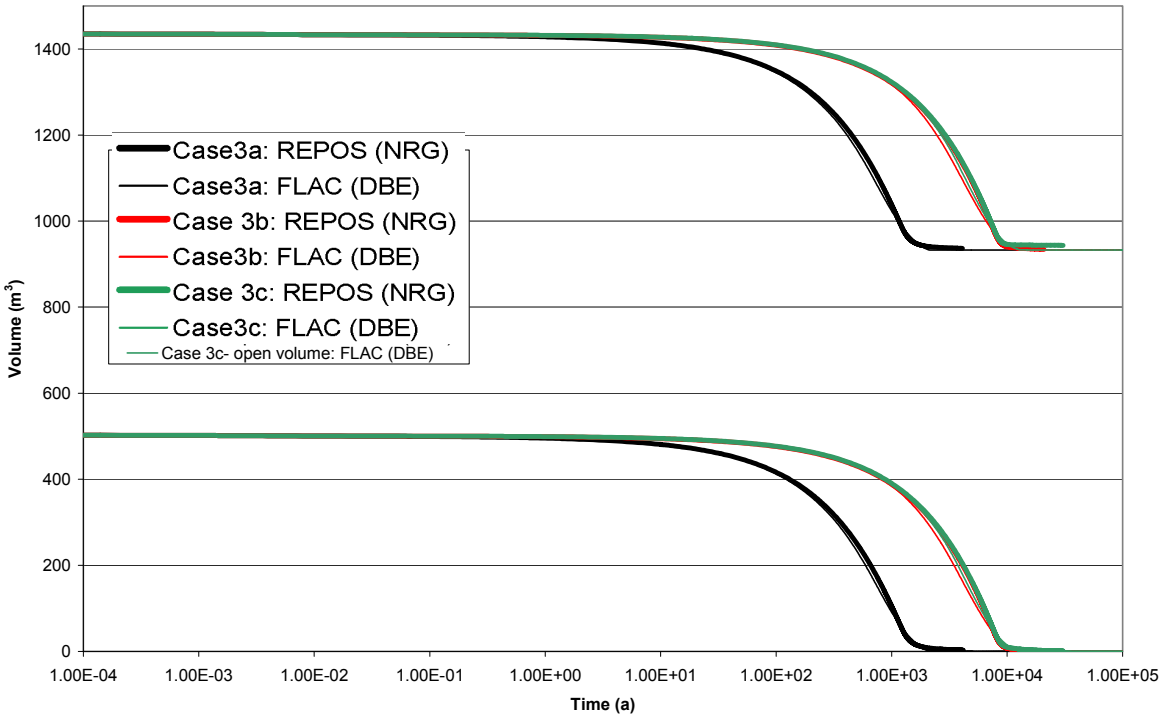

Fig. 2.4.28: Comparison of time evolution of volumes: Cases 3a, 3b, and 3c. The volume of the cavity and the pore volume are shown

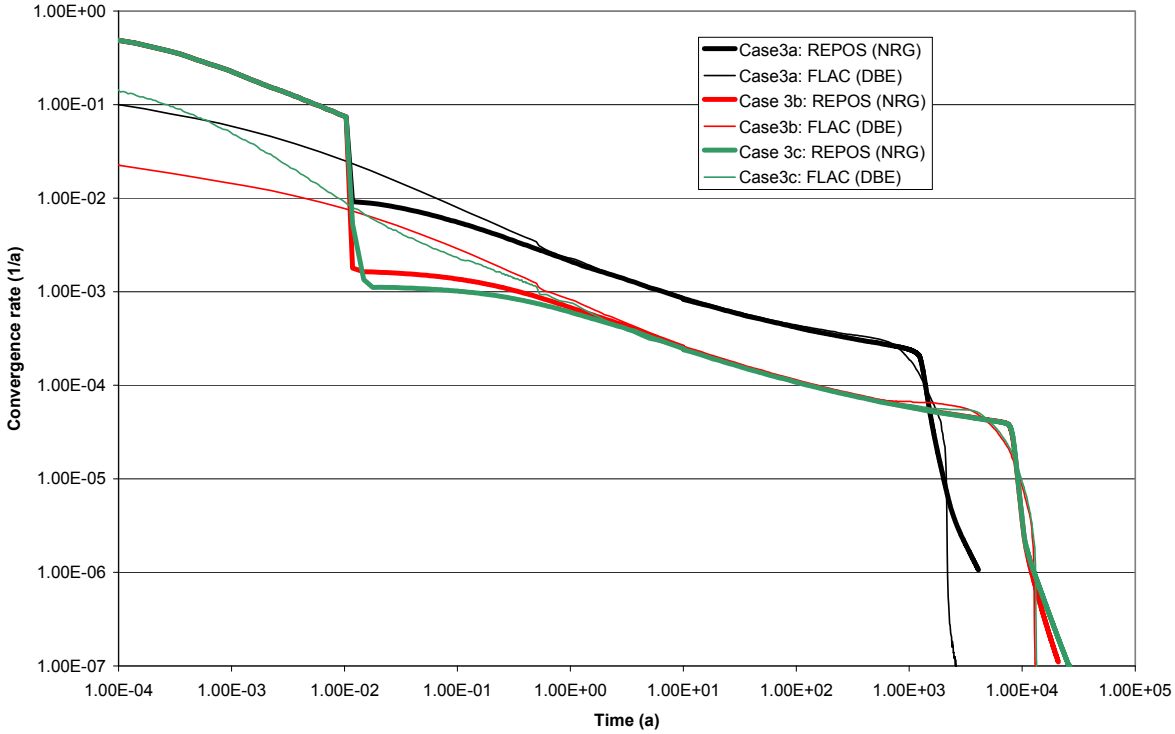

Fig. 2.4.29: Comparison of convergence rates: Cases 3a, 3b and 3c

2.4.3.4 Case 4 – Cavity with a layer of incompactable material at the bottom

The geometric configuration for this benchmark case is shown in section 2.2.2.

Tab. 2.4.4: Description and data for Case 4

	Description	Key data
	Cavity floor covered with a Concrete Layer (615 m^3)	
Case 4a	no backfill in the residual volume, no brine, atmospheric pressure	p_{air} = 0.1 MPa
Case 4b	residual volume backfilled with crushed salt, no brine, atmospheric pressure	p_{air} = 0.1 MPa

The impact of incompactable objects in the excavation on the convergence is not automatically set in REPOS, i.e. it has to be adjusted by user input. Two extreme options to model the effect of the layer of incompactable material on the floor of the cavity have been applied:

1. Modified backfill properties
2. Modified rock salt geometry

For option 1 it is assumed that the impact of the incompactable material can be fully accommodated by modifying the backfill properties, i.e. a representative backfill is assumed which properties are chosen in such a way that it behaves similar to the actual system. The underlying assumption is that the potential rock salt convergence is not affected by the incompactable material (i.e. the mechanical behaviour is like a incompactable fluid - or the incompactable object is fully encapsulated in the backfill). In option 2 it is assumed that the layer of incompactable backfill only affects the rock salt convergence, and has no effect on the compaction properties of the residual volume (i.e. the open volume in case 4a, or the volume backfilled with crushed salt in case 4b).

Option 1: Modified backfill properties

For the REPOS calculations it can been assumed that the (non-compacting) concrete layer on the floor of the cavity does not influence the potential convergence rate of the rock salt as long as there is an open volume in the cavity. For case 4a this means that the calculated convergence rate of the rock salt is identical to case 1a (Open cavity with no backfill, atmospheric pressure) as long as the volume of the cavity (initially 1435 m^3) is larger than the volume of the concrete floor (615 m^3). For case 1a, at 405 years the volume of the cavity has decreased to 615 m^3 and the convergence will immediately stop, since the remaining volume of the cavity is filled with incompactable concrete. (Note: the very small but non-zero compaction rate calculated with REPOS for case 4a after 405 years is an artefact of the approximation REPOS uses to model a non-backfilled open volume.)

For case 4b it is important to recognise that modifying the backfill properties will imply that the compaction rate of the crushed salt is larger than the convergence rate of the rock salt.

Figure 2.4.30 shows the evolution of the volume of the cavity (starting at 1435 m^3 and decreasing to 615 m^3 for Case 4a, and to 1178 for Case 4b), and the evolution of the pore volume (starting at 820 m^3 for case 4a, and for Case 4b at 278 m^3, since the initial porosity of the backfill is 35%, and decreasing to zero).

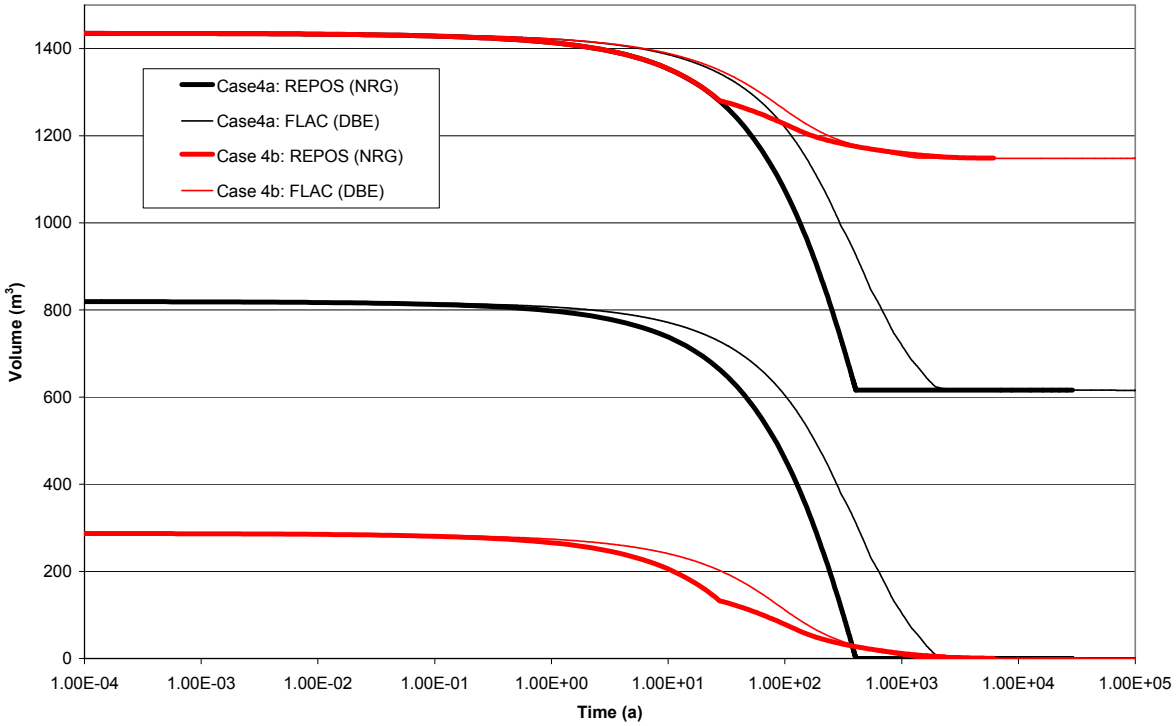

Fig. 2.4.30: Comparison of time evolution of volumes: Cases 4a and 4b using the modified backfill properties option in REPOS. The volume of the cavity and the pore volume are shown

Figure 2.4.31 shows the convergence rate of the residual volume (i.e. the open volume for case 4a, and the backfill volume for case 4b). The peak at 405 years for case 4a is explained by the fact that at that time the residual volume has become almost zero, while the volume change rate dV/dt is not zero, causing $\varepsilon = -1/V_{residual}\ dV/dt$ running up to infinity.

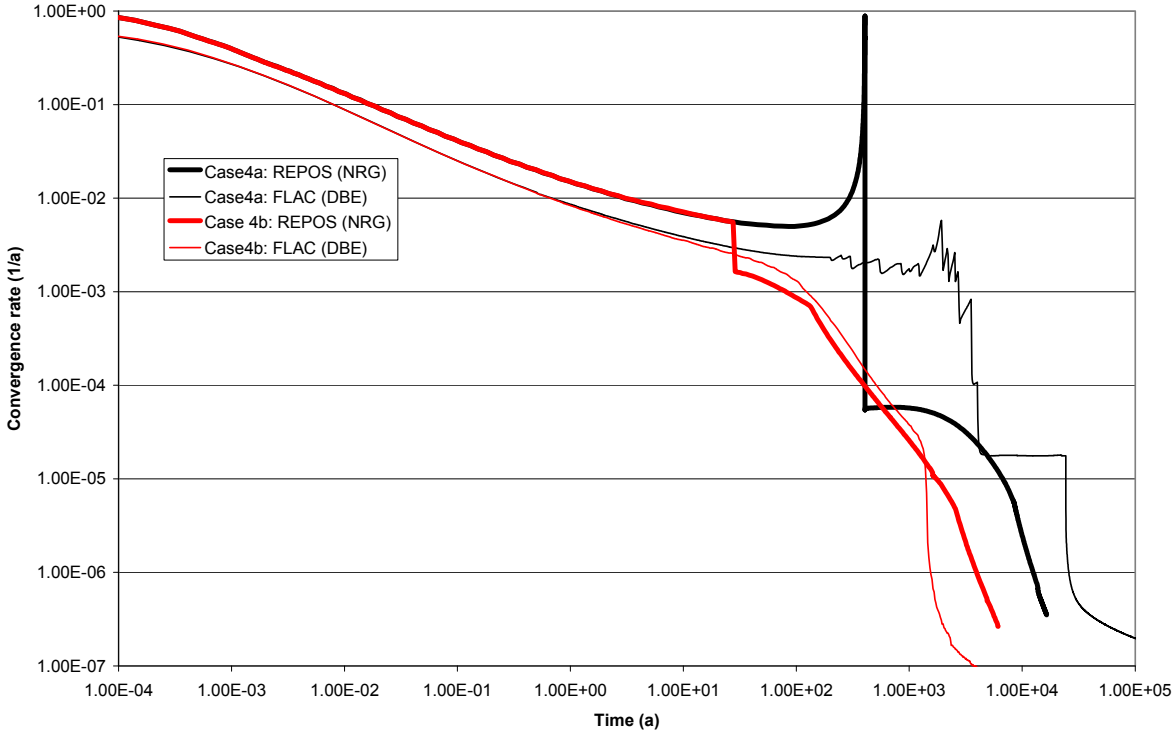

Fig. 2.4.31: Comparison of convergence rates of the residual (open or crushed salt) volume in the cavity: Cases 4a and 4b using the modified backfill properties option in REPOS

Figure 2.4.31 shows that the convergence rate of the residual volume as predicted by REPOS are larger than the convergence rate predicted by the FLAC calculation. The assumption in the REPOS calculation, that the concrete floor of the cavity does not influence the potential convergence rate of the rock salt (as long as there is an open volume in the cavity) will actually lead to an overestimation of the convergence rate, since the rock salt has to flow around the incompactable but also not deformable concrete. This takes extra energy and leads to a smaller convergence rate. In FLAC this flow process is modelled, so this could explain the smaller convergence rate found with FLAC.

Option 2: Modified rock salt geometry

Here it is assumed that the incompactable material at the bottom of the cavity is a part of the rock salt surrounding the residual volume in the cavity. Moreover, it is assumed that the incompactable material does not affect the overall rock salt convergence behaviour. This means that only the rock salt geometry has changed. A change in the geometry of the rock salt surrounding the cavity implies that the geometry of the cavity is changed. For this option it means that the size of the cavity as specified in the REPOS user input is 2m x 4.1 m (see Figure in section 2.2.2), and the backfill material is air (case 4a) or crushed salt (case 4b).

Figures 2.4.32 and 2.4.33 show that the results for this option agree well with the FLAC results. This actually means that the assumption that the incompactable material is part of the rock salt, and that it does not disturb the rock salt convergence process (but only changes the geometry) is a valid assumption.

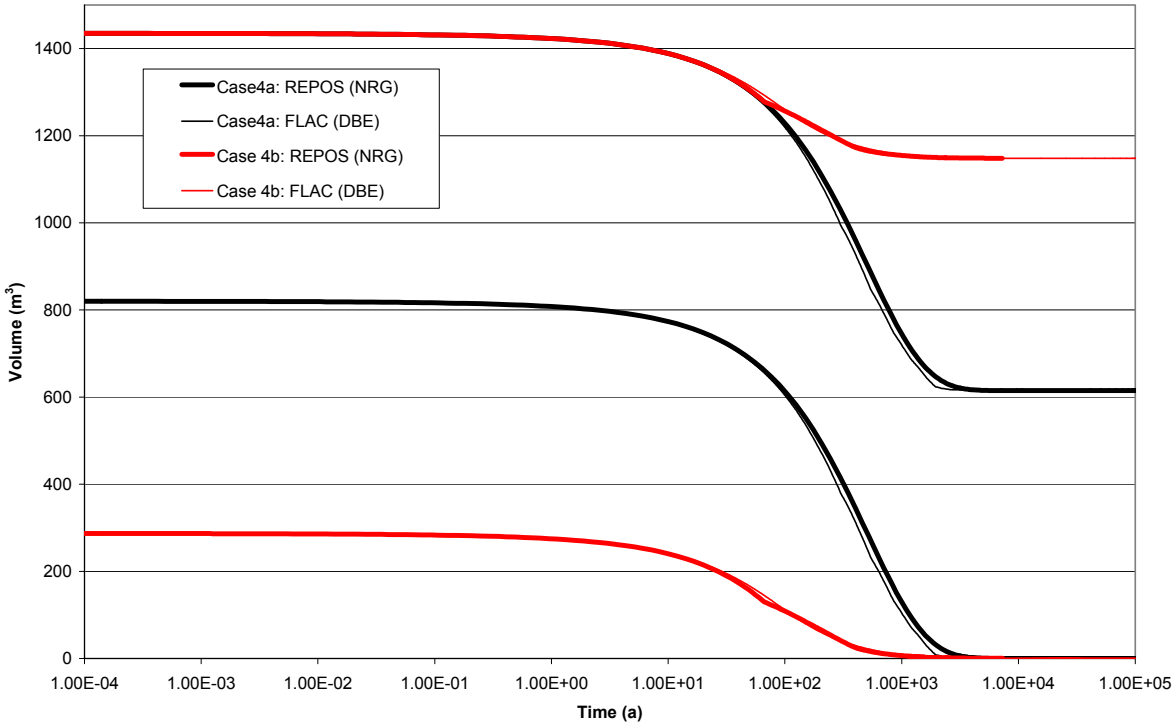

Fig. 2.4.32: Comparison of time evolution of volumes: Cases 4a and 4b using the modified rock salt geometry option in REPOS. The volume of the cavity and the pore volume are shown

The rock salt indeed needs additional energy to flow around the concrete (as concluded from Figure 2.4.31), and this slows down the convergence process. Interestingly, the impact of this effect can be approximated very well by assuming a smaller excavation, i.e. reducing the volume of the excavation by the volume of the incompactable material.

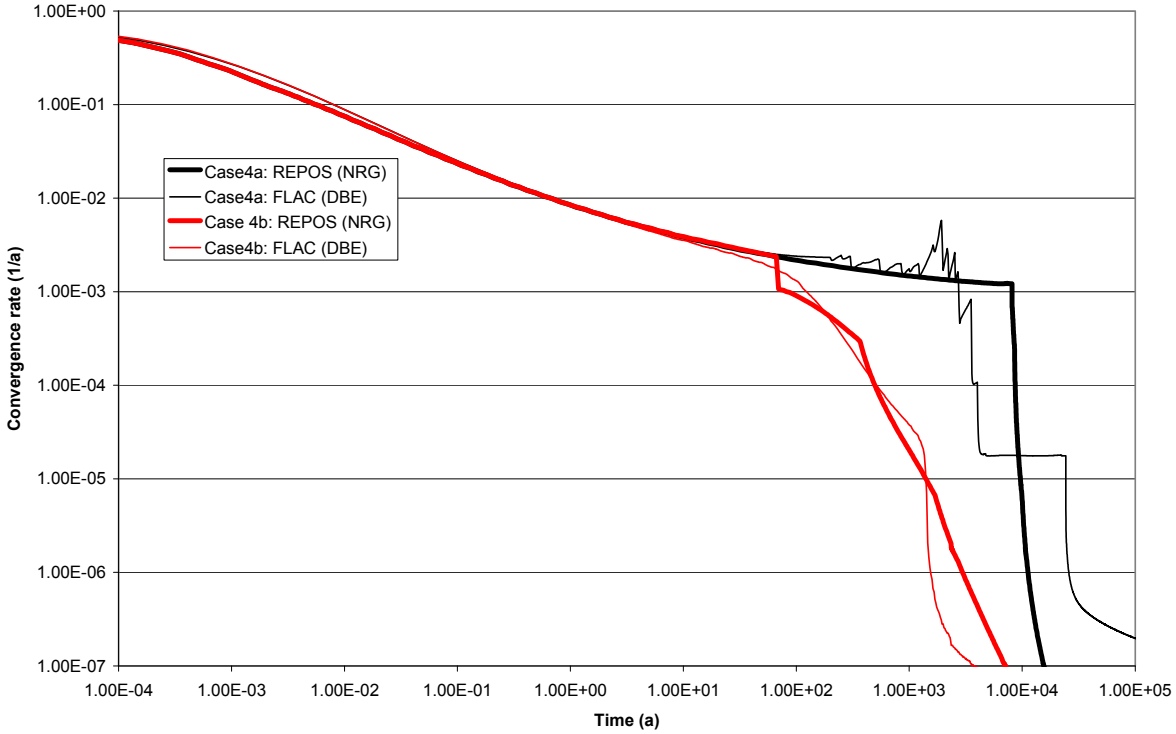

Fig. 2.4.33: Comparison of convergence rates of the residual (open or crushed salt) volume in the cavity: Cases 4a and 4b using the rock salt geometry option in REPOS

2.4.3.5 Case 5 – Cavity filled with crushed salt around a steel container lying on the floor

The Figure in section 2.2.2 shows that the steel canister is fully surrounded by crushed salt, apart from a small area where the cylinder is touching the floor of the cavity. In this geometry it is unlikely that the incompactable steel cylinder can affect the rock salt convergence geometry. It is expected that option 1 (see Section 2.4.3.3) 'modified backfill properties' will give the best result.

This means that the compaction rate of the crushed salt is larger than the convergence rate of the rock salt, initially by a factor 1.16. Taking into account that the residual volume is backfilled, the maximum value of this factor is 1.33.

Tab. 2.4.5: Description and data for Case 5

	Description	Key data
	Crushed salt around a steel container(201 m^3) lying on the floor	
Case 5a	no brine, atmospheric pressure	p_{air} = 0.1 MPa
Case 5b	with constant fluid pressure, brine up to the top of the salt formation	p_{brine} = 5.89 MPa
Case 5c	with constant fluid pressure, brine up to the surface	p_{brine} = 9.42 MPa
Case 5d	with time dependent fluid pressure, brine up to the surface	p_{brine} = 9.42 + p_{dyn} MPa

Figure 2.4.34 shows the evolution of the volume of the cavity (starting at 1435 m^3 and decreasing to 1003 m^3), and the evolution of the pore volume (starting at 431.9 m^3 and decreasing to zero).

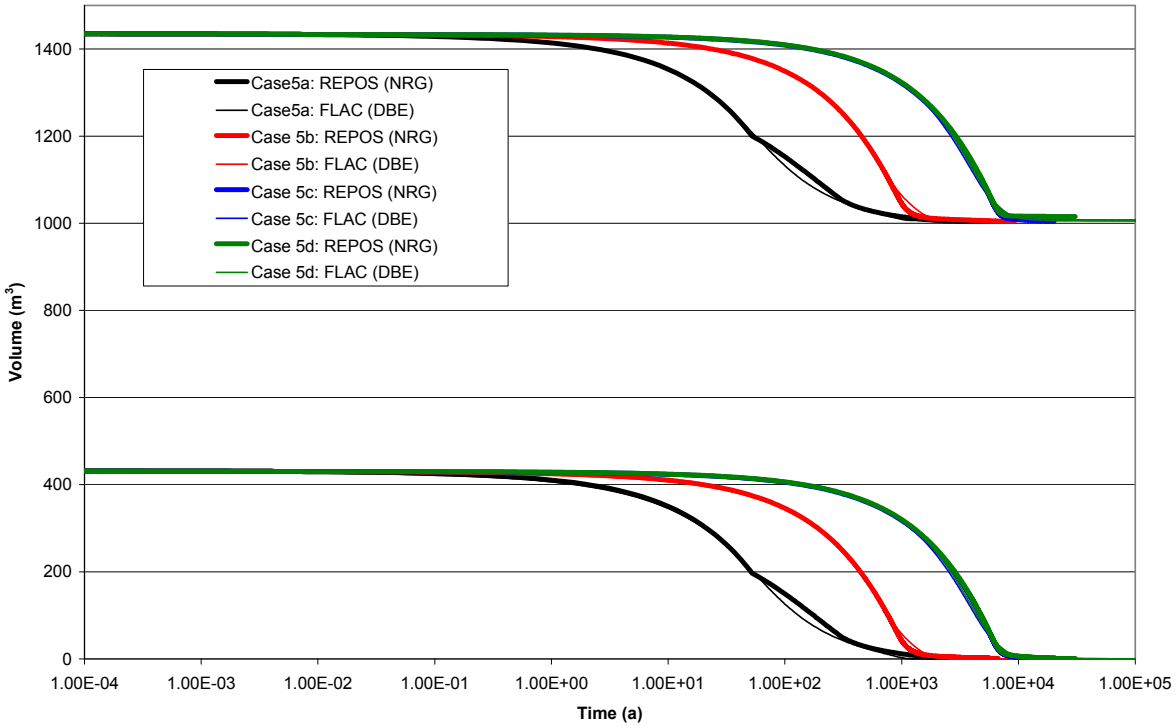

Fig. 2.4.34: Comparison of time evolution of volumes: Cases 5a, 5b, 5c and 5d using the modified backfill properties option in REPOS. The volume of the cavity and the pore volume are shown. (The curves for case 5c are almost fully concealed by the curves for case 5d.)

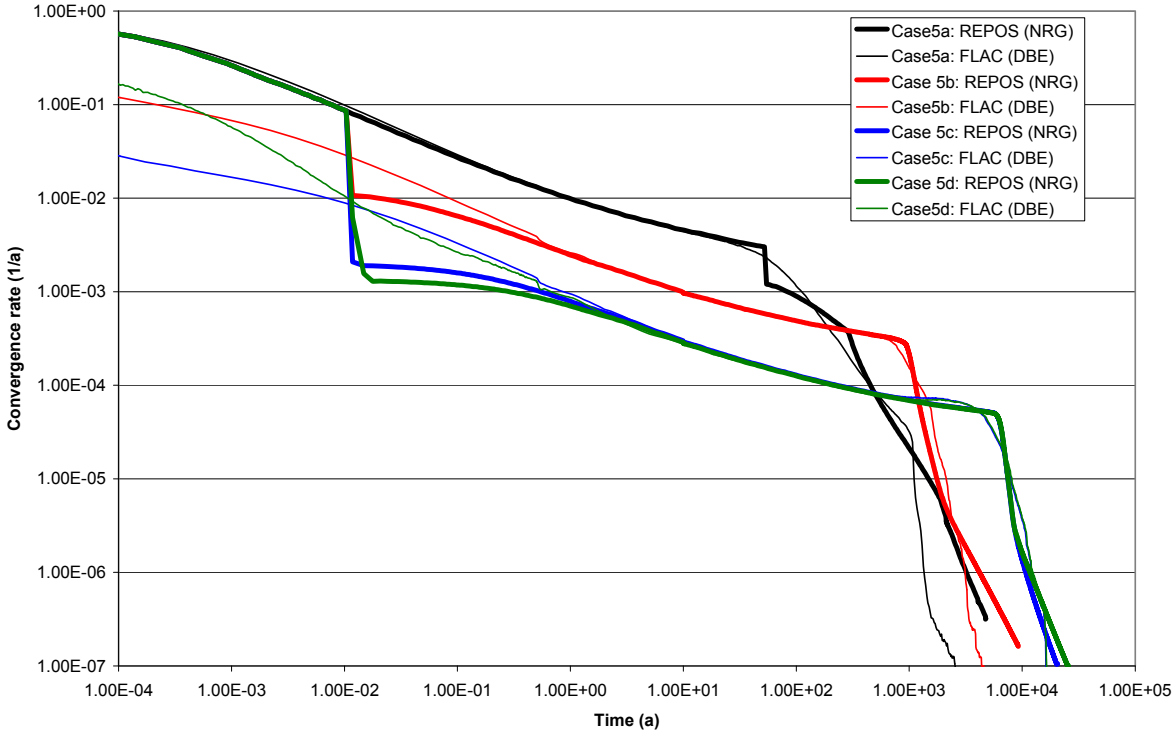

Fig. 2.4.35: Comparison of convergence rates of the volume backfilled with crushed salt: Cases 5a, 5b, 5c and 5d using the modified backfill properties option in REPOS

For study purposes Figure 2.4.36 shows the convergence of the volume backfilled with crushed salt using the modified rock salt geometry option in REPOS. As can be expected, this option deviates from the FLAC results. The difference is relatively small, since the relative volume of the steel cylinder is small (compared to the cavity), and therefore the assumed change in rock salt geometry is also small.

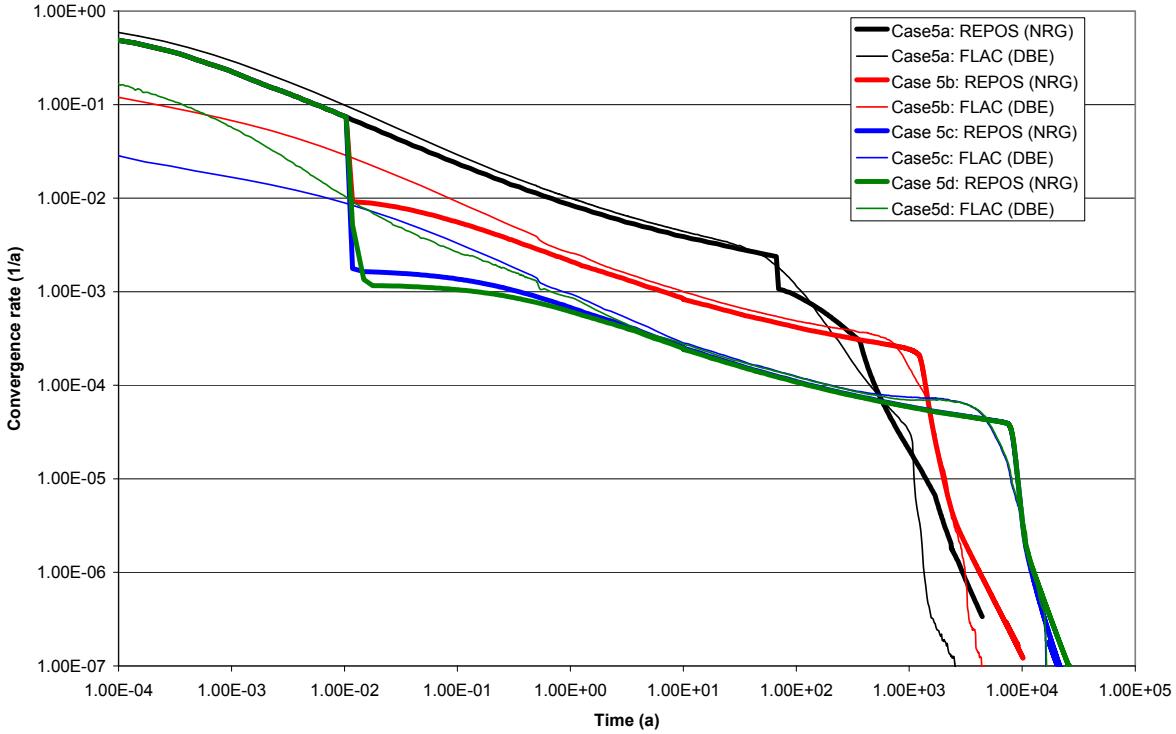

Fig. 2.4.36: Comparison of convergence rates of the volume backfilled with crushed salt: Cases 5a, 5b, 5c and 5d using the modified rock salt geometry option in REPOS

2.5 Conclusions

In the preceding chapters, the results of benchmark tests are separately described for the process-level code FLAC and the PA codes LOPOS and REPOS, respectively. The results from the PA codes and the rock mechanic code are compared to validate the applicability of the models implemented in the PA codes.

Convergence of open excavations at various fluid pressures

Two different boundary conditions have been investigated in this benchmark which are first constant and second variable fluid pressure boundary condition. In both cases the parameterisation of the EMOS model has been achieved by fitting the results of the EMOS calculation to those of the FLAC code for the first case of each set of cases for the respective boundary condition. The parameters than have been used to model the other cases within each set. With these parameter values it is found that for all the three constant-pressure boundaries and the variable pressure boundaries, the convergence rates as well as the volumes match really well the results from the FLAC code.

In general the also results obtained from REPOS agree well with those from FLAC. This was expected since the basic model and parameters for rock salt creep in REPOS and FLAC

have been chosen in such a way that the results match. Nevertheless, the results show that the approach used in REPOS to solve the creep equation in an axi-symmetrical geometry, can be applied to a more rectangular shaped excavation.

A question has been raised with respect to the method that is implemented in REPOS to calculate the response to a sudden increase in the fluid pressure in the excavation. For the benchmark considered in this report this specific transient effect has a marginal impact. However, it would be worthwhile to develop a (future) benchmark where brine intrusion occurs after 20 to 100 years.

It is also recognised that the convergence of the host rock is strongly affected by the impact, geometry and properties of the large scale in homogeneities in the overall rock salt formation. This means that the values for the model parameters for the convergence model for a real site have cannot be derived from the comparison to the rock mechanic code, but have to be determined in situ at the location of interest.

Convergence of backfilled excavations at various fluid pressures

For the EMOS code only one additional parameter was used to model the different benchmark cases for backfilled excavations, which is parameter g_2 chosen accordingly for dry and wet backfill. No additional parameter fits are necessary compared to the benchmarks for open excavations to achieve the results given. The coincidence with results obtained from the corresponding rock mechanics calculations is really well. While there are some differences between the results for the convergence rates, this does only slightly affect the match between the results for the calculated volumes from the EMOS and the FLAC model. Since the volume is the essential parameter for the radionuclide transport calculation, this small discrepancy in the convergence rates is of no impact on the PA calculations.

While for dry backfill it seems that the CCM2-BBM model as implemented in REPOS is overestimating the resistance to compaction compared to the FLAC model, for wet backfill, both REPOS and FLAC predict a very small resistance against compaction, leading to behaviour similar to a non-backfilled (open) excavation. The convergence rate is than dominated by the rock salt convergence.

The assumed behaviour of the backfill in the Recrystallization-facilitated Dislocation Creep range (i.e. $\varepsilon \sim \sigma^5$) is not confirmed in the experiments on the Bambus Backfill Mix, neither is there a proper theoretical basis for the Recrystallization-facilitated Dislocation Creep model. The experimental results suggest that especially at low porosities the compaction resistance is larger than the models predict.

Convergence of excavations that contain non-compactable objects

The results for test cases accounting for non-compactable objects by the LOPOS model were obtained without any additional parameter fitting. The non-compactable objects were either introduced by a reduced volume of the cavity or by the use of waste containers. The

results are very similar compared to those of the benchmarks with only compactable backfill, since the non-compactable objects only affect the convergence for late times when the smaller volume of compactable backfill is notable. Additionally, this yields the same hydraulic pressure in the cavity, since the backfill of that cavity has almost no influence on the flow resistance of the repository as a whole. The coincidence with results from the rock mechanics calculations is really well.

The impact of non-compactable objects in the excavation on the convergence is not automatically set in REPOS, i.e. it has to be adjusted by user input. The benchmark clearly shows that this adjustment in the REPOS input is not straightforward, but on the other hand it seems possible to derive some rules of thumb from the FLAC results. In complicated cases a FEM calculation such as with FLAC will be needed to decide what user input is needed for the specific case. This input can also be used for other complex cases if the overall geometry is similar.

Generally spoken, the results from both PA codes LOPOS and REPOS match considerably well to those of the rock mechanics code FLAC. There are some differences between the two PA codes LOPOS and REPOS which are due to the fact that the calibration of the models is different. While LOPOS calibrates the parameter values to some results of the 3D rock mechanics calculations, the REPOS parameters are calibrated completely independently to results of the previous BAMBUS project [1]. Thus, some of the occurring differences can be explained by this different calibration. The good correlation between the PA and the process-level code yields to the overall conclusion that no additional development of the PA codes currently has to be envisaged to enhance the modelling of the convergence process.

2.6 References

[1] Bechthold, W. et al.: Backfilling and sealing of underground repositories for radioactive waste in salt (BAMBUS project), EUR 19124 EN, Luxembourg, 1999.

[2] BGR: Thermomechanisches Verhalten von Salzgesteinen. - Abschlußbericht zum Forschungsvorhaben BMBF Förderkennzeichen 02 E 85420. - Archiv-Nr. 114 805. Hannover: BGR, 1996

[3] Brüggemann, R. et al.: Modellansätze und Ergebnisse zur Radionuklidfreisetzung aus einem Modellsalzstock. Projekt Sicherheitsstudien Entsorgung (PSE), Abschlußbericht: Fachband 16, Hahn-Meitner-Institut, Berlin 1985.

[4] Gomit, J.M., Hirsekorn, R.-P., Martens, K.-H., Prij, J.: EVEREST Project, Volume 3b: Salt Formation, Sites in France and the Netherlands and Common Conclusions on Salt. Final Report EUR 17449/3b EN, Luxembourg, 1997.

[5] Grupa, J.B.: Transient Convergence of Rock Salt. NRG internal note 21952/08.89640, 2008.

[6] Hirsekorn, R.-P.; Boese, B.; Buhmann, D.: LOPOS: Programm zur Berechnung der Schadstofffreisetzung aus netzwerkartigen Grubengebäuden. Gesellschaft für Anlagen- und Reaktorsicherheit (GRS) mbH, Bericht GRS-157, Braunschweig 1999.

[7] Itasca: FLAC^{3D} Fast Lagrangian Analysis of Continua in 3 Dimensions – Users Manual. Minneapolis: Itasca Consulting Group, 2005

[8] Poley, A.D.: BAMBUS project - Nederlandse bijdrage. NRG 20038/00.30991/C, 2000.

[9] Prij, J.: On the Design of a Radioactive Waste Repository. PhD Thesis, Enschede, Den Haag, 1991.

[10] Prij, J. and Mengelers, J.H.J.: On the derivation of a creep-law from isothermal borehole convergence. Report ECN-89, Netherlands Energy Research Foundation, 1981.

[11] Schröder, T.J.: PAMINA task 2.1.D - Update Model Parameters for Sensitivity Analysis. NRG note 2.1952.21/08.88799 RE/TS/ES, 2008.

[12] Storck, R. et al.: Performance Assessment of Geological Isolating Systems for Radioactive Waste (PAGIS): Disposal in Salt Formations. EUR 11 778 EN, Luxembourg, 1988.

[13] ter Heege, J.H., et al.: Composite flow laws for crystalline materials with log-normally distributed grain size: theory and application to olivine. Journal of Structural Geology 26 (2004) 1693–1705.

[14] Zhang, X. and Grupa, J.B.: NF-Pro deliverable 3.5.7 Compaction behaviour and permeability of low porosity compacted salt grit (dry and wet) NRG 21146/06.77412/P, 2006.

2.7 Appendix

2.7.1 Asymptotic behaviour of the convergence rate (LOPOS)

In the following, the limits of the convergence rate are investigated, which the GRS model yields for a cavity directly after excavation, i.e. at the limit $t \to 0$, and for very late times, i.e. at the limit $t \to \infty$. At the beginning, the fluid pressure is equal to the atmospheric pressure, the cavity is not backfilled and the temperature is not increased. Consequently, one has f_p = 1, f_ϕ = 1 and f_T = 1. For an integration of eq. 2.3.1, however, it is sufficient, that all these three functions are constant and one has

$$-\int_{V_0}^{V} \frac{dV'}{V' f_t(V')} = \int_0^t K_{ref} f_{loc} f_p f_\phi f_T dt' . \qquad \text{A.1}$$

Integration of eq. A.1 yields the inverse function of $f_t(t)$

$$t(f_t) = \frac{A}{C}\left[\frac{1}{f_t - 1} - \frac{\lambda_S}{A} - \ln\left(1 - \frac{\lambda_S}{A + \lambda_S}\right) - \ln\left(1 + \frac{1}{f_t + 1}\right)\right], \qquad \text{A.2}$$

where

$$C = K_{ref} f_{loc} f_p f_\phi f_T . \qquad \text{A.3}$$

This expression is suitable to investigate the limit of the convergence rate for t = 0. For very small λ_S, i.e. $\lambda_S \to 0$, which holds for $t_0 \to 0$, the function f_t tends to infinity:

$$\lim_{t \to 0} f_t(t) \to \infty , \qquad \text{A.4}$$

The right hand side of A.2 can be expanded and one has

$$\lim_{f_t \to \infty} t(f_t) \to \frac{A}{C}\left[\frac{1}{f_t - 1} - \left(\frac{1}{f_t - 1} - \frac{1}{2}\frac{1}{(f_t - 1)^2} + \ldots\right)\right]. \qquad \text{A.5}$$

This result is obtained for very small λ_S (not necessarily 0) considering first order term of λ_S. For $t \approx 0$, i.e. $f_t \gg 1$, approximately one has

$$t \approx \frac{A/2}{K_{ref} f_{loc} f_p f_\phi f_T} \cdot \frac{1}{(f_t - 1)^2} \qquad \text{A.6}$$

or solved for f_t

$$f_t \approx 1 + \frac{\sqrt{A/2}}{\sqrt{K_{ref} f_{loc} f_p f_\phi f_T \cdot t}}. \qquad \text{A.7}$$

Using eqs. 2.3.2 and A.7, the ratio $\eta^0_{1,2}$ of the convergence rates $K(p_1)$ and $K(p_2)$ with constant but different fluid pressures p_1 and p_2 yields

$$\eta^0_{1,2} = \frac{f_t(p_1) f_p(p_1)}{f_t(p_2) f_p(p_2)} \approx \frac{\sqrt{f_p(p_1)}}{\sqrt{f_p(p_2)}} = \left(\frac{1 - \frac{p_1}{p_G}}{1 - \frac{p_2}{p_G}}\right)^{\frac{m}{2}} \qquad \text{A.8}$$

For late times $t \to \infty$, on the other hand, one has

$$\lim_{t \to \infty} f_t(t) = 1 \qquad \text{A.9}$$

and the ratio $\eta^\infty_{1,2}$ is

$$\eta^\infty_{1,2} = \frac{f_p(p_1)}{f_p(p_2)} = \left(\frac{1 - \frac{p_1}{p_G}}{1 - \frac{p_2}{p_G}}\right)^{m} \qquad \text{A.10}$$

This characteristic behaviour is also shown by convergence rates resulting from rock mechanics calculations.

2.7.2 Estimation of the initial convergence rate (LOPOS)

For very early times after the excavation of a repository the initial convergence rate can be calculated explicitly. For this purpose the approximation of the function f_t (eq. A.7) giving the explicit time dependence of the convergence rate at small times can be used. One has

$$K = f_{loc} \cdot K_{ref} \cdot f_p(p) \cdot f_\phi(\phi) \cdot f_T(T) \cdot f_t(t) \qquad \text{B.1}$$

as given in eq. 2.3.2. Initially one has atmospheric pressure p_{atm} in the cavity and there is no compaction of the backfill, additionally the temperature in the cavity equals the rock temperature T_S, thus

$$f_p(p_{atm}) = 1\,,\ f_\phi(\phi \geq \phi_r) = 1 \text{ and } f_T(T_S) = 1\,. \qquad \text{B.2}$$

Therefore, the relation A.7 of appendix A reduces to

$$f_t(t \approx 0) = 1 + \sqrt{\frac{A}{2 \cdot K_{ref} \cdot f_{loc} \cdot t}}\,. \qquad \text{B.3}$$

Replacing A with the help of eq. 2.3.10, where K_0 is the initial value of the convergence rate at $t = 0$, eq. B.3 yields

$$K(t \approx 0) = f_{loc} \cdot \left(K_{ref} + \sqrt{\frac{\lambda_S \cdot (K_0 - K_{ref})}{2t}} \right), \qquad \text{B.4}$$

where

$$K_0 \geq K_{ref} \qquad \text{B.5}$$

must hold. Solving eq. B.4 for K_0 one finally has

$$K_0 = \frac{2t}{\lambda_S} \left\{ \frac{K(t \approx 0)}{f_{loc}} - K_{ref} \right\}^2 + K_{ref}\,. \qquad \text{B.6}$$

This equation also shows that the initial convergence rate K_0 goes to infinity, if λ_S goes to zero. However, integrating B.3 shows, that the volume decrease is proportional to $\sqrt{t}$ and, hence, tends to zero. Additionally, if K_0 becomes very large compared to K_{ref}, eq. B.4 can be approximated by

$$K(t \approx 0) = f_{loc} \cdot \sqrt{\frac{\lambda_S \cdot K_0}{2t}}, \qquad \text{B.7}$$

which shows that the convergence rate at very early times depends on the product of the parameters, $\lambda_S \cdot K_0$, only. This dependence can be used for estimating the K_0 value when λ_S is very small.

3. Benchmark on brine intrusion into a backfilled drift

3.1 Introduction

In a normal evolution of a repository design in rock salt, no transport medium is present in the repository in a salt formation. In case of the analysis of altered evolution scenario, brine intrusion may occur from either outside of the salt formation or from undetected brine inclusions in the neighbourhood of the repository. In both cases, intruding brine may successively fills up the residual voids within the backfilled drifts, chambers or boreholes of the repository, eventually get in contact with the disposed waste Contaminated brine may then be pressed out of the salt formation by convergence of the salt rock or other processes like gas generation. Thus, the process of brine intrusion, where brine percolates through an unsaturated backfill (e.g. crushed salt), is an important safety relevant process, which has to be implemented with sufficient accuracy in a PA code

In the present performance assessment (PA) codes used to model brine intrusion into backfilled drifts, the flow resistance of these drifts is assumed as independent of the gas or brine saturation of the backfill. The permeability only varies as a result of the changing porosity, but not as a function of the gas saturation. Some simplified model, based on a single (fitted) parameter, may be included in the PA codes to account for instance for the settling of crushed salt when becoming wet or the dissolution of backfill by contact with unsaturated brine. To test the relevance of unsaturated flow processes in case of brine intrusion into a backfilled gallery, a benchmark is performed by GRS and NRG. Three different models were used: a numerical 3D programme (HYDRUS2D/3D) [5] and two PA codes, LOPOS [2] and REPOS [6].

HYDRUS software package is able to simulate two- and three-dimensional variably-saturated water flow and the transport of heat and solutes, including sequential first-order decay reactions. The HYDRUS program numerically solves the Richards equation for saturated-unsaturated water flow and convection-dispersion type equations for heat and solute transport. The water flow part of the model considers prescribed head and flux boundaries, boundaries controlled by atmospheric conditions, free drainage boundary conditions, as well as a simplified representation of nodal drains. First- or third type boundary conditions can be implemented in both the solute and heat transport parts of the model. The governing flow and transport equations are solved numerically using Galerkin-type linear finite element schemes.

LOPOS and REPOS are two near-field modules used in different versions of the PA-code package EMOS, and allow a great flexibility in handling complex geometrical structures and various features, events and processes. The geometry of the modelled system is approached by discretizing the relevant parts, or features, in segments. To each segment, a model is assigned – the so-called ‘segment model’, in which the relevant events and processes are taken into account.

3.2 The conceptual model and data for the test case

The model comprises a backfilled drift (grey) of length L with an adjacent fully-saturated shaft at the left, and an empty chamber at the right (Fig. 3.1). The drift is initially dry. The chamber acts as a sink for the outflow from the drift. The initial state of the backfilled region is characterised by the porosity ϕ_s, the permeability k and the residual water/brine saturation ϕ_r. The interface with the disposal chamber may be completely permeable, allowing water to drain freely at atmospheric pressure.

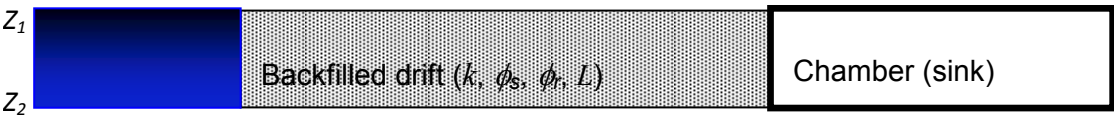

Fig. 3.1: The conceptual model of the Test Case

The test case is to be calculated for the following parameter values for

- L = 50 m
- k = 10^{-14} m^2 and 10^{-18} m^2
- ϕ_s corresponding to power law from [3] eq. (29)
- $z_1 \approx$-800 m, $z_2 \approx$-805 m

Calculated quantity at x=L:

- impermeable ($x \geq L$): head
- atmospheric pressure ($x \geq L$): outflow

Two data sets, displayed in Tab. 3.1, are considered in the following calculations, which describe water movement through an initially dry low and, respectively, high permeable backfilled drift. The variation of the permeability k with porosity ϕ_s is specific to crushed salt backfills and it is given by k = 2.540·10^{-10}·ϕ_s $^{4.175}$ [1]. The saturated hydraulic conductivity K_s depends on permeability k, water density ρ and viscosity μ and is given by

$$K_s = \frac{\rho g k}{\mu} \qquad 3.1.$$

The soil water retention, $\phi(h)$, and unsaturated hydraulic conductivity, $K(h)$, functions are given by Mualem-van Genuchten model [5]. The van Genuchten parameters ϕ_r, ϕ_S, α, n and l are given in Tab. 3.1. The calculations have been performed with a permeable boundary to the right.

Tab. 3.1: Input data for the two models case 1 (high permeability drift) and case 2 (low permeability drift).

Parameter	PAMINA 1	PAMINA 2
Depth of the drift [m]		800
Length L, and height H of the drift [m]		L = 50 m, H = 5 m
Viscosity [Pa·s]		0.0017
Density [kg/m^3]		1200
Van Genuchten parameters		
Residual water content ϕ_r [-]		0.001
Coefficient α [-]		0.2
Exponent n [-]		3.7
Pore connectivity parameter l [-]		0.5
Permeability [m^2]	10^{-14}	10^{-18}
Ssaturated soil water content ϕ_S [-]	0.088	0.0097
Hydraulic conductivity K_s [m/s]	$6.92 \cdot 10^{-8}$	$6.92 \cdot 10^{-12}$

The relationship between the water content θ [-], and the suction pressure (pressure head), h [m], for PAMINA 1 and 2, usually called soil-water retention curves, are displayed in figure 3.2. This curve is a characteristic for different types of soils (materials). Soil suction, expressed as negative pressure values (as p_{atm} = 0) can change from zero, when water content

$$\theta = \frac{volume\ of\ water}{total\ volume\ of\ soil} \qquad 3.2$$

approaches to porosity n, to 100 m when the material is very dry. When the soil is not saturated, water flows downward by gravity flow through interconnected pores that are filled with water and, to a lesser extent, as a film flowing along particle surfaces in pores incompletely filled with water. The behaviour at low water contents (residual moisture) reflects the fact that soil never completely looses all of its water. At the lower limit of the moisture content, water coats the solid soil matrix. When the liquid coating becomes too thick to be held by surface tension, a droplet will pull away and be drawn away by gravity. With increasing water content, more pores fill, and the rate of water movement increases. As the soil approaches to saturation, hydraulic conductivity, and consequently the rate of water movement, increases. Low permeability soils have lower hydraulic conductivity and fill slower then high conductivity materials. Darcy law is valid for unsaturated flow, although the unsaturated hydraulic conductivity varies with the water content.

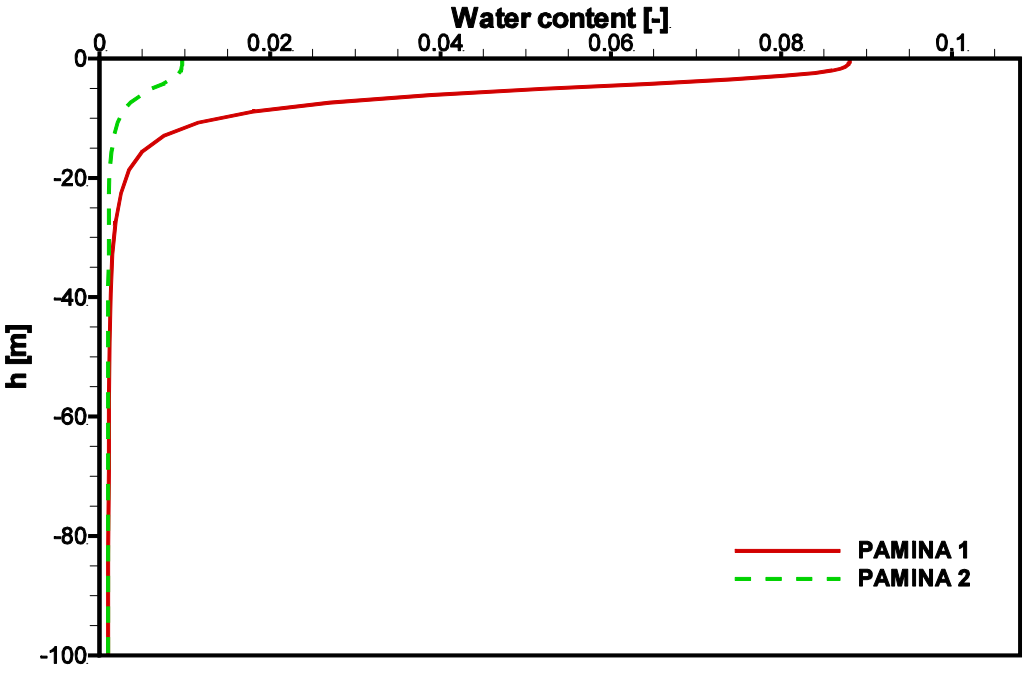

Fig. 3.2: Water-soil retention curve for PAMINA 1 (high permeability) and PAMINA 2 (low permeability) cases

3.3 Results of the test case

3.3.1 HYDRUS calculations

3.3.1.1 Modelling

Two or three-dimensional isothermal, uniform Darcian flow of water in variably-saturated rigid porous media in which the air phase is assumed to play an insignificant role is mathematically described by Richard's equation:

$$\frac{\partial \theta}{\partial t} = \frac{\partial}{\partial x_i}\left[K\left(K_{ij}^{A}\frac{\partial h}{\partial x_j} + K_{iz}^{A} \right) \right] - S \qquad 3.3,$$

where θ is the volumetric water content [-], h is the pressure head [m], S is a sink term, K^A is the dimensionless anisotropy tensor, and K is the unsaturated hydraulic conductivity function. Unsaturated hydraulic conductivity depends on the saturated hydraulic conductivity K_s [m/s], and the relative hydraulic conductivity K_r by:

$$K_s(h,x,y,z) = K_s(x,y,z)\,K_r(h,x,y,z) \qquad 3.4$$

The unsaturated hydraulic properties soil water retention ($\theta(h)$) and hydraulic conductivity $K(h)$ are generally highly non-linear functions of the pressure head. The soil water retention and hydraulic conductivity used in the current exercise are given by van Genuchten expressions:

$$\theta(h) = \begin{cases} \theta_r + \dfrac{\theta_s - \theta_r}{\left[1 + |\alpha h|^n\right]^m}, & h < 0 \\ \theta_s, & h \geq 0 \end{cases}$$

$$K(h) = K_s S_e^l \left[1 - \left(1 - S_e^{\frac{1}{m}}\right)^m\right]^2 \qquad 3.5$$

where

m = 1-1/n, n>1, S_e is the effective water content,

and θ_r and θ_s is the residual and saturated water content, respectively; α is the inverse of the air-entry value, n is the pore-size distribution index, and l is a pore-connectivity parameter.

The backfilled drift is modelled as a 50 m long and 5 m high, 2-dimensional porous media. The top of the drift is located 800 m below the earth surface. The flow domain of 250 m^2 was discretized in 3092 triangular elements and 1657 nodes, corresponding to a distance of 0.5 m between two adjacent nodes.

The initial pressure head distribution is depth-dependent, and it mimics a dry environment, close to the residual moisture content (0.001). Thus, the values of the pressure head imposed on the top of the drift and corresponding to an initial moisture content of 0.0012, are -18.7 m for PAMINA 2 variant and -47.5 m for PAMINA 1 variant, respectively.

The top and the bottom of the drift are assumed impermeable. At the left, the drift is in contact with a water reservoir under hydrostatic equilibrium. The boundary condition to describe such a situation is given as depth varying pressure head, between z_1 = -800 m and z_2 = -805 m. At the right, at x = L, a seepage face is assumed, through which water leaves the saturated part of the flow domain. The length of the seepage face is not known a priori. The code assumes that: a) the pressure is uniformly equal to zero along the seepage face, b) water leaving the saturated zone along the seepage face is immediately removed by no matter which removal mechanism [5].

3.3.1.2 Results

The temporal evolution of the average outflow rates for PAMINA 1 and PAMINA 2 are shown in figures 3.3 and 3.4, respectively. Water breakthrough appears at 22.78 days (PAMINA 1) and 61.2 years (PAMINA 2), respectively.

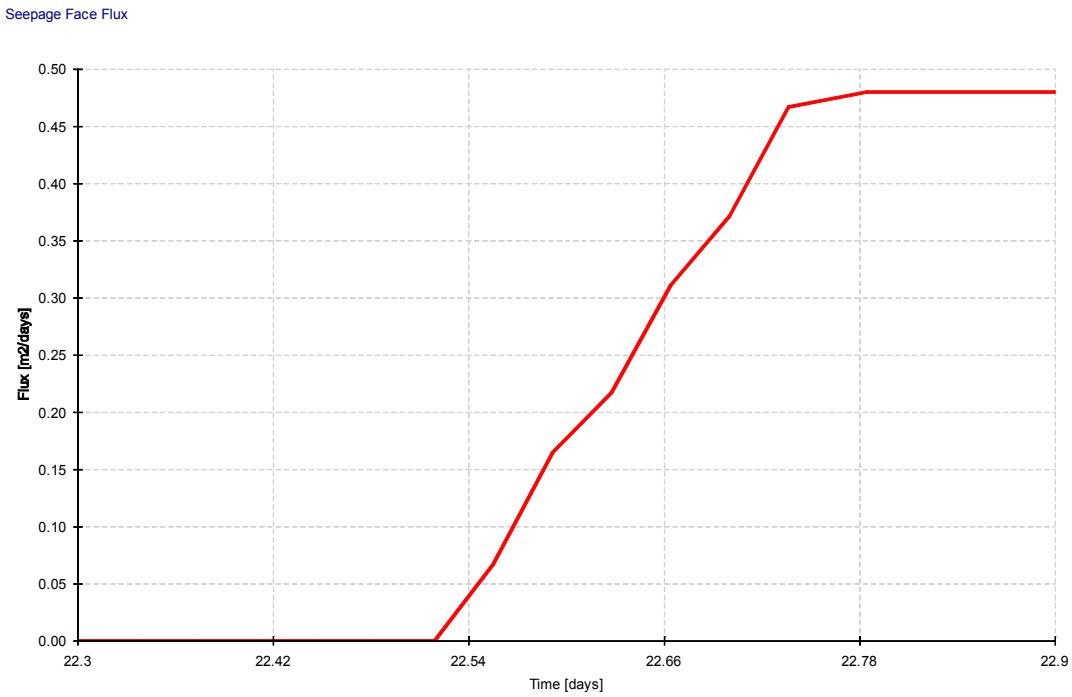

Fig. 3.3: PAMINA 1 - Average right boundary water flux (outflow)

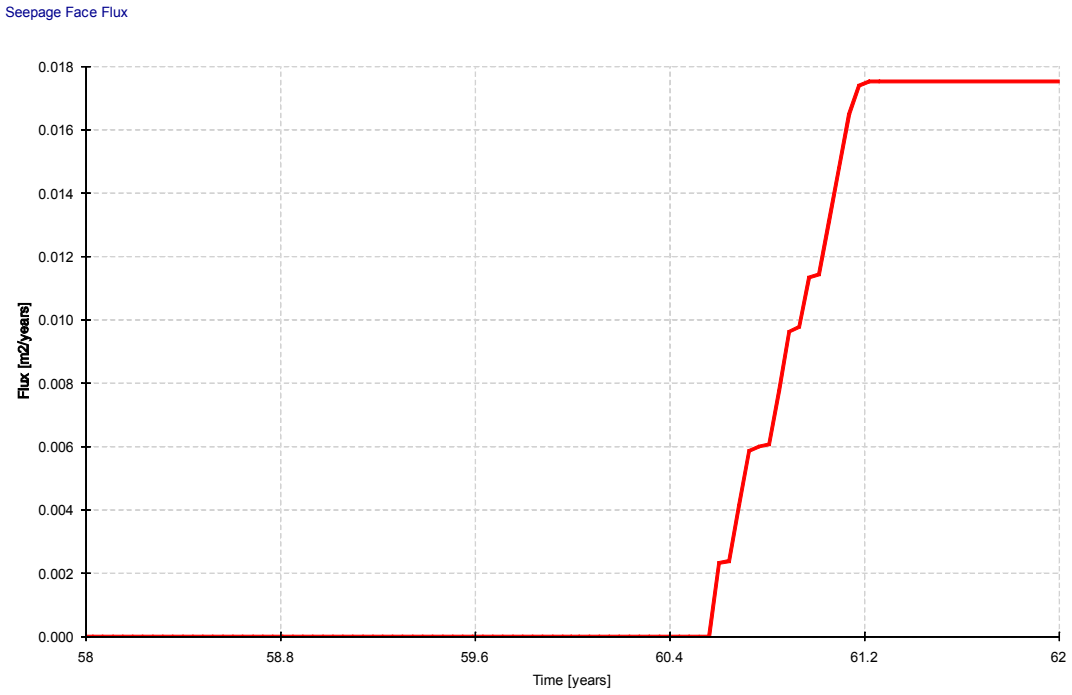

Fig. 3.4: PAMINA 2 - Average right boundary water flux (outflow)

The moisture front through the backfill is rather sharp for both cases, as shown in figures 3.5 and 3.6. The pressure head remains at the initial value until the moisture front arrives, then it reaches the zero pressure head and it becomes active (i.e., water flows through it).

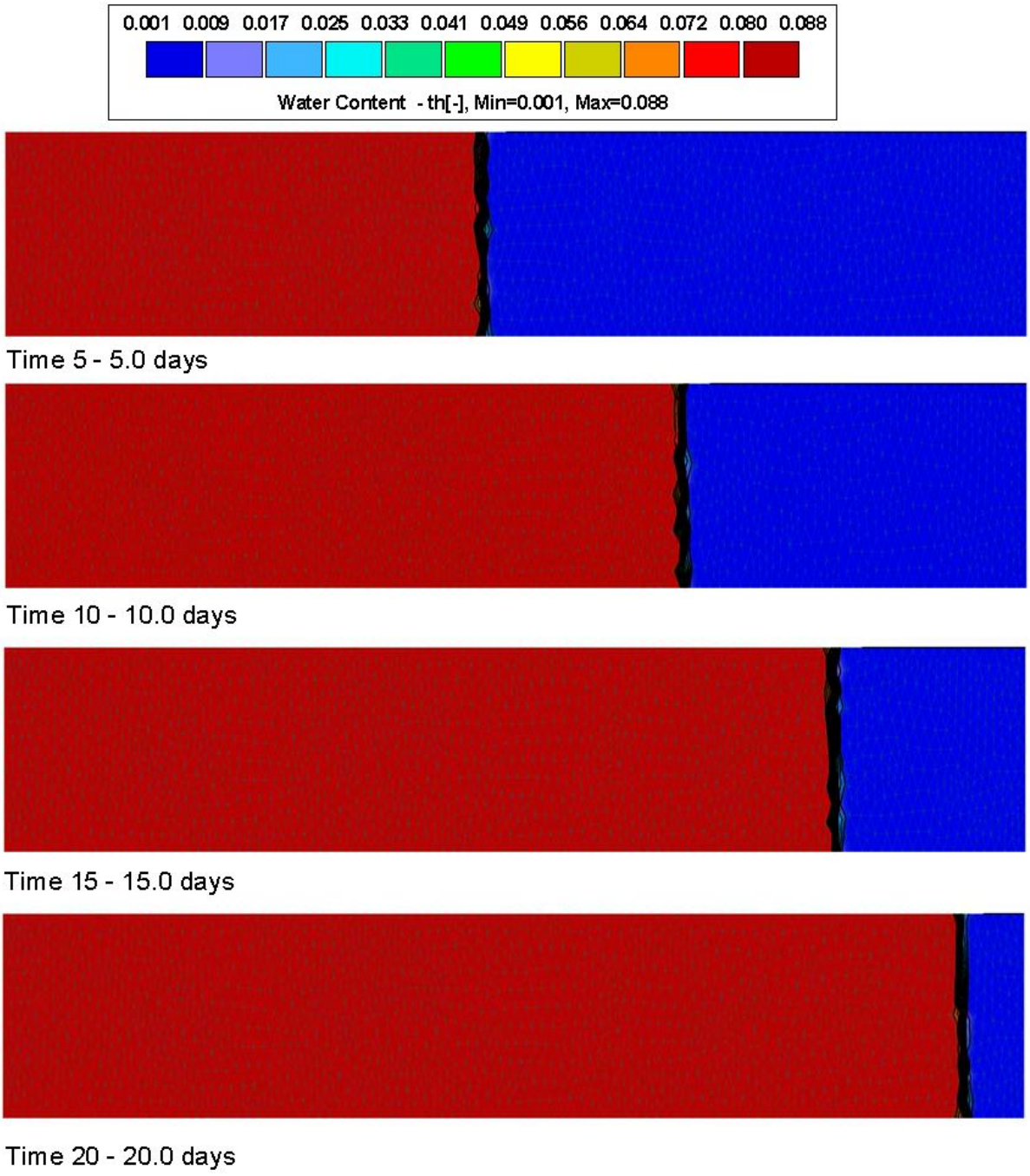

Fig. 3.5: Advance of the moisture front in the high permeable backfilled gallery (PAMINA 1 case).

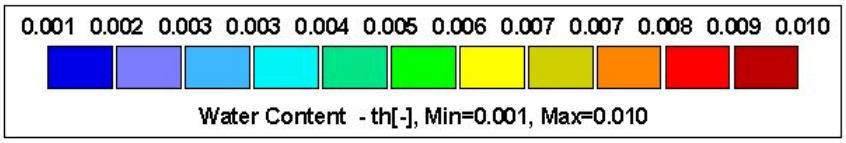

Time 1 - 10 years

Time 3 - 30 years

Time 5 - 50 years

Time 6 - 60 years

Fig. 3.6: Advance of the moisture front in the low permeable backfilled gallery (PAMINA 2 case).

The right boundary is considered a seepage face in the modelling, through which water leaves the saturated part of the flow domain. As a consequence, the breakthrough times in different locations of the right boundary are influenced by the rise of the height of the saturated front. This is shown in figures 3.7 to 3.10. Water leaves the flow domain sooner in the lower parts of the boundary. As the moisture content increases to saturation, the height of the seepage face increases. The breakthrough times for points located closer to the upper boundary (point N2, at z = -800 m) are delayed compared to those which are closer to the bottom (point N1, at z = -805 m). For the low permeability case (PAMINA 2), the domain attains saturation at t = 60.7 years (22.54 days, for PAMINA 1) at the bottom, respectively at t = 61.2 years (22.84 days) at the top, as shown in figures 3.7 and 3.9. The pressure head increases gradually in the same time interval to 0, until full saturation is attained (figures 3.8, and, 3.10 respectively). The effect of the different water contents between high and low porosity cases can be seen from the evolution of the pressure heads. The moisture content at the top is lower then at the bottom, due to gravity which pulls down the water droplets. Consequently, suction is lower at the top, compared to the bottom.

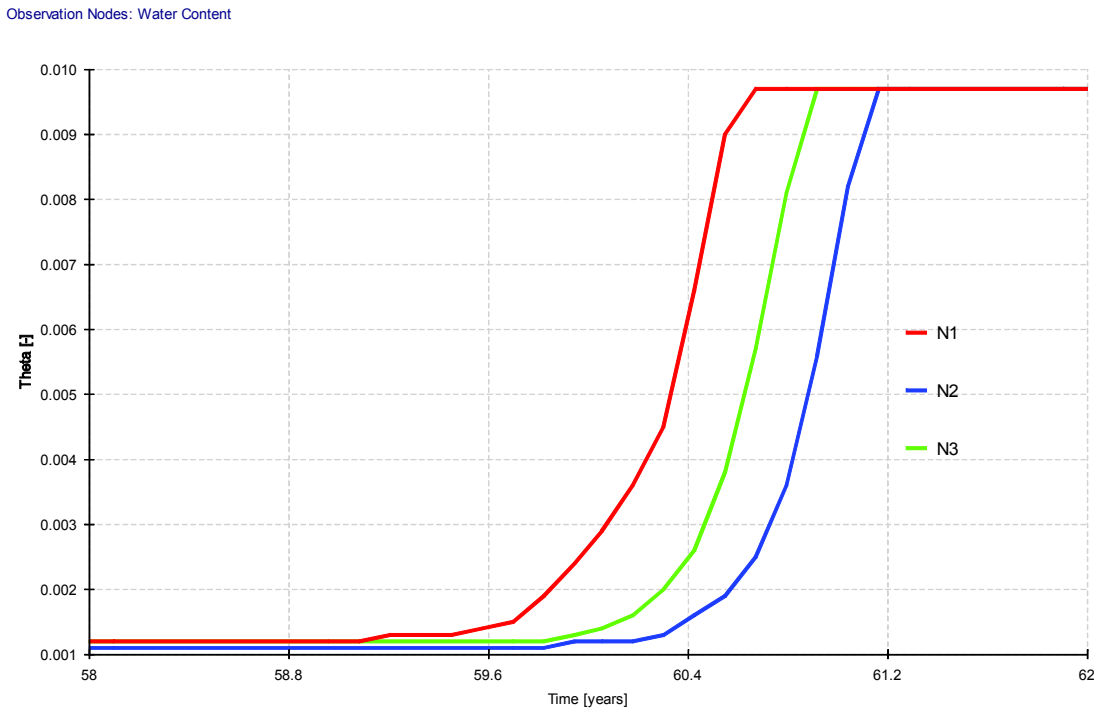

Fig. 3.7: PAMINA 2 - Temporal evolution of the water content for observation points on the right boundary N1(50, -805), N2(50, -800.5) and N3(50, -802.5).

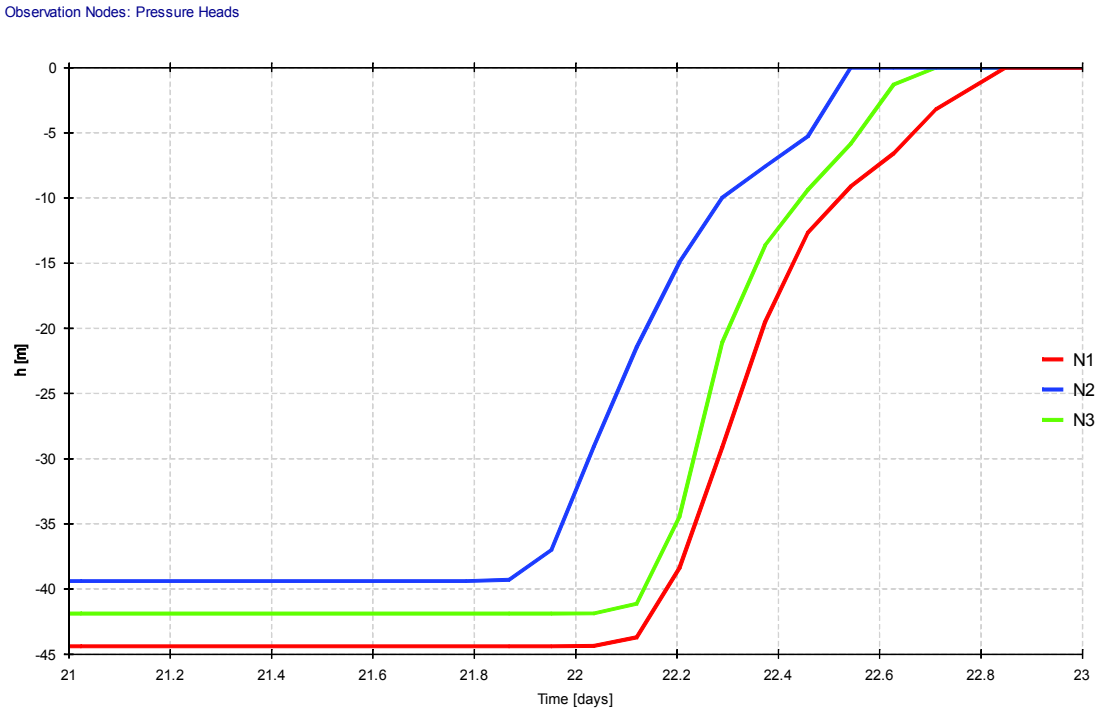

Fig. 3.8: PAMINA 2 - Temporal evolution of the pressure head for observation points on the right boundary N1(50, -805), N2(50, -800.5) and N3(50, -802.5).

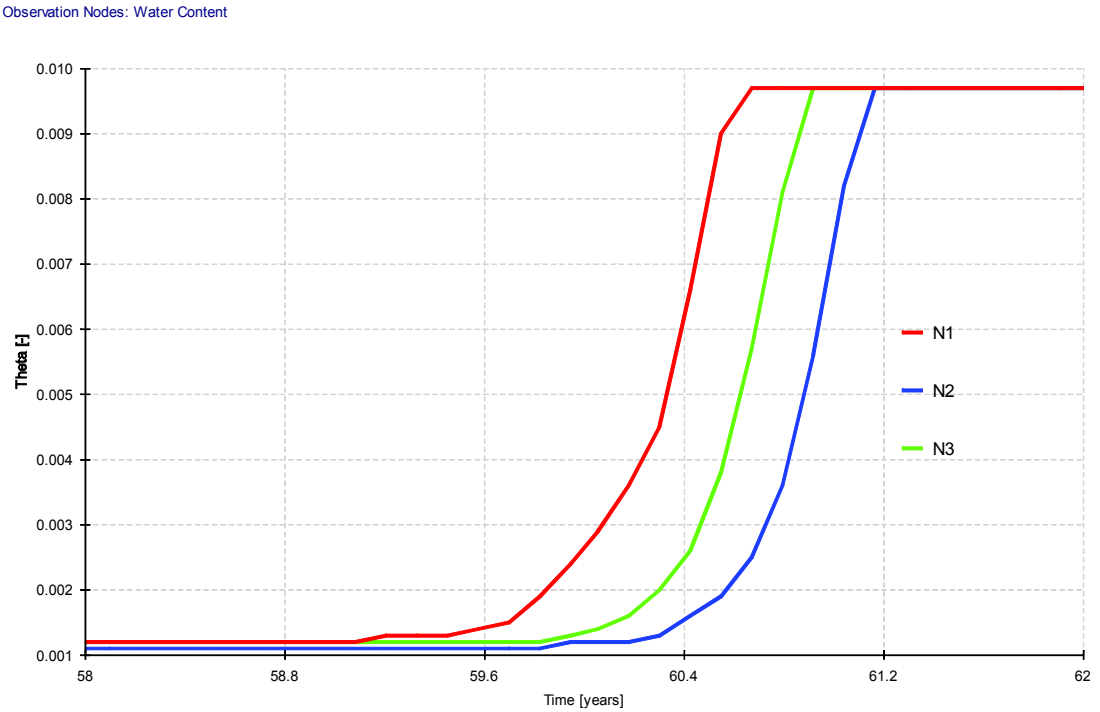

Fig. 3.9: PAMINA 1 - Temporal evolution of the water content for observation points on the right boundary N1(50, -805), N2(50, -805) and N3(50, -802.5).

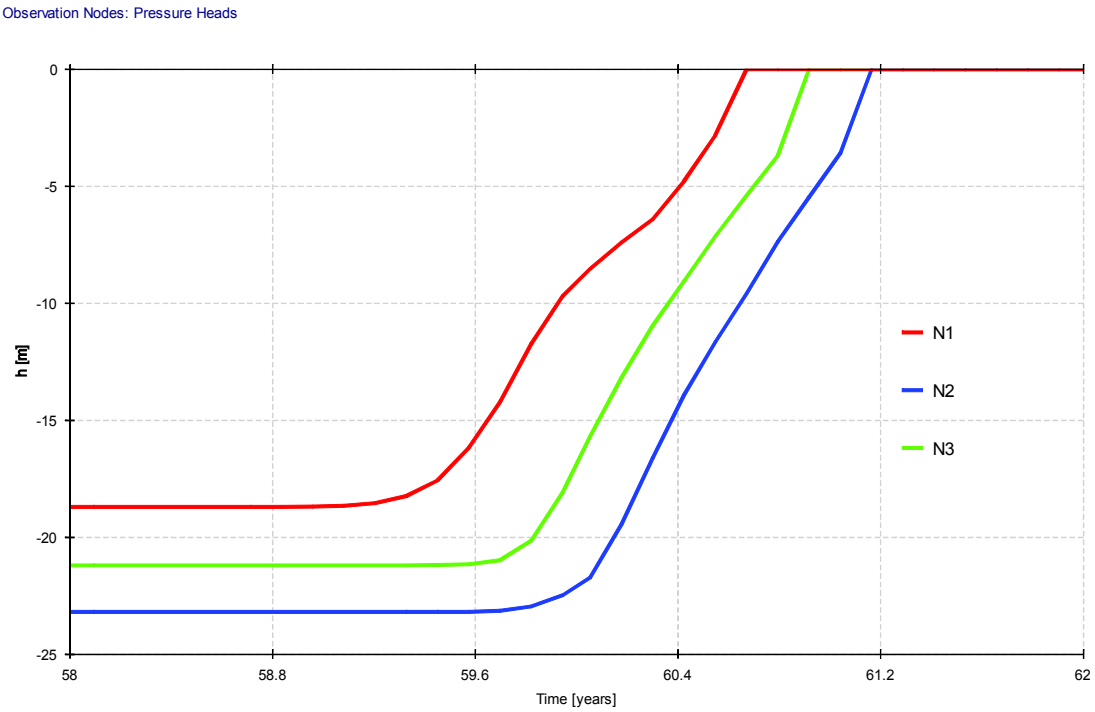

Fig. 3.10: PAMINA 1 - Temporal evolution of the pressure head for observation points on the right boundary N1(50, -805), N2(50, -805) and N3(50, -802.5).

The water inflow and outflow rates, averaged over the height of the gallery, are shown in figure 3.14, and figure 3.15 for PAMINA 2, respectively. The inflow rates show a plateau at the onset of the flow, of approximately $8 \cdot 10^{-4}$ days ($2 \cdot 10^{-6}$ years – the first 5 time steps) for the variant PAMINA 1, and $2 \cdot 10^{-3}$ years (the first 10 time steps) for variant PAMINA 2. During the progressive saturation of the backfill, infiltration (inflow) rates decline exponentially and asymptotically towards a near constant value, corresponding to the saturated hydraulic conductivity of the flow domain (and to the associated pressure head). The infiltration in the low conductivity variant is lower compared to the high conductivity case, and the saturation is completed accordingly at a much later time. The differences in infiltration between the two cases are important, around 4 orders in magnitude.

The outflow rates are constant in both cases (the outflow starts after complete saturation of the drift). Due to the difference in the hydraulic conductivity between PAMINA 1 and 2 (four orders of magnitude), the outflow rate is much higher in PAMINA 1 then in PAMINA 2.

3.3.2 Calculations with the PA code LOPOS

3.3.2.1 Modelling

LOPOS is a near-field module of the performance assessment (PA) code package EMOS [6], which allows a great flexibility in handling complex geometrical structures and various

features, events and processes. The geometry of the modelled system is approached by discretizing the relevant parts, or features, in segments. To each segment, a model is assigned – the so-called 'segment model', in which the relevant events and processes are taken into account.

If the segment i is filled with brine, the following flow balance equation is valid

$$\sum_{j \neq i} S_{i,j} = Q_i \qquad 3.6$$

where the index j describes the neighbouring segments to i. The parameter $S_{i,j}$ indicates the brine flow from segment i to segment j, while the source term Q_i describes the convergence brine flow. This convergence brine flow results as a consequence of the convergence process due to the reduction of the cavity volume of the segment i. For a not-converging drift segment, $Q_i = 0$.

In porous media the Darcy-law is valid for the brine flows $S_{i,j}$

$$S_{i,j} = R_{i,j}^{-1}\left(p_i - p_j\right) \qquad 3.7$$

where $R_{i,j}$ indicates the flow resistance of the Darcy-medium between the centres of the segments i and j.

The flow resistances R of backfilled drifts, boreholes and chambers can be illustrated as function of the permeability k as follows,

$$R = \frac{\mu L}{Fk} \qquad 3.8$$

where μ indicates the dynamic viscosity, L the length and F the cross-section of the backfilled cavity. The flow resistance is therefore dependent on geometric parameters (L, F, k) as well as on dynamic characteristics of the brine μ.

The resistance to flow from segment *i* to the neighbouring segment *j* is calculated as follows:

a) Segments i and j are in line:

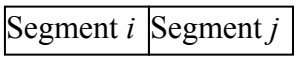

$$R_{i,j} = \frac{1}{2} \cdot \left(R_i + R_j\right)$$

b) Segment j joins segment i vertically:

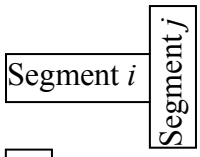

$$R_{i,j} = \frac{1}{2} R_i$$

c) Segment i joins segment j vertically:

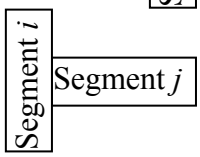

$$R_{i,j} = \frac{1}{2} Rj$$

d) Segments i and j vertical:

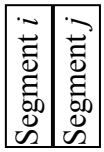

$$R_{i,j} = 0$$ (rulled out)

Vacant or partially filled segments leave their mark in the equation system in the form of boundary conditions. Since these boundary conditions change in the course of time respectively from one segment to another due to further flooding of segments, the equation system also changes with time. For that reason, the equation system has to be extended eventually by further segments after each time step, and therefore by further equations.

The boundary conditions for the brine pressure in vacant and incompletely filled segments are defined in the following. The atmospheric pressure is ignored in all segments. For that reason, a pressure of zero MPa will prevail in vacant segments, in partially filled segments the brine pressure is calculated from the height h_i of the brine in the segment i,

$$p_i = g \rho_L h_i \qquad 3.9$$

where p_i indicates the brine pressure in segment i, g indicates the acceleration due to gravity, ρ_L indicates the density of the brine, and h_i indicates the height of the current brine level in segment i.

The hydrostatic pressure appearing in partially flooded horizontal drifts during the inflow phase can be ignorable small in many cases as opposed to the hydrostatic brine pressure in flooded segments.

The brine pressure for the neighbouring incompletely filled segments appears as boundary condition in the flow balance equation p_j = 0. In case the segment i is horizontal, then the height of the brine level h_i can be expressed by the brine volume V_i^L, the pore volume V_i^P and the height H_i of the segment

$$h_i = \frac{V_i^L}{V_i^P} H_i \qquad 3.10$$

The system modelled for the Test Case is a sequence of three segments: a water reservoir (saturated shaft), a dry backfilled drift and an empty gallery, acting as water sink.

For modelling of the test case with LOPOS code, a horizontal segment structure, with rectangular cross-section has been created, as shown in 3.11. The segment model HIQQN3 has been assigned to the water reservoir, which is also the contact point to the geosphere. The backfilled gallery and the sink were described by the model HKSQNN.

Fig. 3.11: Segment structure and associated segment models used with LOPOS code.

The HIQQN3 segment model is modelling the constant water inflow/outflow rates in a horizontal segment. Segment model HKSQNN describes water (and contaminant) movement through a horizontal gallery with non-compactable backfill. The gallery is modelled as a geometrical volume with high pore volume to allow water inflow over long time (“source”). Inflow into the gallery stops after complete flooding. During flooding, water pressure rises with increase in the water level. When the segment is completely flooded, water pressure reaches hydrostatic pressure.

In order to assess the effect of spatial discretization on the results; the drift segment has been discretized either into 50 parts (in the following called blocks), each one 1 m long, or into one segment.

3.3.2.2 Results

Temporal evolution of the water level, height of the water table, outflow rates and pressures from the gallery for the modelling variant with one block are shown in figures 3.12 and 3.13. The height of the water level rises during the fill-up phase from zero to the height of the segment, while the water content approaches saturation (cf. figure 3.12). As shown in figure 3.13, the outflow starts with first drops of water in the gallery. When the segment is completely flooded, the pressure rises to hydrostatic and the flow rate out of the gallery reaches a plateau. The water pore volume and pressure in the drift increase gradually to saturation, respectively hydrostatic pressure.

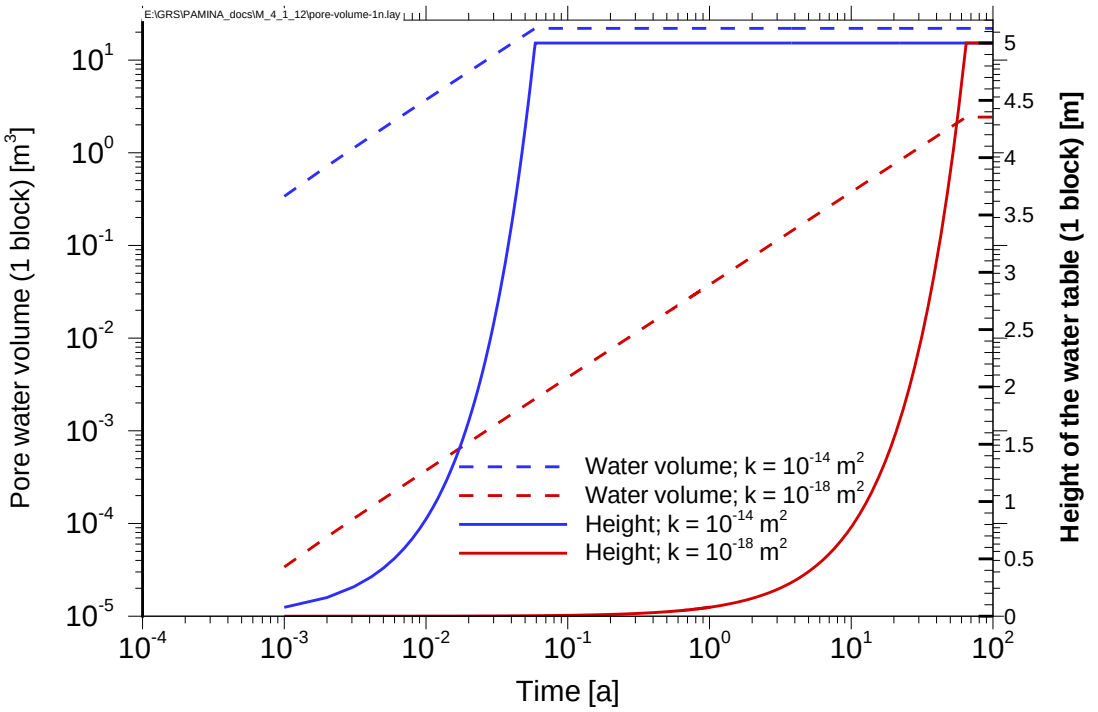

Fig. 3.12: LOPOS model (1 block) - Temporal evolution of the pore water volume and of the height of the water table in the gallery.

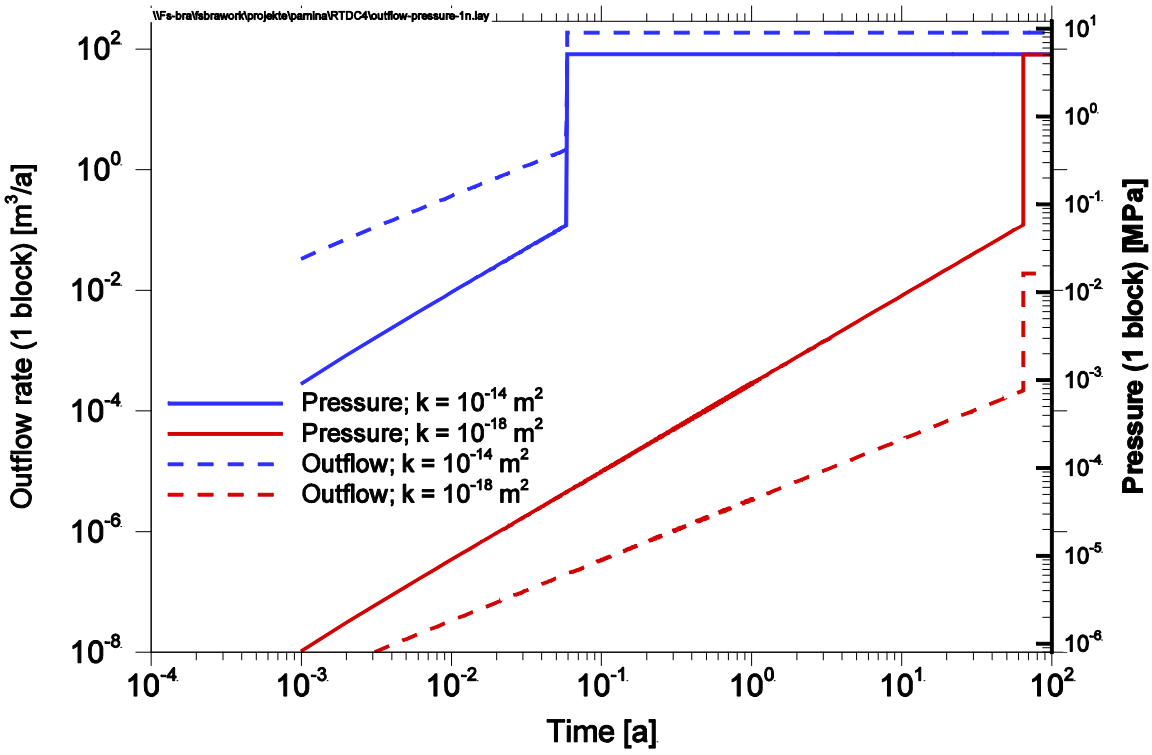

Fig 3.13: LOPOS model (1 block) - Temporal evolution of the outflow from the gallery and of the pressure.

The times when fully-developed flow starts for both discretizations are shown in table 3.2. For the high conductivity case (PAMINA 1), where the two codes show very good agreement, discretization offers a result which is closer to the one obtained with a specialized code. The discretization introduces a delay in the flow calculation with one time step for each block. Flow through unsaturated domain is slower then saturated flow, which is implemented with LOPOS code, and with appropriate choose of the time steps the discrepancy between the two approaches could be handled. The situation is the other way around when flow through a low permeable domain is to be modelled. In this case, a coarser discretization seems more favourable, as the results from PAMINA 1 point out.

Tab. 3.2: Times when fully-developed outflow start (times of attaining the plateau), and the corresponding outflow rates averaged over the height of the drift.

Case	Discretization	Time and (Relative difference %)	Average outflow rate [m^3/a]
LOPOS7 - PAMINA 1	1 block	21.535 d (95.6 – 94)	186.7
	50 blocks	22.63 d (100.5 – 99.1)	186.8
HYDRUS – PAMINA 1 bottom – top		22.52 d – 22.84 d	175.164
LOPOS7 - PAMINA 2	1 block	64.72 a (106.2 – 105.7)	0.01885
	50 blocks	65.62 a (108.1 – 107.2)	0.01885
HYDRUS – PAMINA 2 bottom – top		60.7 a – 61.2 a	0.017525

The water inflow and outflow rates are shown in figure 3.14 for PAMINA 1, and figure 3.15 for PAMINA 2 calculation cases, respectively. The initial time steps are different between LOPOS and HYDRUS. LOPOS7 starts with $\Delta t = 10^{-3}$ years, while HYDRUS 2D/3D has an initial Δt of around 10^{-8} years. Consequently, in the figures the onset of the inflow is set to $t_0 = 10^{-3}$ years. At early times of up to 10^{-2} a, the water inflow rates are slightly overestimated with the 50-blocks model, and strongly underestimated with the 1-block model (by comparison to HYDRUS 2D/3D calculations) (cf. figures 3.14 and 3.15). Afterwards, the inflow obtained with the 1-block model is higher then HYDRUS water inflow, while the 50-blocks model inflow rate is similar to HYDRUS. The time of reaching steady-state is nevertheless the same, no matter of the discretization scheme used. For low permeability domain, the inflow rates obtained with the discretized model show a step-like behaviour. This is an effect of the pressure increase in each block at the time of complete filling.

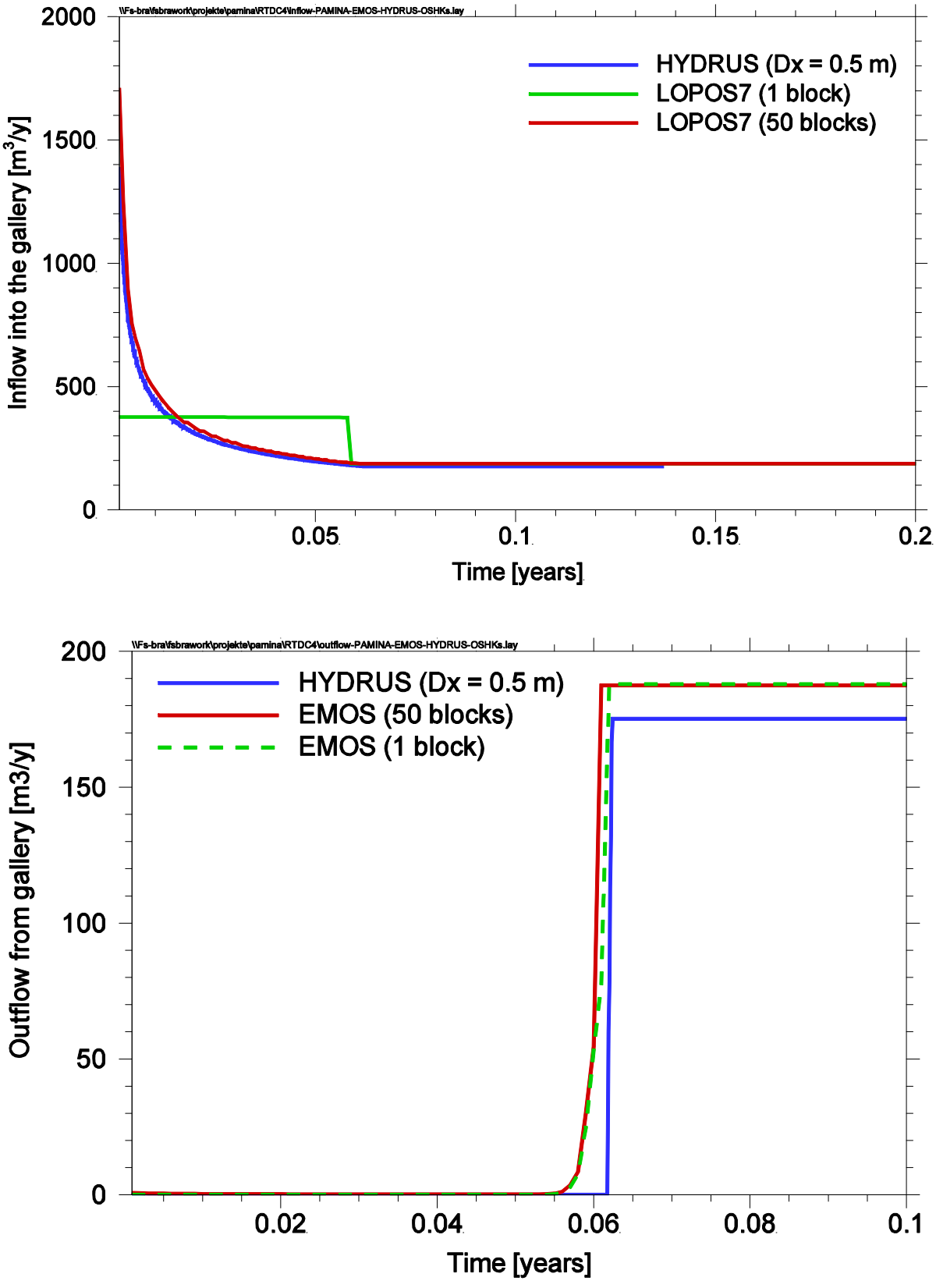

Fig. 3.14: Inflow and outflow into/out of a high permeable backfilled drift (PAMINA 1).

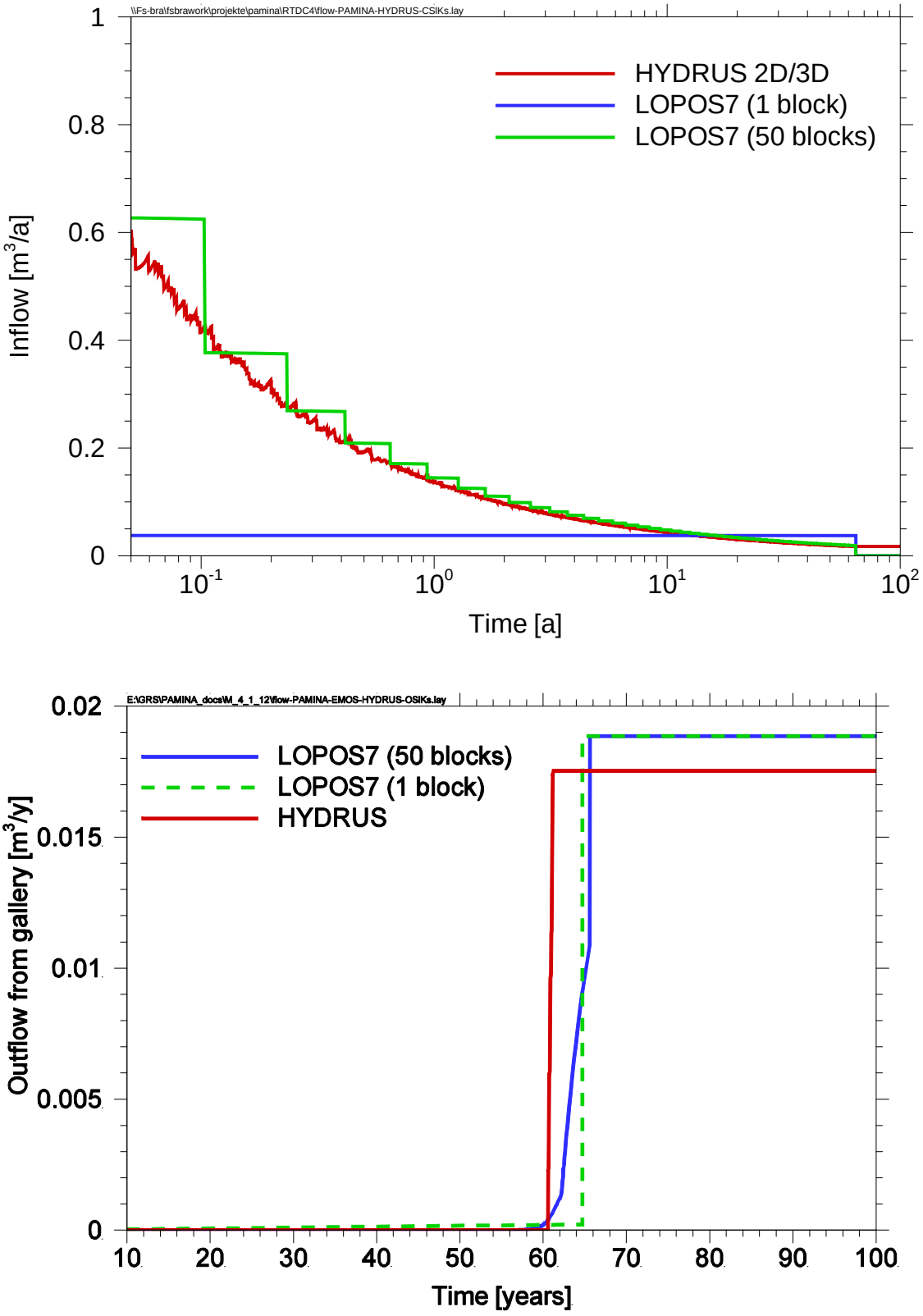

Fig. 3.15: Inflow and outflow into/out of a low permeable backfilled drift (PAMINA 2).

The outflow rates obtained with LOPOS7 are higher then the HYDRUS results with about 7.6% in the low permeability case, and 6.6% for the high permeability case respectively. LOPOS simulations show earlier breakthrough times (about 0.055 years) then HYDRUS results (approx. 0.06 years), at very low rates. That is a consequence of the modelling approach in LOPOS that allows water to flow out of the drift even if this is not completely filled (saturated). The outflow rates increase with several orders in magnitude at the time of the complete filling of the gallery. Enhancement of the outflow rate takes place earlier for highly permeable case, and later for the low permeability case, compared to HYDRUS simulations. Such behaviour indicates an overestimation of the domain conductibility for the high permeability case, while for the low permeability case, the conductive characteristics are underestimated.

Cumulated inflow and outflow rates obtained with LOPOS7, for high and low permeability cases are shown in figures 3.16, and, respectively in 3.17. For the high permeability case, compared to HYDRUS results, the amount of water entering into the modelled domain at t = 50 days is 7% higher for the non-discretized model, and 11% when discretization is involved. The corresponding cumulated outflows are with 13%, respectively 11% above the HYDRUS results. When the permeability is low, the cumulated inflow (at t = 100 years) obtained with LOPOS7 is 10% higher then HYDRUS results, no matter the discretization used. The cumulated outflow drops below HYDRUS results with 2%.

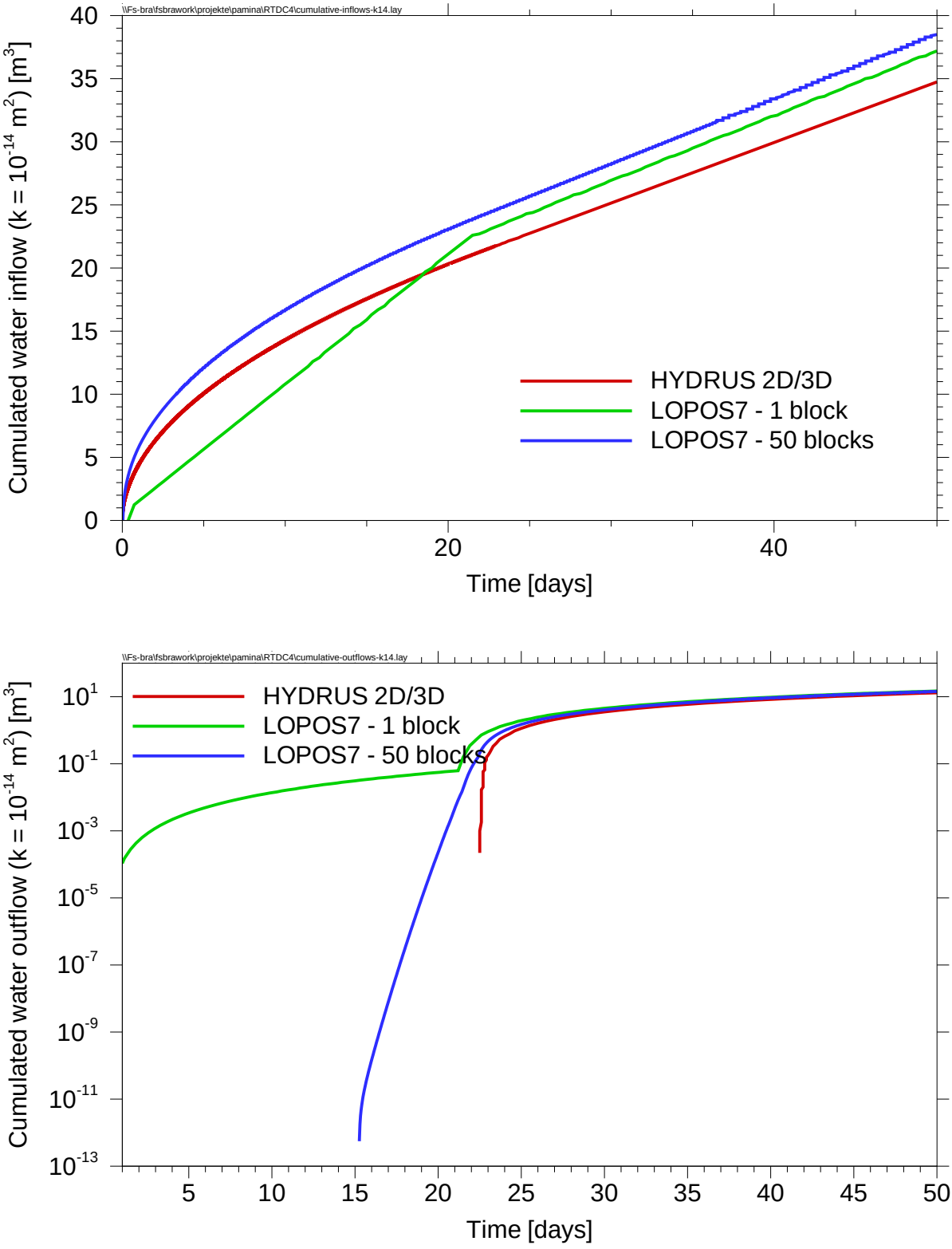

Fig. 3.16: Cumulated water inflow and outflow rates for the high permeability case (LOPOS7 vs. HYDRUS2D/3D).

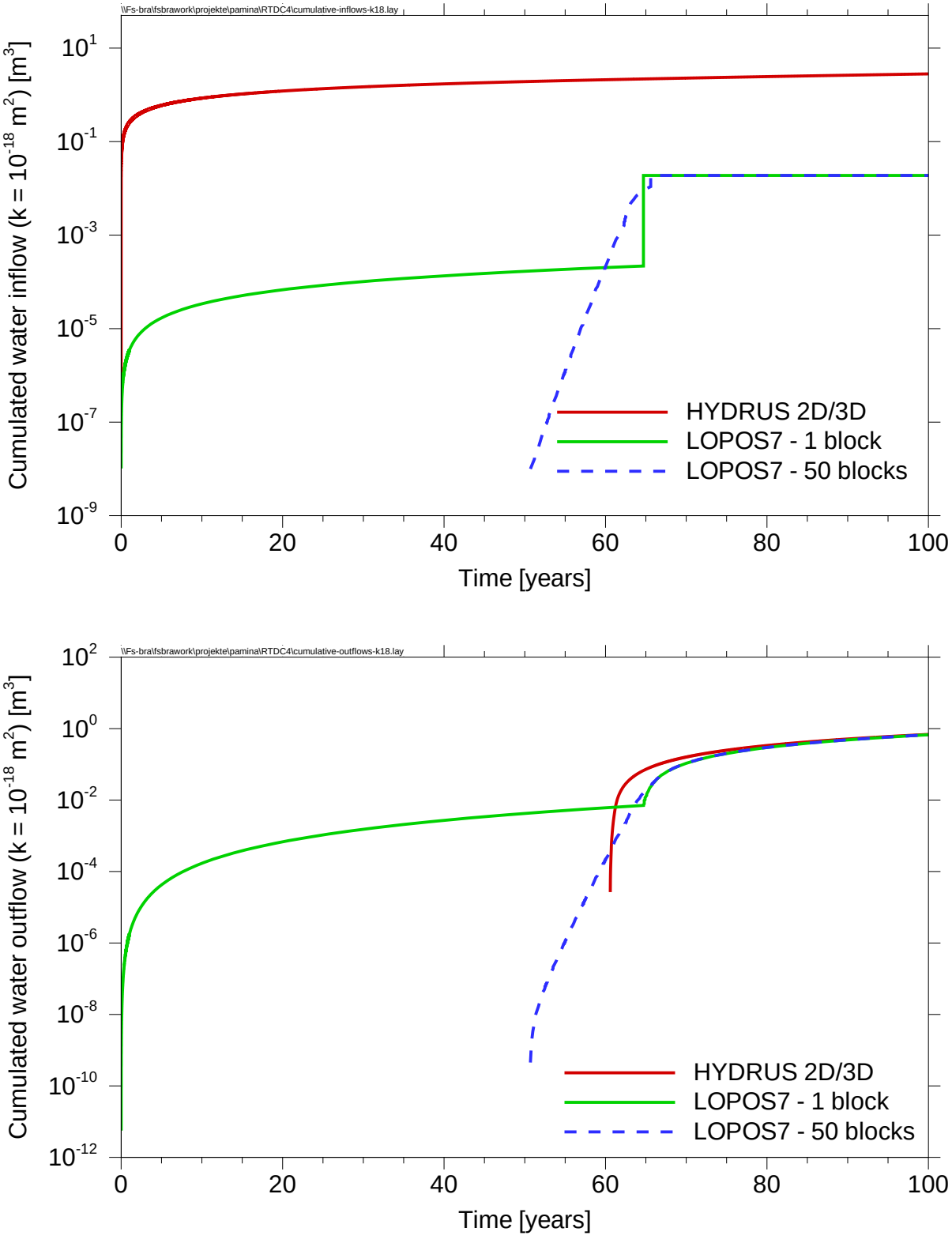

Fig. 3.17: Cumulated water inflow and outflow rates for the low permeability case (LOPOS7 vs. HYDRUS2D/3D).

Preliminary calculations with LOPOS have been performed considering an initially wet gallery, to take into account the residual water content (θ_r = 0.001). For the low permeability case, the results were not very different compared to the case when the residual water content was not taken into account. For the high permeability situation though, significant differences were obtained, especially for the discretized model. The differences might be caused by the fact that, while with HYDRUS model the residual water volume is not free water. With LOPOS the residual water content is considered as free, available to flow water. As a result, outflow starts earlier then in the dry gallery, with a much higher rate (three to five orders in magnitude) as shown in figure 3.18. The residual water volume flows out before the onset of the water inflow from the inner neighbouring block. Then, as more water flows into the block, the pressure starts to rise, and the outflow is re-established. The difference between the early outflows for the two discretization schemes is of about two orders in magnitude.

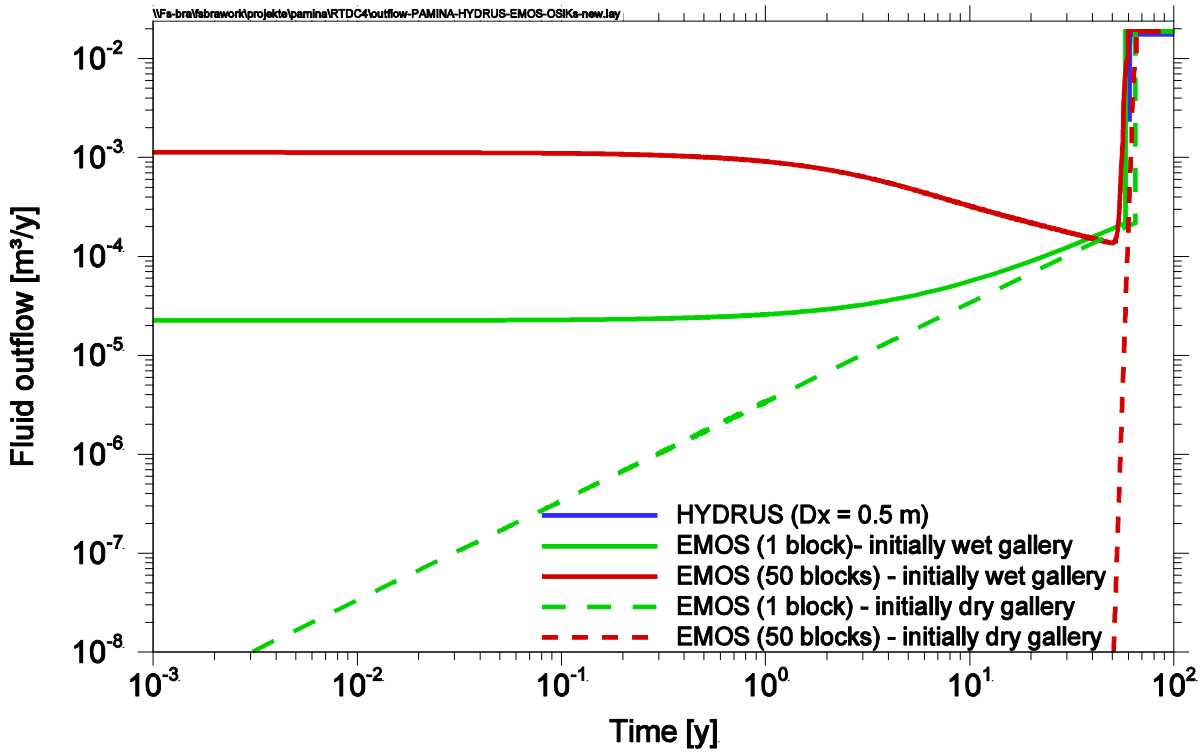

Fig. 3.18: Simulation of the residual water content in the gallery.

3.3.3 Calculations with the PA code REPOS

3.3.3.1 Modelling

REPOS is the near-field module of the version 4 of the PA code package EMOS [6]. It is a predecessor of LOPOS that is discussed in Section 3.3.2. The original EMOS code developed by GRS is extended by NRG/ECN in the past years, mainly with the focus on the modelling of convergence and creep related processes. For the present calculations, the version *ccm2* [4] is used.

As in LOPOS, REPOS is representing a repository by a combination of different segment models. For the segments used in the given benchmark system, the brine flow S_i into a segment i is calculated in REPOS by multiplying the difference of the hydrostatic pressure p on both ends of a segment with the inverse resistance R_{inv}:

$$S_i[m^3/a] = R_{inv}(p_{in} - p_{out}) \qquad 3.11$$

with R_{inv} defined as

$$R_{inv}[m^3/MPa \cdot a] = \frac{A_i}{L_i}\frac{k_i}{\mu} \qquad 3.12$$

and μ indicating the dynamic viscosity of the brine, k_i the permeability (in m^2), L_i the length and A_i the cross-section of a segment i[3].

To correct for the lower resistance of a segment when it is only partially filled, REPOS has the possibility to define a multiplicator that makes REPOS using twice the value of R_{inv} for calculating the transport of brine during the inflow phase.

The system modelled for the test case is a sequence of three segments: a water reservoir (saturated shaft), a dry backfilled drift and an empty gallery, acting as water sink.

For modelling of the test case with REPOS code, a horizontal segment structure has been created, as shown in figure 3.19. The center field segment model *STMF1* has been used to model the brine filled shaft. The backfilled gallery is represented by the *STOVE1* model and for the sink the *ESALG1* model is used.

[3] dependend on the kind of segment, a segment can contain more than one resistance, e.g. a dam and a backfilled area

Fig. 3.19: Segment structure and associated segment models used with REPOS.

In order to assess the effect of spatial discretization on the results; the drift segment has been represented by either one or 50 segments of the *STOVE1* model.

In REPOS, an empty segment can only get flooded when the previous segment is totally filled. This behaviour of REPOS may introduce a small delay of brine transport because the status of a segment must be first change from "inflow" to "full", before in the following time step the inflow in the next cell will be calculated. In case of 50 consecutive segments as in the present benchmark, the delay is cumulating; the error introduced by this behaviour may be as large as 50 times the maximum time step size dt_{max} [4]. To limit the error of the calculated breakthrough times in case of the 50 segment model to less than 1%, dt_{max} values of $5 \cdot 10^{-3}$ days and 0.01 a are necessary (for the high and low permeability cases, respectively). However, such small values of dt_{max} may result in very large numbers of time steps, therefore for the benchmark an adapted scheme for dt_{max} is used. Tab. 3.3 summarized the maximum time step size dt_{max} used for the calculation.

Tab. 3.3 Values of dt_{max} used for the REPOS benchmark calculations

dt_{max}	high permeability case $k=10^{-14}$ m^2	low permeability case $k=10^{-18}$ m^2
1 segment	10^{-4} a	0.1 a
50 segments	10^{-5} a	0.01 a

3.3.3.2 Results

When the heights of the gallery and the effects of unsaturated flow are neglected - as in case of the REPOS model - the breakthrough of brine can be calculated by

$$t_{filled}[a] = \frac{V_{back}}{p_{hydr} \cdot 2R_{inv}} \qquad 3.13$$

With a backfill volume V_{back} of 2.425 m^3, a hydrostatic pressure p_{hydr} of 9.45 MPa and an inverse resistance R_{inv} of 0.0175 m^3/a, the gallery segment should be filled in 69.3 years and 23.0 days for the low and high permeability case, respectively.

[4] the actual time step size may be smaller than dt_{max}, because *REPOS* adapts dynamically the time step sizes

The breakthrough times and outflow rates calculated by REPOS (Tab. 3.4) are very close to the values derived with equations 3.13 and 3.11. The minor deviations found are less than 0.5% and are irrelevant for practical purposes.

Tab. 3.4 Breakthrough times and outflow rate calculated by REPOS

model	high permeability $k=1\cdot10^{-14}$ m^2		low permeability $k=5\cdot10^{-19}$ m^2	
	breakthrough time	outflow rate	breakthrough time	outflow rate
REPOS, 1 segment	23.0 days	0.0175 m^3/a	69.3 a	175 m^3/a
REPOS, 50 segments	23.0 days	0.0175 m^3/a	69.5 a	175 m^3/a
analytical	23.0 days	0.0175 m^3/a	69.3 a	175 m^3/a
HYDRUS2D	22.6 days		60.6 a	

Figure 3.20 shows the evolution in time of the amounts of brine in the gallery and the brine saturated porosities for the single segment models of the high and low permeability cases. The amount of brine increases linear in time, due to the constant resistance of the segment models in the inflow phase. Figure 3.21 shows the outflow rate of brine from the gallery and the hydrostatic pressure in the gallery on a *log-log* scale as calculated by REPOS. For the segment model used for the gallery, a hydrostatic pressure is - unlike in LOPOS - only attributed to the segment when it is saturated with brine. Consequently, no outflow out of the segment occurs before the segment is fully saturated, too.

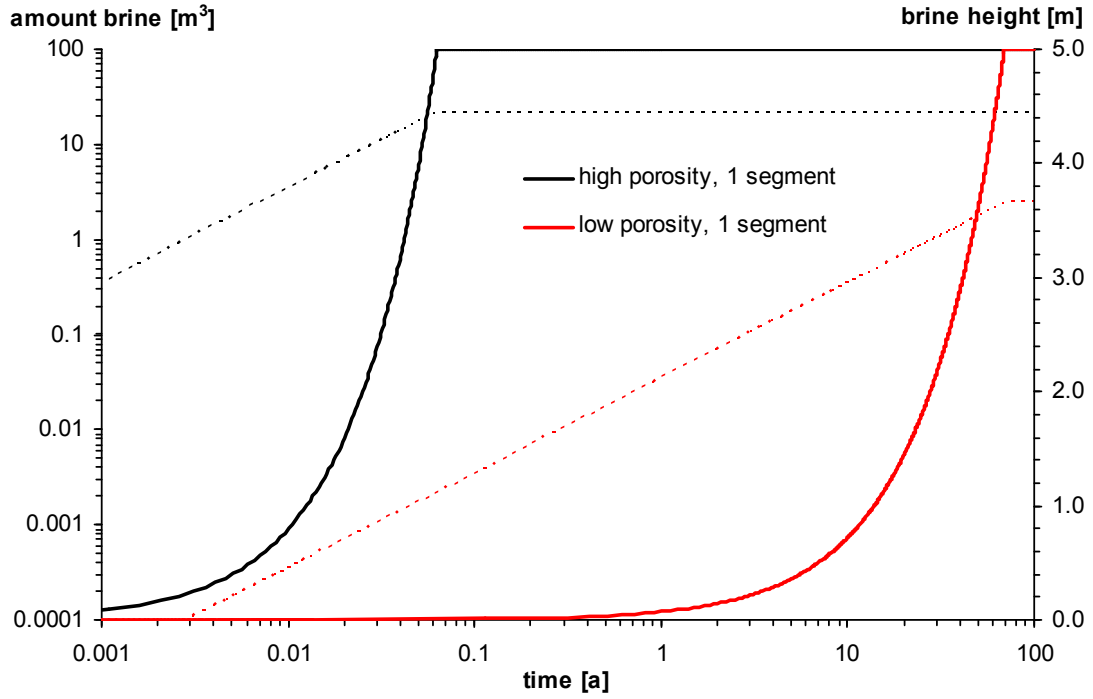

Fig. 3.20 Amount of brine in a gallery (solid line) and saturated porosity in the gallery (dotted line) as calculated by REPOS

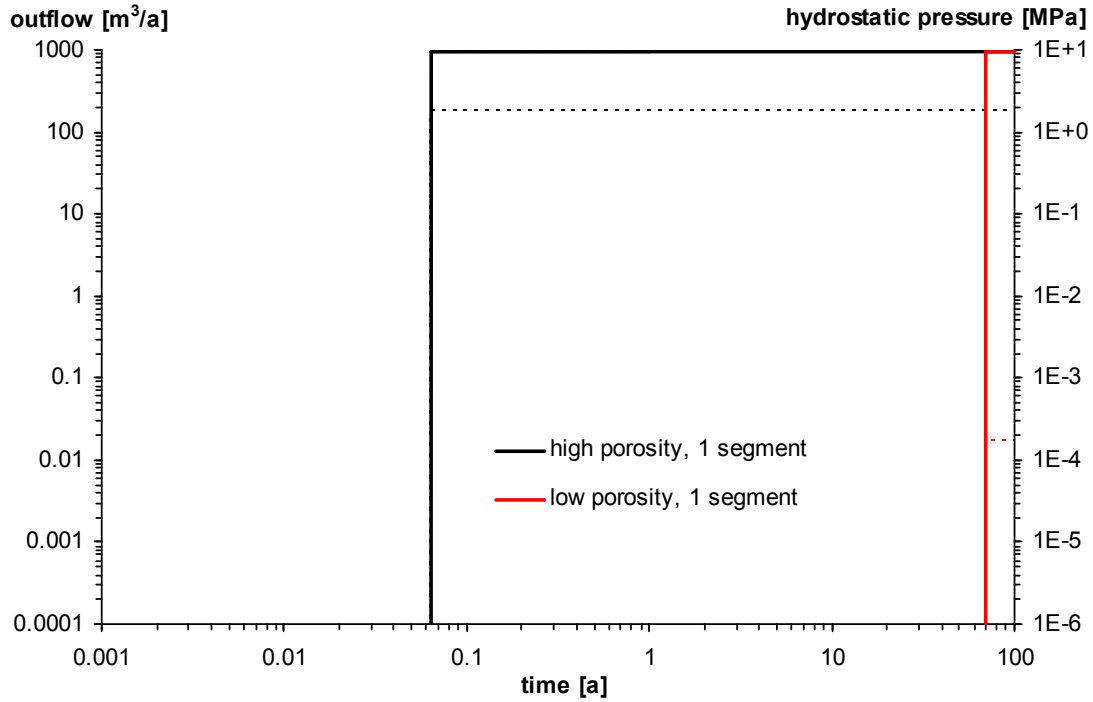

Fig. 3.21 Outflow rate of brine from the gallery (dotted line) and hydrostatic pressure in the gallery (solid line) as calculated by REPOS

Figures 3.22 to 3.25 show the time evolution of the inflow and outflow rates for both cases. In Figures 3.22 and 3.24, for the single segment models it can be seen that the inflow rate decrease by a factor of two as soon as a segment is filled and R_{inv} is set back to its original value. In case of the 50 segment models, the flow diminishes with every additional segment that is hydraulically coupled to the shaft. Note that the steps in figure 3.24 at early times are less steep than in 3.15 due to the larger time step size chosen (see also Tab. 3.3). The outflow rates in figures 3.23 and 3.25 shows, that - unlike in LOPOS - in REPOS no outflow from a segment occurs as long as it is not saturated with brine.

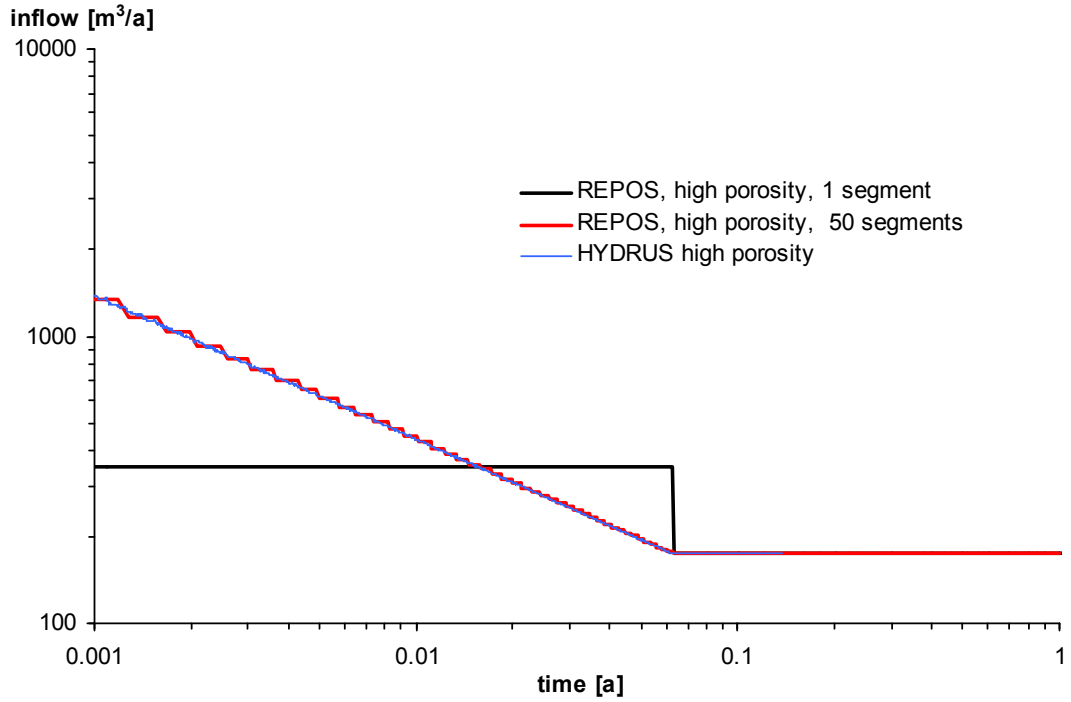

Fig. 3.22 Inflow rate of brine to the gallery for the high porosity case ($k=10^{-14}$ m^2) as calculated by REPOS

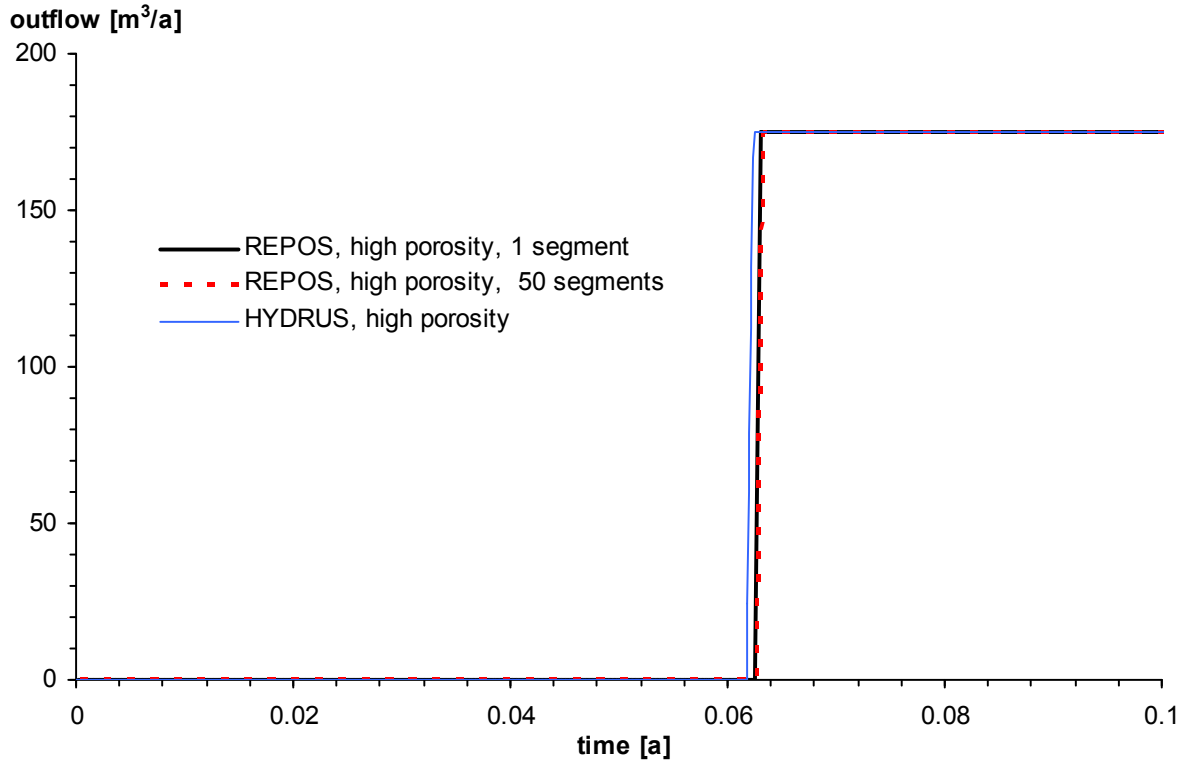

Fig. 3.23 Outflow rate of brine from the gallery for the high porosity case ($k=10^{-14}$ m^2) as calculated by REPOS and HYDRUS

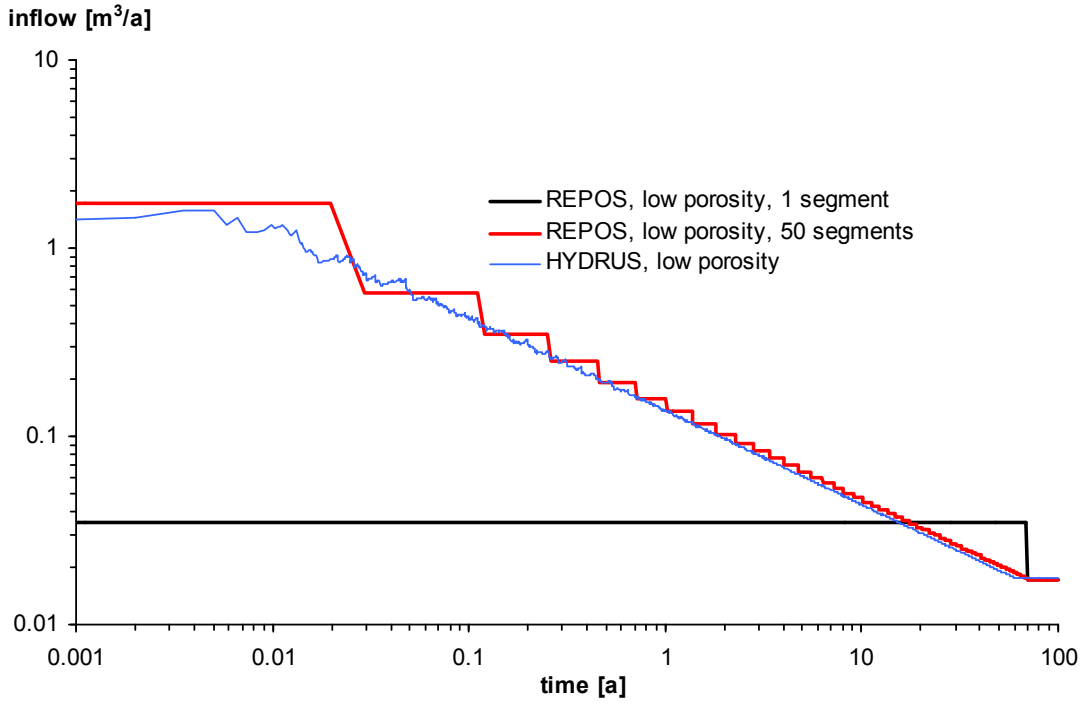

Fig. 3.24 Inflow rate of brine to the gallery for the low porosity case ($k=10^{-18}$ m^2) as calculated by REPOS

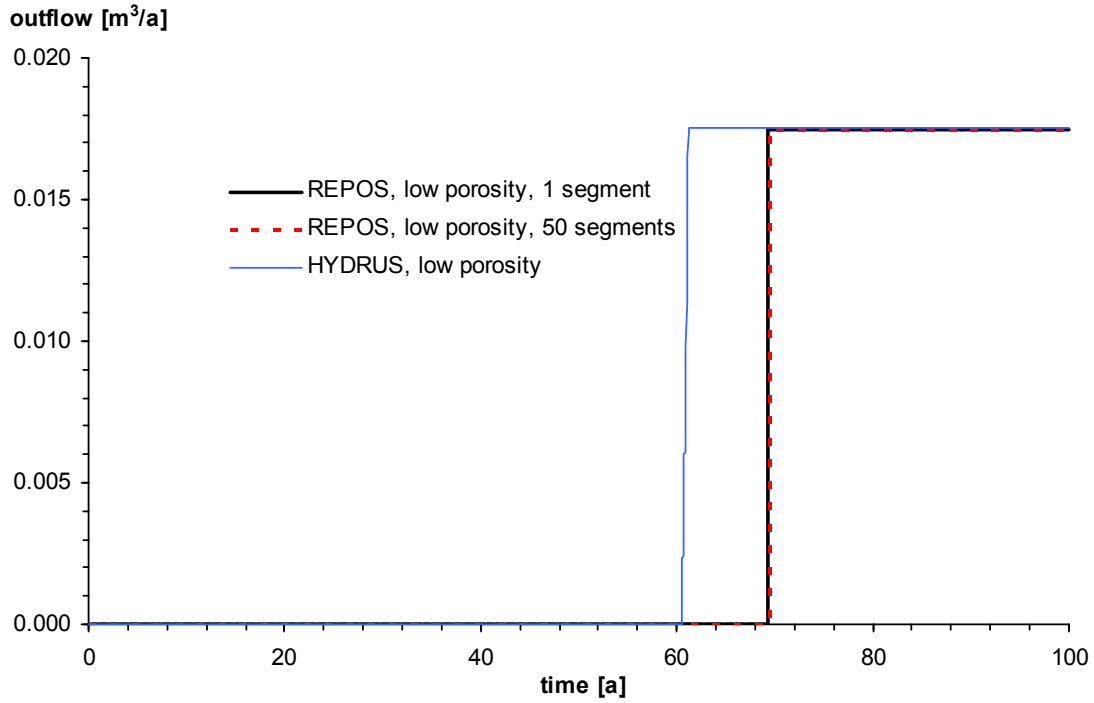

Fig. 3.25 Outflow rate of brine from the gallery for the low porosity case ($k=10^{-18}$ m^2) as calculated by REPOS

Figures 3.26 to 3.29 show the time evolution of the cumulative inflow and outflow rates for both cases. For the cumulative flows, the results of the REPOS and HYDRUS2D calculations are very close together, and the small differences found can be attributed to the differences in breakthrough times as discussed before (the flow rates are virtually the same - see Tab. 3.4).

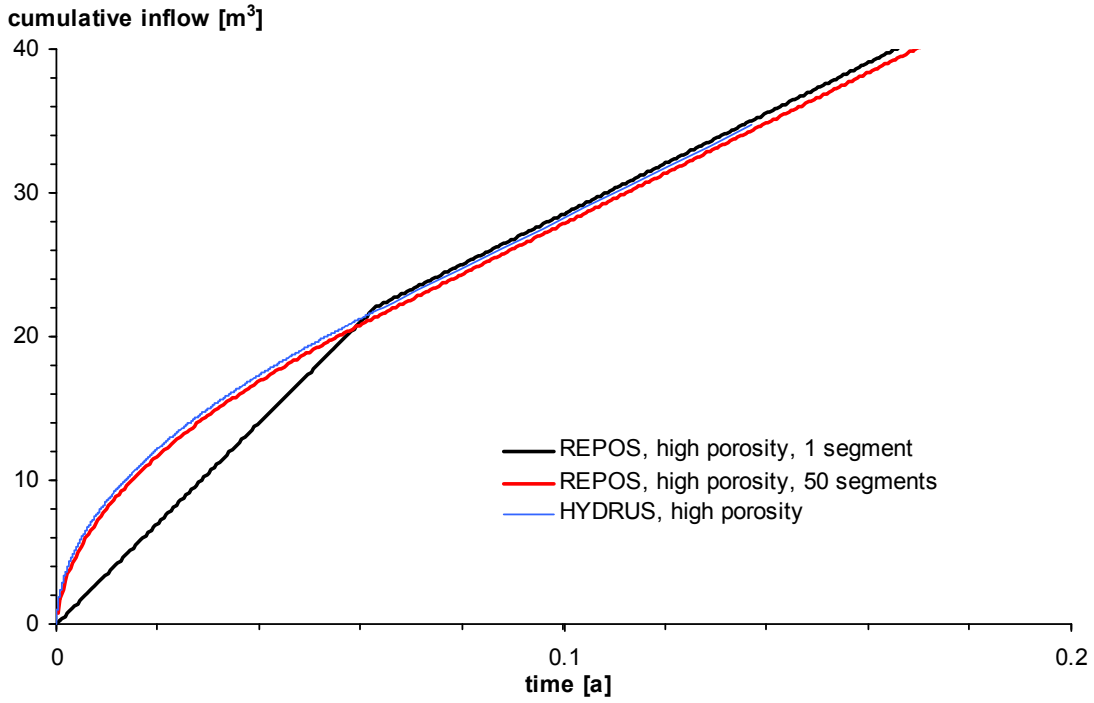

Fig. 3.26 Cumulative inflow of brine into the gallery for the high porosity case ($k=10^{-14}$ m^2) as calculated by REPOS and HYDRUS

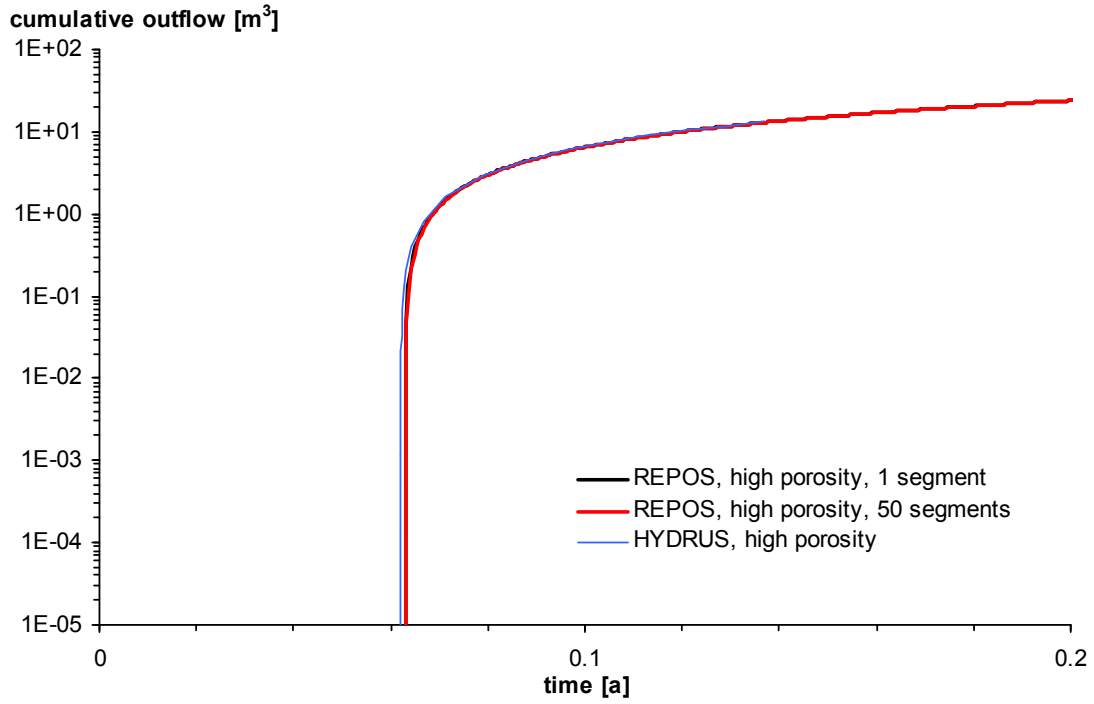

Fig. 3.27 Cumulative outflow of brine from the gallery for the high porosity case ($k=10^{-14}$ m^2) as calculated by REPOS and HYDRUS

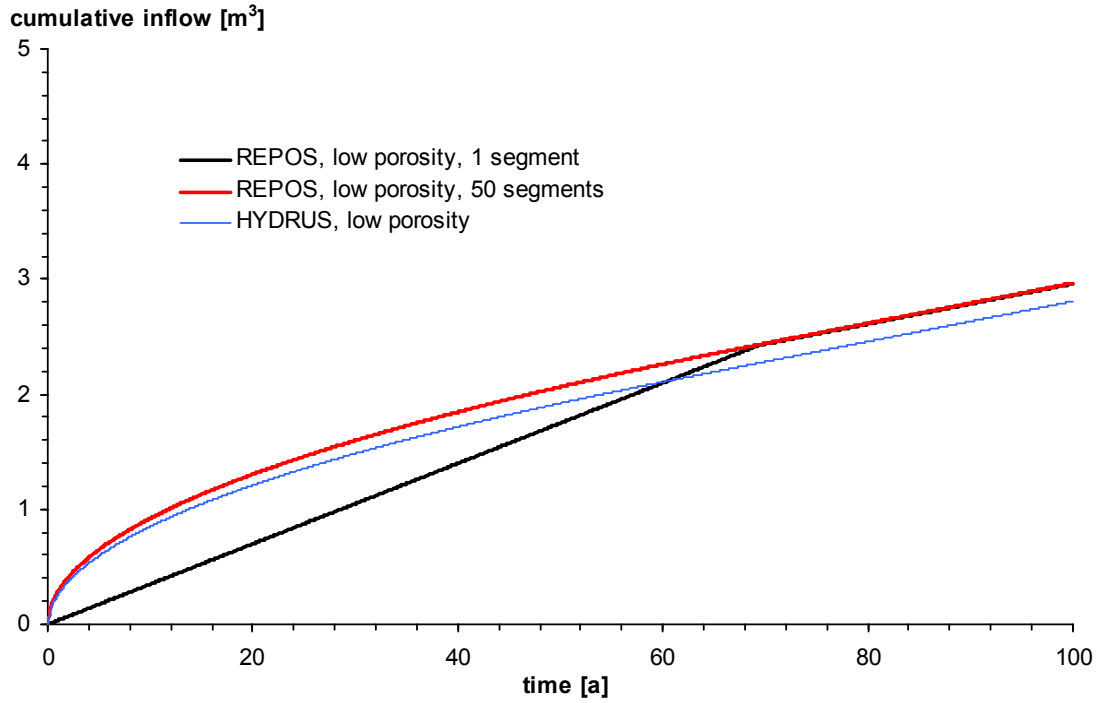

Fig. 3.28 Outflow Cumulative inflow of brine into the gallery for the low porosity case ($k=10^{-18}$ m^2) as calculated by REPOS and HYDRUS

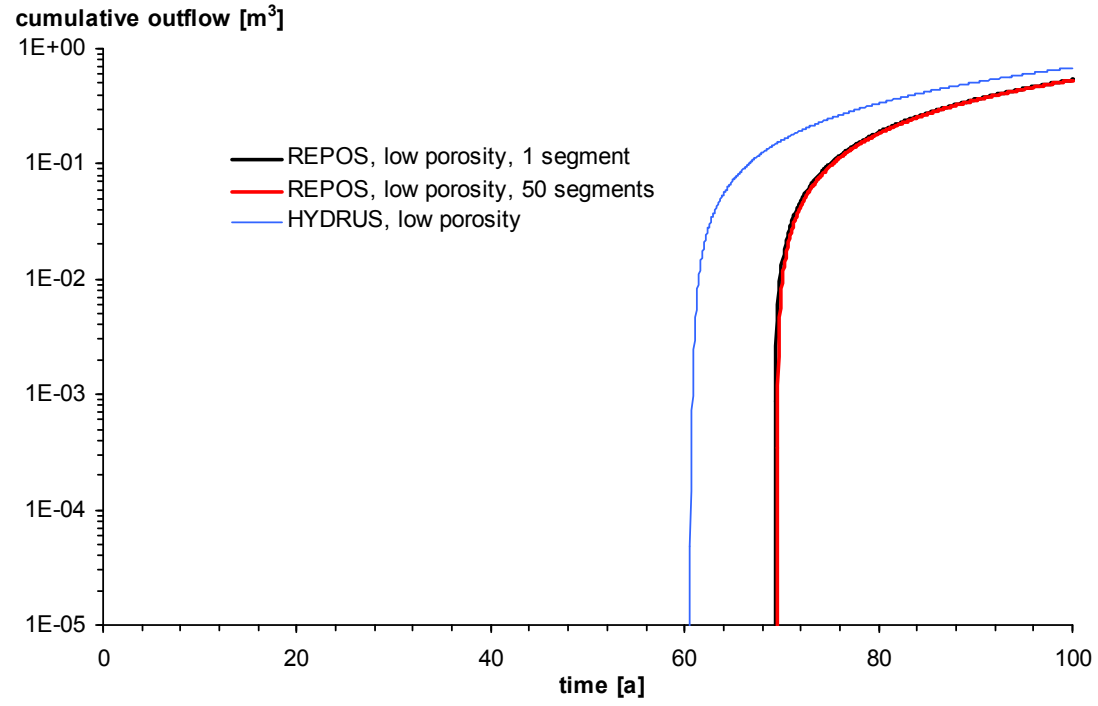

Fig. 3.29 Cumulative outflow of brine from the gallery for the low porosity case ($k=10^{-18}$ m^2) as calculated by REPOS and HYDRUS

3.4 Comparison of results and conclusions

The benchmark exercise is aimed to compare the agreement between a code specialized for modelling two-, or –three-dimensional unsaturated flow (HYDRUS) and a performance assessment one-dimensional code (near-field module LOPOS and REPOS of different versions of the EMOS code). PA codes are generally designed to model features and events that develop over large timescales, while specialized codes may grasp more precisely phenomena that develop over shorter time intervals.

3.4.1 HYDRUS and LOPOS

There is a good agreement between the results obtained for the Test Case with HYDRUS and LOPOS codes. A slight discrepancy can be observed in the inflow rate calculations. At very early times – up to 10^{-2} years, LOPOS results (for the discretized variant) are slightly higher compared to HYDRUS, of around 30% for PAMINA 2 calculations, and 23% for PAMINA 1, respectively. After that time, the discrepancies are strongly reduced, to only 6-7%. The difference is due the size of the initial constant time steps used in LOPOS (100 time steps of 0.001 years), and it is reduced when the code is adjusting the time mesh size. Since LOPOS is dedicated for calculations of saturated water and contaminant transport, it is using the hydraulic conductivity (i.e., the inverse resistance) of the saturated domain. As a result, the flow calculated with LOPOS is faster. The difference in the inflow rates calculated with LOPOS and HYDRUS is diminishing in time, due to the increase of the water content and, consequently of the hydraulic conductivity of the simulated domain. Nevertheless, both codes show very good agreement regarding the times of complete filling of the drift.

The agreement between the two codes is good for the outflow rates (6 to 7% higher outflow rates obtained with the PA code LOPOS7), despite the fact that LOPOS7 code cannot simulate accurately the residual water content. For this reason, this feature was not captured with the models used for the calculations. Nevertheless, if the modelled environment has a very low residual water content, such as rock salt, the differences in the results are negligible. Both codes simulate breakthrough of water through the saturated height of the right boundary (i.e., water can flow out of the domain through the seepage face).

The discretization has an important effect on the results, and this is more obvious in the inflow rates. The calculated outflow rates are influenced by discretization: for the high permeability domain a finer discretization offers more accurate results (compared with HYDRUS outcome).

In conclusion, LOPOS PA code complies with the expectancy when compared with a process-level code for processes developing within relatively short timeframes (up to tens of years).

3.4.2 REPOS and HYDRUS

Comparison of the breakthrough times calculated with REPOS and HYDRUS (Tab. 3.4) shows that neglecting the effects of the unsaturated flow, the two dimensional extent of the gallery and the diffusion/dispersion results in an overestimation of the travel time in REPOS of about 11% for the low permeability case and less than 2% in the high permeability case. The inflow rate for the high permeability case from the REPOS calculations with 50 segments in figure 3.22 is very close to the results gained with HYDRUS (figure 3.14). The inflow rate for the low permeability case (figure 3.24) is also quite comparable to the results gained with HYDRUS (figure 3.15). It should be noted that the large inflow rates in the beginning of the calculation are not that relevant as they appear on the *log-log* scale.

The simplified segment model used in REPOS is - compared to the complex numerical simulations performed with HYDRUS - resulting in sufficient precise results for practical purposes. The results of the benchmark do therefore not show the necessity for a code improvement.

3.4.3 REPOS and LOPOS

The LOPOS outflow rates are slightly higher then the corresponding REPOS results, but the difference does not exceed 10%. By enhancing the flow resistance (that controls the flow rates) as long as a segment is not completely filled, REPOS could calculate the expected breakthrough time accurately. LOPOS calculates resistance to flow as for a fully saturated domain. The different approach LOPOS uses, enables it to take the flow of water through a seepage boundary into account. This feature in LOPOS allows water to flow out during the filling of a segment, while in the segment model used in REPOS, outflow only can occur after complete filling of the simulated domain. These different approaches explain partially the differences between the results of LOPOS and REPOS. The LOPOS code uses the resistance to flow corresponding to the saturated conditions, which gives higher water flow rates and earlier breakthrough times.

3.4.4 Conclusion

The comparison of the segment based PA codes REPOS and LOPOS and the finite element based code HYDRUS shows a considerable degree of agreement for all four benchmark cases. The differences between the PA code and the finite element code are less than 20% in all cases and can be attributed for the major part to the neglect of the unsaturated flow by the two PA codes. Although the PA codes underestimate the breakthrough times, the results are sufficiently precise for practical purposes.

The use of 50 segments in the PA codes delivers for REPOS no advantage against the use of a single segment but can introduce some extra delay to the transport of brine. This extra delay can - however - be limited to irrelevant small numbers by the choice of proper maximum times step sizes.

As for LOPOS, discretization adds also a delay to the transport of brine. The discretized model gives a better fit of the breakthrough time by progressively increasing the inverse resistance to flow, as new flooded segments join to the flow system.

Although there is a very good agreement between results obtained with LOPOS and HYDRUS codes, in order to improve the accuracy of the results, LOPOS code could be modified to appropriately take into account the variation of the hydraulic conductivity during the inflow phase.

3.5 References

[1] Buhmann, D.: Das Programmpaket EMOS. Ein Instrumentarium zur Analyse der Langzeitsicherheit von Endlagern. Gesellschaft für Anlagen- und Reaktorsicherheit (GRS) mbH, GRS-159, Braunschweig, Juli 1999.

[2] Hirsekorn, R.-P.; Boese, B.; Buhmann, D.: LOPOS: Programm zur Berechnung der Schadstofffreisetzung aus netzwerkartigen Grubengebäuden. Gesellschaft für Anlagen- und Reaktorsicherheit (GRS) mbH, GRS-157, Braunschweig, 1999.

[3] Müller-Lyda, I.; Birthler, H.; Fein, E.: Ableitung von Permeabilitäts-Porositätsrelationen für Salzgrus, Gesellschaft für Anlagen- und Reaktorsicherheit (GRS) mbH, GRS-148, Braunschweig, 1999.

[4] Schröder, T.J., EMOS versie ccm2 voor PAMINA WP2.1D: aanpassingen van de porositeit-permeabiliteit relatie en de compactiesnelheid in EMOS ccm1. NRG Note 2.1952.21/08.89397, Petten, 4 June 2008

[5] Šimůnek, J.; van Genuchten, M. Th.; Šejna, M.: The HYDRUS Software Package for Simulating the Two- and Three-Dimensional Movement of Water, Heat, and Multiple Solutes in Variably-Saturated Media, Technical Manual, March 2006.

[6] Storck, R., D. Buhmann, R.P. Hirsekorn, A. Nies, and H. Rausch. EMOS: Programmpaket zur Langzeitsicherheitsanalyse eines Endlagers für radioaktive Abfälle - Version 4. GSF-Bericht /90, TL/90, September, 1990

4. Benchmark on convective flow

4.1 Introduction

After the emplacement of radioactive waste canisters in a repository in salt, the waste chambers or boreholes as well as the galleries may successively be backfilled with salt grit as part of the closure procedure. After backfilling of the all excavated volumes and backfilling and sealing of the shafts the repository will be closed.

One aspect that is important in a repository in salt is that after backfilling of the drifts, boreholes, and chambers the remaining void volume will decrease over time due to the convergence process of the surrounding rock salt. In a normal evolution, in general, all open volumes will close and compactable material, such as salt grit, will be compressed and become impermeable at a certain point in time. This provides for the long-term isolation of the waste from our environment, since no medium is present that could mobilize and transport radionuclides from the waste forms to the geosphere.

An important altered evolution scenario that has to be considered in the performance assessment of a repository in rock salt assumes the intrusion of brine into the repository and the subsequent corrosion of waste packages and the leaching of radionuclides into the brine. Because of the creep of the rock salt and the associated convergence of the brine filled volumes, the brine carrying the radionuclides will gradually be squeezed out of the salt formation and pressed into the overburden.

Because the creep of rock salt under hydrostatic conditions is relatively slow, other transport processes for the contamination in the brine can be relevant. One of these processes is the density gradient driven exchange of fluids in adjacent open volumes that are connected by e.g. a gallery. In case, for example, the density of brine in heated sections of the facility (due to heat generating waste) is decreased due to thermal expansion, a density difference may arise between brine in the heated section and in a non-heated section. Density differences may also arise from the chemical interaction between brine and the materials that may be used to immobilize the waste, such as cement. Such density differences may lead to convective, density-driven exchange flows that have the potential to carry radionuclides throughout the different sections of a repository. In some cases the density-driven exchange flows can be more effective than advective transport of contamination.

In a salt-based repository for radioactive waste buoyancy-driven flows between two volumes (e.g. a waste chamber and a shaft) may in general only occur if cement is used for the immobilization of the radioactive waste [8]. Upon the intrusion of brine into the waste chamber, an ionic exchange reaction between the brine and the cement may occur, and change the chemical composition of the brine. This may affect the brine density. Depending on various conditions, such as composition of the intruding brine, type of cement, other materials in the waste, the density of the brine may increase or decrease. For this study it has been assumed that the brine density decreases as a result of the reaction with the waste. The resulting den-

sity difference between the two considered volumes that can be connected by a gallery or a shaft can be a driving force for a free convective flow [8]. This situation is schematically depicted in Fig. 4.1.

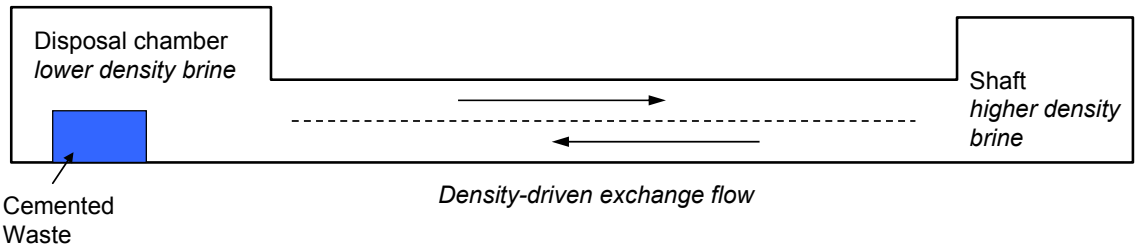

Fig. 4.1 Density-driven exchange flow of brine through a gallery

In Fig. 4.1 the dashed line in the gallery represents the interface between lighter and heavier brine. The lower density brine flows counter-currently on top of the higher density brine. This flow pattern, where two fluid layers are flowing more or less horizontally on top of each other, is named a 'stratified flow'. Because of the density difference between the two brine layers, vertical flows are suppressed in the vicinity of the interface between the high- and low-density brine. The buoyancy will prevent brine moving from one 'stratum' to the other.

This benchmark exercise aims to compare the results from PA codes and a more complex code like PORFLOW to validate the applicability of the models for density-driven exchange flows that are implemented in the PA codes.

4.2 Benchmark tests

4.2.1 Geometry

The test case comprises a backfilled gallery (grey) with an adjacent disposal chamber at its left side (green), and a volume modelling a shaft on the right (blue).

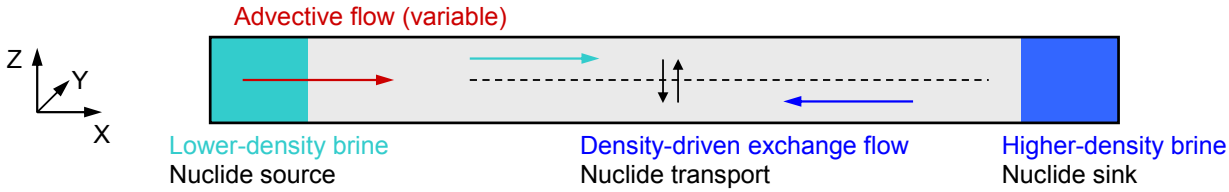

Fig. 4.2: Test case for investigating the radionuclide transport by density-driven exchange

The disposal chamber on the left side has the following characteristics (see also 4.5):

- The density of the converted brine is constant and at the **lower** value (1274 kg/m^3)

- The disposal chamber releases 3 different nuclides with distinct values of the effective diffusion coefficient but otherwise have the same and constant properties. The concentration C_i of the nuclides is set at a constant value of 100 Bq/m^3.

- The disposal chamber acts as a source of low-density brine so that, in addition to the density-driven exchange flow, different values of an advective flow from left to right are established (see also below).

The back-filled gallery is characterised by constant values of the porosity *n*, the permeability *k* and complete brine saturation, as given in 4.5. It is assumed that the nuclides do not adsorb on the salt grit backfill.

The shaft on the right side has the following characteristics (see also 4.5):

- The density of the fresh brine is constant and at the **higher** value (1300 kg/m^3);

- The shaft is a sink volume for both the advective flow and the 3 different nuclides that are released in the waste chamber.

4.2.2 Advective flow rates

Based on 4.1 and the parameter values in the following 4.5 the value of the density-driven exchange flow in the absence of an addiiotnal advective flow is estimated as $Q_{exchange,0}$ = 2,19·10^{-7} m^3/s (6,93 m^3/yr). In the benchmark exercise the values of the advective flow rate have been imposed as a source of brine in the disposal chamber, taking into account that $Q_{advective} = n * Q_{exchange,0}$, with n = 1,2,3,4. By imposing these discrete values of the advective flow rate of brine, additional to the density-driven exchange flow, it can be established when the density-driven exchange flow is counteracted by the advective flow, and how the transport of nuclides with different values of the diffusion coefficient is affected.

4.2.3 Modelling aspects

Since the involved processes are slow the test case will only consider **stationary** conditions. For the horizontal case that is considered here the main flows will occur between the disposal chamber and the shaft, and variations of the nuclide concentrations are anticipated to occur primarily in the XZ-plane (cf. Fig. 4.2). Therefore the test case will be solved for a **2D** geometry.

4.2.4 Parameter values

An overview of the numerical values of the different input parameters is given in table 4.5.

Tab. 4.5: Overview of model parameters

Section	Symbol	Value	Comments
Brine			
Dynamic viscosity	μ	$1{,}5 \cdot 10^{-3}$ Pa s	
Density - Higher value (“ fresh” brine - Lower value (“converted” brine) Density difference	 ρ $\Delta\rho$	 1300 kg/m^3 1274 kg/m^3 26 kg/m^3 (2%)	
Gallery			
Length	L	30 m	
Width	W	4 m	
Height	H	4 m	
Diffusion coefficient of nuclide *1*	D_1	$3{,}0 \cdot 10^{-10}$ m^2/s	0,00947 m^2/y
Diffusion coefficient of nuclide *2*	D_2	$3{,}0 \cdot 10^{-9}$ m^2/s	0,0947 m^2/y
Diffusion coefficient of nuclide *3*	D_3	$3{,}0 \cdot 10^{-8}$ m^2/s	0,947 m^2/y
Partition coefficient of nuclides	k_D	0.0 m^3/s	No adsorption
Backfill material (Salt grit)			
Porosity	n	0,35	Constant value, no convergence
Permeability[1]	k	$4{,}84 \cdot 10^{-12}$ m^2	
Density	ρ_{salt}	2200 kg/m^3	
Disposal Chamber			
Constant lower density value of brine	ρ	1274 kg/m^3	
Constant concentrations of nuclides *1, 2, 3*	C_1, C_2, C_3	100 Bq/m^3	
Imposed advective flow rates			Source
$Q_{advective} = 0 * Q_{exchange}$		0,0 m^3/s	0,0 m^3/yr
$Q_{advective} = 1 * Q_{exchange}$		$2{,}19 \cdot 10^{-7}$ m^3/s	6,93 m^3/yr
$Q_{advective} = 2 * Q_{exchange}$		$4{,}39 \cdot 10^{-7}$ m^3/s	13,9 m^3/yr
$Q_{advective} = 3 * Q_{exchange}$		$6{,}58 \cdot 10^{-7}$ m^3/s	20,8 m^3/yr
$Q_{advective} = 4 * Q_{exchange}$		$8{,}78 \cdot 10^{-7}$ m^3/s	27,7 m^3/yr
Shaft			
Constant higher density value of brine	ρ	1300 kg/m^3	
Constant concentrations of nuclides *1, 2, 3*	C_1, C_2, C_3	0.0 Bq/m^3	Sink
Sink for the advective flow rates, imposed in the “Disposal Chamber”			

[1] Calculated with the relation $3{,}90 \cdot 10^{-10} \cdot n^{4{,}18}$

4.2.5 *Output values*

The following **steady-state** output values are of interest in the benchmark (see also Fig. 4.3) and are used for comparison of the result of the different models:

- The nuclide concentrations C_1, C_2, C_3 along the Z-axis in the centre of the gallery at 7,5 m, 15 m (middle of the gallery), and 22,5 m;
- The pressure distribution along the Z-axis in the centre of the gallery at at 7,5 m, 15 m (middle of the gallery), and 22,5 m;
- The Darcy velocity distribution along the Z-axis in the centre of the gallery at at 7,5 m, 15 m (middle of the gallery), and 22,5 m;
- The total brine flow rate $Q_{advective}$ + $Q_{exchange}$ along the Z-axis in the centre of the gallery at at 7,5 m, 15 m (middle of the gallery), and 22,5 m;
- The net exchange flow rate due to the density-driven exchange $Q_{exchange}$ along the Z-axis in the centre of the gallery at at 7,5 m, 15 m (middle of the gallery), and 22,5 m;
- The acitivity flux (Bq/a) of the nuclides at the exit of the gallery.

and optionally (cf. Fig. 4.4):

- The concentration profiles of the three nuclides in the XZ-plane of the gallery;
- The velocity vectors in the XZ-plane of the gallery.

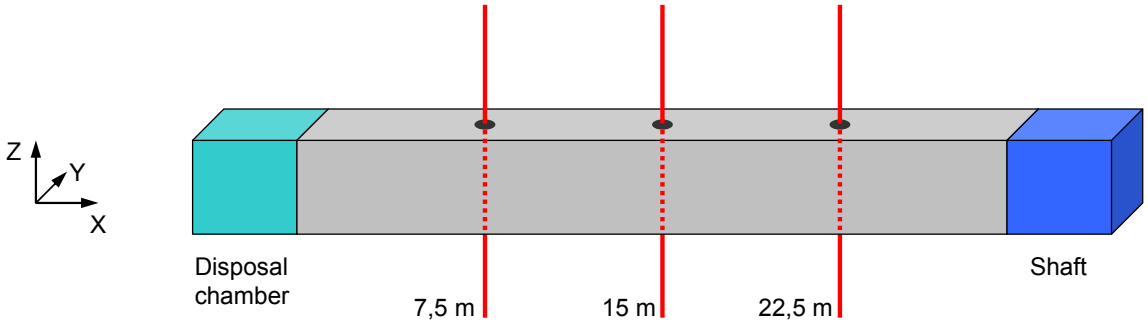

Fig. 4.3: Location of the Z-axis in the centre of the gallery at different distances from the disposal chamber

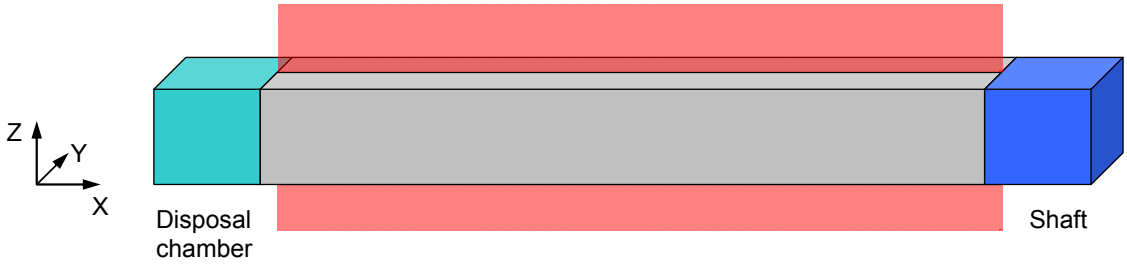

Fig. 4.4: Location of the XZ-cross-section in the centre of the gallery

4.3 Description of the models

4.3.1 Extended analytical model

The buoyancy-driven flow between two volumes at different elevations that are connected by a gallery that may be inclined is illustrated in figure 4.5. In this case it is supposed that the lower (left) volume represents a waste chamber which is partially filled with cemented waste containers. As a result of the corrosion of cement by Mg-rich Q-brine, the Q-brine in the waste chamber is converted into the lower-density Mg-depleted C-brine. The lower-density fluid is then transported by natural convection from the lower chamber to the upper chamber. If the upper volume or chamber contains or is connected to a source of higher-density fluid, an exchange flow pattern can develop as indicated in figure 4.5.

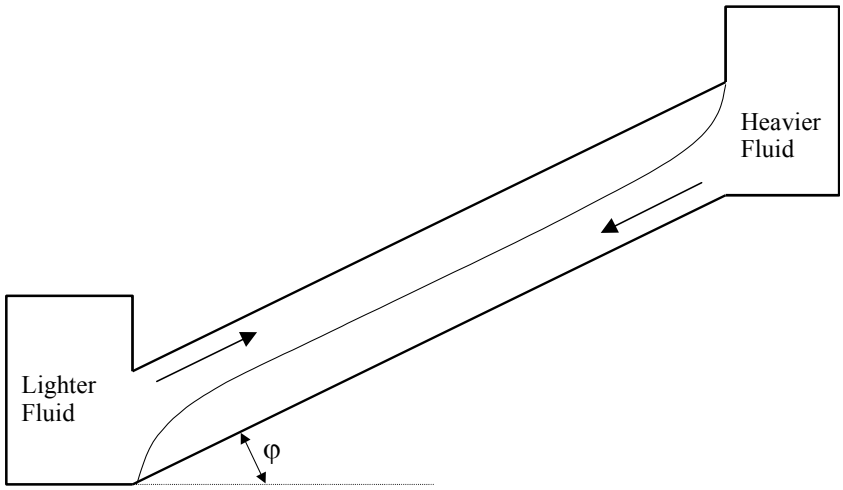

Fig. 4.5: Density-driven flow in a gallery

For the exchange flow in respectively the lower part ($Q_{ex.bottom}$) and the upper part ($Q_{ex.top}$) of a horizontal gallery the following equations apply:

$$Q_{ex,bottom} = -\frac{WkH_{gal}^{2} g \cdot (\rho_r - \rho_\ell)}{8\mu L} \quad \text{with } \rho_\ell < \rho_r \qquad 4.1$$

$$Q_{ex,top} = +\frac{WkH_{gal}^2 g \cdot (\rho_r - \rho_\ell)}{8\mu L} \quad \text{with } \rho\ell < \rho r \qquad 4.2$$

where:

W	(m)	width of a gallery
H_{gal}	(m)	height of a gallery
g	(m/s^2)	gravity constant
ρ_ℓ	(kg/m^3)	density of low-density fluid
ρ_r	(kg/m^3)	density of high-density fluid
k	(m^2)	permeability
μ	(Pa·s)	dynamic viscosity of the fluid
L	(m)	length of the gallery

An important feature of rock salt as a host rock for a repository is the plastic behaviour of the material. Induced by the pressure of the surrounding rock, openings in salt rock tend to converge. This means that rock salt has the ability to seal the waste containers from its surroundings. In addition, the convergence of rock salt induces a volume decrease of excavated chambers. When these chambers are filled with brine, the convergence process may act as a driving force to squeeze out the brine from the chambers. For the situation considered in the present report of an already present buoyancy-driven exchange flow, the additional advective flow can partially counteract the exchange flow. Taking that into account the advective flow may become so large that the density-driven exchange flow is suppressed completely.

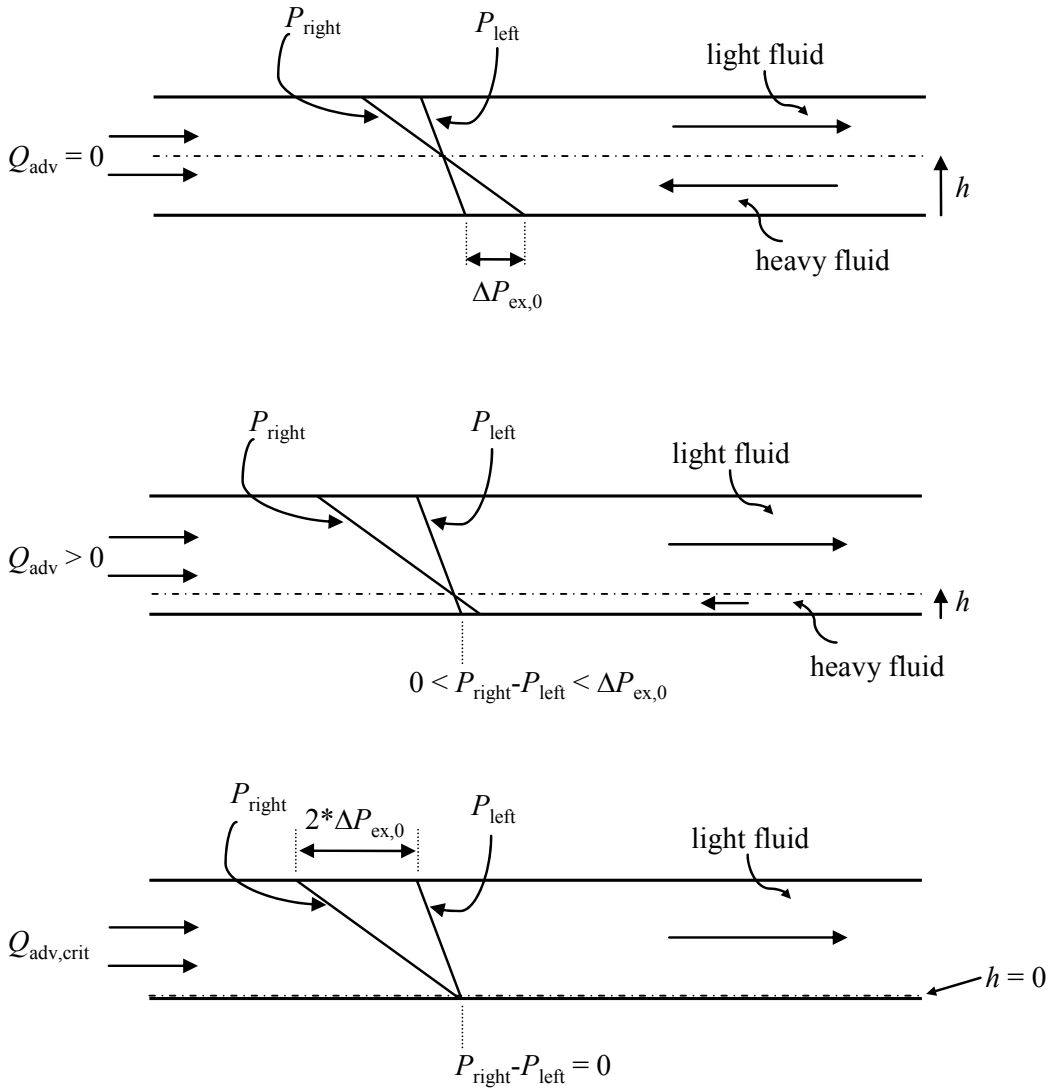

Fig. 4.6: Pressure distribution in a horizontal gallery - top: no advective flow; middle: advective flow of light fluid reduces density-driven exchange flow of heavy fluid; bottom: advective flow of light fluid counteracts density-driven exchange flow of heavy fluid

The effects of an advective flow of low-density fluid on a buoyancy-driven flow has been indicated schematically in figure 4.6. It changes the pressure distribution amongst the height of the gallery and it affects the locus of the height h in the gallery of the dividing line between the lower-density fluid in the upper part and the higher-density fluid in the lower part of the gallery. The pressure gradient $\Delta P_{ex,0}$ determines the magnitude of the velocity, and therefore the buoyancy-driven exchange flow, in the upper and lower parts of the gallery.

It was derived in [5] that the locus of the dividing line between the lower-density fluid and the higher-density fluid can be obtained from:

$$h = 0.5H_{gal} * (1 - |\Delta P_{adv}| / (2 * \Delta P_{ex,0})) \quad 4.3$$

which can be converted to:

$$h = 0.5H_{gal} * (1 - |Q_{adv}| / (4Q_{ex,0})) \quad 4.4$$

The exchange flow rate $Q_{ex,0}$ in the absence of an advective flow rate can be calculated with equation 4.1. From equation 4.4 it follows that for Q_{adv} = 0, h = 0.5H_{gal} and the buoyancy-driven exchange flow has a maximum flow area available, which implies that in that case Q_{ex} has its maximum value. On the other hand, for Q_{adv} = 4*$Q_{ex,0}$, h = 0 and the buoyancy-driven exchange flow of high-density fluid on the bottom of the gallery is completely suppressed by the low-density advective flow.

The assumptions made in the present section have been validated with PORFLOW simulations for the cases of fully developed density-driven exchange flows and additional advective flows in a horizontal gallery.

4.3.2 PORFLOW Model

This section describes the PORFLOW model for the simulations of buoyancy-induced mixing in a model of a horizontal gallery as described in the definition of the benchmark. The results of the calculations have been used to examine quantitatively whether the flow of brine through a gallery can be described with the model as outlined in the preceding section, both for a natural-circulation flow and a combination of natural-circulation flow and advective flow. This is relevant with respect to the modeling of the transport of fluid in the EMOS computer program.

The PORFLOW software package, that has been developed by Analytic and Computational Research, Inc. (ACRi) is a comprehensive mathematical model for the steady-state or transient simulation of multi-phase fluid flow, heat transfer, and mass transport processes in variably saturated porous and fractured media [1]. The geologic medium may be anisotropic and heterogenous, and may contain distinct embedded elements such as, discrete fractures or boreholes within a porous matrix. The code provides a unified theoretical treatment of concepts relevant to fluid flow and transport.

The PORFLOW model of the horizontal gallery has been depicted in figure 4.7. The model consists of a two-dimensional rectangular geometry of 32 m length and 4.0 m height. The "third" dimension of the model has been modeled by one cell of width 4.0 m. The grid consists of cell sizes 0.125 x 0.125 x 4.0 m (width x height x depth).

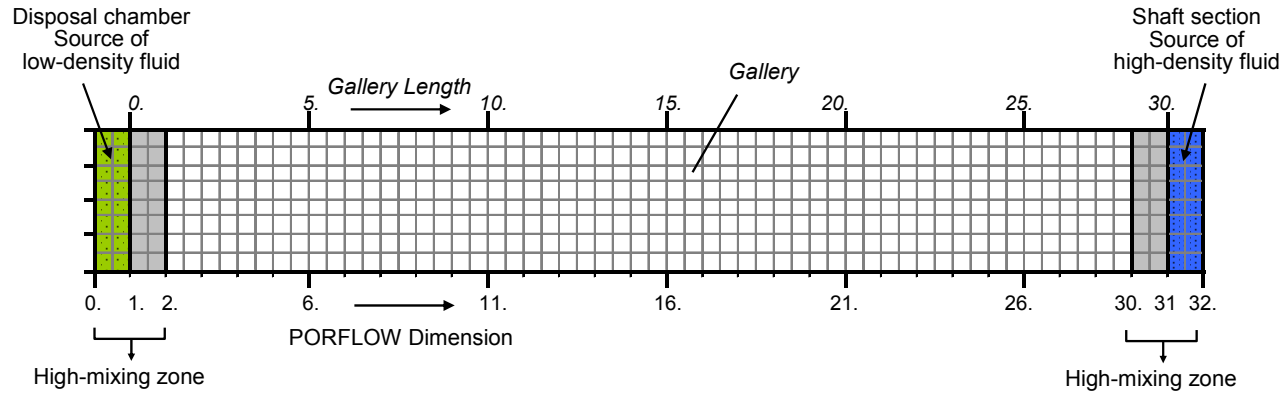

Fig. 4.7: PORFLOW model of a gallery

The volume is filled with non-sorbing material that simulates the salt grit inside an actual gallery. Relevant parameters such as the porosity and permeability have been set according to the benchmark specifications (table 4.5)]. In the left as well as in the right 2 m of the computational model (the “High-mixing zones”) the values of the permeability k and the diffusion coefficient D have been set respectively 10 and 10^3 times higher than the values in the Gallery section. This has been done to obtain a thorough mixing in these zones and so to minimize the boundary and/or entrance/exit effects near the boundaries of the computational model at X = 0 m and X = 32 m. The left 1 m of the computational model contains a source of lower-density brine. It models the inflow of low-density brine (ρ_ℓ = 1274 kg/m^3) from the adjacent waste chamber. The right 1 m of the model contains a source of higher-density brine (ρ_r = 1300 kg/m^3) and represents a shaft.

The simulations including additional advective flow rates were performed in one single PORFLOW run. The additional advective flow rates were modeled as steps of n times (n = 0, 1, 2, 3, 4, see also table 4.5) the buoyancy-driven exhange flow rate $Q_{ex,0}$ (density-driven exchange flow without advection). Upon each step of the imposed advective flow rate the simulation was performed as long as necessary to obtain a stationary flow field in the gallery. The advective flow was imposed as a flow of low-density brine on the left side of the model as depicted in figure 4.7.

The radionuclides C_1, C_2, and C_3, that are released in the disposal chamber have been modeled as solubility-limited sources in the Disposal Chamber section of the model. The concentrations of the nuclides in that section have been set a constant values of 100 Bq/m^3. Upon the development of the flow field, both with and without advective flows, the nuclides will be transported throughout the gallery. Note that the radionuclides C_1, C_2, and C_3 are distinguished by their respective diffusion coefficients (cf. table 4.5).

The concentrations, velocities and pressures were monitored at different vertical planes in the PORFLOW model, at 7.5 m (X = 8.5 m), 15 m (X = 16 m, middle of the gallery), and 22.5 m (X = 23.5 m) into the gallery (see also Fig. 4.3).

4.3.3 REPOS model

REPOS is a modular uni-dimensional, two-layered numerical code. On the first layer are the segment models, by which various components of the repository system are described in terms of individual FEPs. The second layer refers to models of various events and processes that might take place in the repository. The segment model is an assembly of geometrical features, material properties, events and processes characterizing a particular repository component.

The output of each segment model consists of time-dependent parameters describing motion (water and contaminant flow rates) and state (pressure, temperature, concentration). The output parameters are *averaged* values over the pore volume of the segment. Motion parameters are assigned to the segment inner and outer boundaries, while state parameters are assigned to the centre of the segment.

The density gradient may be due to temperature or concentration changes. The magnitude of the exchange flow under steady state condition is calculated with the following equation [2]:

$$Q_{exchange} = \frac{gk\beta H^2 W}{8\nu} \cdot \frac{\Delta T}{L} - \frac{gkH^2 W}{8\mu} \cdot \frac{\Delta \rho_C}{L} \qquad 4.5$$

where:

$Q_{exchange}$	(m^3/s)	the exchange rate of the brine
g	m/s^2	gravity
k	m^2	permeability
β	K^{-1}	thermal expansion coefficient
H	m	height of the gallery
W	m	width of the gallery
ΔT, $\Delta \rho_C$	(K, kg/m^3)	temperature, density difference
μ	(Pa·s)	dynamic viscosity
ν	(m^2/s)	kinematic viscosity
L	(m)	length of the gallery

The transport rate of material i, Q_i, due to exchange processes and diffusion-dispersion is calculated as:

$$Q_{i,exchange} = Q_{exchange} \cdot (C_{i,left} - C_{i,lright}) - (D_m(T) \cdot A \cdot n + \alpha_L \cdot Q_{advective}) \cdot \frac{\Delta C}{L} \quad 4.6$$

in which $C_{i,left}$ and $C_{i,right}$ are concentrations of material i in the left, respectively right compartment, A (m^2) is the cross-section area of the flow domain, n (-) stands for porosity, D_m (m^2/s) is the molecular diffusion coefficient (temperature dependent) and α_L is the dispersion length (m).

The advective transport rate is calculated as:

$$Q_{i,advective} = Q_{advective,left \rightarrow right} \cdot C_{i,left} \quad 4.7$$

The fictive diffusion flux, respectively diffusion activity flux are given by:

$$\dot{V}_D = -\frac{D(T) A \Phi}{\Delta L} \quad 4.8$$

$$\dot{A}_D = -D(T) A \Phi \frac{\partial C}{\partial x} \quad 4.9$$

where $D(T)$ is the temperature-dependent diffusion coefficient, T is the temperature, A is the cross-section of the section, Φ is the porosity, $C(x, t)$ is the concentration and ΔL is the length over which diffusion takes place (either length of the section as in model DVOVE1, or length of the sealing, as in model ESALG1, or it may be specified by user, as for model SGMIF2).

Two models have been set up for the calculation. The processes considered in the exercise, their correspondent segment models together with the constraints and requirements that needed to be addressed in the modeling with EMOS code are summarized in Tab. 4.6. The discretization of the drift is illustrated in figure 4.9 and figure 4.8.

Model 1:

The constraints imposed on the expected output parameter values, namely prescribed space points for which output values were requested, could only be fulfilled by division of the drift in sections, in such a way that the space points for the output (left and right boundaries, and x = 7.5 m, 15 m, and, respectively 22.5 m) are to be located in the middle of the sections. That implied adding an additional segment model to the drift.

One of the characteristic features of the EMOS code is that it assigns averaged values of the state parameters to the centre of the segment. The requirements imposed on output values for prescribed locations inside the drift lead to considering an artefact in the model, at the expense of increasing artificially the pore volume of the drift. An increase of the pore volume

in the drift adds more dilution to the dissolved concentrations, and also a delay of the output fluxes.

Nuclide concentrations at given locations, pressure, exchange and advective fluxes can be calculated with this model. However, although pressures and prescribed advective flow values could be obtained, the total resistance of the drift could not be preserved, and therefore the results are not conclusive for the purpose of the exercise. Calculations with this particular setting are not presented in the report.

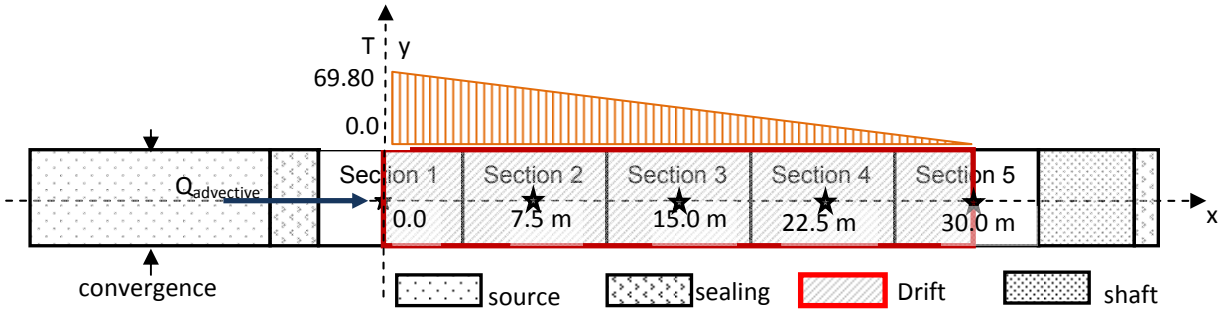

Fig. 4.8: *Model 1* The segment structure used for the EMOS code. Section highlighted in red represents the drift that has to be modeled. Sections in black illustrate the segment structure used in EMOS.

Tab. 4.6: Processes considered for the benchmark calculation and the corresponding models in EMOS code.

Process/Phenomena/ Constraints	Requirements	Segment model	Remarks
FLOW			
Constant advective flow $Q_{advective}$	$Q_{advective}$ = N· $Q_{exchange}$, N = 0, 1, 2, 3, 4; Constant concentration source term (C_i = 100 Bq/m^3); Source of the advective flow through convergence;	ESALG1	Very permeable sealing (two orders of magnitude lower than the backfill)
Density-driven flow, due to Mg concentration gradient between the shaft and the waste chamber	$Q_{exchange}$ = 6.93 m^3/y; Additionally, diffusion flux	DVOVE1	Density-driven flow simulated through temperature gradient driven flow; Dispersion neglected by setting appropriate input parameter values
The interface to geosphere (the shaft)	Sink term (C_i = 0.0 Bq/m^3);	SGMIF2	Large volume segment, to mimic interface to geosphere (the shaft); very permeable sealing;
INPUT / OUTPUT			
Input and output parameter values at imposed space points	Boundary conditions at: x = 0.0 m (left boundary); x = 30.0 m (right boundary)	-	*Model 2*: The drift has been modeled as consisting of 1 component (30 m – long).
	Output parameters at x = 7.5 m, 15 m, and 22.5 m	-	*Model 1*: The drift has been modeled as consisting of 5 components, each 7.5 m-long.

Model 2:

If, on the other hand, the desired output for comparison with other codes is the boundary radionuclide flux, or cumulated activity boundary flux, then there is no need for discretization of the drift, and the pore volume and system resistance to flow can be conserved. The model is illustrated in figure 4.9.

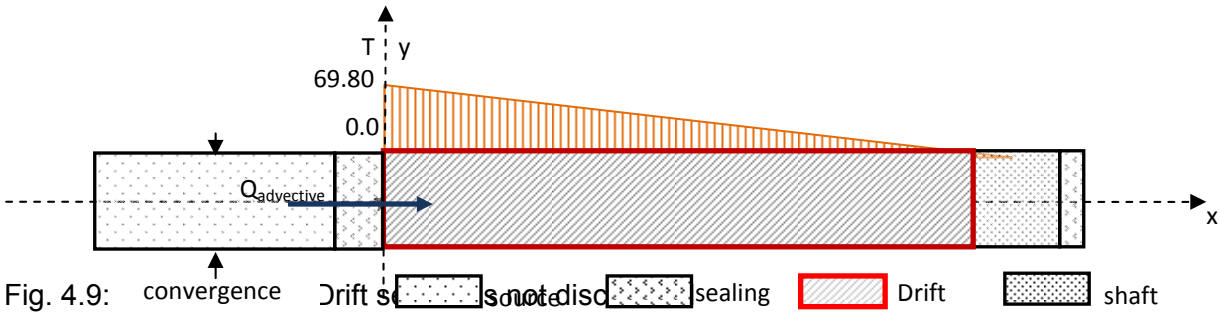

Fig. 4.9: convergence Drift s[illegible] source disc[illegible] sealing Drift shaft

The model used for the drift (DVOVE1) cannot account directly for Mg concentration gradient- driven flow. The Mg concentration is transferred as input parameter to the segment model, and it is the result of a special type of model for emplacement drift for medium-active waste. The Mg concentration could not be assessed with sufficient accuracy to obtain the prescribed concentration gradient. Therefore, the density-driven flow was simulated by means of temperature gradient. This effect is accounted for in the segment model.

EMOS calculates the density-driven flow as superposition of two effects that can result in density differences: through concentration of the dissolved substances and through temperature gradient. The resulting flow is calculated according to equation 4.5.

The effect of the concentration gradient was mimicked solely by use of the temperature gradient, by setting the concentration difference to zero. The value of the equivalent temperature-driven flow is met with the parameter values given in [2], and with $F_5 = \frac{gk\beta}{8\nu} = 9.59 \times 10^9$. For the chosen drift segment model, parameters are not influenced by temperature, or by temperature gradient. The temperature gradient applies between the first and the last drift sections, as shown in figure 4.9.

The source term is modelled with ESALG1 segment model. The ESALG1 model is used to simulate the source term for emplacement of various types of containers with radioactive waste in a backfilled and sealed drift. The backfill is supposed to undergo convergence, while the sealing is rigid. The model takes into account exchange processes (diffusion, dispersion, density gradient and gas) through the sealing.

The source term is a reservoir of contaminants, and has to provide a constant water flow throughout the simulation time. This is obtained by means of convergence of a very large cavity filled with water. With adequate choice of the parameter values, the prescribed values for the advective flow were met. The 'no-flow' case was modeled by setting the convergence rate to a very small value ($8.9701 \cdot 10^{-16}$ y^{-1}), corresponding to a value of the advective flow of 10^{-10} m^3/y.

The convergence flow, $\dot{V}_C$, is calculated in EMOS according to:

$$\dot{V}_C = -K(p;\Phi;T)\cdot V(t) \qquad 4.10$$

where $K(p, \Phi, T)$ represents the convergence rate of the backfill material, and $V(t)$ is the time-dependant void volume. The convergence rate is a function of pore water pressure p, porosity Φ, and temperature T, and the functional dependence is:

$$K(p;\Phi;T) = K_r \cdot f_r \cdot f_1(p(x,t))\cdot f_2(\Phi(t))\cdot f_3(T(x,t)) = \beta(V,\Phi,T)\cdot f_1(p(x,t))$$

$$f_1(p(x,t)) = \left(\frac{p_G(x) - p(x,t)}{p_G(x_r)}\right)^m,$$

$$f_2(\Phi(t)) = \begin{cases} \Phi\left(1-\frac{\Phi}{\Phi_r}\right)\left(\left(1-\frac{\Phi}{\Phi_r}\right)^2 + \left(\Phi\left(1-\frac{\Phi}{\Phi_r}\right)\right)^{\frac{1}{m}}\right)^{-m}, & \Phi < \Phi_r \\ 1, & \Phi \geq \Phi_r \end{cases} \qquad 4.11$$

$$f_3(T) = \frac{1}{1+a}\left[e^{\frac{Q_1}{R}\left(\frac{1}{T_G}-\frac{1}{T}\right)} + a\cdot e^{\frac{Q_2}{R}\left(\frac{1}{T_G}-\frac{1}{T}\right)}\right]$$

where indices G stands for rock, and r for the reference level. Q_1 and Q_2 represent activation energies for two salt rock creep mechanisms, and a is an empirical parameter.

The prescribed advective flow was obtained using appropriate values of the reference convergence rate (which is an input parameter in EMOS), calculated with the formula:

$$K_r = \frac{\dot{V}_C}{f_r \cdot f_2(\Phi(t))\cdot f_3(T(x,t))\cdot V(t=0)} \times \left(\frac{R_0^{-1} p_G}{R_0^{-1}(p_G - p_H) - \dot{V}_C}\right)^m \qquad 4.12$$

where $R_0 = \frac{\mu L}{Ak}$ is the flow resistance of the segment.

The initial pore volume of the source segment was assigned in such a way to ensure a reduction of the pore volume at t = 100 y of less then 1%. The contaminant dissolved activity in the pore water is set to 10^8 Bq, and the resulting source concentration activity applied to the left boundary of the drift is 100 Bq/m^3. The temperature of the source segment is set at the rock temperature. Thus, exchange via temperature gradient does not take place in the sealing. Dispersion processes are discarded by setting the dispersion length value to zero. Gas production is also discarded. The only exchange process left is due to diffusion that affects the outflow of the activity from the source section. Diffusion coefficient (dispersion, also) is a global parameter, and since the exercise requires diffusion processes to be taken into account in the drift, it cannot be neglected.

The interface to the geosphere (the shaft, in our exercise) was modelled as a non-converging backfilled drift with a very permeable and non-converging sealing, using the SGMIF2 segment model.

In fact, the model assumes that the backfill converges. The code allows for local variations of the convergence rate, and this feature was used to model the backfill in the interface section as a rigid, non-converging environment.

The model stands for interface of the near-field with the geosphere, and it models spontaneous groundwater intrusion into the disposal system, followed by expulsion of intruded contaminated water back into the far-field. The dissolved contaminants are transported by advective flow, and are subjected to diffusion/dispersion in the sealing. Exchange effects are taken into account in the sealing, and are modeled by means of two input parameters, namely effective length and cross-section. No temperature dependence was assigned to this segment either, and as for the rest of the model, mechanical dispersion has been neglected.

In EMOS code, instantaneous saturated conditions are achieved by considering that the segment receives instantaneously a volume of water above a threshold value (10^6 m^3).

4.3.4 d^3f and r^3t models

The programs d^3f and r^3t [3, 4] are part of a set of programs which were developed to model the water and contaminant transport in the overburden of a nuclear waste repository. Besides these two programs, there are pre- and post processors to handle the data and to visualize the results. The abbreviation d^3f stands for “distributed density-driven flow”, while r^3t stands for “radionuclides, reaction, retardation and transport”.

The numerical model d^3f was developed from 1994 to 1998 while r^3t was generated from 1998 until 2003. Six and four working groups, respectively, of German or international universities were involved in the development lead-managed by GRS. Both of the codes use Finite-Volume discretisation and unstructured grids to enhance the resolution of hydrogeological heterogeneities. Adaption techniques controlled by a-posteriori error estimators are applied to the grid and the time steps to ensure the optimal length in time and space. As the most effective solvers for large and sparse systems of equations multigrid algorithms are taken. Additionally the entire codes are parallelised so that they can be run on workstations, PCs, cluster of PCs, and massively parallel computers, too.

4.3.4.1 The density-driven flow model d^3f

Figure 4.10 shows the 2d model and its boundary conditions for the density-driven flow simulation. The model has a length of 30 m and a height of 4 m. Top and bottom boundary are closed for flow and transport. At the left hand boundary a value of c = 0 as a Dirichlet boundary condition for the concentration represents the Mg-depleted brine, that has a density ρ of 1274 kg/m³. A constant velocity is defined as a Dirichlet boundary condition too, whereas

$v_{exchange,0} = k \cdot Q_{exchange,0}/16\ m^2$ with k = 0 to 4 for the different cases. At the right hand boundary a hydrostatical pressure is assumed. In case of the velocity field indicates a brine inflow over this boundary, the concentration is set to c = 1 representing Mg-rich brine with a density of 1300 kg/m³. Otherwise concentration on the boundary assumes the value of the nearest node inside.

Fig. 4.10: d³f-model for the density-driven flow simulation

The parameters used for flow modelling are summarized in table 4.7. Density is a linear function of Mg-concentration. The test case description gives no specifications of dispersivity and diffusivity of the Mg compounds, therefore generally applied, low values are used.

Tab. 4.7: Overview of model parameters

Parameter	value
Porosity n	0.35
Permeability k	$4.84 \cdot 10^{-12}$ m²
Longitudinal dispersivity α_L Transversal dispersivity α_T	0.1 m²/s 0.01 m²/s
Diffusivity D	$1.0 \cdot 10^{-10}$ m²/s
Minimum density ρ_{min} Maximum density ρ_{max}	1274 kg/m³ 1300 kg/m³
Dynamic viscosity μ	$1.5 \cdot 10^{-3}$ Pa s
$v_{exchange,0}$	$k \cdot 1.36875 \cdot 10^{-8}$ m/s

A triangulation with 71 808 elements was used for the flow and transport simulations, what results in a triangle edge length of about 0.055 m.

4.3.4.2 The nuclide transport model

Based on the velocity fields calculated by d³f, the transport of three different nuclides was simulated using r³t in a next step. These nuclides only differ in their diffusion parameters. Effects as sorption and radioactive decay were neglected.

The transport model with its boundary conditions is depicted in figure 4.11. The left boundary is tagged with a concentration of 100 Bq, and the concentration is set to 0 Bq at the right hand boundary in case that an inflow is detected. Otherwise the concentration assumes the value of the closest node inside the gallery.

Fig. 4.11: r³t-model for the simulation of nuclide transport

The velocity field and the triangulation were adopted from the d³f model. Table 4.8 shows the parameters used for the transport modelling.

Tab. 4.8: Overview of transport model parameters

Parameter	value
porosity n	0.35
rock density	2200 kg/m³
longitudinal dispersivity α_L transversal dispersivity α_T	0.1 m²/s 0.01 m²/s
diffusion coefficient nuclide 1 diffusion coefficient nuclide 2 diffusion coefficient nuclide 3	$3.0 \cdot 10^{-10}$ m²/s $3.0 \cdot 10^{-9}$ m²/s $3.0 \cdot 10^{-8}$ m²/s

4.4 Results of benchmark calculations

4.4.1 Application of PORFLOW and the extended analytical model

The results of the PORFLOW calculations are discussed in the following sections. When applicable, the PORFLOW results are compared with the extended analytical model.

4.4.1.1 Exchange flow rates

At the start of the simulations the 'sources' of the scalar C and those of the nuclides C_1, C_2, and C_3 become effective. As a result of the imposed density differences, a buoyancy-driven flow starts to develop. The advective flow rates Q_{adv} of low-density brine were imposed in five different steps ranging from 0 (no advective flow) to 4 times the fully-developed buoyancy-drive exchange flow $Q_{adv,0}$ (without advection).

Figure 4.12 shows the calculated exchange flow rates Q_{ex} of brine through the lower part of the gallery (colored curves) as a function of the imposed advective flow rates Q_{adv} of low-density brine. This plot shows that starting from a gallery filled with high-density brine and no additional advective flow (Q_{adv} = 0), it takes several years for low-density brine to establish a stationary flow pattern in the gallery as a result of the density differences between the opposite sides of the gallery. This plot also confirms that for each additional advective flow rate of

low-density brine the simulation was extended sufficiently long to reach a stationary condition.

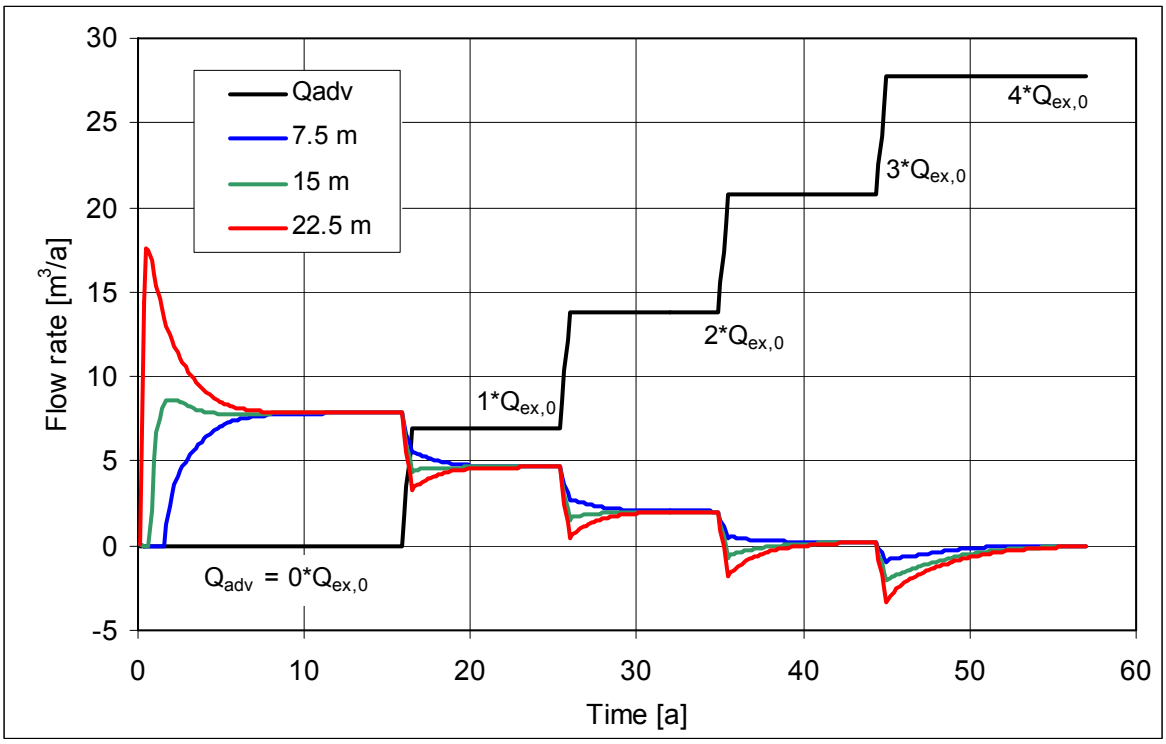

Fig. 4.12: Exchange flow rate through the lower part of the gallery (colored curves) as a function of advective flow rates of low-density brine, at different locations in the gallery - PORFLOW

In the cases where additional advective flow rates of low-density brine are imposed (at the left side of the gallery) it takes a period of several years for the flow field to reach a new stationary condition. As a result of the advective flow of low-density brine the buoyancy-driven exchange flow is more and more suppressed. If the advective flow rate Q_{adv} has reached 4 times the magnitude of the buoyancy-driven exchange flow $Q_{ex,0}$ (without advection) the flow of the higher density brine has completely been terminated. This is in line with the theoretical model.

The buoyancy-driven exchange flows that have been derived from the PORFLOW calculations under stationary conditions have been compared with the theoretical model in figure 4.13 and table 4.9. This comparison shows that the agreements between the PORFLOW results and the theoretical model are quite well, although the theoretical model calculates somewhat lower values of the exchange flow rates than the PORFLOW model. A probable cause of this may be the fact that in the PORFLOW calculation the dividing plane between the two opposite flows is not flat and located in the middle of the gallery, but is instead “S-shaped (see next section). In addition, PORFLOW also calculates a velocity component in the vertical direction. These two features are not captured by the theoretical model.

For the case $Q_{advective}$ =4 * $Q_{exchange,0}$ a slightly negative value for the exchange flow rate is calculated by PORFLOW. The probable reason is that in this case the simulation is not extended long enough to obtain a fully stationary flow field.

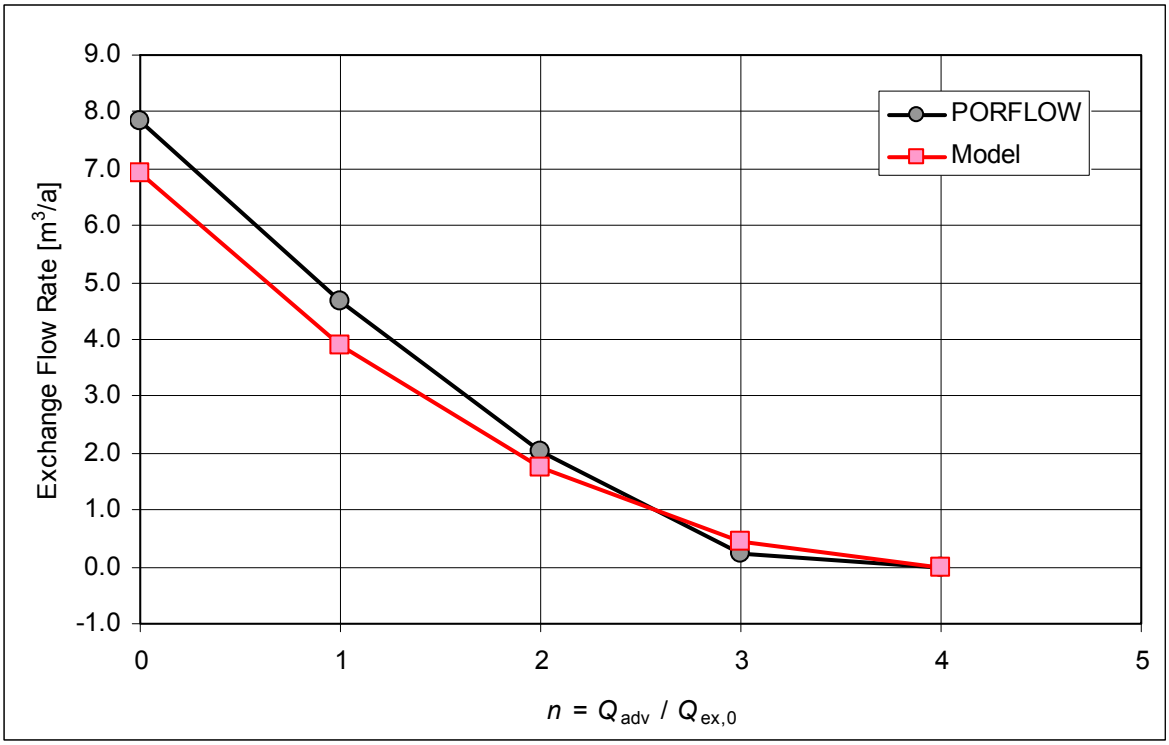

Fig. 4.13: Comparison of PORFLOW results and model calculations for the buoyancy-driven exchange flow rates

Tab. 4.9 Comparison of PORFLOW results and model calculations for the buoyancy-driven exchange flow rates

Imposed advective flow rate	Source m^3/yr	Q_{ex} (PORFLOW) m^3/yr	Q_{ex} (Model) m^3/yr
$Q_{advective}$ =0 * $Q_{exchange,0}$	0.0	7.84	6.93
$Q_{advective}$ =1 * $Q_{exchange,0}$	6.93	4.66	3.90
$Q_{advective}$ =2 * $Q_{exchange,0}$	13.9	2.03	1.73
$Q_{advective}$ =3 * $Q_{exchange,0}$	20.8	0.22	0.43
$Q_{advective}$ =4 * $Q_{exchange,0}$	27.7	-0.02	0.00

4.4.1.2 *Density profiles*

Figure 4.14 shows the density profiles, calculated by PORFLOW, inside the gallery for different values of the additional advective flow rate of low-density brine under stationary conditions. The source of low-density brine is located on the left whereas the source of high-density brine is located on the right side of the gallery.

As a result of the density difference between the left side and the right side of the gallery, the buoyancy-driven flow develops and is maintained as long as the density differences exist. The higher-density brine flows from right to left on the bottom of the gallery. On top of the high-density brine, the low-density brine flows from left to right. Note that the dividing plane between the two opposite flows is not straight or located at a uniform height throughout the length of the gallery. Instead, the dividing plane is “S”-shaped. This geometrical feature is not captured by the theoretical model derived in section 4.3.1.

When more and more additional advective flow of low-density brine is injected into the left side of the gallery, the locus of the “S”-shape is driven more and more towards the right side of the gallery. Note that even in the case that the advective flow rate Q_{adv} = 4*$Q_{ex,0}$, there is still a density profile present inside the gallery. However, the buoyancy-driven flow of high-density brine from right to left has come to a stop in that case.

Another remarkable feature is the low degree of mixing in the vertical plane of the gallery. The density profile shows that in the vertical direction the mixing zone is only about 70 cm in height. This means that the two layers of brine are well separated on top of each other. Above and below the mixing zone the low-density brine and the high-density brines have an almost uniform density profile.

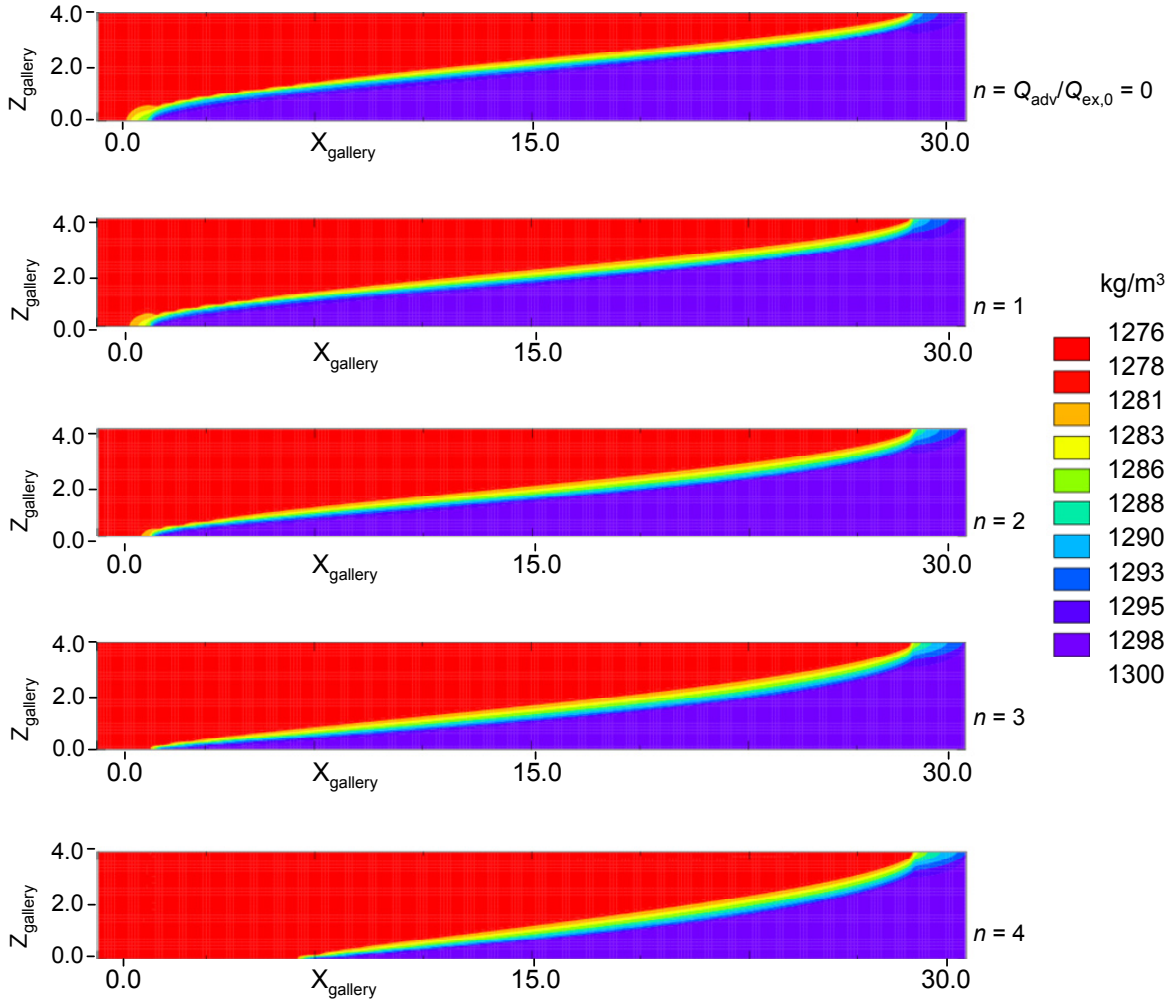

Fig. 4.14: Stationary density profiles in the gallery for different advective flow rates - PORFLOW

A schematic sketch of the density profiles that has been calculated using the analytical model has been depicted in figure 4.15. The locus of the dividing line between the higher density fluid and the lower density fluid has been obtained from equation 4.4.

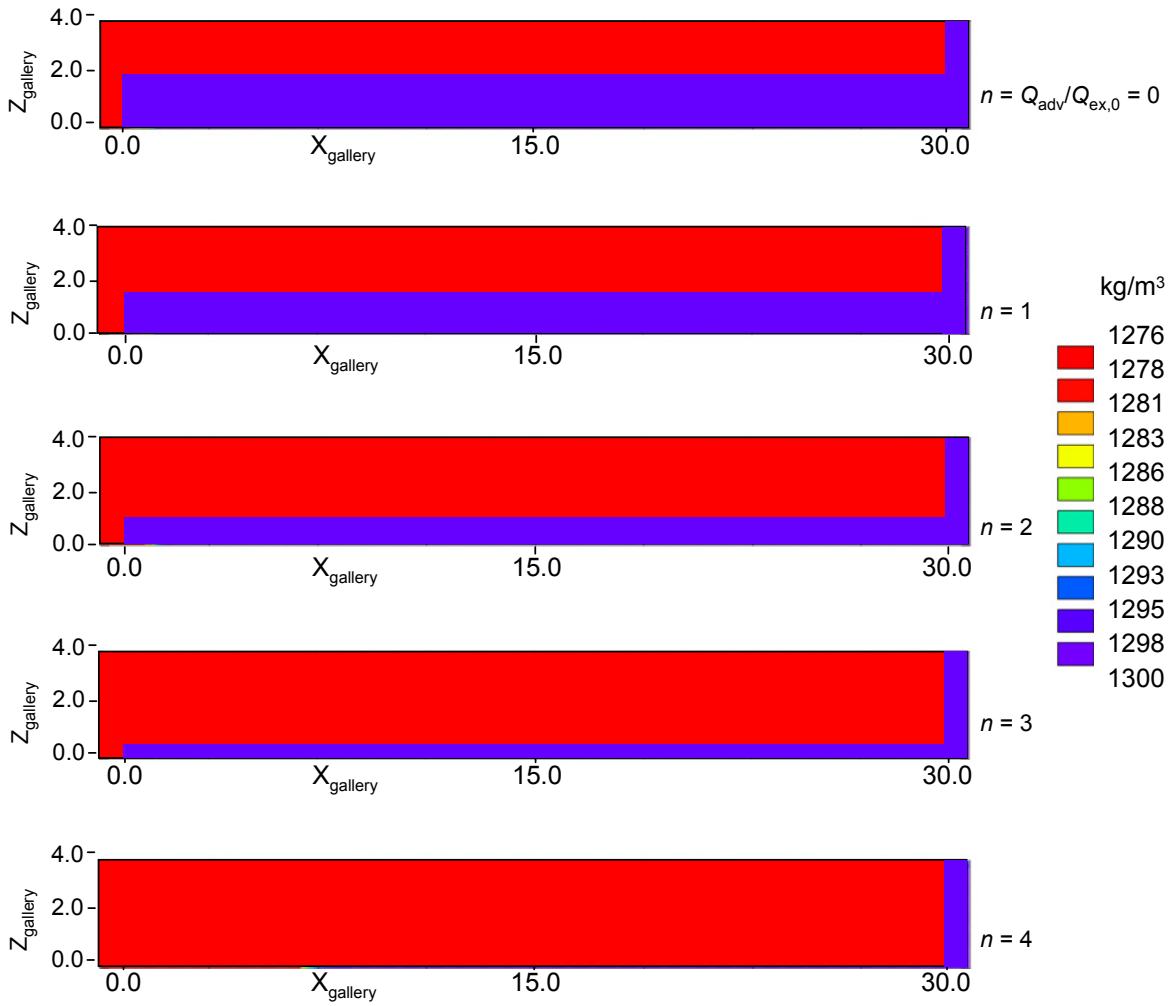

Fig. 4.15: Density profiles in the gallery for different advective flow rates - extended analytical model (schematic draft)

4.4.1.3 Pressure distribution

The pressure distribution in the gallery determines the magnitude and the direction of the advective and exchange flows. In figure 4.16 an indication is given of the pressure gradient in the gallery during the buoyancy-driven flow and for the combination of the exchange flow and advective flows.

It can be noticed from figure 4.16 that for the buoyancy-driven flow only (Q_{adv}=0*$Q_{ex,0}$) the pressure gradient across the gallery is distributed symmetrically between the upper half and the lower half of the gallery, and that at a height of 2.0 m (cf.: h in equation 4.4) the pressure difference equals zero. In the upper half of the gallery, the pressure difference is positive, resulting in a flow from left to right, whereas in the lower half the pressure difference is nega-

tive. This results in a buoyancy-driven flow in the lower part of the gallery from the higher-density area (right) to the lower-density area (left).

The pressure gradient as calculated with the analytical model has been depicted in figure 4.17. It is clear that the S-shaped pressure gradient profile has not been captured with the analytical model. However, the average values of the pressure gradient obtained from the PORFLOW calculations match the pressure gradient values of the analytical model within approximately 10%.

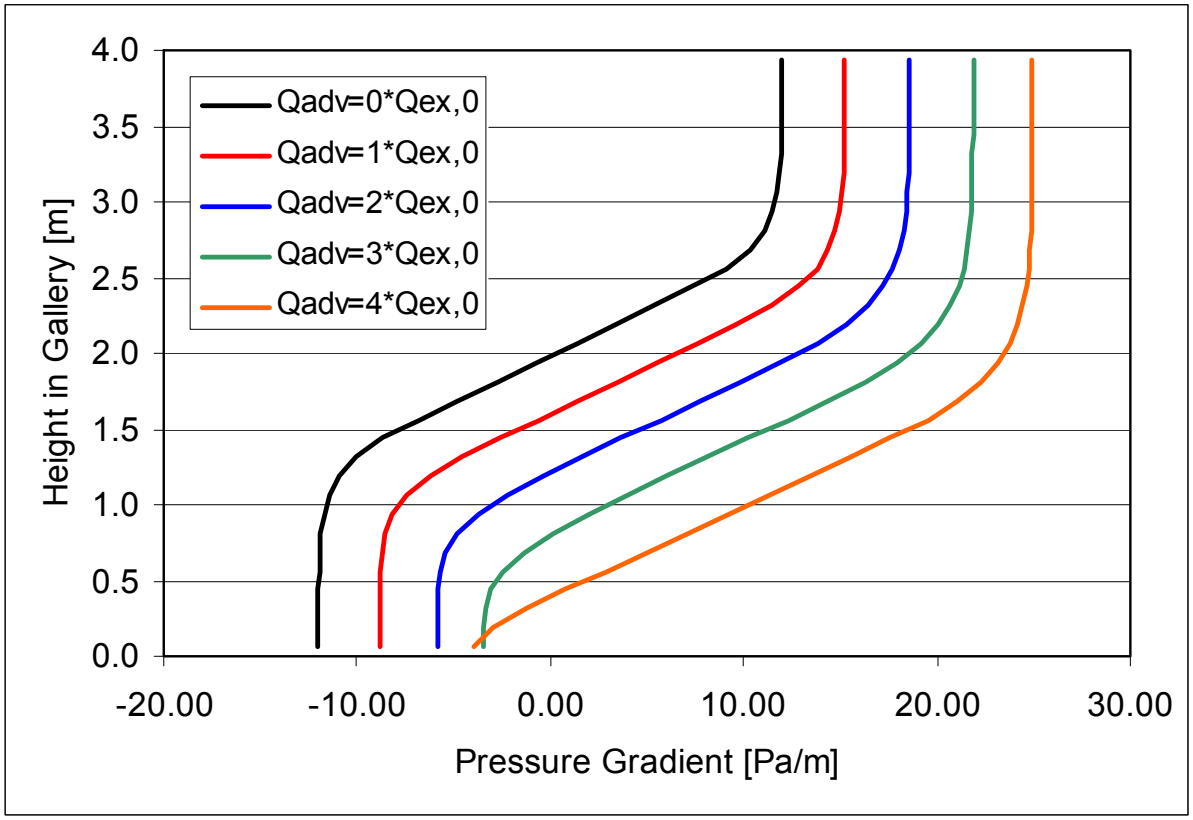

Fig. 4.16: Pressure gradient in the gallery - PORFLOW

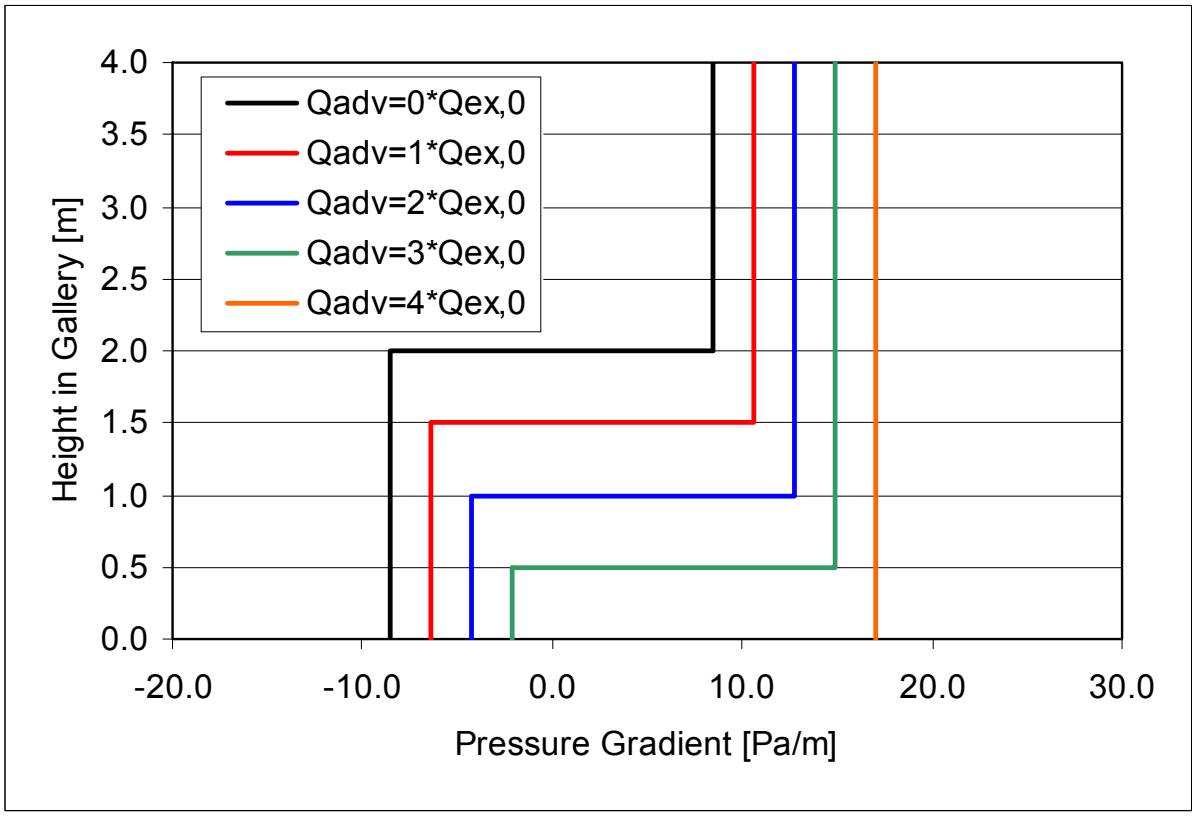

Fig. 4.17: Pressure gradient in the gallery - analytical model

4.4.1.4 Velocity profiles

The Darcy velocity profiles as calculated by PORFLOW in the middle of the gallery (X = 15 m), are depicted in figure 4.18. Figure 4.19 shows the Darcy velocity profiles that have been calculated using the analytical model.

In the case of no advective flow (Q_{adv} = 0*$Q_{ex,0}$) , the velocity profile is symmetrical and opposite in direction in the lower part and the upper part of the gallery. The Darcy velocity in the bottom part as well as in the top part equals 1.16 m/year, and, with a backfill porosity of 0.35, the average velocity equals 3.31 m/year. Taking into account the development of the velocity profile along the gallery this means that it will take approximately 9 years for fluid to flow from one side of the gallery to the opposite side.

In the case of additional advective flows, the Darcy velocities are shifted to higher values and the velocity profiles become less symmetrical for the larger advective flow rates. Figure 4.18 shows that in the middle of the gallery (X = 15 m), in the case of Q_{adv} = 4*$Q_{ex,0}$, PORFLOW still calculates that the low-density brine flows in the direction opposite to the direction of the advective flow. The velocity in that location is however small.

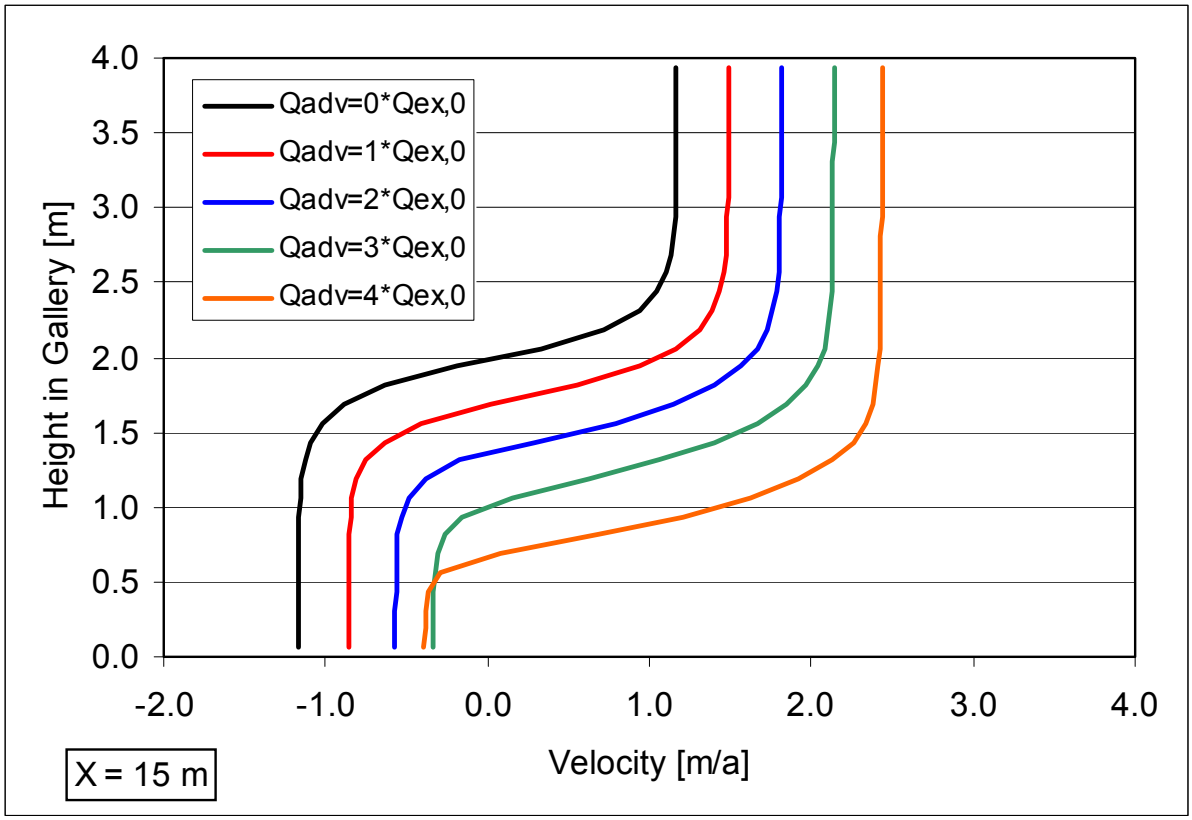

Fig. 4.18: Darcy velocity profile in the gallery at X = 15 m

The Darcy velocity profiles that have been calculated using the analytical model (4.19) roughly catch the PORFLOW results. The average values that can be obtained from the PORFLOW results match the values of the analytical model by approximately 10%. The difference can be explained by the straightforward approximation of the analytical model, and the fact that the analytical model does not comprise longitudinal velocity components.

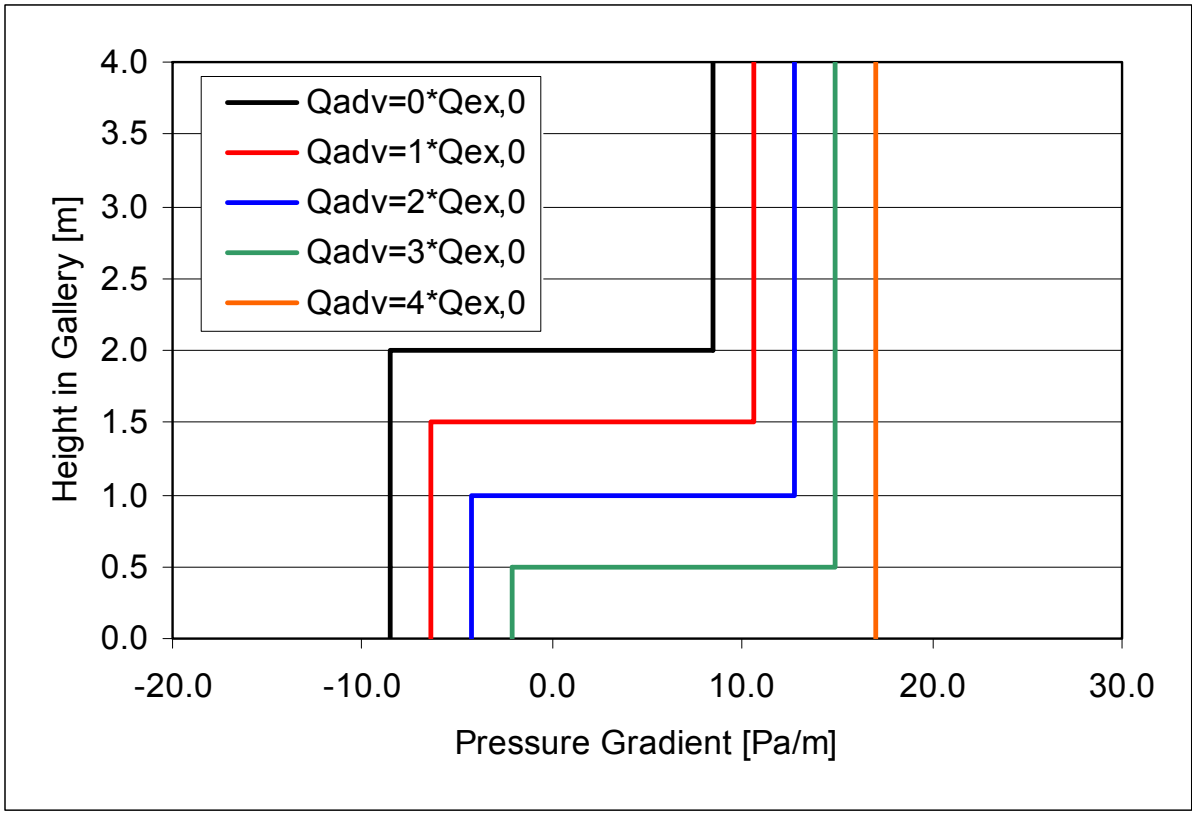

Fig. 4.19: Darcy velocity profile in the gallery - analytical model

4.4.1.5 Effect of diffusion on nuclide exchange efficiency

The extended analytical model does not account for the effect of diffusion on the nuclide exchange efficiency. Diffusion will in general cause a net movement of nuclides from the high nuclide-concentration flow layer to the flow layer with a low nuclide-concentration. The PORFLOW model includes diffusion and thus allows to evaluate the effect of diffusion. Three nuclides (or species) C_1, C_2 and C_3 have been considered, each with different diffusion coefficients (C_1: slow diffusion; C_3: fast diffusion).

Examples of the concentration profiles of the nuclides C_1, C_1, and C_3, at different locations in the gallery have been depicted in the following figures. These plots reveal that:

- for the non-advective case, Q_{adv} = 0*$Q_{ex,0}$, the concentration profiles in the middle of the gallery (X = 15 m) are symmetrical in vertical direction, which is in line with the calculated velocity profiles;

- for the advective cases, Q_{adv} > 0*$Q_{ex,0,}$ the concentration profiles are more and more shifted towards the right-hand side of the gallery, i.e. in the direction of the advective flows;

- for smaller values of the diffusion coefficients of the nuclides, the nuclides are hardly mixed in vertical direction throughout the gallery. An additional advective flow does not enhance this vertical mixing of nuclides;

- for larger values of the diffusion coefficients of the nuclides, the nuclides are distributed more evenly in the gallery both in horizontal and in vertical direction.

In relation to the calculated velocity profiles these observations imply that in case radionuclides are released inside a waste chamber and transported by diffusion and/or advection through a gallery, no back-flow of nuclides exists that might be caused by density-driven buoyancy flows. This is also revealed when the nuclide fluxes are considered, see next section.

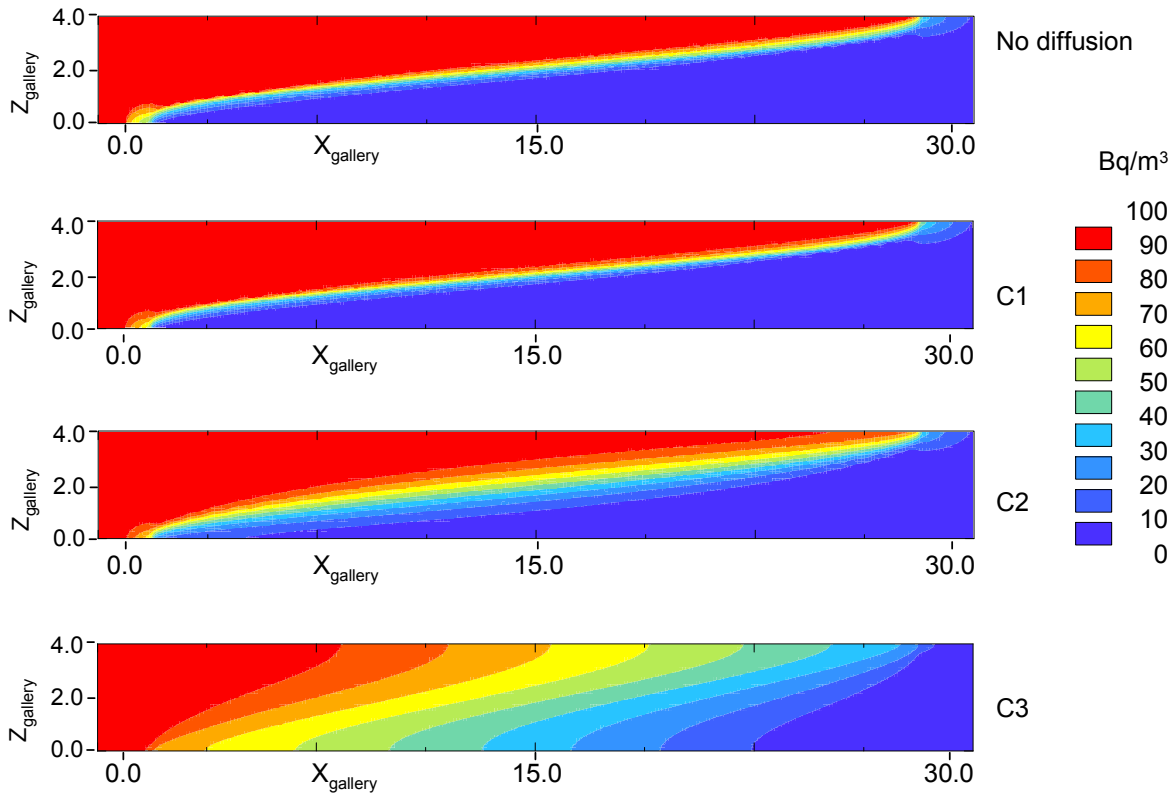

Fig. 4.20: Concentration distributions in the gallery for non-advective flow, C_1 (diffusion coefficient $D_1 = 3.0 \cdot 10^{-10}$ m^2/s), C2 ($D_2 = 3.0 \cdot 10^{-9}$ m^2/s) and C3 ($D_3 = 3.0 \cdot 10^{-8}$ m^2/s)

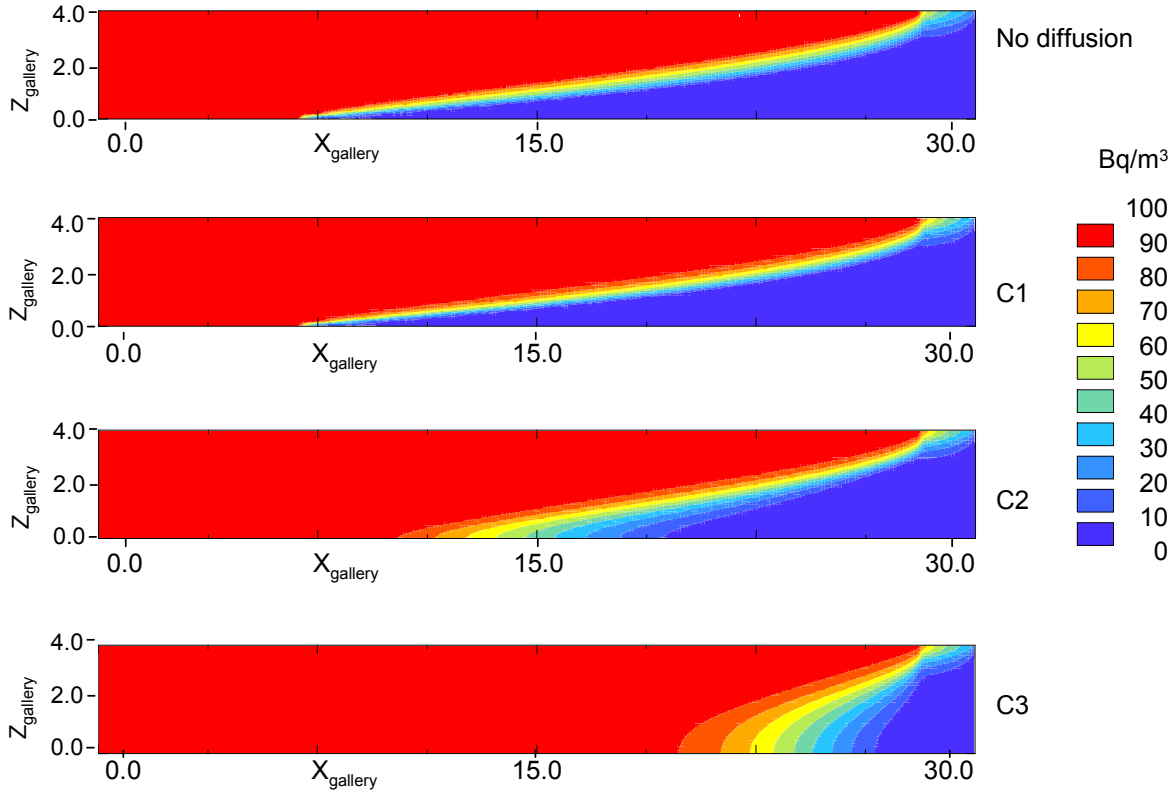

Fig. 4.21: Concentration distributions in the gallery for the case $Q_{advective}$ = 4 * $Q_{exchange}$, C_1 (diffusion coefficient D_1 = $3.0 \cdot 10^{-10}$ m^2/s), C_2 (D_2 = $3.0 \cdot 10^{-9}$ m^2/s) and C_3 (D_3 = $3.0 \cdot 10^{-8}$ m^2/s)

4.4.1.6 Nuclide activity fluxes

The net nuclide fluxes [Bq/a] of the three nuclides C_1, C_2, and C_3 at the exit of the gallery as calculated by PORFLOW are depicted in figure 4.22. This figure shows that:

- in the non-advective flow case (Q_{adv} = 0*$Q_{ex,0}$) a net flow of nuclides is established as a result of the buoyancy-driven exchange flow that carries along the nuclides from the waste chamber, where they are released, through the gallery to the shaft section;

- for the case Q_{adv} = 0*$Q_{ex,0}$ the net flow rate of nuclides is smaller for the nuclides with the larger values of the dispersion coefficient (C_4 < C_3 < C_2). This observation indicates that part of the nuclides with the larger values of the dispersion coefficient are transported back in the direction of the waste chamber by the higher-density fluid through the lower part of the gallery;

- as a result of the diffusion-driven exchange flow the total flow of nuclides may be enhanced compared to the non-advective flow case (e.g. for the nuclides C_2 and C_3 for the cases Q_{adv} = 1*$Q_{ex,0}$ and Q_{adv} = 2*$Q_{ex,0}$) if an additional advective flow exists from the waste chamber to the shaft section;

- in case of a better dispersion (larger values of the diffusion coefficient), the flow rates of nuclides follow more closely the “No Diffusion” case if an additional advective flow exists from the waste chamber to the shaft section.

These observations are important in relation the Safety Case in that respect that in the case of advective flow rates from a waste chamber through a gallery to an adjacent shaft the total flow rates of radionuclides may be enhanced as a result of the buoyancy-driven exchange flow that may exist in a gallery due to differences in the fluid density on both sides of the gallery.

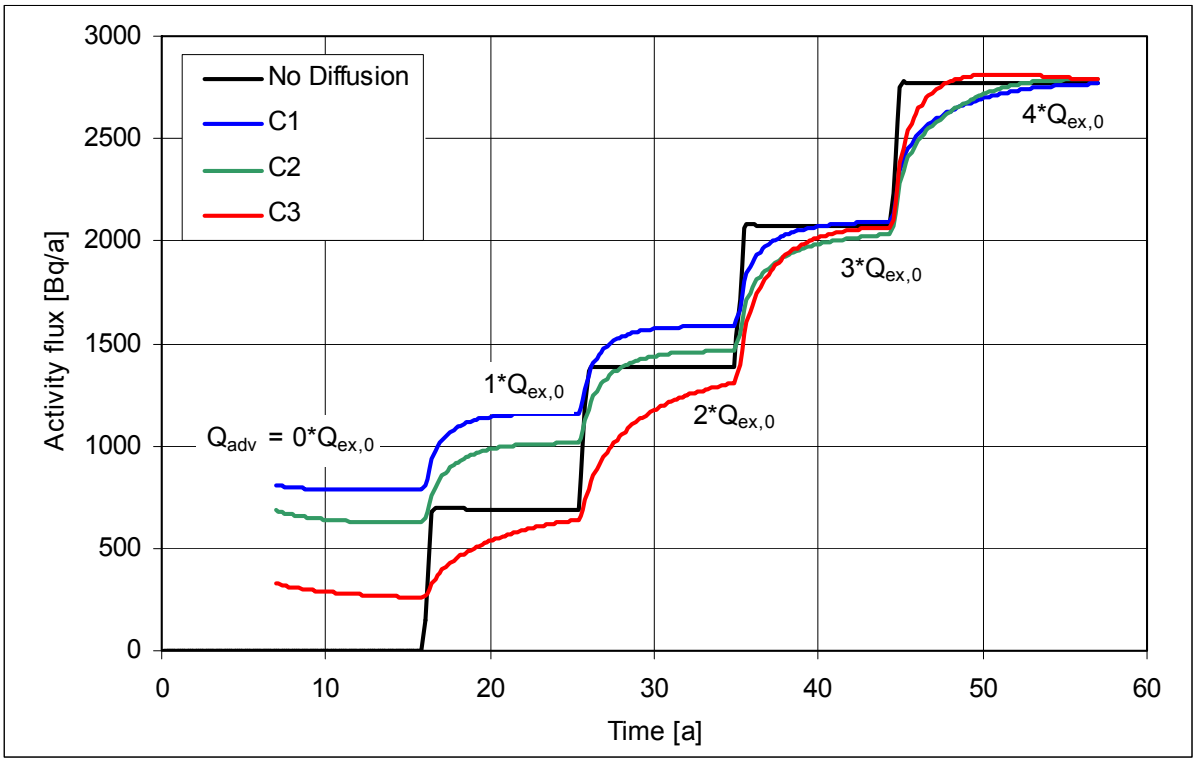

Fig. 4.22: Activity flux at the exit of the gallery (X = 30 m) for the nuclides C_1 , C_2 and C_3 for different advective flow rates

4.4.2 Application of REPOS

The specifications of the benchmark exercise envisage modeling of the exchange processes involved in water flow and contaminant transport through a backfilled drift, subjected to density variations. The model used for simulation of the benchmark exercise with EMOS/REPOS code consists of three parts: the source-term, the drift, and the contact to geosphere.

The source term is described through a flooded large cavity undergoing convergence, in which dissolved contaminants are spread homogeneously in the pore water. The source term provides the constant concentration on the left boundary of the drift, and inputs the advective water flow into the drift.

The advective and exchange fluxes obtained with EMOS for all 5 variants through the drift are represented in figure 4.23 and figure 4.24 respectively. Both models tested (drift discretised in 5 parts, or drift not discretised) have provided the values specified in the test case. At higher values of the convergence rate, a slight decrease of the resulting flow can be observed in figure 4.23. The decrease of the advective flux at t = 1000 years ranges between 99.1% for k = 1, to 95.3% for k = 4.This is due to enhanced convergence that was needed to implement such a value of the advective flux, combined with limitation of the volume of the source segment. In order to maintain a constant value of the advective fluxes for a longer time, one has to increase the volume of the source cavity. Pressure in the drift is hydrostatic (10 MPa).

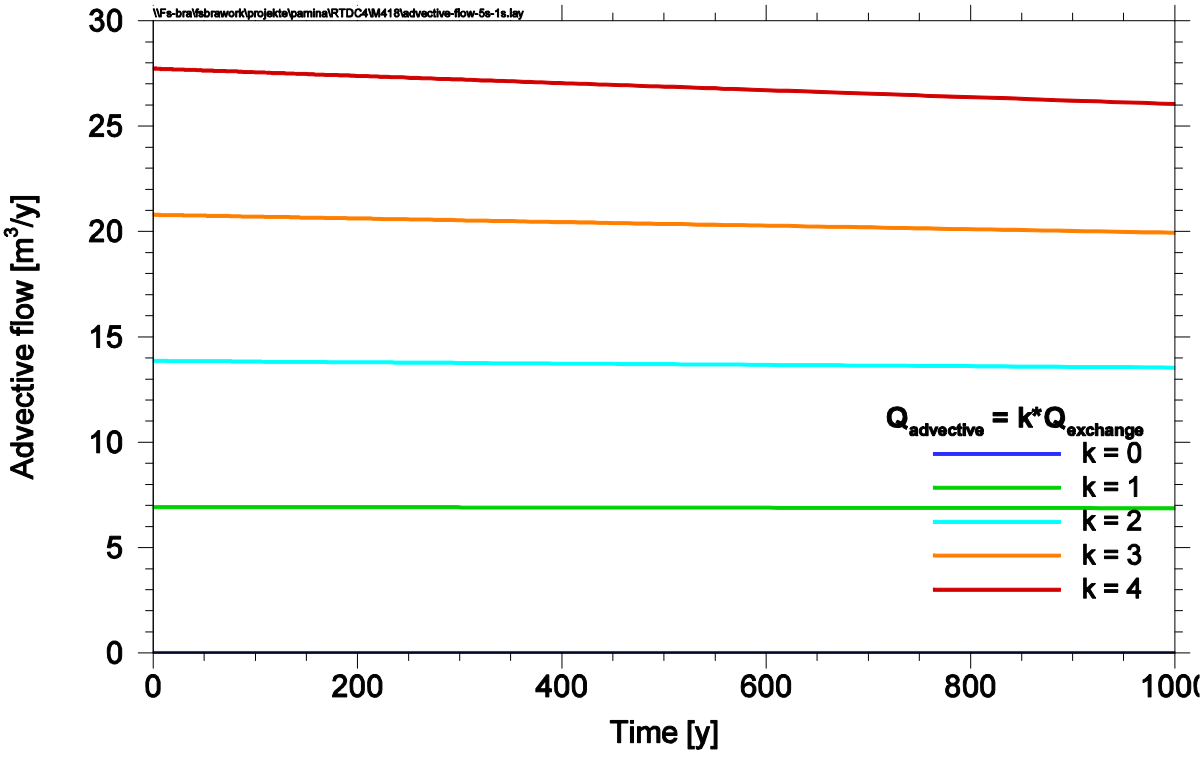

Fig. 4.23: Advective fluxes produced by convergence of the source model (EMOS model 1 and 2).

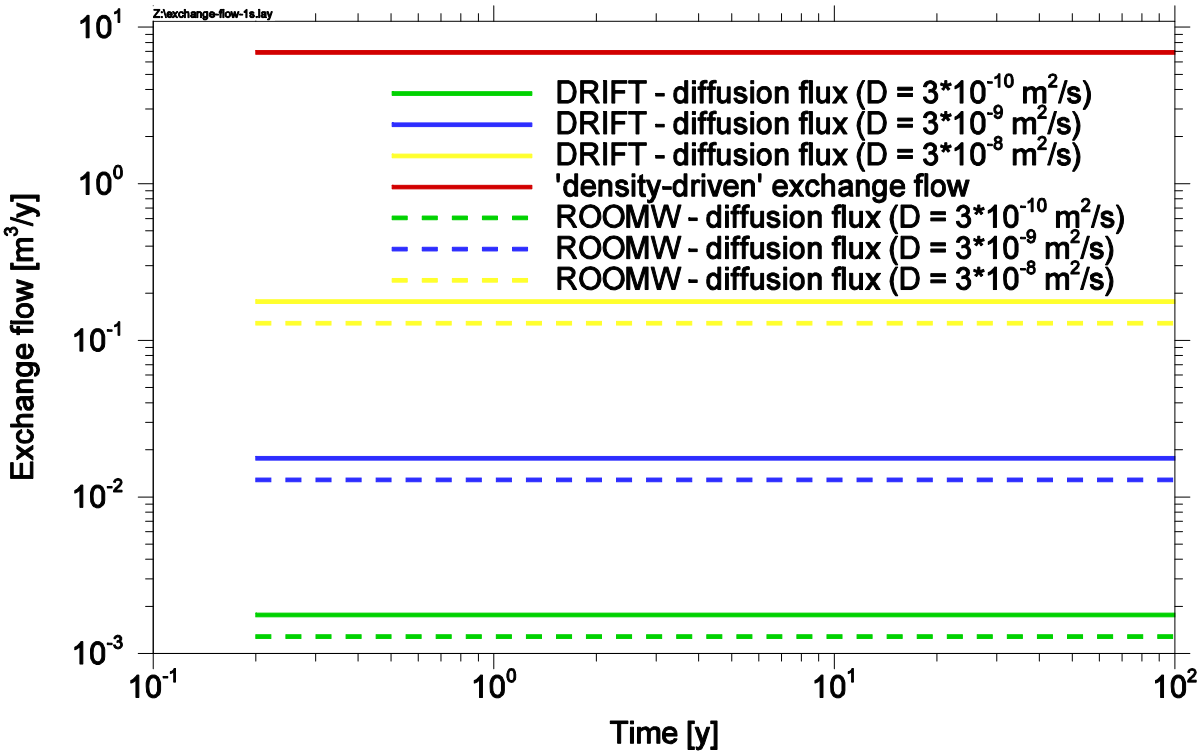

Fig. 4.24: Exchange fluxes in the drift (models 1 and 2).

The density-gradient was implemented via an equivalent temperature gradient. As shown in 4.24, the associated exchange flux obtained with EMOS has the value of 6.912 m^3/y and it matches the value imposed in the problem specification (99.7% of the prescribed value). The diffusion fluxes are constant: $1.77 \cdot 10^{-3}$ m^3/y for $D_1 = 3 \cdot 10^{-10}$ m^2/s, $1.77 \cdot 10^{-2}$ m^3/y for $D_2 = 3 \cdot 10^{-9}$ m^2/s, and $1.77 \cdot 10^{-1}$ m^3/y for $D_3 = 3 \cdot 10^{-8}$ m^2/s respectively. The difference in the values of the diffusive fluxes in the source segment (ROOMW) and the drift is due to the fact that the length of the source sealing is shorter then the length of the drift, and the porosity of the source sealing is much higher then the porosity of the drift backfill.

The activity fluxes flown into the drift through the left boundary, and the activity fluxes flown out of the drift are shown in figure 4.25. The average concentrations in the drift are shown in 4.27. The inflow fluxes are shown in dotted lines, and outflow fluxes are depicted in continuous lines. The "$D = 3 \cdot 10^{-10}$ m^2/s" calculation case has no symbol attached, while "$D = 3 \cdot 10^{-9}$ m^2/s" is marked with a circle, and respectively "$D = 3 \cdot 10^{-8}$ m^2/s" with triangle. Line colours point for the characteristics of the advective flow. Thus, dark blue is assigned to $k = 0$, green to $k = 1$, cyan to $k = 2$, and red to $k = 4$.

Mobilization of the contaminant starts at t = 0.1 years. In one timestep, the entire activity is mobilized into the pore water of the source segment. Inflow into the drift starts at t = 0.2 years (respectively, outflow from the source section). The constant concentration of 100 Bq/m^3 is attained in the next timestep (at t = 0.3 y), for all the simulation cases.

The influence of the diffusion into the source sealing on activity outflow from the source segment is negligible, with the exception of the no-flow cases (k = 0). This is due to the prevalence of the advective (due to convergence of the backfill) transport, as shown in figure 4.25.

The outflow from the drift starts at the third timestep, at t = 0.4 y, from zero and, later in time, it reaches a sort of stationary state, characterized by equal inflow and outflow rates. The times of attaining this state (constant concentration profiles, as shown in figure 4.27) are influenced by the advective transport. For constant advective flow, exchange processes affect the time of attaining the plateau. Higher diffusion delays the attainment of a more or less stationary release.

In the absence of density driven flow and advection, the activity fluxes are due to diffusion only, and they are considerably smaller, between seven (for enhanced diffusion) and, respectively one order in magnitude (for low diffusion). It can be seen that the effect of exchange processes consists of enhancement of the release rates. When advection is present, lack of exchange by density-driven flow causes decrease of the activity flow to cca 91% for small diffusion, respectively 99.5% for increased diffusion. In the absence of exchange, activity rates show a slower increase in time. The contribution of the exchange processes to contaminants release rates is diminishes with enhanced diffusion. That suggests that higher diffusion slow down exchange processes, by accelerating the mixing process. Thus, the concentration gradients within the domain are reduced.

Figure 4.26 shows the activity fluxes from the drift, but on a linear scale. It can be seen that for the no-flow case (k = 0) the activity flux increases with the diffusion coefficient of the nuclide while it is the other way round for all cases taking advection into account. This result for the no-flow case clearly contradicts the results found from the PORFLOW and d^3f/r^3t (see next section) simulations, where it is found also for the no-flux case that the activity flux increases the slower, the higher the diffusion coefficient of the nuclide. This is due to radionuclides that are transported by diffusion from low density brine in the upper layer of the drift into the higher density brine in the lower part of the drift. Consequently, the transport direction of those radionuclide is changed into the opposite direction.

Despite the equal input and release rates, the concentrations in the drift settle below the input boundary concentration (cf. figure 4.27). This is because of the contribution of the exchange processes only, since sorption is not considered.

For the no-flow case, diffusion and temperature (density) gradient are the only driving forces for contaminant transport. The average concentrations, assigned to the center of the drift, are higher with increasing of the diffusion coefficient.

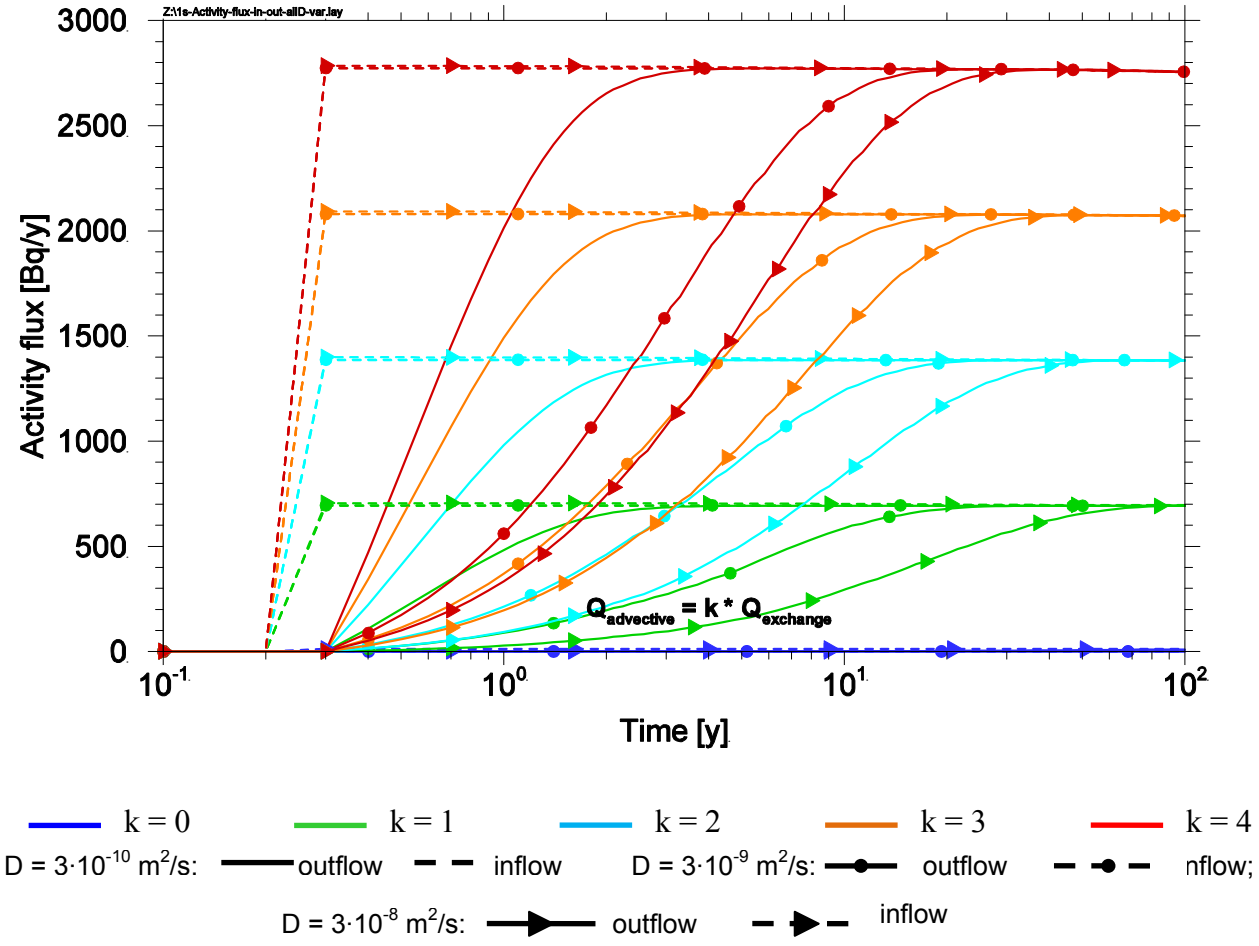

Fig. 4.25: Inflow and outflow activity fluxes [Bq/years] for the drift.

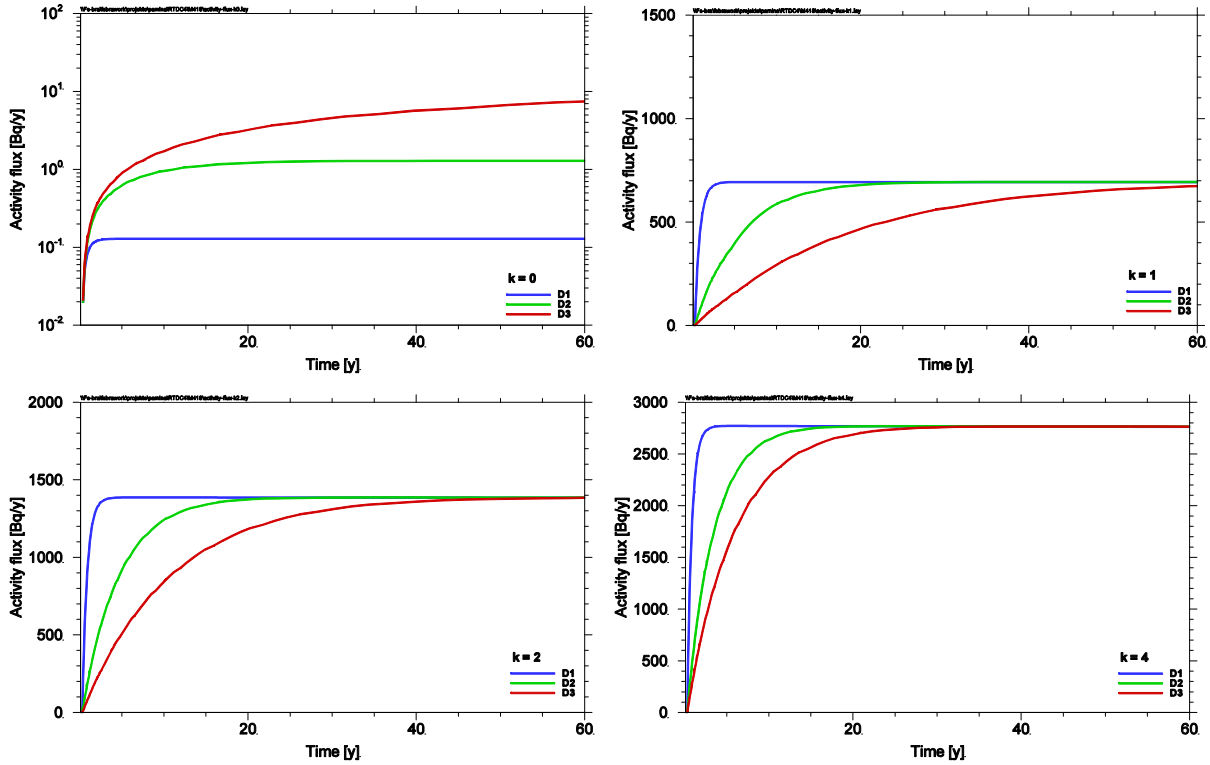

Fig. 4.26: Outflow activity fluxes [Bq/years] for the drift for k=0, 1, 2 and 3.

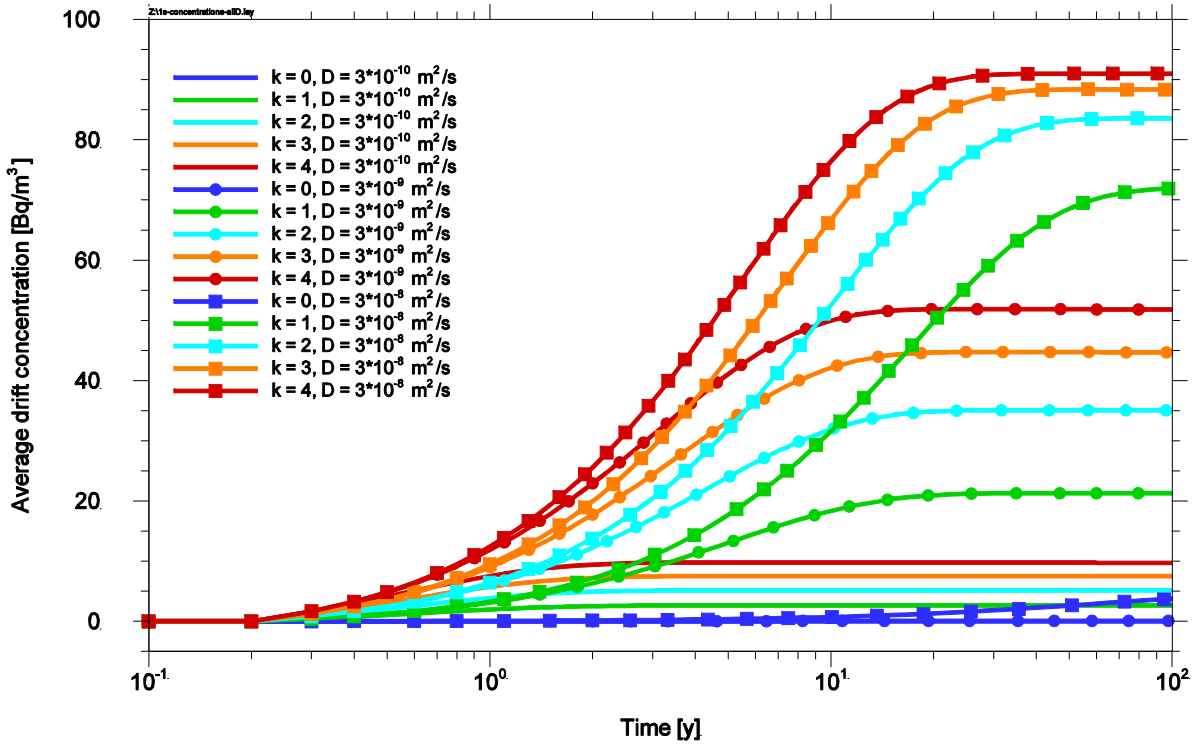

Fig. 4.27: Average concentrations in the drift.

The time dependence of the cumulated activity fluxes, for the three types of contaminants, is shown in figures 4.28, 4.29, and 4.30 respectively. In all simulations, the disposed inventory was not completely released from the system up to 100 years.

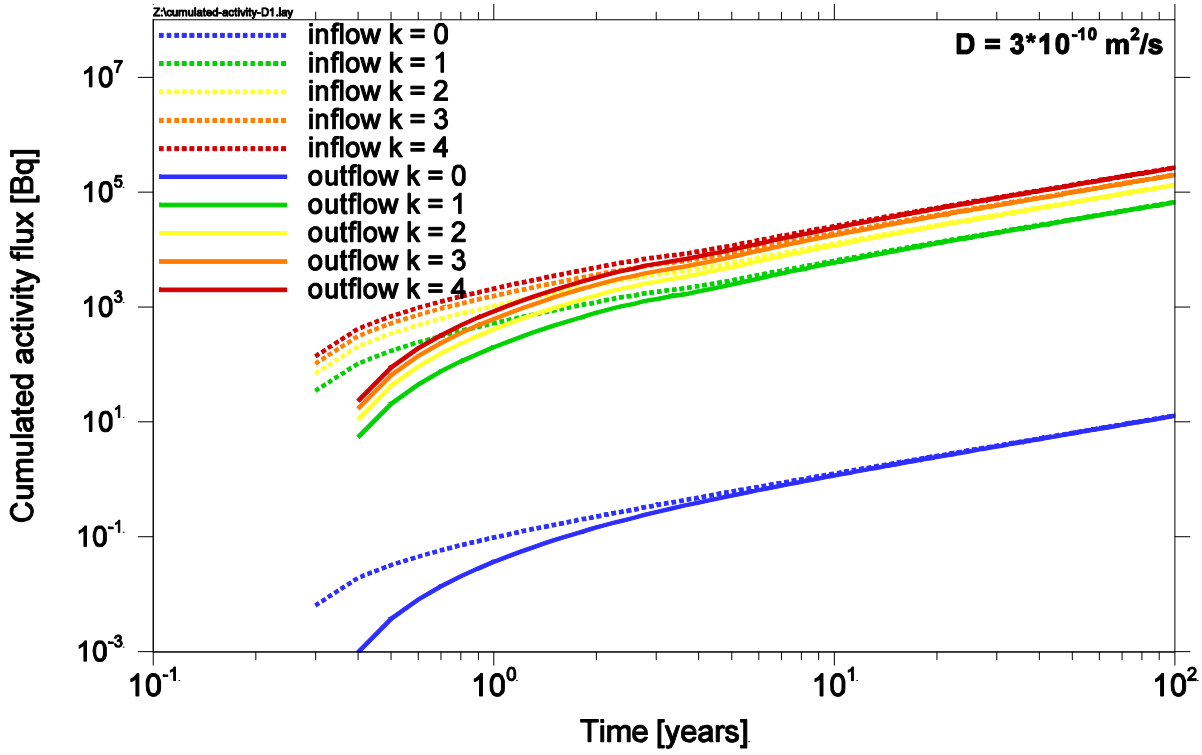

Fig. 4.28: Cumulated activity inflow and outflow for low diffusion case ($D_1 = 3 \cdot 10^{-10}$ m^2/s).

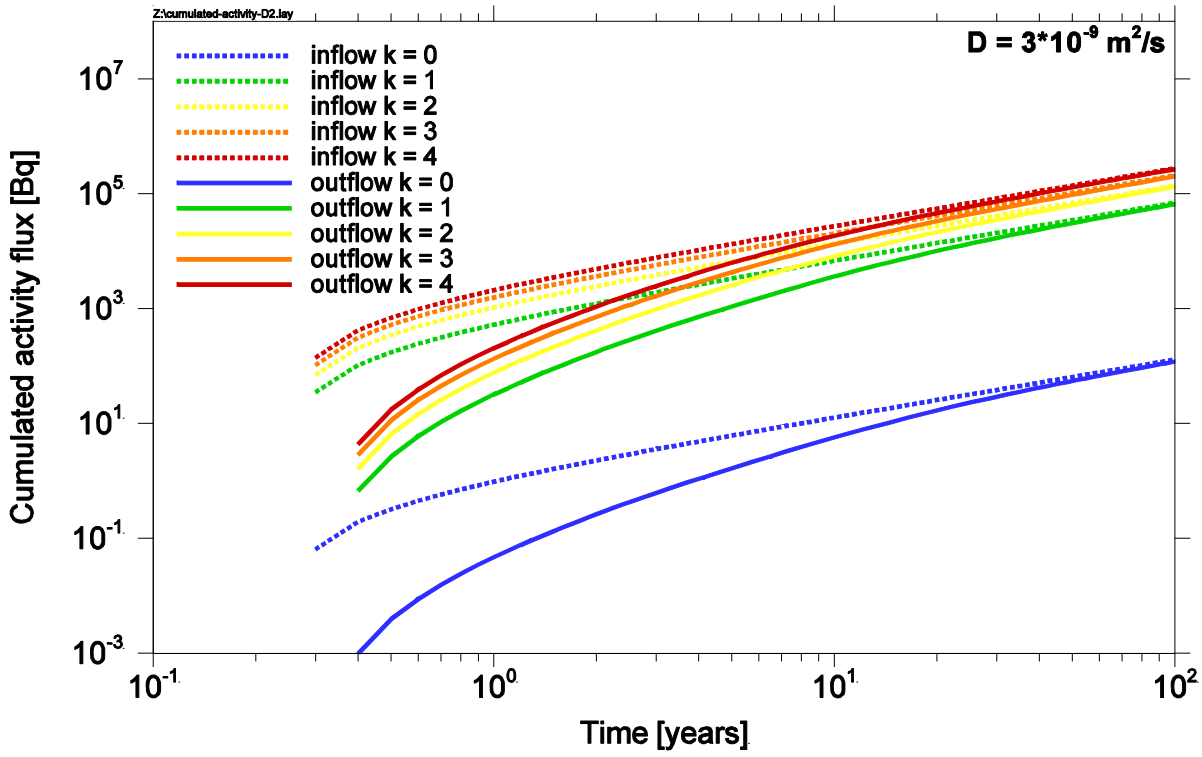

Fig. 4.29: Cumulated activity inflow and outflow for medium diffusion case (D_2 = 3·10^{-9} m^2/s).

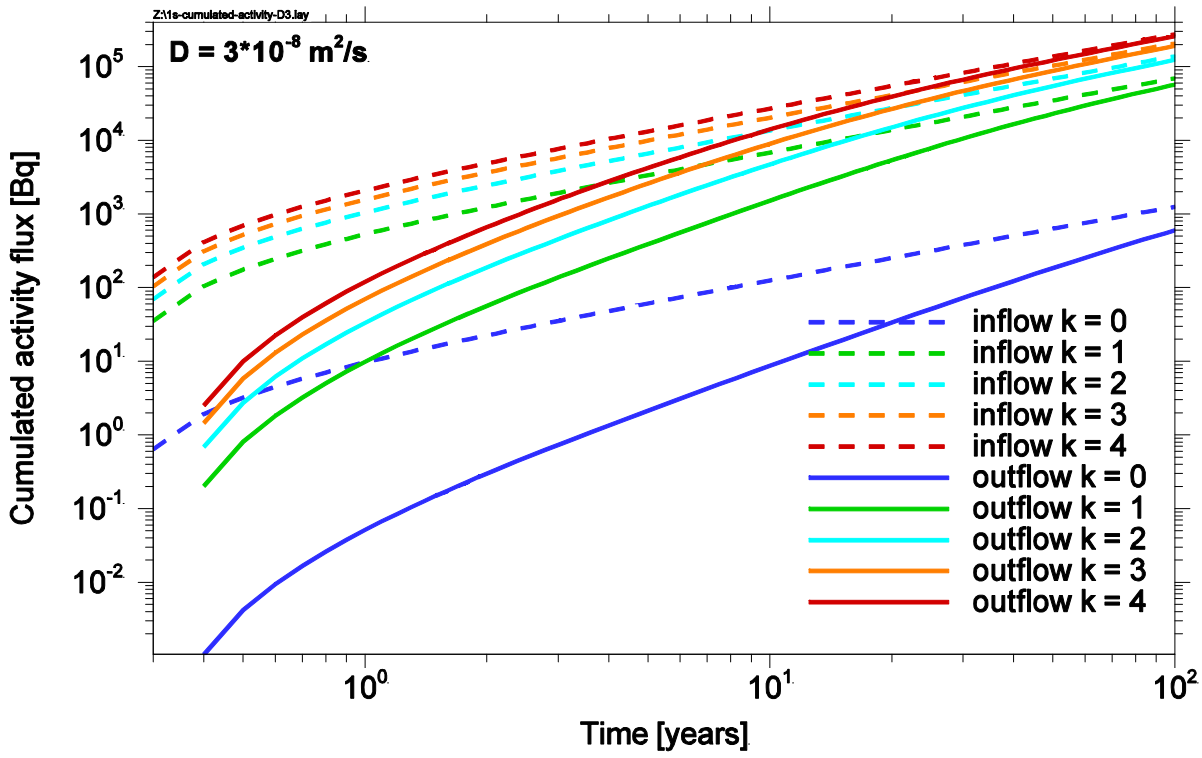

Fig. 4.30: Cumulated activity inflow and outflow for high diffusion case (D_3 = 3·10^{-8} m^2/s).

Cumulated inflown and outflown mass from the drift, at t = 100 years, relative and absolute releases are shown in 4.10. Relative released mass refers to the activity flown into the drift; absolute released mass refers to the total dissolved activity in the source segment (10^8 Bq). Calculation cases are labelled as *D*i*Q*k, where *D* stands for the diffusion coefficient, *i* = 1, 2, 3 represents each of the three values considered for diffusion, *Q* stands for the advective flow, and *k* is the multiplication factor ($Q = k^* Q_{exchange}$).

The results presented in table 4.10 show that slower exchange processes, combined with higher advective rates give the highest relative release (above 90%). An output of the individual contributions from each transport mechanism is not yet implemented in EMOS, therefore it is difficult to analyse the individual contributions of each transport mechanism.

Tab. 4.10: Cumulated in- and out- activity fluxes, relative and absolute variation of the released mass at 100 years.

Case	Cumulated outflow [Bq]	Cumulated inflow [Bq]	Relative released mass [%]	Absolute released mass [%]
D1-Q0	12.75	69127.44	0.02	0.00001
D1-Q1	68664.92	138253.50	49.67	0.06866
D1-Q2	137389.35	207284.82	66.28	0.13739
D1-Q3	206021.36	276315.44	74.56	0.20602
D1-Q4	274674.10	276315.44	99.41	0.27467
D2-Q0	119.34	128.28	93.03	0.00012
D2-Q1	65509.86	69199.09	94.67	0.06551
D2-Q2	132156.18	138175.39	95.64	0.13216
D2-Q3	199357.13	207016.79	96.30	0.19936
D2-Q4	266828.33	275701.72	96.78	0.26683
D3-Q0	603.93	1255.02	48.12	0.00060
D3-Q1	57178.84	69619.56	82.13	0.05718
D3-Q2	123974.46	138409.54	89.57	0.12397
D3-Q3	191949.83	207184.78	92.65	0.19195
D3-Q4	260172.53	275838.16	94.32	0.26017

4.4.3 Application of d^3f and r^3t

4.4.3.1 Simulation of flow with d^3f

The steady state density profiles and velocity fields inside the gallery resulting from the d³f-simulations are shown in figure 4.31. The lower density brine flows, in case of k = 1 to 4 additionally driven by advection on the left hand boundary, from the left to the right at the top of the domain, while the higher density brine inflows from the right hand boundary at the bottom. With growing inflow velocity of the lower density brine, the interface to higher density brine moves more and more to the right, while the mixing zone becomes smaller.

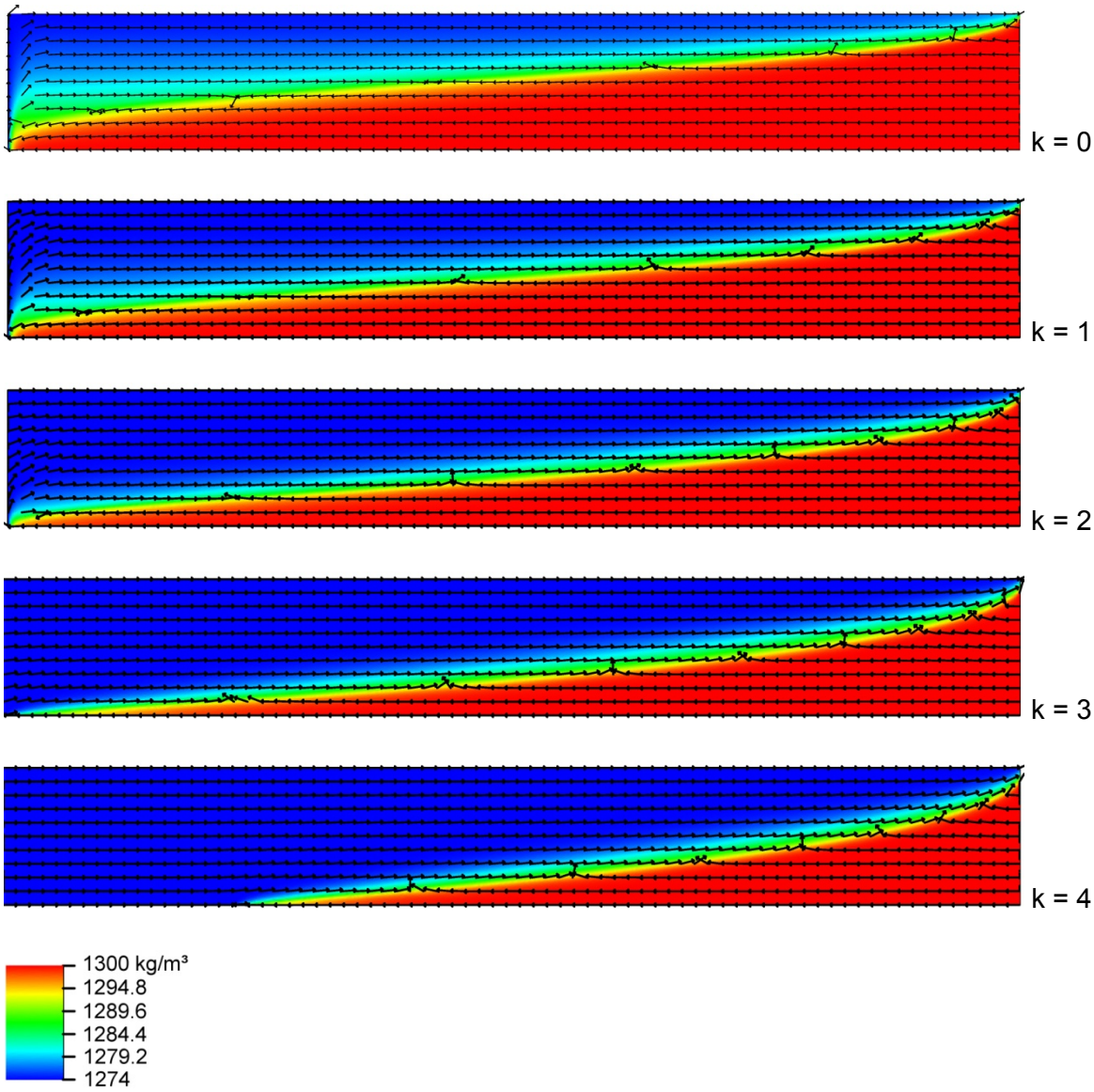

Fig. 4.31: Steady state ensity profiles and velocity fields as results of d³f-simulations for the different cases of inflow

Compared to Porflow, d³f needs no mixing zones, because the different brine densities are given as boundary conditions. Therefore the interface reaches the corners of the modelled domain without any disruption. Because d³f uses a finer grid size than Porflow, one can expect less artificial diffusion effects. A difference in the results consists in the larger transition zone as a result of d³f simulation compared to Porflow. In case of d³f a diffusivity coefficient of only 10^{-10} m²/s was used and dispersivity coefficients of 0.1 m²/s and 0.01 m²/s, respectively.

The velocity profiles in the centre of the gallery (x = 15 m) are depicted in figure 4.32. In contrast to Porflow, the profile is not symmetrical in case of no advective flow, which is probably an effect of diffusion. The Darcy velocity is about 1.01 m/y at the top of the gallery, and 0.77 m/y at the bottom.

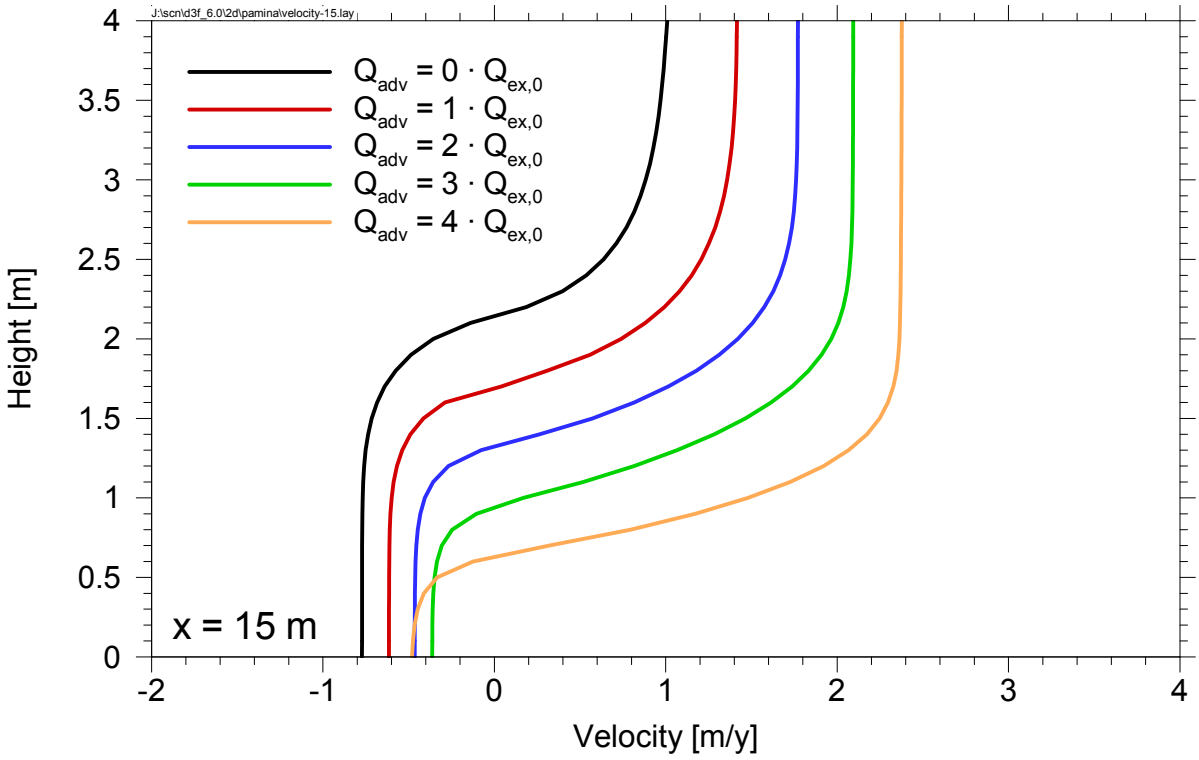

Fig. 4.32: Relative values of Darcy velocity in the centre over the height of the gallery at the steady-state

The nuclide concentrations in the gallery for two cases are depicted in figure 4.33 and 4.34. In case of non advective flow and lower diffusion coefficients the r³t-results obviously show a much larger transition zone than the Porflow-results. In case of $Q_{advective} = 4 \cdot Q_{exchange,0}$ this effect diminishes. One reason of this difference is at least the larger diffusion zone in the density driven flow model, as already seen in figure 4.31. As mentioned above, the finite volume grid may not cause a larger transition zone because only half the grid size of Porflow was used by d³f and r³t. Dispersion effects are also to rule out as a reason because disper-

sivity is scaled by velocity in the equations, and therefore one would expect a larger effect if $Q_{advective} = 4 \cdot Q_{exchange,0}$.

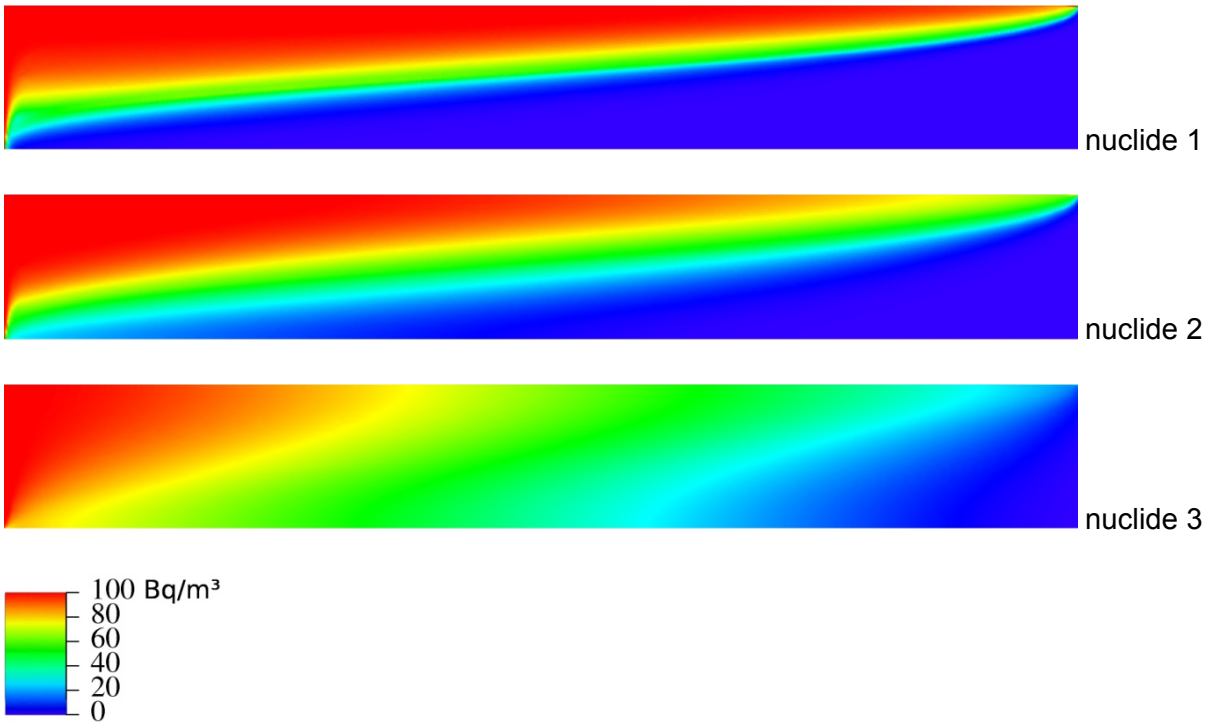

Fig. 4.33: Nuclide concentration in the gallery for non-advective flow

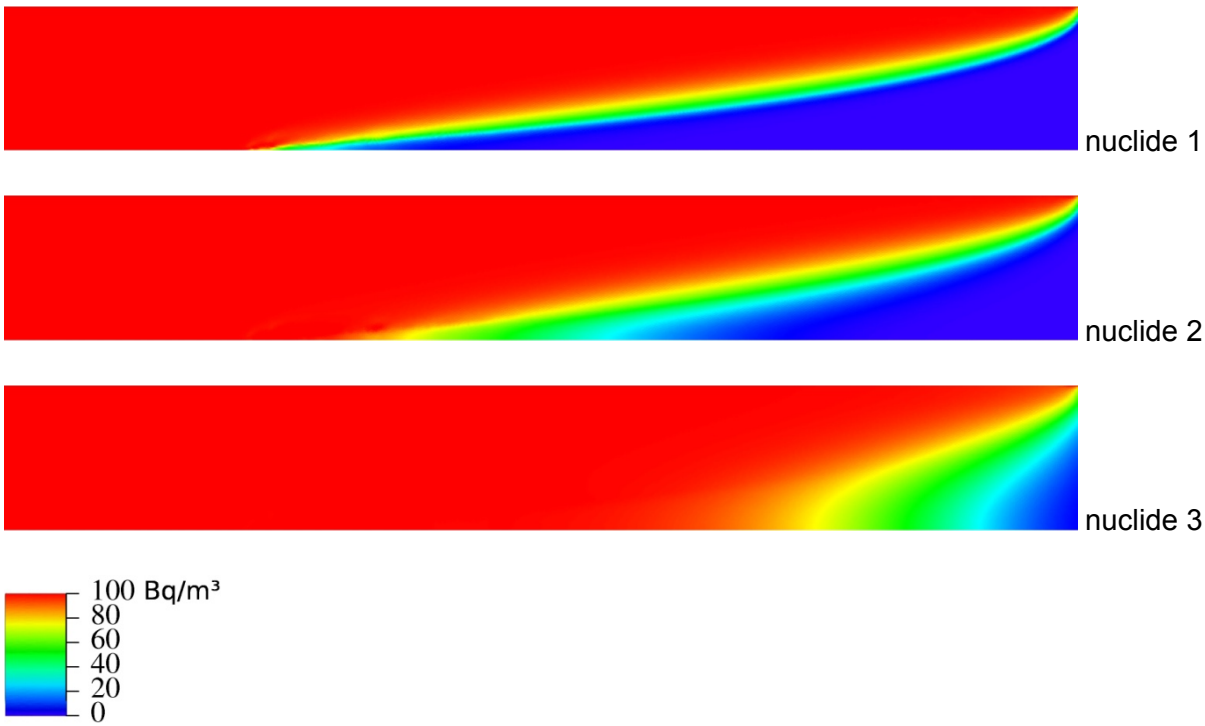

Fig. 4.34: Nuclide concentration in the gallery for the case $Q_{advective} = 4 \cdot Q_{exchange,0}$

Figure 4.35 shows the activity flux through the right hand boundary for the different inflow velocities. Here, the red curve, representing the largest diffusion coefficient, is in all cases the curve of least slope, while it is the steepest and reaches the largest values in case of the highest inflow velocitiy of the Porflow results. In case of k = 0 to 3 the steady-state outflow calculated by r³t is slightly smaller than in the Porflow case, but much higher than in the results of EMOS. Otherwise, the steady-state results of all three Codes fit very well for the higher velocities considered.

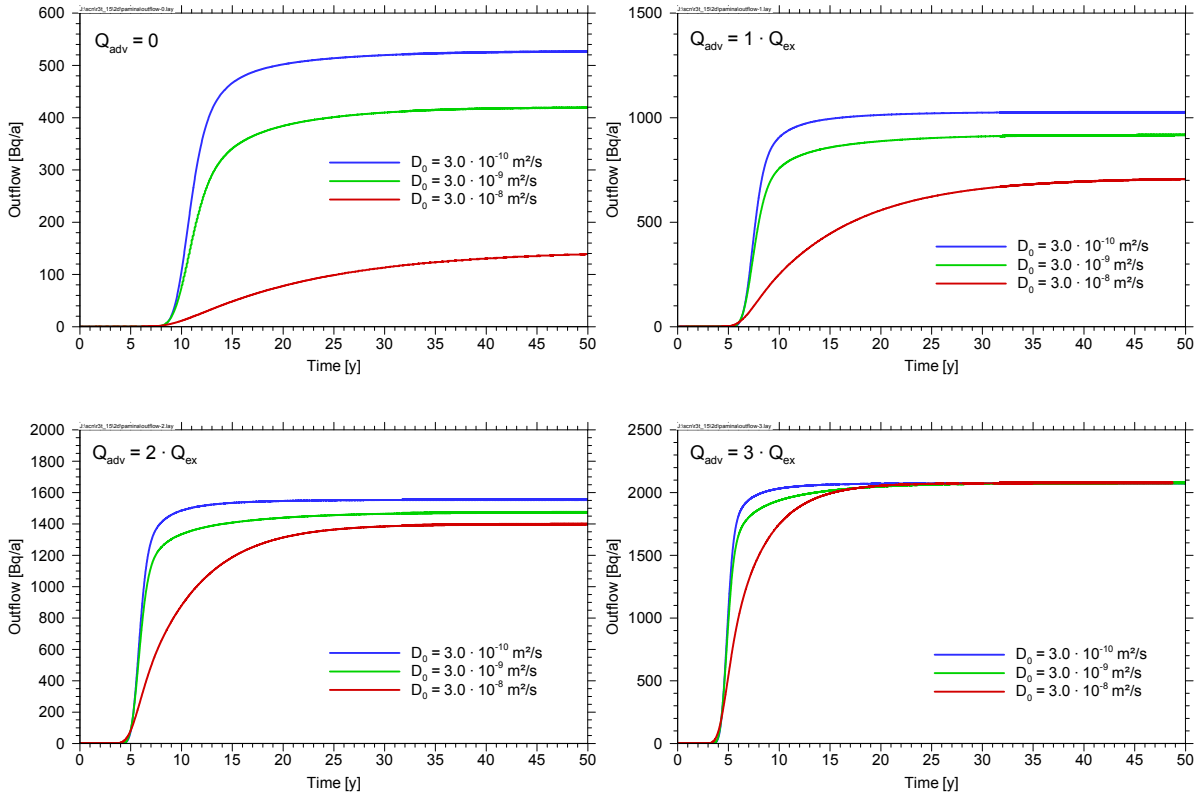

Fig. 4.35: Activity flux at the exit of the gallery for the nuclides 1 to 3 for different advective flow rates

4.5 Conclusions

A theoretical model has been advanced to describe the buoyancy-driven flow of brine as a result of density differences in horizontal galleries in the presence of an additional advective flow. The model has been verified with calculations using the PORFLOW code.

The calculational results show a reasonable to almost quantitative agreement with the results of the theoretical model with regards to the buoyancy-driven exchange flow. The model predicts that the buoyancy-driven flow through a horizontal gallery is completely suppressed by an additional advective flow if the so-called critical advective flow rate equals 4 times the non-advective buoyancy-driven flow rate ($|Q_{adv}| \geq 4*Q_{ex,0}$). The results of the PORFLOW simulations also confirm this value of the critical advective flow rate.

If however the advective flow is less than 4 times the non-advective buoyancy-driven flow, the buoyancy-driven exchange flow results in an enhancement of the total flow rate from a converging waste chamber through a gallery to an adjacent shaft. As a consequence, the enhanced fluid flow can carry nuclides through the gallery also at an increased rate. For the Safety Case this means an increased release of radionuclides in a shaft, which may lead to somewhat enhanced dose rates into the biosphere.

The PORFLOW results show that for nuclides having relatively small values of the diffusion coefficient, the mixing of nuclides between the two overlying fluid flow layers is almost absent. For nuclides having relatively large values of the diffusion coefficients considerable mixing of nuclides between the two overlying layers can be expected. This effect reduces the net transport of nuclides from a waste chamber through a gallery to an adjacent shaft since part of the nuclides will mix with the fluid layer on the bottom part of the gallery and will therefore be transported back into the direction of the waste chamber.

2D simulations which have also been performed with the program package d^3f/r^3t show a good agreement with the results from the PORFLOW code with respect to the density and radionuclide distributions calculated from both programs. However, there are some differences in the details which are most probably due to the different ways of the implementation of the boundary conditions.

The results from the PORFLOW and d^3f/r^3t models were finally compared to simulations performed with the PA code EMOS. With regard to capabilities of EMOS code to represent convective transport processes it has to be concluded that the EMOS code cannot represent the convective driven transport of radionuclides in a sufficient way. This is in particular obvious for the test cases without an additional advective component of the flow. In this case, the activity flux released from the drift increases with the diffusion coefficient. This contradicts the results found from the PORFLOW and d^3f/r^3t simulations, where it is found also for the no-flux case that the activity flux increases the slower the higher the diffusion coefficient of the nuclide. As stated above, this behavior is due to the vertical transport of radionuclides between the two layers of different density which is not considered in the 1D PA code.

4.6 References

[1] ACRi PORFLOW – A Software tool for multiphase fluid flow, heat and mass transport in fractured porous media – User's Manual version 4.00. California, 1999.

[2] Buhmann, D.: Das Programmpaket EMOS zur Analyse der Langzeitsicherheit eines Endlagers für radioactive Abfälle. Gesellschaft für Anlagen- und Reaktorsicherheit (GRS) mbH, GRS-122, Braunschweig, März 1996.

[3] Fein, E.; Schneider, A.: d3f - Ein Programmpaket zur Modellierung von Dichteströmungen. Gesellschaft für Anlagen- und Reaktorsicherheit (GRS) mbH, GRS-139, Braunschweig, Dezember 1999.

[4] Fein, E.: Software Package r3t. Model for Transport and Retention in Porous Media. Final report. Gesellschaft für Anlagen- und Reaktorsicherheit (GRS) mbH, GRS-192, Braunschweig März 2004.

[5] Hart, J.:Radionuclide transport by density driven exchange. PAMINA Milestone M 4.1.13, NRG Report 21952/09.96554/P, Petten, July 2009

[6] Hirsekorn, R.-P.; Boese, B.; Buhmann, D.: LOPOS: Programm zur Berechnung der Schadstofffreisetzung aus netzwerkartigen Grubengebäuden. Gesellschaft für Anlagen- und Reaktorsicherheit (GRS) mbH, GRS-157, Braunschweig, 1999.

[7] Schröder, T., “PAMINA task 2.1.D - Update Model Parameters for Sensitivity Analysis”, NRG Note 2.1952.21/08.88799 RE/TS/ES, Petten, 11 April 2007.

[8] Storck, R., D. Buhmann, R.-P. Hirsekorn, A. Nies, H. Rausch, “EMOS: Programmpaket zur Langzeitsicherheitsanalyse eines Endlagers für radioaktive Abfälle – Version 4“, GRS Braunschweig, September 1990.

5. Conclusions

Three benchmarks have been performed in the PAMINA project to test whether relevant processes for a repository in a rock salt formation are adequately represented in the current PA codes. The benchmarks were performed by comparing the results from simulations with detailed state of the art process level codes with those of current PA codes from NRG and GRS. The three processes regarded are the convergence of void spaces in the repository mine, the inflow of brine into a backfilled gallery and the density driven flow.

For the convergence benchmark the results of the two PA codes REPOS and LOPOS were compared with the result of the rock-mechanic program FLAC3D for 14 different test cases. The simulations with LOPOS use the results of the program FLAC for the simplest test case for calibration. The model parameters derived from this calibration are used to model all other cases without any further adaptation. While the LOPOS model is therefore depending on the rock-mechanics calculations by FLAC the convergence model used by REPOS is calibrated independently on experimental results.

It has been shown that both PA codes are able to represent the convergence process in an adequate way and no current need for program development to represent the convergence process in one of the PA codes used was identified.

For the brine intrusion benchmark the results of the two PA codes REPOS (NRG) and LOPOS (GRS) were compared with the 3D process-level code HYDRUS which is capable to simulate variably-saturated flow. For this benchmark, the van Genuchten approach was used in HYDRUS to model the unsaturated flow. There is a good agreement between the results obtained for the test case with HYDRUS and the two PA codes. In both cases the agreement has been found to be better for the test case with a low permeable backfill, representative for the later lifetime of a repository, when the backfill already has been compacted by convergence. The use of a finer discretization in the PA models yielded better results in some details, but the differences where not significant with regard to the total amount of water flown from the drift (i.e. the cumulated outflow) an important parameter for the description of the filling of the repository in case of brine intrusion. It has been shown that both PA codes are able to represent the inflow to a backfilled drift in an adequate way in comparison with the van Genuchten model.

In the third benchmark for buoyancy driven flow the results of two process level models with the codes PORFLOW and d^3f/r^3t have been compared with a semi-analytical model and the PA code REPOS. The results from the two process-level model show some differences that can be explained by the different boundary conditions used.

The results from the semi-analytical model show a reasonable to almost quantitative agreement with the results of the process-level code with regards to the buoyancy-driven exchange flow. From the comparison of the results of the process-level simulations with REPOS it has to be concluded that the REPOS code cannot represent the convective driven

transport of radionuclides in an adequate way. This is in particular obvious for the test cases without any additional advective component of the flow. In this case, the activity flux released from the drift shows a completely different dependency of the total radionuclide flow on the diffusion coefficient compared to the results of the process-level codes PORFLOW and d^3f/r^3t. The representation of the convective transport processes in the REPOS code will have to be further developed in the future.